Development and Integration of Tactors onto a Prosthetic Socket for Tactile sensory feedback in Upper Limb Amputees

by

Katherine R. Evans

A thesis submitted in partial fulfillment of the requirements for the degree of

Master of Science

Department of Mechanical Engineering
University of Alberta

Abstract

Myoelectric prostheses have recently undergone extensive developments in their complexity and movement patterns, yet controlling these devices can be difficult as they lack the sensory feedback provided by traditional body powered prostheses. With targeted sensory reinnervation surgery, sensory nerves are relocated within the residual limb so that when touched on part of the reinnervated skin, the patient feels as though they are being touched on their missing limb. This restored hand map can be harnessed to provide feedback to the patient such that when they grip something with a robotic hand, a small device (termed *tactor*) pushes into their reinnervated skin and they feel as if they are gripping the object directly.

The aim of this thesis work was to refine the design of this tactor system, evaluate various methods of system measurement and control, and integrate the tactor system onto an above-elbow prosthetic limb. A review of existing sensory feedback devices was conducted, where modality matched mechanotactile feedback was found to be the most promising non-invasive method of providing feedback to the user. Two tactor designs were investigated; a linear tactor, and a cable-driven tactor with a reduced vertical profile. Tactor parameters were optimized and evaluated to improve functionality, minimize size, cost, and weight, as well as quantify system capabilities. Two cable-driven tactors were integrated onto an above-elbow prosthetic socket for initial system evaluation with a participant with a transhumeral amputation, a task that has yet to be demonstrated elsewhere. Recommendations from this evaluation led to further investigation into methods of system measurement and control, as well as a preliminary investigation of various sealing methods for tactor integration, where an optimal membrane seal was determined. This tactor system is significantly less expensive than research versions currently available, however there is a trade-off in closed-loop control performance, which yields less accuracy and responds outside of the 200 ms threshold of noticeable delay. There is a need for improved measurement and control, collection of usability data to provide guidance for further refinement of the design, as well as further study into the long term performance of the system.

While future work is warranted, this thesis provides significant contributions to the body of knowledge surrounding the design and integration of tactor systems onto a prosthetic socket. These findings will aid in effective translation of these devices to a clinical setting, which has the potential to improve the quality of life for upper limb amputees.

Preface

This thesis contains information from three journal articles authored and co-authored by the writer. Two of these papers are under review as of the publication of this thesis.

1. Schofield, J.S.; Evans, K.R.; Carey, J.P.; and Hebert, J.S. *Applications of Sensory Feedback in Motorized Upper Extremity Prosthesis: A Review*. Expert Review of Medical Devices. June 13, 2014.
2. Evans, K.R.; Schofield, J.S.; Dawson, M.R.; Carey, J.P.; and Hebert, J.S. *Optimization of Tactor Parameters to Improve Discrimination and Comfort for Sensory Feedback in Upper Limb Amputees*. IEEE Transactions on Neural Systems & Rehabilitation Engineering. Under review as of September 23, 2015.
3. Schofield, J.S.; Evans, K.R.; Hebert, J.S.; Marasco, P.D.; and Carey, J.P. *The Effect of Biomechanical Variables on Force Sensitive Resistor Error: Implications for Calibration and Improved Accuracy*. Journal of Biomechanics. Under review as of November 8, 2015.

In study number (1) the writer shared the work of collecting papers for the literature review, distilling information, and writing the article. In study number (2) the writer led the planning, data collection, analysis of the data, and writing of the article. In study number (3) the writer shared the design of the study, analysis of results, and revising of the manuscript.

Approval for the studies within this thesis was obtained from the institutional Health Research Ethics Board, and all participants provided written informed consent. Able-bodied participants are covered under “Development of a myoelectric training tool for above elbow amputees” (Pro00017008), while amputee participants are covered under both “The development and clinical testing of advanced myoelectric technologies” (Pro00030709) and “Restoring upper limb movement sense to amputees” (Pro00034663).

Acknowledgements

I would sincerely like to thank all of those who I have interacted with over the past two and a half years; each and every person has had a lasting impact of my development as a researcher, scholar, and member of society.

Firstly I would like to thank my co-supervisors, Dr. Jason Carey and Dr. Jacqueline Hebert. Both have helped to foster a very positive and encouraging environment which I truly appreciate. Jason has not only been my mentor during my graduate degree, but also throughout my undergraduate degree, both as a supervisor and program coordinator. His guidance has been invaluable towards my research and career success thus far. Jacqueline has developed a very strong team of researchers and clinicians within the Bionic Limbs for Improved Natural Control (BLINC) lab. This environment allows us to perform strong work that has the potential to have a real impact on the patients we are dedicated to helping. She graciously welcomed me into her lab just over two years ago and has encouraged my involvement in many interesting projects and supervisory roles. Her clinical perspective and support have been invaluable towards the completion of this project. Both Jason and Jacqueline have shown strong dedication to their research and supervisory roles, for which I am very grateful.

I am very grateful for the funding support I have received from the Natural Sciences and Engineering Research Council of Canada, Alberta Innovates Technology Futures, and National Institute of Health. Thank you to the Glenrose Rehabilitation Hospital Foundation for their support of this project.

This work has been completed with extensive advice and guidance from an interdisciplinary team of researchers and clinicians from the BLINC lab. In particular I would like to thank Michael Rory Dawson and Jonathon Schofield for their support throughout my time in the lab. They have continuously provided advice and feedback and play a large role in making the lab a fun and encouraging environment. Thank you also to Michael Stobbe for his practical advice and contribution of ideas. Thank you to Dr. Patrick Pilarski and Dr. Ming Chan for their encouragement and enthusiasm. And thank you to the other students, clinicians, and researchers in the lab who

I do not have space to thank here but have had a huge impact on my life in terms of their support, interesting discussions, and good company.

Thank you also to the members of the Composite and Biomedical Materials Research Group for being so supportive with coursework, teaching, and professional development. I have had the great privilege of getting to see these lab mates through various stages of their careers and am confident that they will all be very successful in whatever paths they choose to follow. I am also very grateful for their good company and wonderful sense of humor. This encouraging environment has been an important part of my degree.

Thank you to all of the professors on campus who have provided me with guidance through my degree, in particular thank you to Dr. Renee Polziehn for her insights and inspiration, and her dedication to serving the University of Alberta and community.

Finally I would like to thank my family and friends for their love and support. My parents have always encouraged me to pursue further education and follow my own path; I truly appreciate all they have done in raising me and my sister. On top of their dedication to their work they have always valued the importance of family, for which I am extremely grateful. Thanks to my sister Susan for being such a great supporter; she always makes sure humor is a constant in my life. And thank you to my extended family, especially the Erdmanns who have been our close family since moving to Edmonton over ten years ago. Thank you to my friends who I have met over the years, from high school to university and beyond; I cannot mention everyone here but their friendship is something I truly treasure. Finally, thank you to my fiancée Travis Schoepp for his love, encouragement, and friendship. He has been my biggest supporter over the past four years and his kindness, intelligence, and dedication are inspiring and something I hope to emulate in everything I do.

Table of Contents

Chapter 7. Sealing Methods ... 115

List of Figures

List of Tables

Chapter 1. Introduction

1.1 Problem

Upper limb loss can significantly reduce a person's quality of life, leaving an amputee feeling less capable and independent. Myoelectric prosthetic devices are becoming more complex and dexterous, with major advances in control and functionality [1]. However, it has been reported that up to 25% of myoelectric prostheses are rejected, and sensory feedback is often cited by amputees and clinicians as a desirable improvement [2, 3]. While various sensory feedback methods have been explored in literature, no devices are commercially available [4]. As well, integration of these devices onto a prosthetic socket have not been explored in detail, which is a substantial barrier to clinical translation [4].

1.2 Objectives

The focus of this thesis is on developing a mechanotactile feedback system, in which pressure is sensed on the terminal device and translated as a pushing force onto the residual limb, thus matching the modality of the stimulus sensed on the prosthetic hand [4, 5]. This pushing force is translated onto the residual limb by a device (termed *tactor*), which is mounted onto the socket on the residual limb or over accessible skin areas [4, 5].

In order to effectively translate these tactors, the objectives that must be met include: (1) optimize tactor parameters to improve information transfer, (2) refine and evaluate the overall tactor system, (3) develop a control system to map between forces measured on the prosthetic hand to forces applied to the residual limb, and (4) develop a method for integrating this system onto a socket without compromising functionality.

1.3 Chapter Summary

In Chapter 2, a general background discussion of the epidemiology of the target population is provided, as well as a brief history of prosthetic device development, current prosthetic technology, and desirable features for a prosthetic limb. It summarizes the different types of sensory feedback that have been investigated for prosthetic applications, and outlines characteristics of an ideal feedback system.

In Chapter 3, the optimal size and shape of the tactor head (the component touching the skin) is determined in order to provide the most information to the user while maintaining maximum comfort. A designed experiment was conducted through participant trials comparing two-point discrimination and comfort of different combinations of parameters.

In Chapter 4, the design refinements to the tactor system as well as evaluation of system abilities are outlined. Design modifications to both the linear and cable-driven tactors are discussed, and a compliance matrix is provided.

In Chapter 5, integration of the cable-driven tactor system for testing with both able-bodied and amputee participants is outlined. Preliminary testing of the tactor system on a temporary prosthetic socket was conducted with a participant with a transhumeral amputation. Required improvements to the system were identified, including a need for force quantification of applied tactor forces and a method for maintaining a suction seal within the socket.

In Chapter 6, force measurement, signal processing, and control of the tactor system are detailed. Various sensors are evaluated based on research and bench top testing, and several filtering techniques are investigated. Open- and closed-loop control systems are contrasted, with time-delay and accuracy considered.

In Chapter 7, the integration of the tactor onto a prosthetic socket such that the air-tight seal of the socket is not compromised is detailed. Bench-top testing of various sealing membranes is outlined, with a final sealing method recommended for further evaluation.

The potential impact of this tactor system will be an inexpensive, practical, and feasible sensory feedback system that can be easily integrated into sockets for upper limb amputees to help them improve their function with myoelectric devices. The lessons learned from the pilot data collected will feed into future improvements and research trials. Overall, this project aims to improve the function and quality of life for patients living with the loss of an upper-limb by providing sensory feedback from their prosthesis, and could have an impact across Canada and worldwide due to the novel and inexpensive approach to a challenging problem.

Chapter 2. Background

2.1 Prosthetic Arms

2.1.1 Population

In 2005 there were an estimated 1.6 million people living in the United States with the loss of a limb [6]. While epidemiology data specific to Canada could not be found, the country may show similar proportions to the United States. Major limb loss is defined as loss of a limb above the ankle or wrist, as opposed to minor limb loss which is an amputation of the toes, fingers, or partial hand and foot. Major upper limb loss accounts for between 6 and 10% of the major amputations in the United States (Figure 2.1) [6, 7]. This introduces challenges to upper limb prosthesis treatment, as the relatively low number of upper limb amputations results in fewer practitioners with the skills for proper fitting and therapy [1, 8].

The main causes of amputation in those living with limb loss (prevalence) in the United States are dysvascular disease (38 to 54%), trauma (39 to 45%), and cancer (1 to 23%) [6, 7]. The majority of persons with major upper limb loss had traumatic amputations (89 and 71% of below and above elbow, respectively) [7]. People with traumatic amputations are younger on average than those whose amputations are the result of disease (47 versus 56 years old on average) [7], where 73% of those with a traumatic amputation are younger than 65 years old [6]. This means that those with upper limb loss will often live with their amputation for many years.

Major upper limb loss is one of the most difficult challenges for prosthetic replacement, given the complexity of fine sensory input and dexterous function of a hand, and the loss of a hand can significantly reduce quality of life leaving a person with an amputation feeling less capable and independent [1, 9].

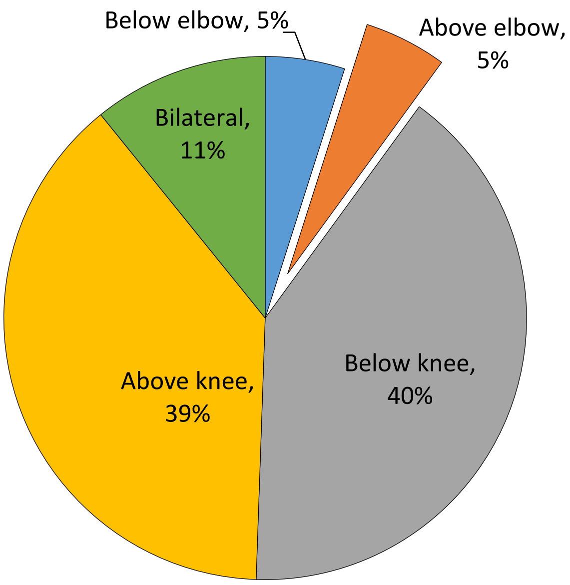

Figure 2.1 Proportions of major limb loss [7]

2.1.2 Brief History

Prosthetic devices have been found throughout history. The earliest written account is from India between 3500 and 1800 BC, where the Warrior-Queen Vishpla lost her leg in battle and was fitted with an iron prosthesis to enable her to return to battle. One of the first prostheses found was the prosthetic toe of an Egyptian mummy, dated from the fifteenth century BC. Prosthetic devices during the Dark Ages were typically heavy and crude and were most often battle related, or acted to hide the existence of an amputation [10]. In the 1500s, Ambrose Paré improved amputation surgery and developed new orthotic and prosthetic designs for upper and lower limb prostheses using wood, metal, and leather materials. Some of his designs incorporated moving components such as pulleys in place of joints [11].

With the emergence of 20th century industry, the demand for upper limb prostheses unrelated to warfare began to drive further advancements [8]. Many improvements to prosthetic design were made as a direct result of the two World Wars. The main advancements during this time were the development of laminated plastic sockets, locking and sliding clutch mechanisms to close grippers, multiplier lever systems, hollow-casted finger mechanisms, improved cable designs, and electrically powered systems [12].

2.1.3 Current Technology

Prostheses are typically passive, functional, or a combination of both. Functional prostheses are subdivided further into body-powered or myoelectric prostheses [1, 9] (Figure 2.2).

Body-powered prostheses (Figure 2.3) are controlled with movements of the body, via a cable and harness system, generally attached across the back using straps. They are durable and relatively inexpensive, but have limited movement and strength. The

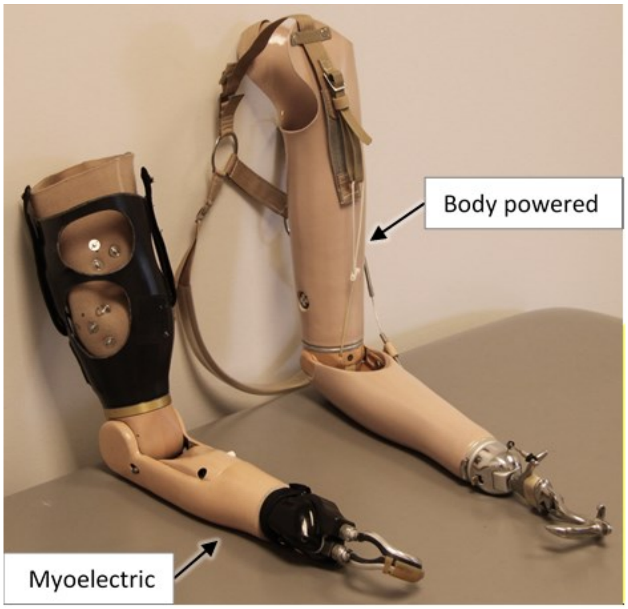

Figure 2.2 Image of myoelectric and body powered prostheses

terminal device is typically restricted to open and close movements activated by shoulder and scapular movement, making many daily tasks challenging [9, 13].

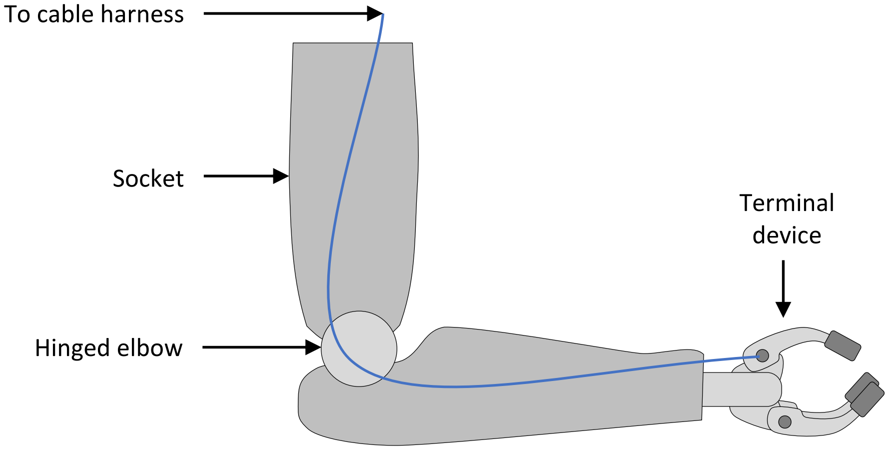

Figure 2.3 Diagram of a body powered prosthesis

Recently, there have been extensive advances in myoelectric prosthetic arms (Figure 2.4) which are dexterous, multi-functional, and motorized, capable of a wide range of grasps for use in restoring functionality to those with upper limb amputations. The prostheses are typically controlled using surface electromyogram (EMG) signals generated by the muscles. These signals are measured by electrodes and can be used to control various aspects of the arm, such as the position of the joints, grasp pattern, and grip force [9, 13].

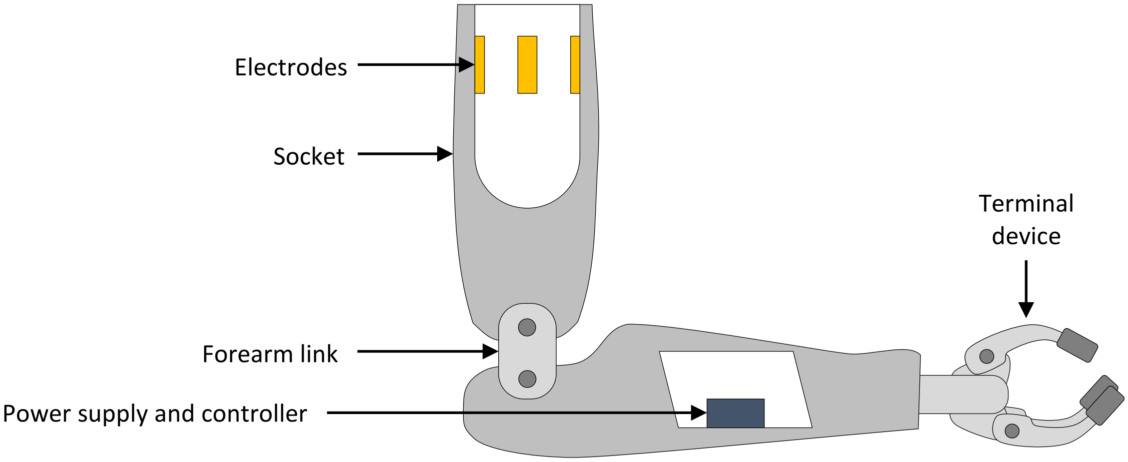

Figure 2.4 Diagram of a myoelectric prosthesis

One of the most advanced myoelectric arms is the Modular Prosthetic Limb (MPL) developed at Johns Hopkins University (Figure 2.5). This arm allows for movement in the same degrees of freedom (DOF) as a human arm (22 DOF), has anthropometric geometries, strength, and dexterity, and is fully sensorized [14]. Another is the DEKA arm (DEKA Integrated Solutions Corp.) which is smaller and lighter, uses endpoint control, and can be positioned in various ways including foot controls, but with fewer powered DOF than the MPL (10 plus the wrist) [15]. While these prosthetic arms are currently not available commercially due to high cost and complexity, they are valuable in research settings.

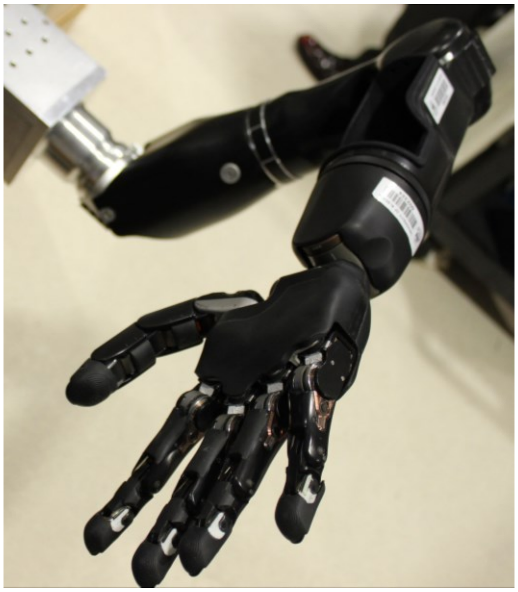
Figure 2.5 Image of MPL

Designers have begun to leverage the use of rapid prototyping to manufacture prosthetic components. Rapid prototyping is an additive manufacturing technique which builds a part layer by layer based on an input Computer Aided Design (CAD) model, and is available in a wide range of materials [16]. With rapid prototyping, patient specific prosthetic devices can be optimized, assembled, ventilated, and customized more easily than using traditional manufacturing techniques [17]. Inexpensive hands have been developed, such as the e-NABLE hand, developed by a volunteer based community which aims to provide low-cost body-powered prosthetic hands to those in need [18].

2.1.4 Desirable Features

Despite their advancements, myoelectric arms are not used widely in clinical settings, with the traditional cable-driven, body powered hook-and-pulley system still being the most common [1]. This is partially due to the high cost of the newer prostheses, but also to the lack of sensory feedback provided as compared to the body powered prostheses that provide feedback through mechanical coupling from the gripper to the shoulder straps [19].

In a survey of upper limb amputees in Australia, it was found that 56% of people wear their limbs “once in a while” or “never”. Prostheses are most often worn “all the time” during work (35%) and social activities (30%) [20].

Device abandonment is detrimental as people can become less able to function; in the case of those with a unilateral amputation, they will rely more heavily on their sound arm which can lead to repetitive stress syndromes, resulting in pain and reduced functionality [8]. Between 22 and 30% of upper limb amputees completely abandon their prosthesis [21]. Device abandonment can be influenced by a multitude of factors, such as lack of effective control, weight, comfort, appearance, fitting time frame, level of amputation, reliability, and durability, to name a few [2, 3, 22, 23]. In a survey of clinicians and amputees, it was determined that comfort is considered to be the most important factor for unilateral amputees, while function is more important for bilateral amputees; in both cases, comfort and function are more important than cosmesis [22]. Somewhat intuitively, those born with a congenital amputation are likely to reject their prosthesis, potentially as they have adapted to function without the limb from birth. People with an acquired amputation are more likely to accept their prosthesis to at least partially replace the lost function they are accustomed to [13].

Lack of sensory feedback is listed as a main reason for rejection of myoelectric prosthetic limbs [1, 24], and integration of sensory feedback, particularly grip force and proprioception, are of great importance to prosthesis users [25]. However, as of yet there are no standardized methods to clearly quantify the benefits of incorporating sensory feedback into a prosthetic socket.

2.2 Sensory Feedback Methods

Sensory feedback provides information to the user about the state of their prosthesis, and can be provided using a variety of different methods. A simple, reliable sensory feedback system may improve the use and acceptance of myoelectric devices (Figure 2.6).

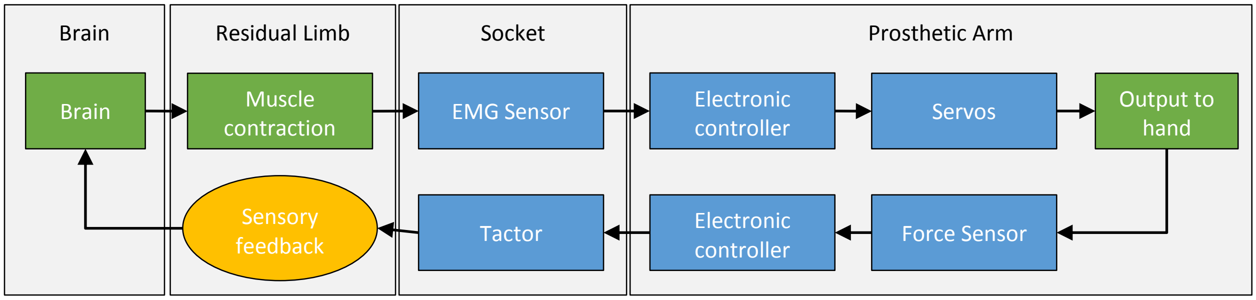

Figure 2.6 Schematic of the process used to control a prosthetic device, incorporating sensory feedback

Feedback can be provided using substitution (in which feedback is delivered through a different afferent (sensory) pathway than normally used), modality-matched (in which feedback is delivered through the same afferent pathway that is normally used), and somatotopically-matched (in which the feedback is perceived as being applied at the correct location) [4, 5]. These different methods are summarized in Figure 2.7. For further discussion of methods for sensory feedback in upper limb amputees, see review paper [4].

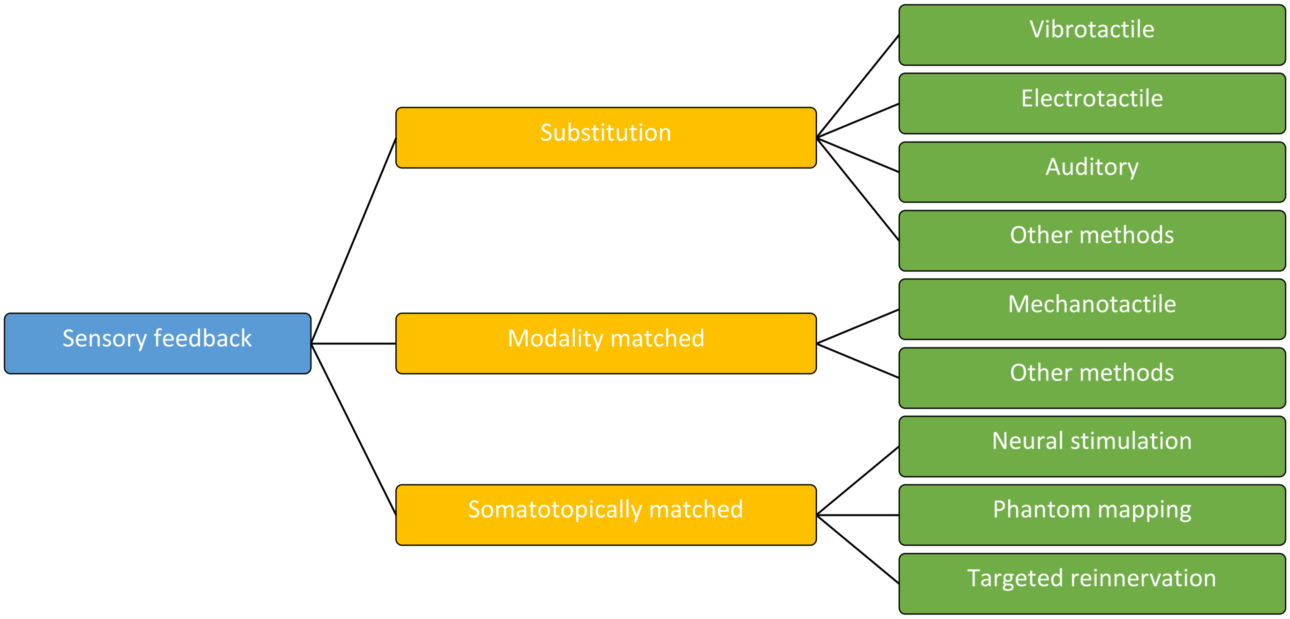

Figure 2.7 Schematic of types of sensory feedback

2.2.1 Substitution Methods

With body-powered prosthetic systems using a hook and cable, sensory feedback occurs as the brain learns to remap one particular sense to correspond to another. For example, people can learn to associate strength of prosthetic grip with the tension in the shoulder straps of their body-powered prosthesis. Sensory substitution methods could be used for myoelectric prostheses as well, by associating grip strength with various different stimulations.

Substitution methods (Figure 2.8) can be vibrotactile, where the skin is mechanically vibrated at various frequencies and amplitudes [26-35], electrotactile, where afferent nerve endings are stimulated by a local electrical current [36-42], or less common modalities, such as auditory cues [43], skin stretch [44], or torques about the elbow [33, 45]. Of these methods, vibrotactile feedback is most commonly used, as is it compact and has relatively low power demands [4].

It is generally thought that substitution methods require a larger amount of concentration to interpret, or a higher cognitive load, but may be the most technically straightforward and flexible of the various methods [4].

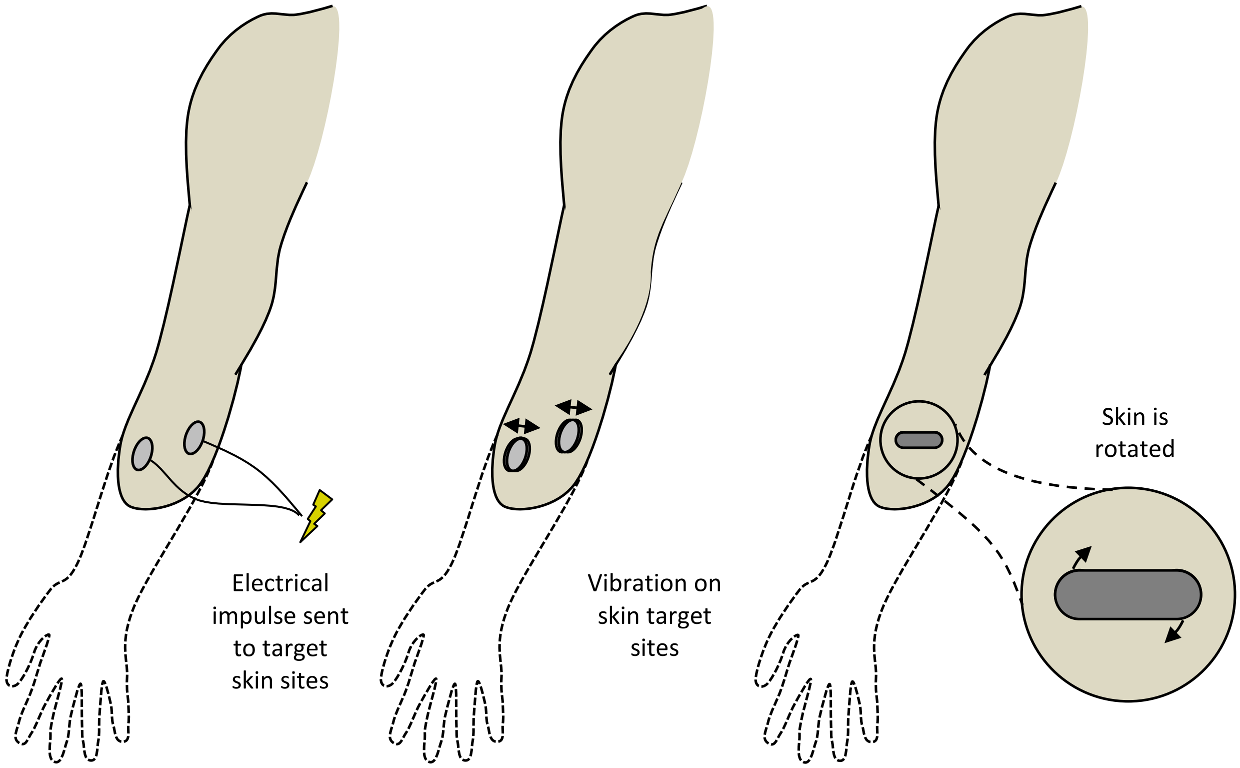

Figure 2.8 Schematics of potential substitution methods, adapted from [4]

2.2.2 Modality Matching

Modality-matched feedback (Figure 2.9) incorporates the ability to match the type of stimulus with the input (modality matching) and may improve intuitiveness (i.e. touch and grip pressure represented by increasing force input).

Examples of modality matched feedback include mechanotactile stimulation where a normal force is applied to the skin using a tactile stimulator (termed *tactor*) when the prosthesis is stimulated by touch [26, 28, 34, 35, 46-52], and thermal stimulation where a heat flux is applied to the skin when the prosthesis is subjected to heat [47].

Multimodal tactors have also been developed which can provide perpendicular and tangential force, vibration (to indicate slipping and texture), and temperature [34, 47, 49, 53]. The usefulness of providing this large amount of information has yet to be investigated, as it may involve a larger degree of conscious attention [4, 34].

One drawback of modality matching is that these systems may respond with a longer time delay compared to other feedback methods [5].

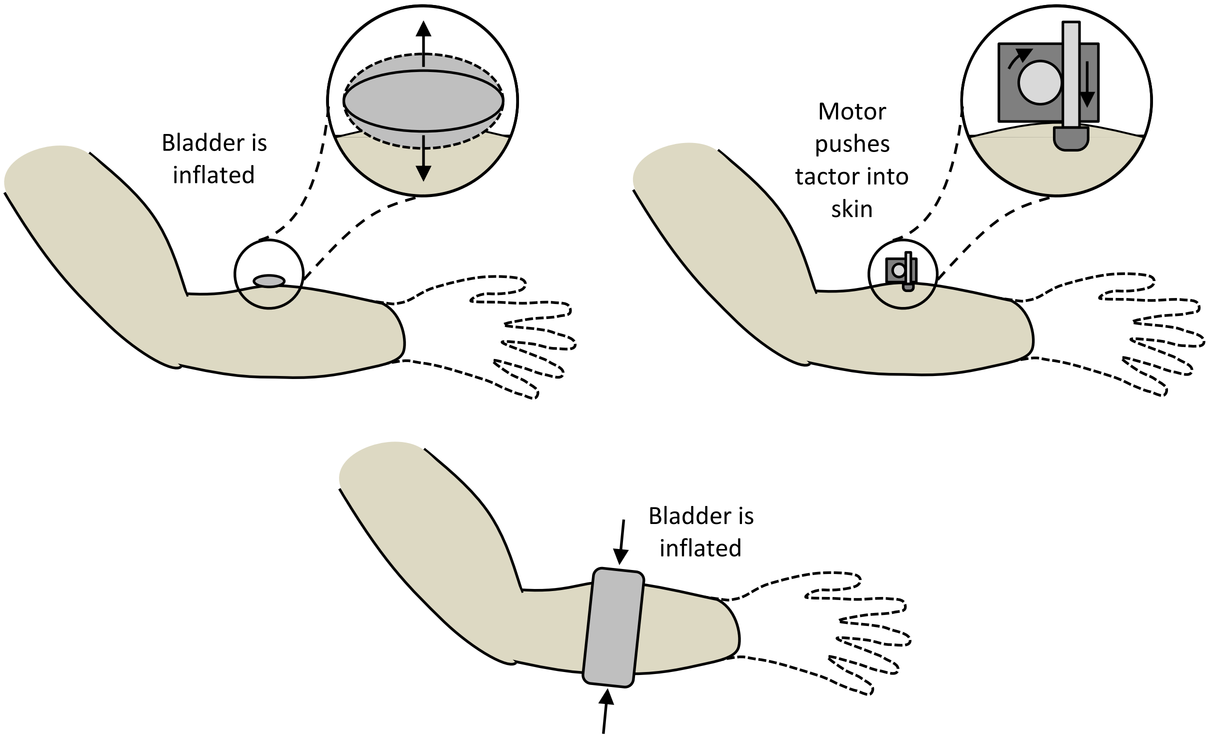

Figure 2.9 Schematics of potential modality matched methods, adapted from [4]

2.2.3 Somatotopic Matching

Even with modality matching, a limitation to these methods has been the lack of ability to somatotopically match the input and stimulus (i.e. touch to the prosthetic digits feeling like touch to the missing fingers). Providing somatotopically matched feedback (Figure 2.10) may reduce the cognitive burden placed on the user [4].

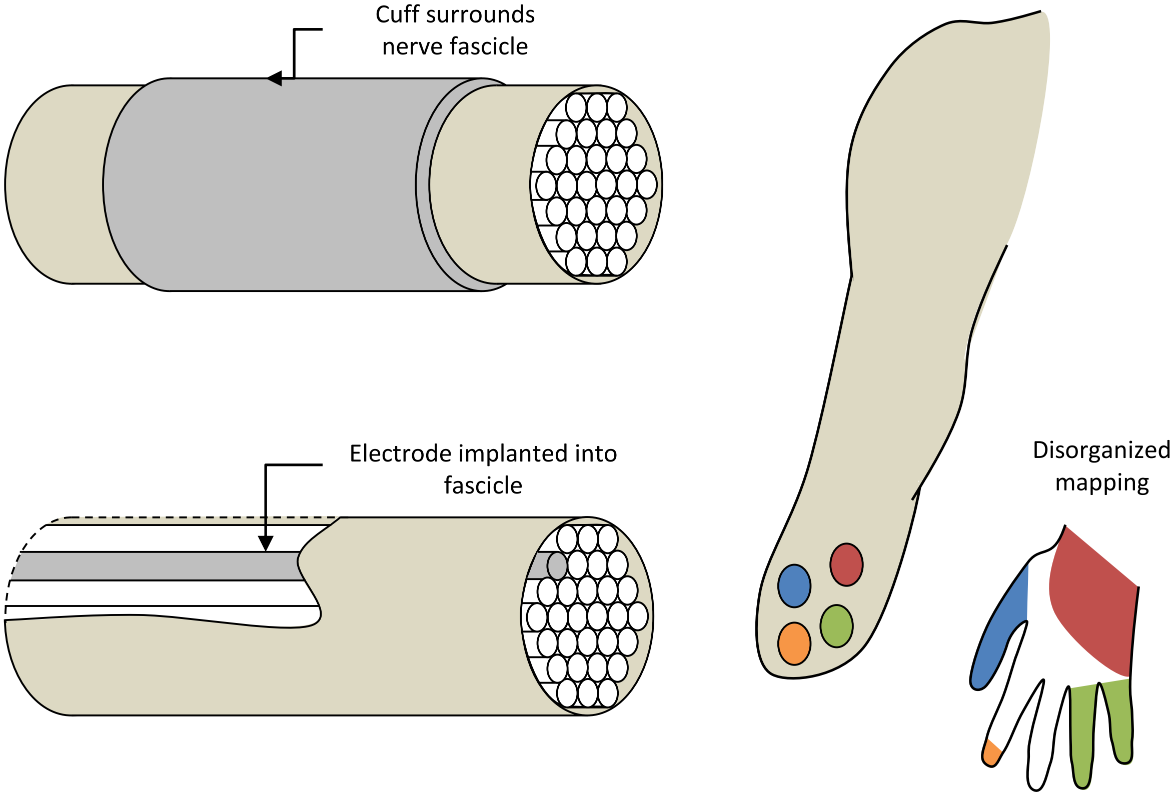

Figure 2.10 Schematic of somatotopic matching methods, adapted from [4]

Somatotopic matching may involve direct neural stimulation where invasive neural electrodes are implanted into the peripheral nervous system in the nerves that previously received feedback from the missing limb [54], or less invasive methods of matching feedback to the naturally occurring phantom map or intervening with targeted sensory reinnervation (TR).

Targeted reinnervation (Figure 2.11) is a surgical procedure that moves the motor (TMR) and sensory (TSR) nerves that previously innervated the amputated limb to muscle and skin target sites on the residual limb or chest [55, 56]. The reinnervated muscles are then used to intuitively control the prosthesis, by the patient thinking about moving the missing limb and mapping the corresponding muscle contraction to prosthesis control. The redirected sensory afferents also reinnervate the overlying skin and create an expression of the hand map so that when touched on the target skin, patients feel as if they are being touched on the missing limb [4, 38, 57]. Edmonton has the only team in Canada performing this TR procedure, and is also the first in the world to pioneer a novel sensory reinnervation approach to control the sensory reinnervation territory [58, 59].

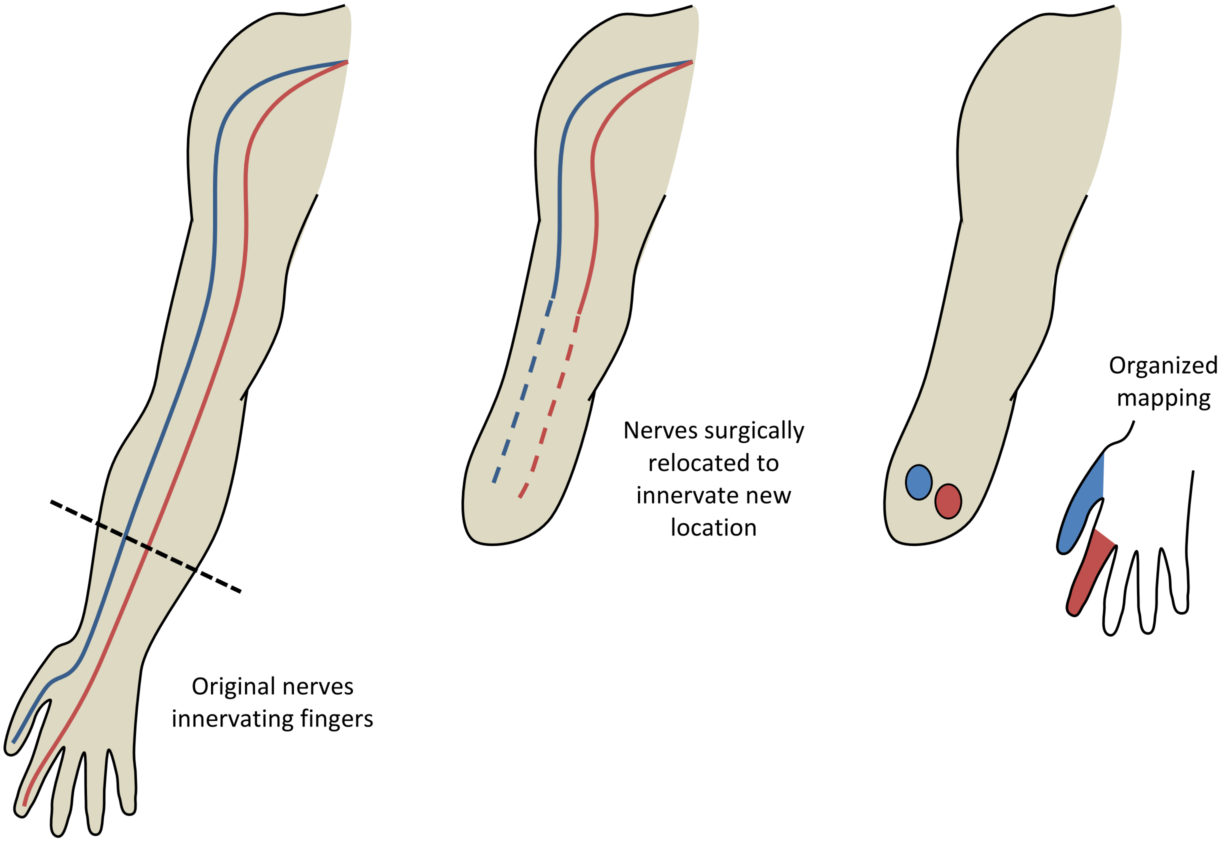

Figure 2.11 Schematic of targeted sensory reinnervation, adapted from [4]

Taking advantage of naturally occurring or surgically arranged cutaneous reinnervation of sensory afferent from the hand (so called “referred phantom hand sensation”) on the residual limb provides an opportunity to somatotopically match the location of the stimulus on the prosthesis to the experienced sensation of the amputee.

2.2.4 Ideal Feedback System

Ideally, sensory feedback could be provided to the user in a way that is intuitive, non-invasive, and relatively inexpensive. Combining sensory input that is matched in modality and somatotopy into a practical socket design is expected to provide a dramatic advancement in the ability for patients to achieve more intuitive control of their prosthetic limb. One of the most basic senses that amputees may want to feel is that of touch, to allow them to sense and modulate grip force while holding an object with their prosthetic hand. A mechanotactile tactor is able to provide touch and force modality matched sensation. Combining this approach with targeted sensory reinnervation for somatotopic matching would be an ideal situation.

Our goal was therefore to design, control, and integrate a mechanotactile tactor that can be used in research trials to evaluate its strengths and limitations for use in amputee subjects with referred hand sensations. This tactor must have a small footprint to allow for multiple tactors to be integrated into a single socket, should be comfortable to the user, and must be easily removed from contact with the limb as the socket is doffed. Ideally this tactor system should require minimal power consumption, and should not interfere with the overall fit of the socket or the operation of the EMG electrodes being used to control the movements of the arm.

Chapter 3. Optimization of Tactor Heads

This work has been submitted to IEEE Transactions on Neural Systems & Rehabilitation Engineering (manuscript number TNSRE-2015-00292).

3.1 Introduction

This study has been conducted to determine the optimal tactor head shape and size for improving comfort and the ability to discriminate between multiple tactors. Results from the study will provide a guideline for determining minimum allowable distance between tactors which will aid in clinical translation of the device.

3.2 Background

In literature examining mechanotactile feedback, many different unique tactors have been used. The component that contacts the skin, termed the *tactor head*, varies substantially between studies in terms of shape, axial-symmetry, and size [28, 46, 47, 49, 60] (Figure 3.1).

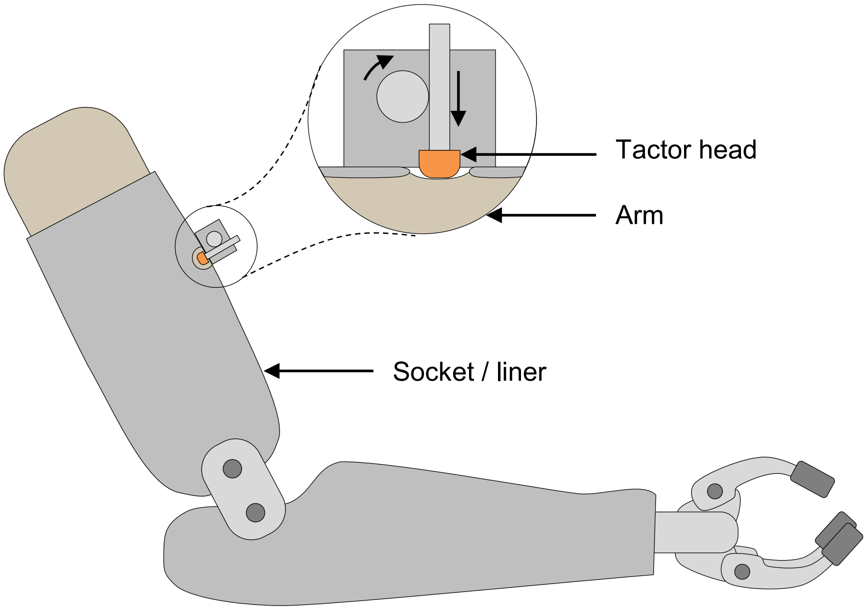

Figure 3.1 Schematic of a linear prosthetic tactor mounted on a socket.

Some studies look at the capabilities of the tactor system [28, 47, 49]. Others focus on determining the best method to communicate forces to the prosthetic user, such as translating the measured force in discrete force steps versus continuous loading [46, 60]. Because tactor heads vary between studies, it is unclear if results can be directly compared. Therefore, it is desirable to test the range of parameters used in literature in order to ensure that fair comparisons are being made across studies.

Several studies have investigated the effect of tactor size and array density for use in fingertip devices, particularly for virtual haptic applications [61, 62]. Discrimination of ridge angle, shape recognition, and sinusoidal gratings have been used to evaluate feedback effectiveness. These studies demonstrate that the best performance is obtained with higher tactor diameter (1 mm) and lower spacing, plateauing at 1.1 mm [61], as well as larger tactile arrays (1 cm^2) with smaller spacing (1.8 mm) [62]. Different tactor head shapes were not investigated, and similar studies have not been conducted in the upper arm or in particular for prosthetic applications.

Factors influencing tactor placement on the residual limb may include skin sensitivity, tissue compliance, or accessibility of skin. The tactors may be separated far apart to ensure they can easily be distinguished from each other. Some studies have determined tactor placement based on average two-point discrimination, or the smallest distance between two points of force application that can be clearly distinguished as separate points [46, 60]. Two-point discrimination varies substantially across participants, time, location and orientation, as well as on different sides of the body, among other factors [63-66]. It has been suggested that shape, location, and indentation of tactors should be studied, as these factors are known to impact tactile perception [67]. To the authors' knowledge, there have been no documented studies to investigate how clinical two-point discrimination translates to discrimination between tactor heads in the upper arm, nor has tactor placement for prosthetic limb applications been extensively discussed.

It is expected that there are optimal tactor parameters that improve one's ability to discriminate between different tactors, allowing optimal placement of tactors on the residual limb, with the aim of providing more information about the state of the prosthesis. Additionally, comfort should be maximized, as this is listed as a factor related to acceptance of a prosthetic limb [2, 3].

The objectives of this study are to optimize tactor head parameters to improve discrimination and comfort, as well as determine a method to decide on placement of tactors on the residual limb. We hypothesized that a large triangular tactor head would provide the best discrimination since it has the largest change in contact area as it is applied, while a large domed head would provide the highest comfort since no edges would contact the skin. Procedural and apparatus changes have been noted to have a large effect on standard test results [64], thus it was expected that tactor and clinical two-point discriminations would be different, as well as discriminations tested at different force levels. Tactor two-point discrimination was expected to differ by participant, over time, and at different locations, as with clinical two-point discrimination [63-66].

3.3 Materials and Methods

3.3.1 Design Variables

The manipulated (independent) variables of primary interest were tactor head shape, head size, and force applied. Other variables included the participant, the specific location on the arm, and the timing of testing (before or after a break).

Manipulated variables were chosen based on ranges found in literature (Figure 3.2). Head shapes were axisymmetric and included triangular, domed, and flat profiles. Head diameters were either 8 or 12 mm. Forces included light touch (25% of the individual participant's maximum comfortable force) and heavy touch (75%), and were measured using a load cell (Omega LCM-703-10) in series with the custom designed two-point discrimination device (Figure 3.3). The maximum comfortable force was determined for each participant by slowly loading a single small triangular tactor head onto their arm until it was reported to feel slightly uncomfortable, up to a maximum of 3 N. This maximal comfortable force test was repeated and the lower of the two measurements was set as the maximum force that would be applied throughout the experiment. Maximum tactor forces applied in literature range from 3 to 13 N [26, 47-49, 52, 58, 60]. From pre-trials we found that participants reported a threshold of discomfort of 4 to 5 N. Thus an upper limit of 3 N was selected

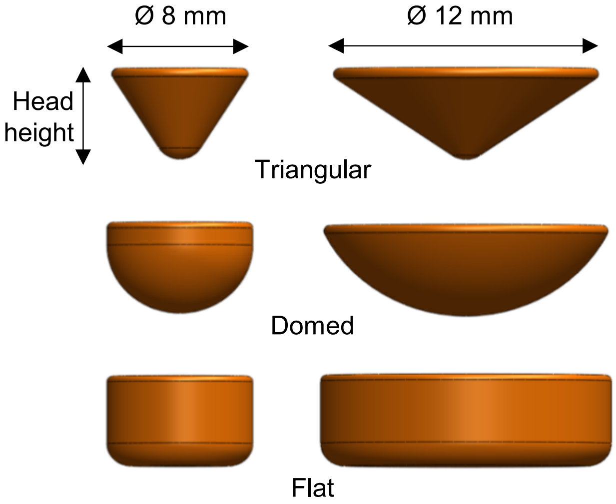

Figure 3.2 Schematic of tactor head shape combinations tested.

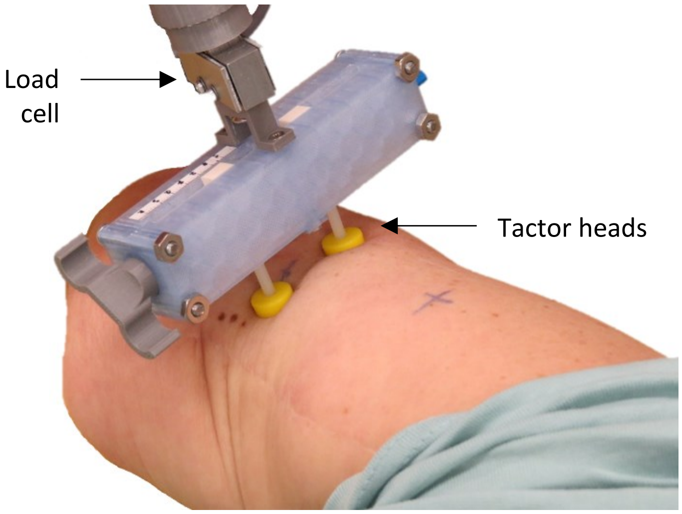

Figure 3.3 Two-point discrimination device used to apply tactor heads to skin

conservatively to minimize tissue irritation over multiple trials, while still remaining within ranges defined in previous literature.

Four of the able-bodied participants were tested at two different locations; the anterior side of the arm 25% of the humeral length proximal to the elbow (predicted to give the best discrimination on the upper arm [63]), and the lateral side of the arm 75% proximal to the elbow. Two participants were tested only at the anterior location, and the remaining two only at the lateral location. This allowed investigation into whether tactor two-point discrimination varies between different locations, as with clinical two-point discrimination [63, 64, 68], and would demonstrate if consistent spacing of tactors is permissible, or if it should vary across the residual limb.

Several factors were held-constant. Tactor head height was fixed at 4 mm. Participants were seated comfortably with arms supported at the elbow, and testing was conducted on the non-dominant arm. Vision and hearing were occluded to prevent participants from receiving secondary sources of sensory feedback. Tactor heads were applied parallel to the transverse plane, as orientation has a large impact on discrimination, and the transverse plane has been shown to be optimal [63, 69]. Tactor head placement was evenly distributed about marked locations on the arm ± 0.5 cm (Figure 3.3), as in previous discrimination testing [70].

Allowed-to-vary factors included arm musculature, time of day, gender, diameter of arm, and activities conducted prior to testing. Forces were applied by hand to compensate for natural shifting of the participant's arm and to reduce total testing time.

3.3.2 Measured Parameters and Responses

The responding (dependent) variables included tactor two-point discrimination and comfort, discussed below.

Two-point discrimination for each tactor and force combination was determined [64]. First the gross-medium staircase method [70, 71] was used to determine the approximate two-point discrimination by randomly applying the two tactor heads at various increments of 10 mm, and asking the participant to report how many "distinct and separate" tactors they felt. Next the multiple random staircase method [70, 71] was applied at 2 mm increments to determine a more precise threshold. Threshold was considered the lowest distance that could be identified as two separate points 2/3 of the time, with higher distances also identified correctly at least 2/3 of the time. The device used to separate the tactor heads at set distances operates using an opposing threaded screw mechanism to separate the tactor heads symmetrically about the central axis to help apply forces evenly across each tactor head (Figure 3.3).

Comfort was reported on a Likert scale of 1 to 5, defined as: 1, very uncomfortable (could not be used); 2, uncomfortable (would not use longer than duration of test); 3, neutral (would need to remove sometimes throughout the day); 4, comfortable (could be used most of the day); 5: very comfortable (could be used all day).

Clinical two-point discrimination using pointed tips (to mimic standard clinical equipment) was tested at the beginning, middle, and end of each participant's trials, following the staircase procedure outlined previously (Figure 3.4).

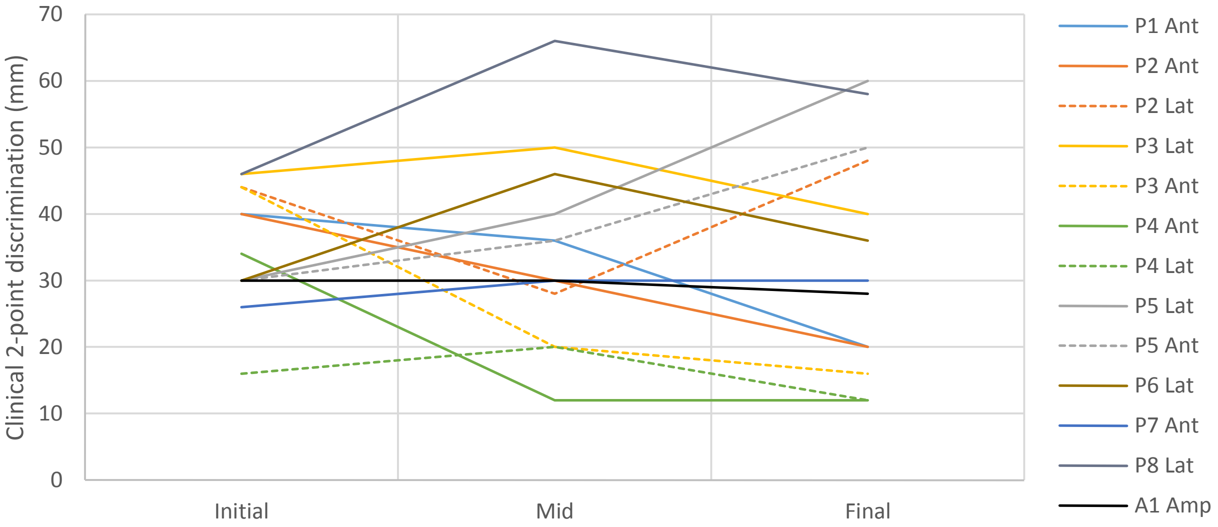

Figure 3.4 Changes to clinical two-point discrimination across trial

The skin sensitivity of each participant was also measured at these time points using monofilaments to ensure that it remained above the threshold for loss of protective sensation [64], and skin sites were monitored for redness and irritation (Figure 3.5). Participants were given short breaks between repeats of the testing procedure and were allowed to rest as desired. One amputee participant was outside of the protective sensation range, as is common with amputees who often wear their prosthesis [72], so extra care was taken to limit applied force, monitor for skin redness, and enforce breaks.

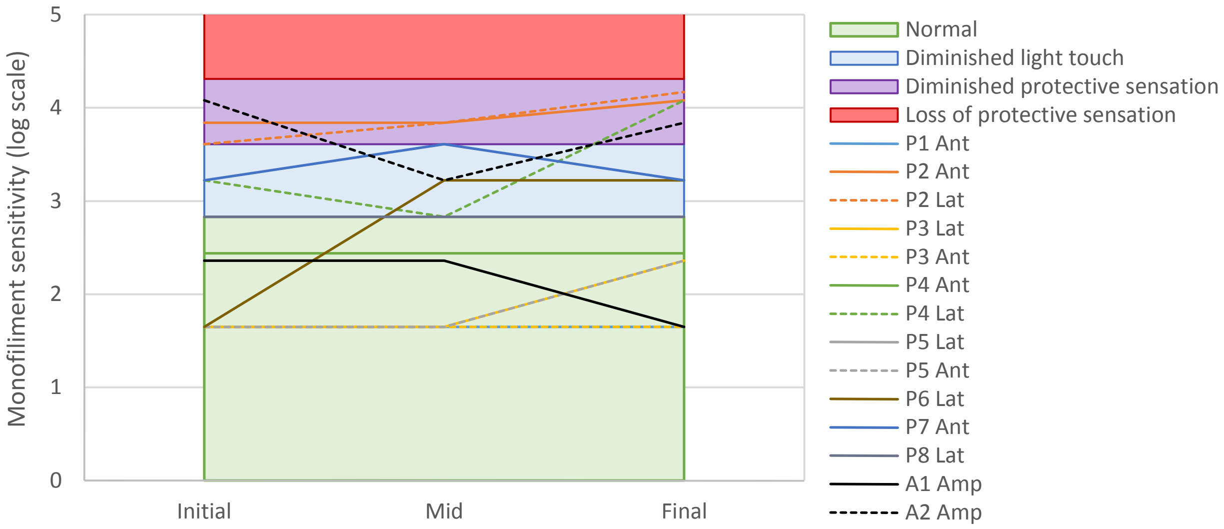

Figure 3.5 Changes to monofilament sensitivity across trial

3.3.3 Participants

A 2-way Analysis of Variance (ANOVA) power analysis calculation was conducted [73] to identify clinically relevant differences in two-point discrimination of at least 4 mm, given a standard deviation of 12 mm, where the alpha and minimum power values were set to 0.05 and 0.90, respectively. Based on this analysis, eight able-bodied participants were recruited for this study, where four of the participants were tested at two different locations on the arm. Given this sample size, a second power analysis demonstrated that the minimum comfort difference that could be identified was 0.28, using the same power values and a standard deviation of 0.8. This is arguably much less than a clinically relevant difference, and is therefore deemed acceptable. Two trans-humeral amputee participants were also recruited as a preliminary investigation of clinical translation and application. Participant measurements are summarized in Table 1.

Table 3.1 Average ± Standard Deviation of Participant Measurements

	Able-bodied	Amputee
Time required for site testing (hr)	1:31 ± 0:16	1:06, 0:45
Gender	7 male, 1 female	Males
Age (years)	24 ± 3	69, 28
BMI (kg/m^2)	26 ± 5	30, 23
Handedness / amputation	All right	Right, left
Length of upper arm (cm)	30 ± 2	29, 26
Arm diameter, 50% proximal to elbow (cm)	32 ± 6	35, 28
Resting arm angle (°)	126 ± 8	130, 143
Maximum comfortable force (N)	2.8 ± 0.3	1, 3
Time since amputation (years)	n/a	2, 9
Average prosthesis wear (hours per day/days per week)	n/a	9/5, 7/4
Targeted muscle reinnervation (TMR)	n/a	None, TMR
Prior activities	Sleep, work, walk, commute	Work, commute

3.3.4 Methodological Design

A full factorial design-of-experiments approach was followed which involved testing each combination of parameters and repeating to check for consistency. Trials were conducted in a random order to reduce bias over time, yielding a total of 24 tests for each participant at each location tested. This resulted in an average testing time of 1.5 hours per participant per location.

Mixed Effects ANOVA was used to analyze all results, with a *p*-value of 0.05 used to indicate significance. An initial test was conducted to determine which manipulated parameters had a significant influence on two-point discrimination and comfort, blocking by participant. In all following analyses, location and time variables were included as blocking variables to account for variability. Follow-up analyses were conducted for each tactor head shape, as this is a qualitative variable [73], to determine the effects of tactor head size and applied force. Finally, an analysis was conducted to determine if there was a difference between clinical (pointed tips) and tactor (small flat, domed, and triangular) two-point discrimination.

3.4 Results and Discussion

All data was checked using a normality test and was found to be distributed normally with no obvious trend in residuals versus case number, indicating that there was no change in testing procedure across trials [73].

3.4.1 Effect of Participant, Location, and Time

Both tactor two-point discrimination and comfort were found to differ significantly by participant, by location on arm, and over time (Figure 3.6). This is consistent with clinical two-point discrimination results reported in literature [63, 64, 68]. These parameters were blocked for all subsequent analyses. Measured values fell within the typical clinical two-point discrimination range for the upper arm of 12 to 67 mm [63, 65, 66, 68]. On average, all comfort scores were above a rating of 4/5, or within the "comfortable (and could be worn most of the day)" range. Amputee data fell within the ranges measured from the able-bodied participants.

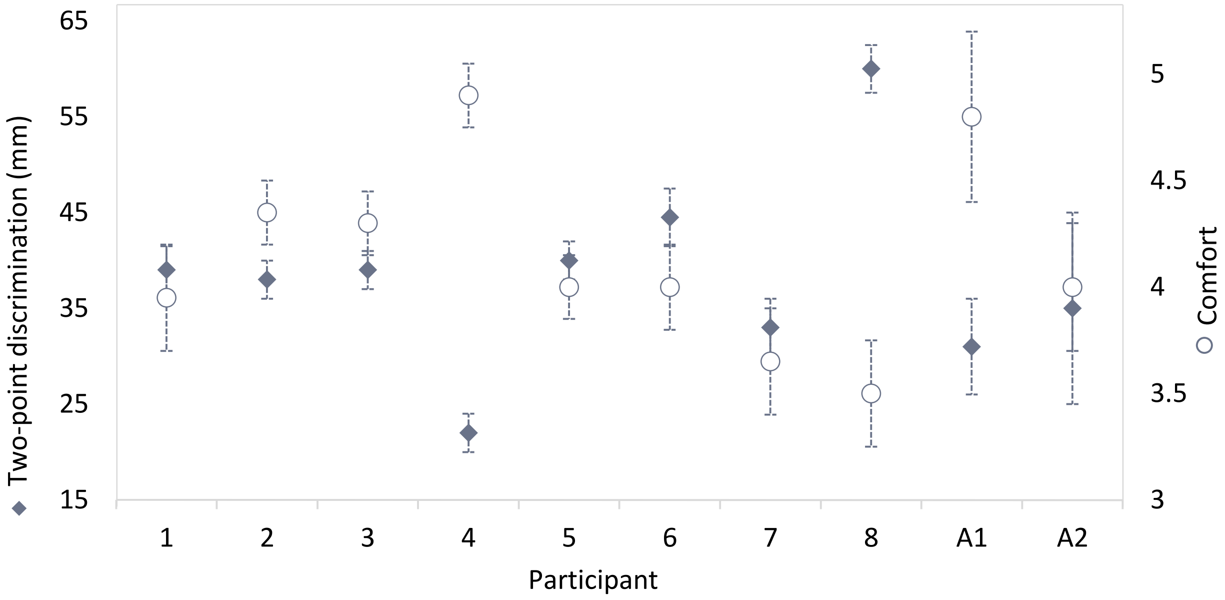

Figure 3.6 Results of two-point discrimination (distance in mm) and comfort (5-point Likert scale) by participant, where A1 and A2 represent the amputee participants.

3.4.2 Tactor Two-point Discrimination

Data for each tactor head shape was analyzed separately as this variable is nominal. For each head shape it was determined that the force applied did not have a significant impact on discrimination. Head diameter had a significant impact on discrimination for the flat head shape, but not for the triangular or domed head shapes. For this reason, the flat head shape was divided into two groups for further analysis.

Each head shape was then compared, with the flat shape broken into the small and large diameters. This demonstrated that the large flat head yields the worst two-point discrimination (average resolution of 40 mm), where the other heads provide significantly better discrimination (average resolutions of 37 mm) (Figure 3.7).

Observing discrimination of the two amputee participants, it appears that the data follows a similar trend to the able-bodied statistically significant results. Average discrimination values fell within one standard deviation of the able-bodied results.

Data was analyzed to determine if there was a difference between clinical (pointed tips) and tactor (small flat, domed, and triangular) two-point discrimination. It was determined that there is a significant difference between discrimination values, where the clinical tool provides an improved resolution compared to the tactor resolution. On average this improvement is 3 mm, but is up to 5 mm within a 95% confidence interval.

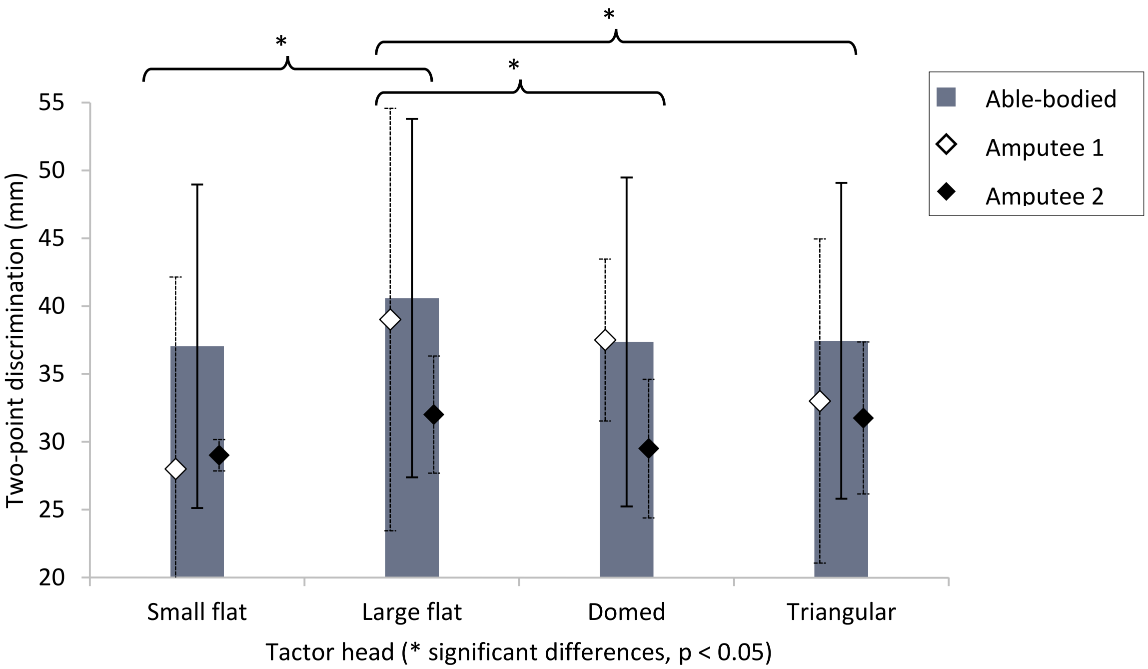

Figure 3.7 Graph of two-point discrimination by tactor shape and size, where error bars indicate standard deviation.

3.4.3 Comfort

Data for each tactor head shape was analyzed separately. For each head shape it was determined that the force applied did not have a significant impact on comfort. The maximum force applied for each participant was limited to 3 N, where three of the eight able-bodied and one of the two amputee participants identified maximum allowable force below this level (2.4 ± 0.2 N, and 1 N respectively). Head diameter had a significant impact on comfort for the triangular head shape, but not for the flat or domed head shapes.

Each head shape was then compared, with the triangular head shape broken into small and large diameters. This demonstrated that the domed and large head shape yields the highest comfort (average of 4.3/5.0), where the large triangular head shape is not significantly different than the domed, and small triangular is the least comfortable (average of 4.0/5.0) (Figure 3.8).

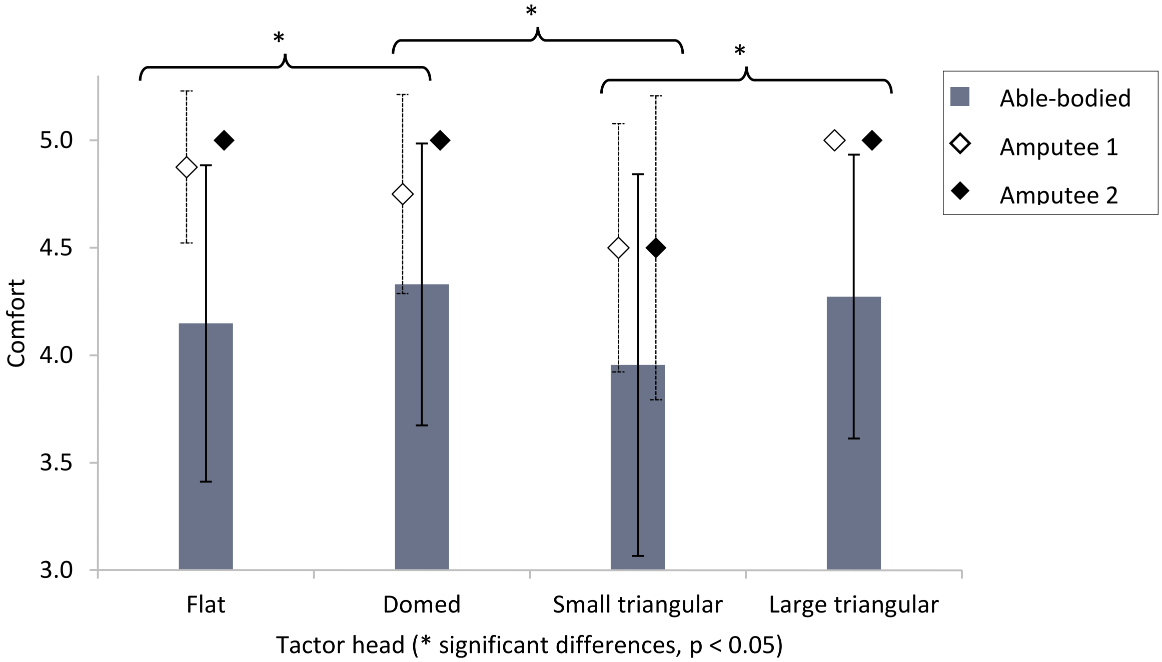

Figure 3.8 Graph of comfort by tactor shape and size, where error bars indicate standard deviation.

Observing comfort of the two amputee participants, the large triangular head provided the highest comfort, where flat and domed are similar. Differences between able-bodied and amputee participants are not statistically significant due to the low amputee participant sample size. Amputee results fell within or just outside one standard deviation of the able-bodied population.

3.4.4 Discussion

The domed and large triangular tactor head shapes are recommended to optimize both two-point discrimination and overall comfort, as they optimized both parameters for the statistically significant able-bodied results, and amputee results follow similar trends. By reducing two-point discrimination, these tactors can be placed closer together on the residual limb compared to using a different head shape. This will allow for higher tactor density, therefore allowing the display of more sensory information to the amputee. It is important to keep in mind that while the comfort levels are significantly different, a change in 0.3 on a 5-point scale may not be clinically relevant; as mentioned all combinations on average were rated above “comfortable (and could be worn most of the day)”. Trials were conducted over an average duration of 1.5 hours, but given that amputees typically wear their prostheses for long periods of time, such as during work or social activities [20], it is possible that this spread in comfort may increase if tactors were applied over longer periods of time. Furthermore, some participants were more sensitive to the different tactor heads, the most extreme case being one participant who assigned a value of 2 to the small triangular head; “uncomfortable (would not use longer than duration of test)”. Therefore to select a tactor head that will work universally for all participants, the small triangular head should be avoided.

For the domed shape, tactor head size of 8 or 12 mm did not have a significant impact on discrimination or comfort, meaning that this variable can be selected based on other design limitations, such as minimizing the power draw of the system. Force level did not significantly impact discrimination or comfort, but this may be partially due to the small force range tested (up to 3 N).

Two-point discrimination varies significantly from person to person as well as by location on the arm, so exact tactor placement must be patient specific and should vary by location. Tactor discrimination resulting from the use of the domed tactor head or the large triangular head has a resolution 5 mm worse than clinically measured two-point discrimination within a 95% confidence interval. This will help with clinical translation, as clinicians will not require new equipment or training to determine optimal tactor placement; they can simply measure two-point discrimination using existing clinical techniques, and add a factor of 5 mm to account for the difference. Because two-point discrimination changes over time, it is recommended that it be measured a few times throughout fitting, and the worst case selected for tactor placement.

3.4.5 Limitations and Future Directions

Common limitations associated with two-point discrimination measurements include applying inconsistent forces between measurements and between tactor heads, as well as high inter-rater discrepancies [74, 75]. To reduce these limitations, the device was connected in series with a load cell so that consistent forces could be applied, care was taken to apply forces evenly across each tactor head at a relatively consistent velocity, and the same experimenter and device were used to conduct each test. One limitation of the device was that it separates tactors linearly, so at large separation distances the tactor heads were not tangent to the arm.

Another limitation is the lack of amputee participants tested. This study could be expanded by including more amputee participants, which would also allow investigation into differences such as the effect of naturally occurring nerve changes or targeted sensory reinnervation [38, 58, 72]. As well, it could provide better confidence in using able-bodied subjects as translational equivalents to amputee testing. It would be useful to extend the testing to more closely mimic the conditions of a tactor integrated onto a prosthetic socket by testing over a longer period of time, including a socket and liner, and pressing into the exact same location repeatedly as would be the case if the tactor were fixed in place. It would be valuable to investigate skin irritation over longer time periods. For some participants, discrimination accuracy improved over time and for others it worsened. This may be a combination of learning, fatiguing, skin desensitization, or other factors, and further investigation is warranted. Other manipulated parameters could also be investigated, such as non-axisymmetric tactor head shapes that have been used in literature [49], or applying uneven forces to determine if a tactor applying a large force masks a tactor applying a lighter force, as seen with clinical two-point discrimination [64].

This experiment suggests that a domed or large triangular tactor head could be used interchangeably, however it is desirable to narrow this selection further to a single geometry. One possible extension could be to conduct a follow-up study to investigate the effect of tactor head shape and size on sensitivity to small force changes; if one particular geometry improves sensitivity, the overall amount of information that could be communicated to the user would be increased.

3.5 Conclusion

This study has demonstrated that the optimal tactor head shapes for improving both two-point discrimination and comfort are domed (where a diameter of 8 and 12 mm are equivalent) or large (12 mm) triangular, where applied force (up to 3 N) has no significant effect. It is important to measure a patient’s clinical two-point discrimination during tactor placement, as this can vary substantially from person to person as well as by location on the arm and over time. In the upper arm, clinicians can use existing equipment to locate the tactors on the prosthetic socket during the fitting process, and simply increase the measured resolution by a factor of 5 mm. This factor may differ for discrimination in other parts of the body, such as in the forearm. In future tactor studies it is recommended that the influence of tactor head geometry on force sensitivity be investigated to further narrow down optimal tactor head geometry.

Chapter 4. Mechanical Design

4.1 Introduction

While several mechanotactile tactors have been presented in literature, none have yet to be implemented onto a commercial prosthetic system. This may be due in part to their relatively large size, added complication to prosthetic limb construction, and high cost. Therefore a small, simple, and inexpensive tactor system should be designed to improve clinical translation.

4.2 Background

4.2.1 Mechanotactile Tactor Designs

Several types of mechanotactile tactors have been reported in literature (Table 3.1). These tactors typically include a motor to provide the pushing force, some gearing or linkages to transmit forces, and a tactor head which contacts the skin and applies the force. These tactors range in terms of the maximum force they can apply, whether they control the applied displacement or force, and vary significantly by size and weight.

Table 4.2 Design of mechanotactile tactors in literature

Designed	Modality	Motor	Transmission	Skin contact	Force (N)	Force sensing	Mass (g)	Dimensions (mm)
Antfolk, Lund University [26, 48, 60]	Normal	Digital servo motor	15 mm long motor shaft lever	12 mm diameter plastic button	9	None	UNS	Unspecified ≥ 17 mm throw
Armiger, Johns Hopkins APL [47]	Normal	Brushless DC motor	Gearbox and linkages	8 mm dome electrode	3	Unspecified	UNS	46.5 x 18.5 16.4
Kim, Kinea Design [49]	Normal and shear	Brushless DC motor	Gearbox and linkages	G6 and G10: Triangular head, 11 mm wide **[28]** P10: Rectangular head, 14 mm wide **[34]**	9	G6 and G10: Force sensors on end effectors P10: Torque sensors between actuator and mechanism	G6: 16 G10: 41 P10: 45	G6: 60 x 35 G10: 65 x 35 P10: 80 x 32 Height UNS 10 mm throw
Meek, University of Utah [52]	Normal	UNS	Direct drive	25.4 mm square	13.3	Force transducer on end effector	UNS	No attempt to miniaturize

*UNS – Unspecified

4.2.2 Design Specifications

4.2.2.1 Desired Force Range

Applied tactor forces in literature range from 3 to 13.3 N [26, 47-49, 52, 60]. One paper mentions that a single targeted reinnervation participant began to feel discomfort at 5.8 N and pain at 8.8 N, corresponding to 10 mm penetration with an 8 mm diameter tactor head, however no mention was made of the effects of repetitive loading [49]. However, to date no rigorous studies have been conducted to determine the maximum stress that should be applied by a tactor intermittently to the residual limb. Given a tactor head diameter of 8 mm as suggested by the optimization study (Chapter 3) as well as a desire to reduce power consumption, the following approximate pressures are developed in the residual limb at various applied forces using the equation below.

$$P = \frac{F}{A} = \frac{F}{\pi r^2}$$

Where P is pressure (kPa), F is force (N), A is area (mm^2), and r is radius (mm).

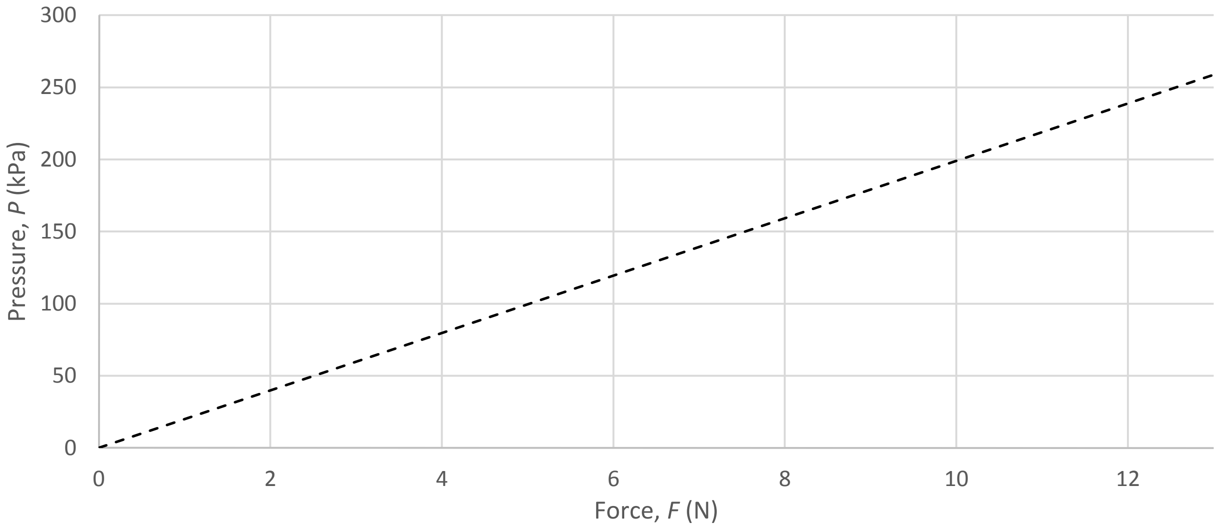

Figure 9 Pressure applied by tactor head at various force levels

Extended high loads should be avoided to reduce the risk of pressure ulcers, which typically form when high pressures are maintained for extended periods of time, resulting in the reduction of blood circulation [76]. Past studies have generally been conducted on a time scale of hours to days, so extrapolating the maximum allowable force for an interval shorter than an hour may not be relevant. One older study found that alternating pressure at five minute intervals greatly reduced or eliminated destructive pathologic changes to muscle fibres in tests conducted up to 3 hours at 32 kPa [77]. Another study indicated that cell death will begin to occur when engineering strain in muscle exceeds 77 ± 7% [78], however this is difficult to relate to physical limits due to the presence of other tissues of varying thicknesses over the muscle, including fat and skin.

It is therefore difficult to infer the maximum force that should be applied by the tactor, as the closest related studies focus on pressures applied for long durations and are distributed over large areas. Consequently, it is important to ensure that the users possess protective sensation or minimum sensitivity to applied forces. As well, they should be comfortable when forces are applied, and any trials should be closely monitored for signs of discomfort or skin irritation.

4.2.2.2 Maximum Temperature of Device

The hot temperature threshold for pain depends on several factors including temperature, duration of contact, and material contact conductance. However, it is suggested that any material with a temperature below 45°C will meet the touch temperature requirements set by the National Aeronautics and Space Administration [79].

4.2.2.3 Other Design Specifications

Other design specifications are listed in 0 and include requirements such as reducing the overall cost, weight, and size. The specifications are broken into mechanical, electrical, and software requirements. The final design compliance values are also provided in 0.

4.3 Tactor Design

4.3.1 Linear Tactor

The linear tactor operates using a servo motor with rotational motion converted to linear via rack and pinion gears, where the rack gear has a tactor head on the end which pushes onto the residual limb (Figure 4.10). A limitation of the linear tactor is that is must be placed in an area of "high real estate"; its large base may interfere with other prosthetic components such as EMG electrodes and socket attachments. It also extends out from the socket which limits its placement to the outside of the arm to avoid interference with the torso when the arm is at the user's side.

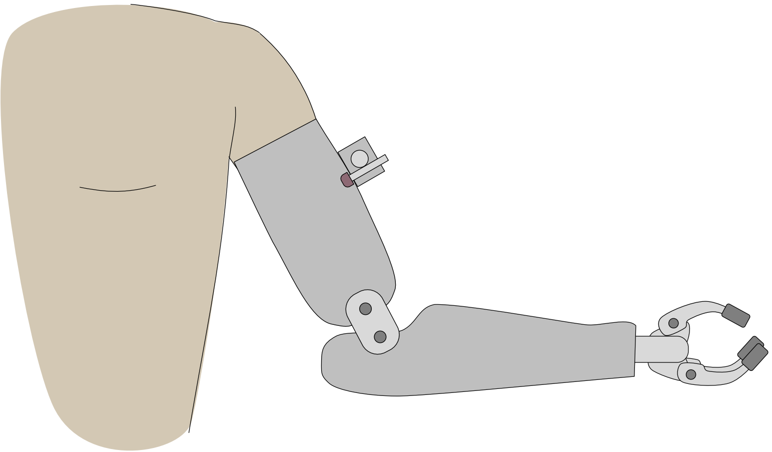

Figure 4.10 Linear tactor placement is limited by overall device footprint

4.3.2 Cable-driven Tactor[1]

A novel cable-driven tactor was proposed by the BLINC group to reduce the vertical profile of the device and to capitalize on the limited space available on the residual limb, in order to make it practical to integrate onto a socket (Figure 4.11). The concept is to distance the motor from the tactor head and connect the components with a Bowden cable. The motor could be placed over less important areas of the arm, such as on the shoulder or within the forearm of the prosthesis itself, while the tactor head could be placed where needed to provide feedback, and therefore require a smaller footprint over the areas of "high real estate".

---

[1] The cable-driven tactor concept was initially proposed by Michael Stobbe, a BLINC lab member and Certified Prosthetist

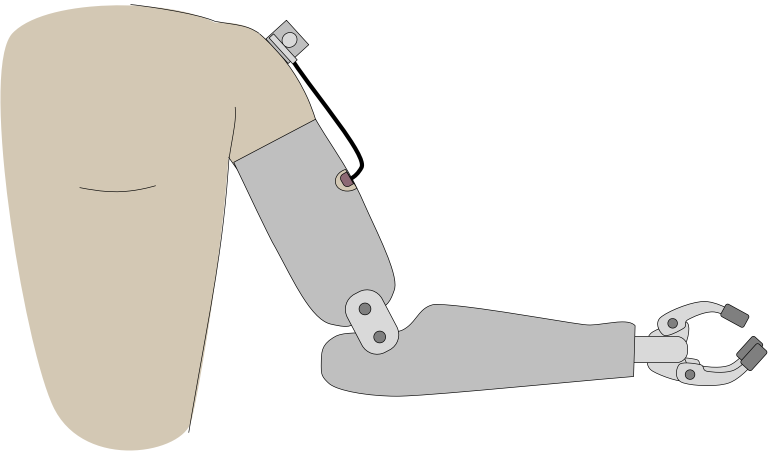

Figure 4.11 Cable-driven tactor placement is more vertatile due to smaller profile of tactor head

A Bowden cable allows forces to be transmitted in both the push and pull directions, and is used to translate forces from the motor to the skin. This allows horizontal motions of the rack and pinion gear to be translated to vertical motions at the tactor-skin interface (Figure 4.12).

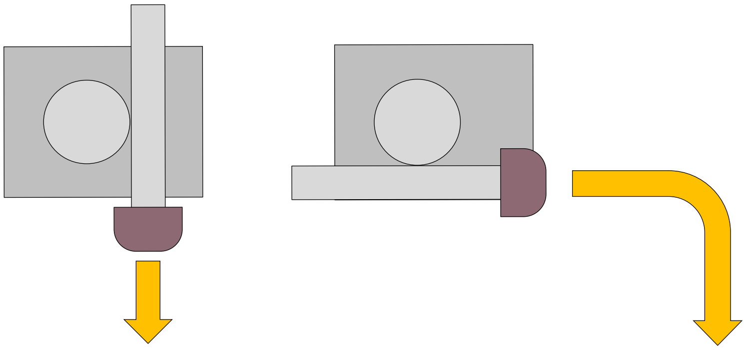

(a) (b)

Figure 4.12 Schematic showing direction of applied tactor forces (a) vertical linear tactor, and (b) vertical force applied using horizontal tactor with Bowden cable to change direction of applied force

This Bowden cable (Hosmer, USA) is made of two components, an inner cable made of wound stainless steel and a hollow helical coiled wire outer housing which is fixed and guides the inner cable (Figure 4.13). A Teflon liner sits between the cable and conduit to reduce friction [80].

Figure 4.13 Bowden cable components

4.4 Previous Development

4.4.1 Linear Tactor[2]

The BLINC group previously developed an upright linear tactor able to apply varied force levels to the residual limb (Figure 4.14). This research tactor was used to demonstrate the ability of an amputee participant to identify object shape and size while blindfolded and controlling a robotic training tool, guided only by sensory feedback [58, 59].

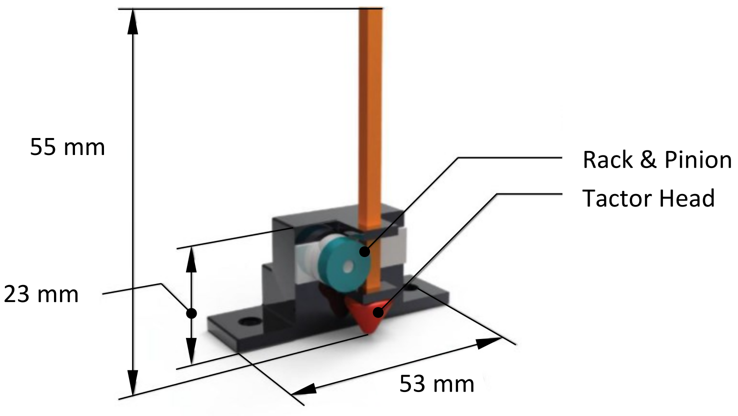

Figure 4.14 Linear tactor designed with vertical profile

4.4.2 Cable-Driven Tactor[3]

An initial prototype of the cable-driven tactor was designed by the BLINC lab prior to this thesis work (Figure 4.15).

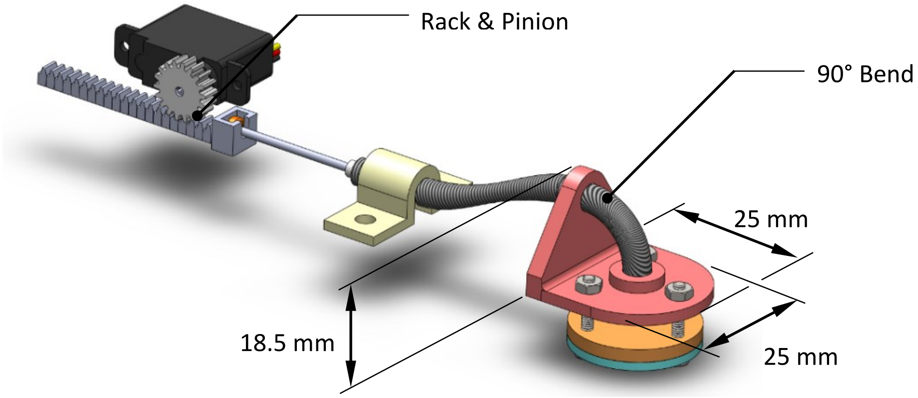

Figure 4.15 Cable-driven tactor designed with horizontal profile

---

[2] The linear tactor was initially developed in the BLINC lab spanning several different part-time students and led by Michael Rory Dawson, with testing described in [58, 59]

[3] The cable-driven tactor was initially designed and tested by Kent Herrick during a summer work term

The following initial tests were conducted prior to this thesis work to validate the design of the tactor, and are summarized below. Testing was conducted using an apparatus constructed from aluminum extrusions (OpenBeam, Solarbotics Ltd.), where the tactor was pressing onto a load cell (FS01, Honeywell International Inc., USA) to quantify applied forces (Figure 4.16).

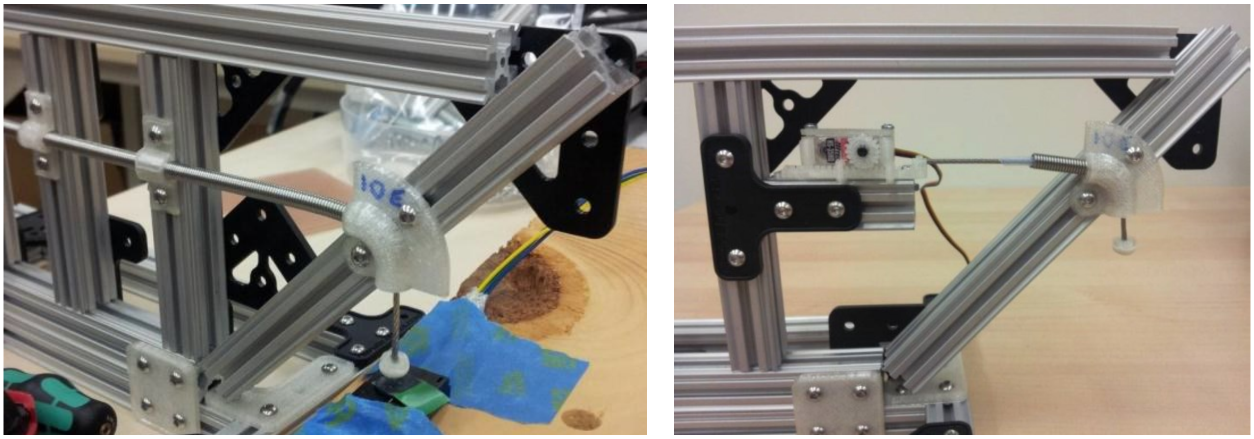
(a) (b)

Figure 4.16 OpenBeam apparatus constructed for testing (a) cable and friction, and (b) servo motor

4.4.2.1 Cable Selection

Optimal Bowden cable configuration was determined by measuring the friction between various diameter cables and conduits. The configuration producing the least friction was a 1.4 mm diameter cable within a Teflon lined conduit.

4.4.2.2 Static Friction in Elbow

The cable must be pushed around a 90° bend to transfer force from the horizontal to vertical direction, so various elbows were tested to investigate the friction caused be different bend radii. The friction was shown to increase with decreasing bend size (Figure 4.17). Size is more of a concern than the 1 N friction force resulting from the 10 mm bend, so this elbow was selected. It was determined that this iteration of the elbow design did not allow the tactor head to exit at a true 90° bend, so changes to the exit guide structure were required.

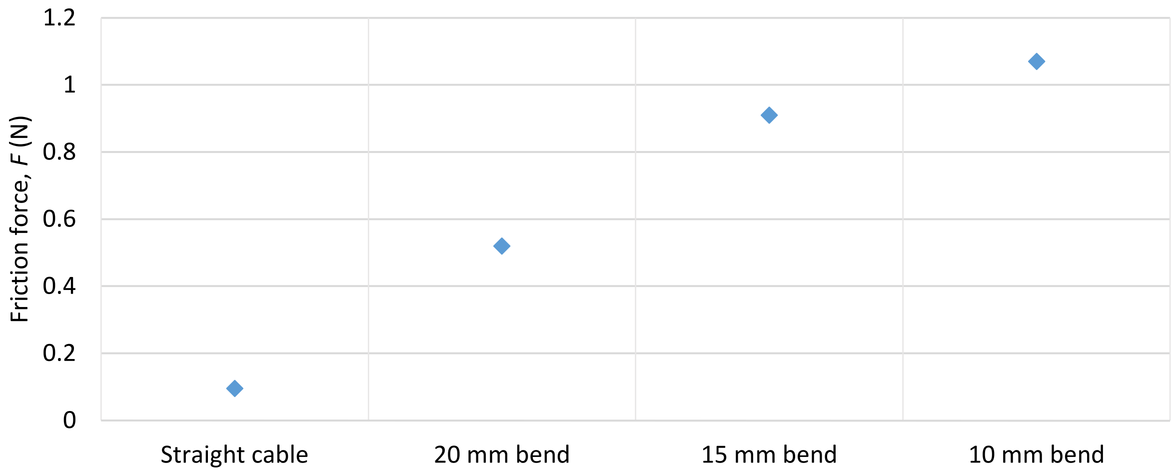

Figure 4.17 Graph of static friction produced for various bend radii

4.4.2.3 Cable Bucking

Buckling of the cable must be avoided to ensure that the proper force is applied to the residual limb. It was found that the force required to buckle the cable is above the 13 N range of the load cell used for testing, demonstrating that buckling would not affect the limits of the tactor.

4.4.2.4 Servo Testing

The servo motor must be able to provide adequate force to the tactor head, so capabilities of the servo were tested by pushing on a load cell through various rubber balls to simulate soft tissue. After improving the gear attachment from the servo motor to the output shaft it was found that the tactor could transmit forces in excess of 13 N.

4.5 Design Refinement

Based on recommendations and preliminary testing, several changes to the tactor designs were implemented, both generally and specifically to the linear and cable-driven tactors.

4.5.1 General Refinement

4.5.1.1 Servo Motor Evaluation[4]

An initial evaluation of several different servo motors was conducted to determine the optimal motor for implementation into the tactor systems, based on forces that can be applied, current draw, and temperature rise. Five motors were initially selected based on their relatively low cost, light weight, small profile, and availability (Table 4.3).

Table 4.3 Servo motor selection

Motor	Company	Price ($CAD)[(a)]	Mass (g)	Motor Type	Speed sec/60° 4.8 V/6.0 V)	Torque kg/cm (4.8 V/6.0 V)	Size (mm)
TS541S Analog Nano	Turnigy	$4.20	4.3	Analog, coreless	0.12/0.11	0.7/0.8	19 x 19.5 x 8
HS – 35HD Ultra Nano	Hitec RCD	$24.99	4.5	Analog	0.10/NA	0.8/NA	18.6 x 15.5 x 7.6
HS – 5035HD Servo	Hitec RCD	$30.99	4.5	Digital	0.10/NA	0.8/NA	18.6 x 15.5 x 7.6
11305 D47 Power Servo	Dymond,	$19.95	4.7	UNS[(b)]	0.18	1.1	21.6 x 17.7 x 8
HS – 40 Nano	Hitec RCD	$9.99	4.8	Analog	0.12/0.10	0.6/0.75	20 x 17 x 8.6

(a) Not including shipping costs

(b) UNS – unspecified

A linear tactor was constructed from each motor using a custom housing. Displacement was set by an Arduino GUI (Guino), force was measured from a load cell calibrated to ± 0.02 N accuracy (Omega, LCM703-5) using Simulink Realtime (Mathworks Inc., 2014), current was read using a multimeter (Fluke, 189), and temperature using an infrared temperature reader (Artech IR Thermometer, A350). For the force and current tests, the tactor heads were displaced onto the load cell in approximate 2 N steps, until the maximum holding output of the servomotor was reached. Force, displacement, and current were read at each step. This process was repeated

---

[4] This servo motor evaluation was performed by Megan Ogle, under supervision of the author

three times in the up and down directions. For the temperature tests, the tactor was again displaced in approximate 2 N steps and held in place for 5 minute intervals at each step. Temperature was recorded at the front and back of the motor at the beginning and end of each interval. Two replicates were conducted with different motors for each test.

Displacement values were shifted such that a value of 0 µs corresponded to a force of 2 N to ensure fair comparisons (Figure 4.18 (a)). Results indicate that the force against displacement curve for each motor are similar, suggesting that motors operate with similar positional control. The D47 servo motor is able to apply the highest holding force (Figure 4.18 (b)). Each of the motors is able to hold a steady force up to a current of approximately 200 to 250 mA. Of the motors tested, the D47 motor draws the least current for the same applied force.

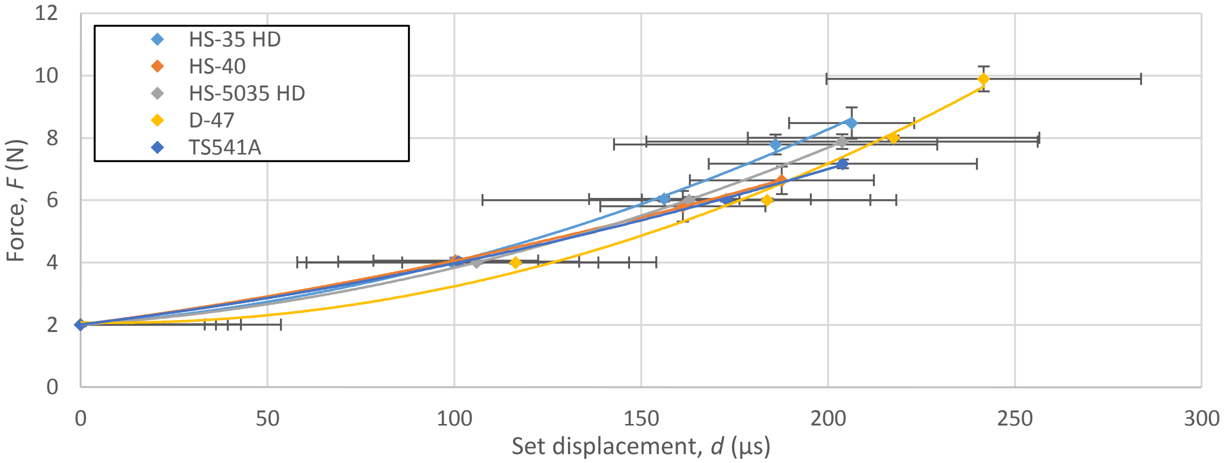

(a)

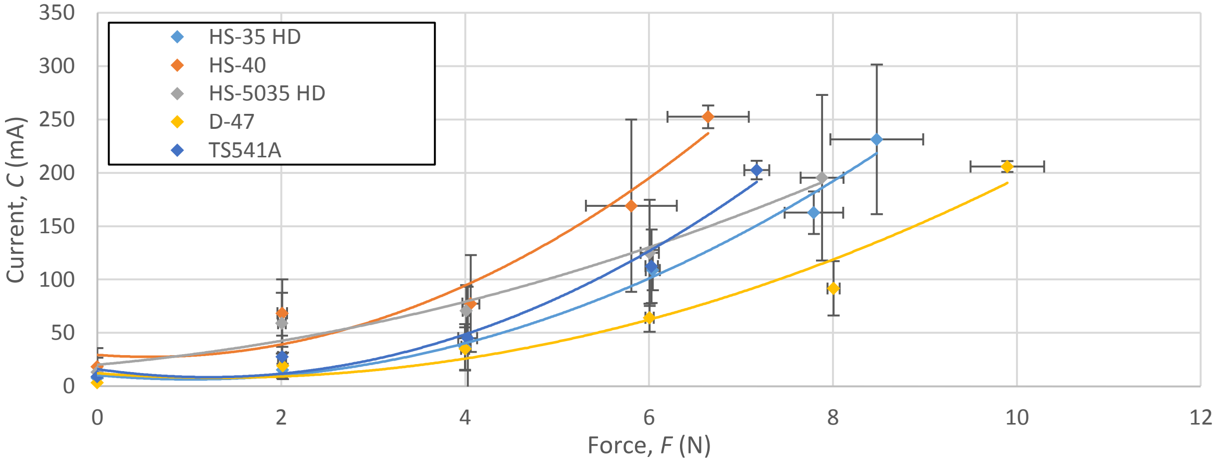

(b)

Figure 4.18 Results of force displacement test where (a) shows force against displacement, and (b) shows current against force

The temperature-time curves suggest that the D47 motor maintains the lowest temperature, while the digital HS-5035 HD operates at the highest overall temperature (Figure 4.19).

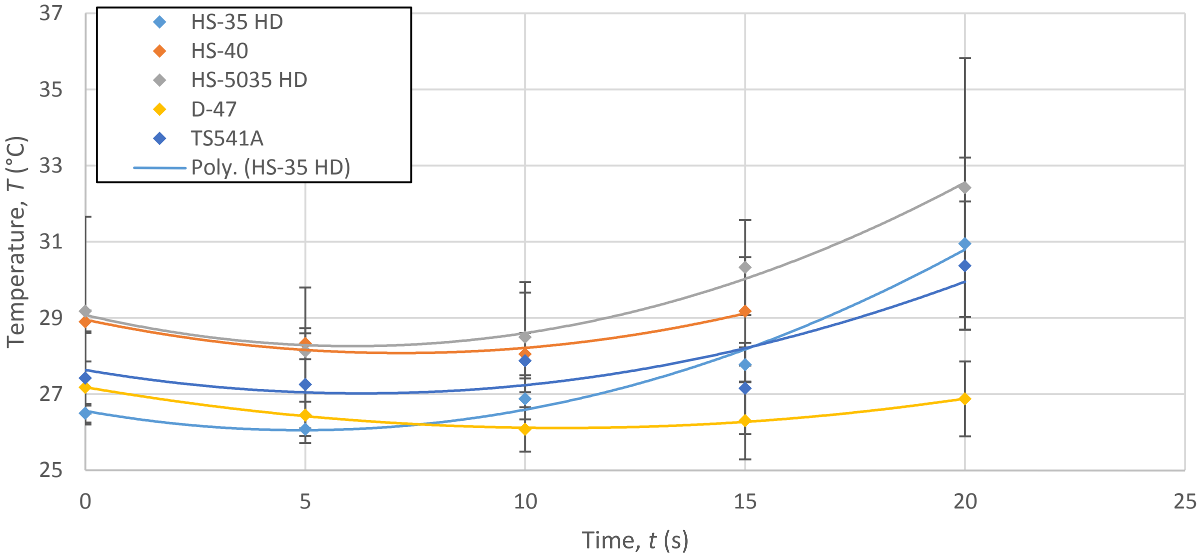

Figure 4.19 Results of temperature against time test

The D47 Power Servo is able to maintain the highest load of 9.9 ± 0.4 N, draws less current for a given force, and given similar applied forces over time, the average temperature was the lowest of the motors tested (after 20 minutes, at 27 ± 1°C). The next strongest motor is the HS-35 HD, which was able to apply loads up to 8.5 ± 0.5 N. Comparing these motors, the HS-35 HD is 0.2 g lighter, costs 20% more ($5 difference), and is 30% smaller by volume.

The HS-35 HD motor was selected for several reasons. It is the smallest of the motors tested, and is easy to obtain from the supplier. It also naturally limits its maximum holding force closer to the design specification limiting the maximum applied force to 7 N. Finally, the availability of the digital version of the motor opens further possibilities to investigate regarding response time of the system. However, if further testing reveals that more strength is required from the servo motor, it is recommended that the D47 motor be implemented into the tactor design.

4.5.1.2 Mechanical Limit

As mentioned, one design specification is to limit the maximum allowed applied force to 7 N. This force was selected as it was measured in-lab to be the upper limit of force that could be applied comfortably. The highest recorded forces for the linear and cable-driven tactors were 15.0 and

8.3 N, respectively (see section 4.6.1); these forces cannot be held by the motors, but can be applied temporarily. This suggests that the linear tactor at least needs a method to limit the maximum force that it can apply. A limit has been implemented into the software by constricting the maximum displacement that the tactor can move. A physical limit was also implemented as added security in case of software malfunction; a mechanical stop was used to ensure that the tactor physically cannot extend beyond a set extension limit. Because every user will have a different definition of a maximum allowable extension, this stop must be adjustable for each specific tactor and applied at the time of the fitting.

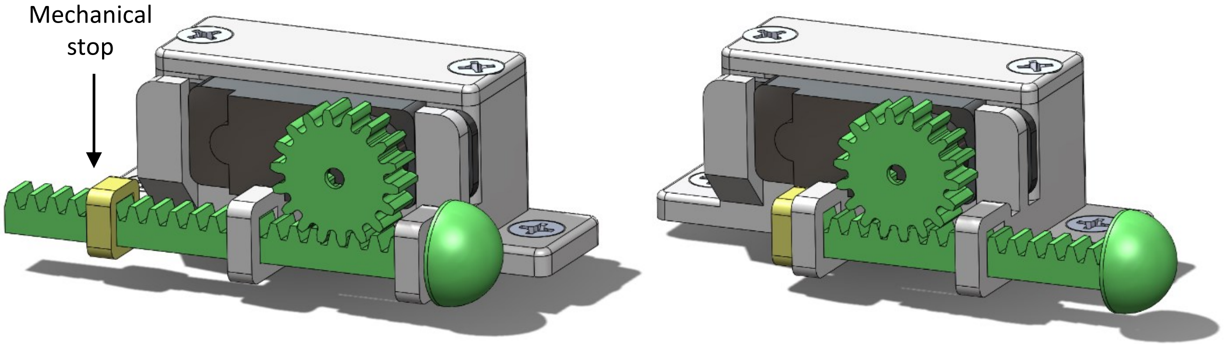

(a) (b)

Figure 4.20 Mechanical stop preventing overextension (a) application, and (b) at limit

A simple solution is to glue a bumper to the rack gear based on input from the user to prevent overextension (Figure 4.20 (a)). The portion of the rack gear behind the stop would be removed, and acts as an additional backup (Figure 4.20 (b)); if the mechanical stop fails, the rack gear will fall thorough the supports and the pinion will no longer be engaged, preventing additional forces from being applied.

The strength capabilities of the mechanical stop were tested by attaching the mechanical stop to the rack gear using superglue, and applying a load to the connection (Figure 4.21). The mechanical stop was able to support a weight of 19.6 N for a test duration of 2 hours with no visible signs of damage or deformation, which is sufficient to ensure that the mechanical stop can prevent excessive forces from being applied by the tactor.

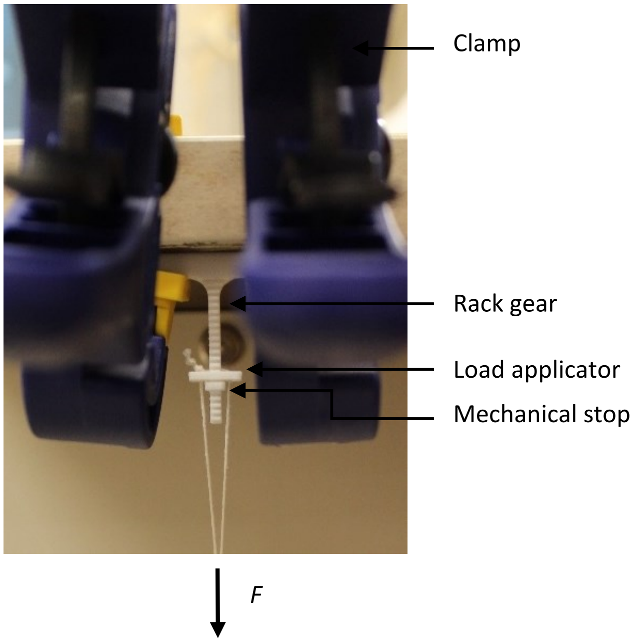

Figure 4.21 Test apparatus to confirm strength of mechanical stop

4.5.1.3 Heat Mitigation

With strenuous testing, it was observed that the servo motors could heat up significantly. This could be uncomfortable to the user, and could also lead to the motors ceasing to function until cooled and reset. Ventilation of the housing and cover was increased to allow more airflow to the motor (Figure 4.22). This was not found to change the structural integrity of the tactor.

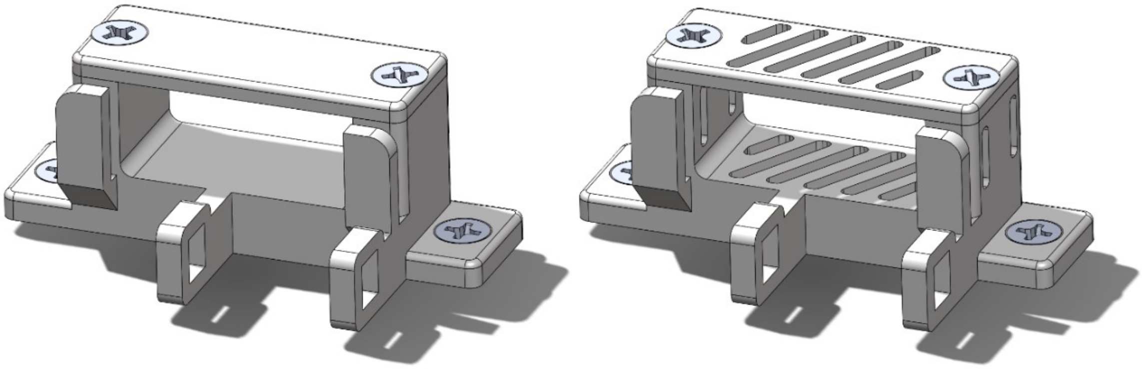

(a) (b)

Figure 4.22 Servo mount housing and cover (a) original, and (b) with additional ventialtion

4.5.2 Linear Tactor

Some of the features from the cable-driven tactor design were incorporated, such as an improved gear connection to the servo motor using a spline interface (Figure 4.23). Bulk was minimized to reduce size and weight. The tactor head was updated to use an 8 mm domed head shape, as one of the recommendations in the optimization study (Chapter 3). The vertical tactor head extends below the base of the servo mount by 3 mm, approximately the thickness of a thermoplastic socket. The exact means of attachment can be modified easily depending on conditions required, such as fixing it in place with screws or adhesives, or allowing for adjustability with rails or sliding mechanisms.

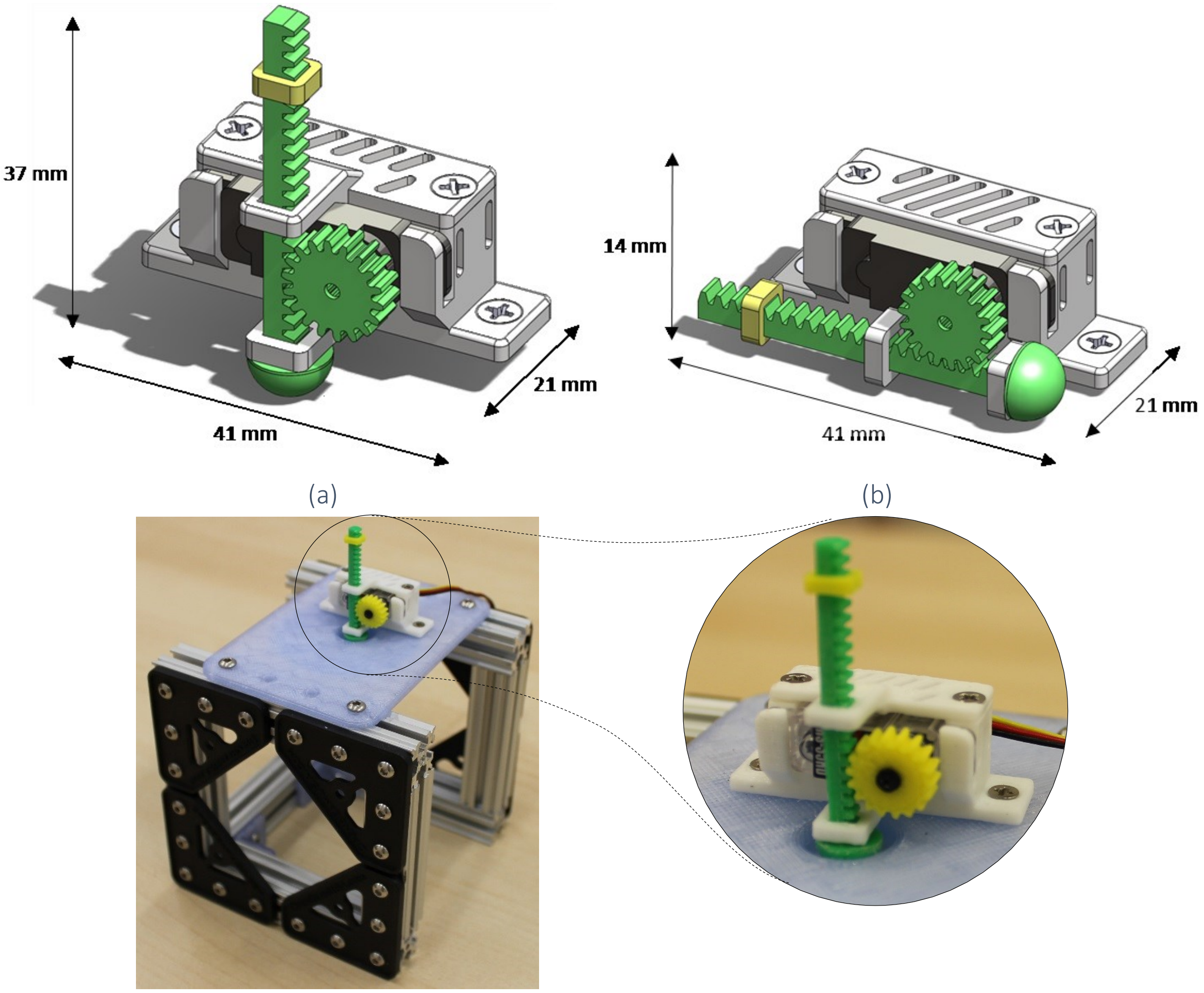

(a)

(b)

(c)

Figure 4.23 Updated linear tactor (a) vertical design, (b) horizontal design, and (c) prototype

4.5.3 Cable-Driven Tactor

The 90° bend was updated to include a printed guide for the cable conduit to help the tactor head exit from the bend at a true right angle (Figure 4.24). The tactor head was updated based on recommendations from the optimization study. A Force Sensitive Resistor (FSR) was integrated into the design to allow for forces applied by the tactor to be quantified, with calibration and control discussed Chapter 6. The segment allowing for the FSR integration adds an additional 30 mm to the minimum length, so should only be used where a large distance between the servo motor and tactor head is planned; otherwise the FSR can be placed in-line with the rack gear.

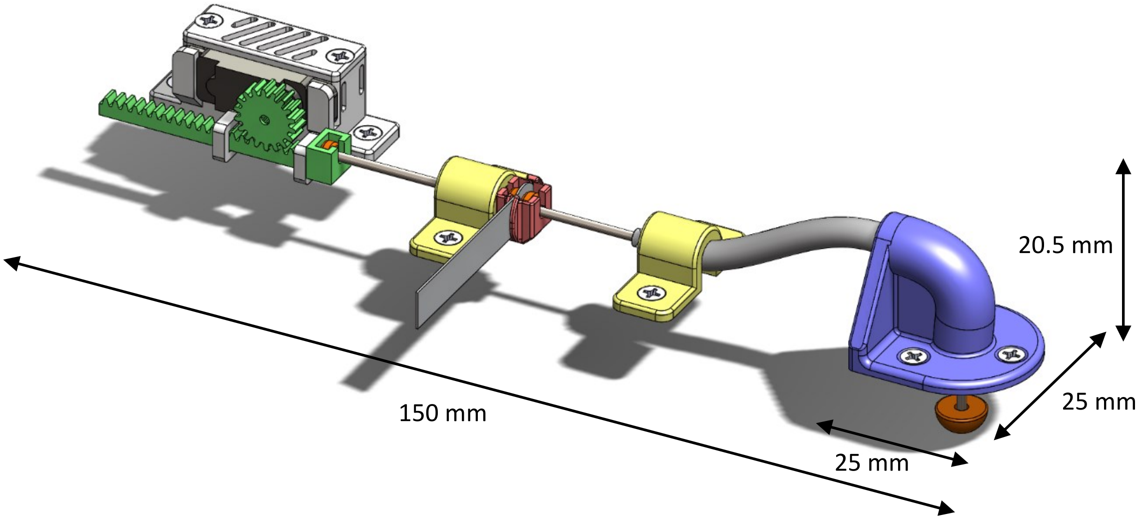

(a)

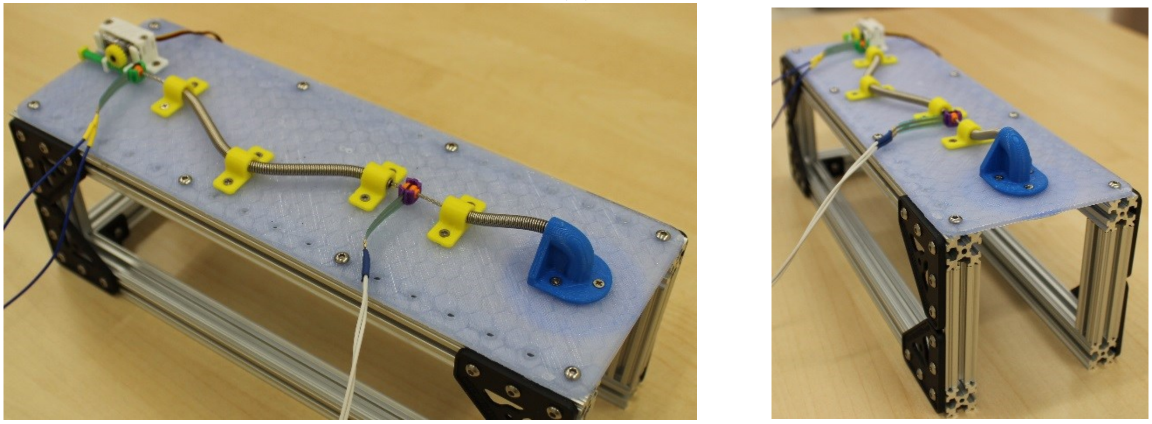

(b)

Figure 4.24 Updated cable-driven tactor (a) design and (b) prototype

4.5.3.1 Friction Testing[5]

Testing was conducted to determine the influence of various bends in the Bowden cable of the tactor on overall friction forces in the system. The test set-up allowed for different curves of the Bowden cable to be created, and frictional forces measured by hanging weights from the loop attachment until the system just began to slip (Figure 4.25).

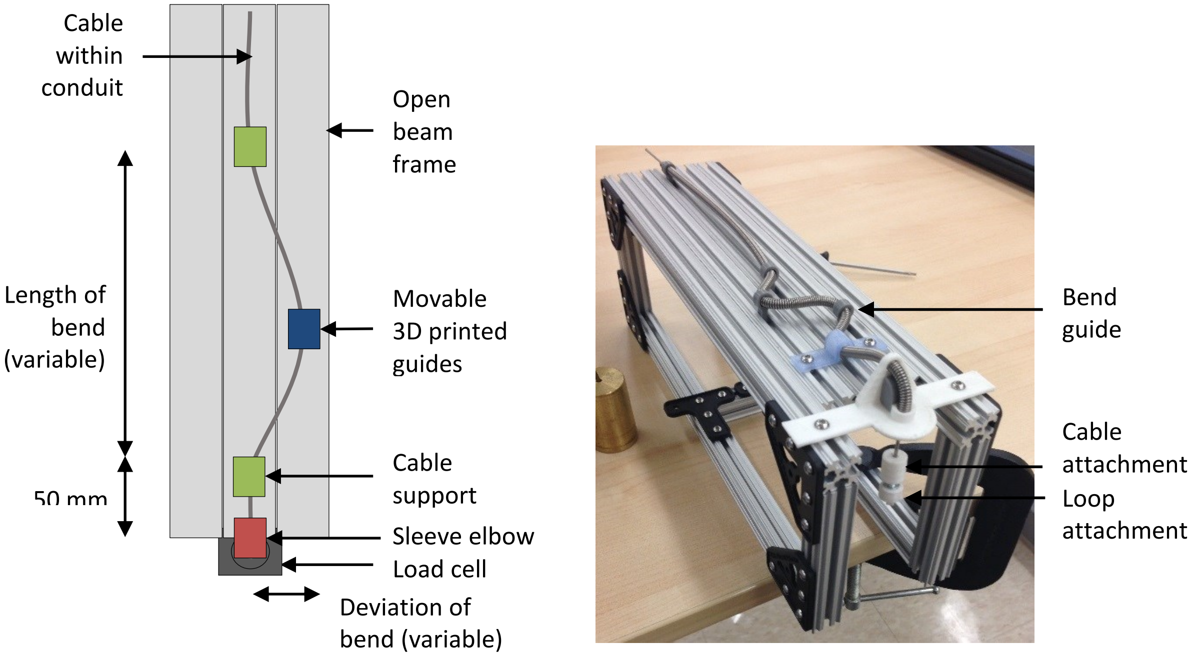

(a) (b)

Figure 4.25 Test setup for Bowden cable frictional testing (a) proposed, and (b) assembled

Two cases were quantified; straight and curved. Note that total length is from the cable support to the end of the conduit, and does not include the 50 mm from the cable support to the other end of the conduit attached to the sleeve elbow. In the straight case, the cable length was varied (100, 150, and 250 mm). In the curved case, cable length (150 and 250 mm), curve length (50, 75, and 100 mm), and curve deviation (15, 22.5, and 30 mm) were varied. All measurements were repeated three times. Results were analyzed using the software Statistica (StatSoft, 2014), with a *p*-value ≤ 0.05 indicating significance. The resolution of frictional forces applied was 0.1 N, thus contributions from variables less than this value were removed from final regression equations.

---

[5] This friction testing was performed by Heather Williams, under supervision of the author

ANOVA and linear regression were used for the straight cable case, and mixed levels ANOVA and multiple-regression for the single curve case. Linear, quadratic, and interaction effects were investigated. Data was checked for normality and no obvious trends in residuals were observed.

In the straight cable case it was found that an increase in cable length corresponds to a linear increase in friction (Figure 4.18), following the regression equation below with an R^2 value of 0.89.

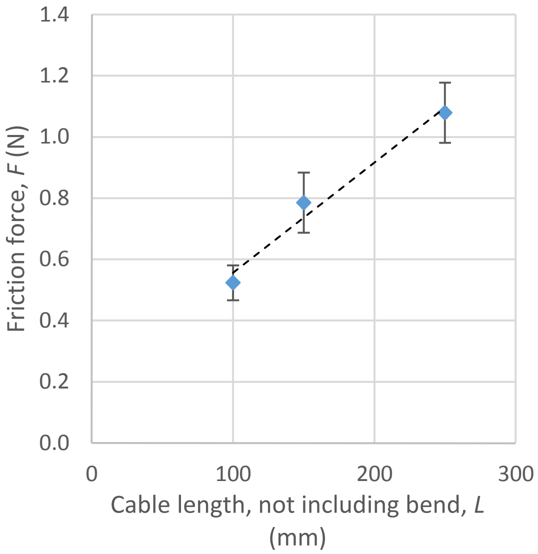

Figure 4.18 Friction force in response to different length cables

$$F = 0.0036L + 0.2$$

Where *F* is the friction force (N) and *L* is the cable length (mm).

In the curved cable case, it was found that friction increases linearly with an increased curve deviation and decreases linearly with an increased curve length (Figure 4.27). Curve length has a significant quadratic effect. There is an interaction between curve length and deviation, where a shorter length and higher deviation will significantly increase friction. Counterintuitively, an increase in total length was shown to statistically reduce the friction; however, the contribution was lower than the 0.1 N resolution of the measurements taken. Upon further inspection, it was found that the shorter cable contained a slight permanent deformation, which may be responsible for the increased friction; total length was excluded from the remaining analysis.

The resulting regression equation is shown below with an R^2 value of 0.97.

$$F = 0.1161D - 0.0742C + 0.0004C^2 - 0.0007DC + 4.2$$

Where *F* is the friction force (N), *D* is the curve deviation (mm), and *C* is the curve length (mm). The large intercept indicates that with the addition of a single tight curve, the overall friction in the system increases substantially (4.2 N compared to 0.2 N).

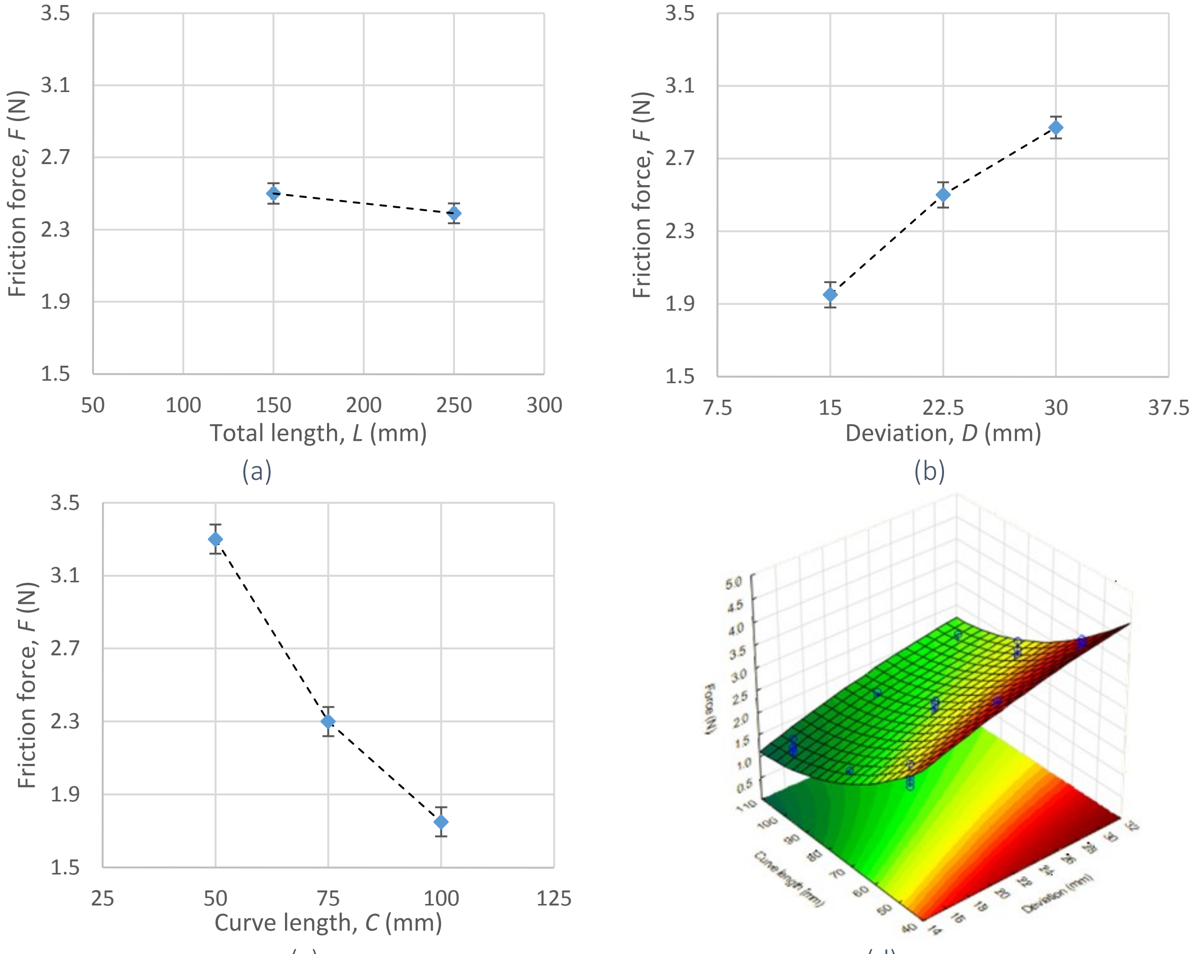

(a) (b)

(c) (d)

Figure 4.27 Friction force in response to manipulated variables (a) total length, (b) deviation, (c) curve length, and (d) interaction between deviation and curve length

This study indicates that introducing curvature to Bowden cables will increase overall frictional forces, meaning that curves should be avoided or designed to be as gradual as possible, depending on other socket constraints. Should significant curvature be introduced, it is possible that a more powerful motor is required to overcome the friction in the system to ensure that sufficient force can still be applied to the residual limb.

A future study could be conducted to determine the effect of permanent deformation of the cable (such as a kink or gradual curvature), change in cable properties over time, implementing multiple bends, or unrestricted bend movement as would likely be present should the cable cross the prosthetic elbow.

4.6 Comparison of Tactors

4.6.1 Current Draw and Peak Applied Force

The current draw at various static loads was measured using the same tools as listed above for both the linear and cable tactor (Figure 4.28) and was found to be fairly repeatable across different motors. The peak applied forces were measured by applying a pseudo-step function from zero to maximum displacement; for some of the motors a true step function caused the gears to slip as the motor tried to move too quickly, so the displacement input was set using a manual slider instead. It was found that the forces dropped off quickly (Figure 4.29). Three different motors were tested and while there is little variability between motors, there is a difference between tactors due to the friction present in the cable tactor. It is likely that the current drawn while the system is moving dynamically could differ from the static current, so this requires further investigation. Generally speaking, the longer the cable the more current is required to apply a given force, and the lower the maximum force that can be applied. This is likely due to the friction in the cable, as discussed previously.

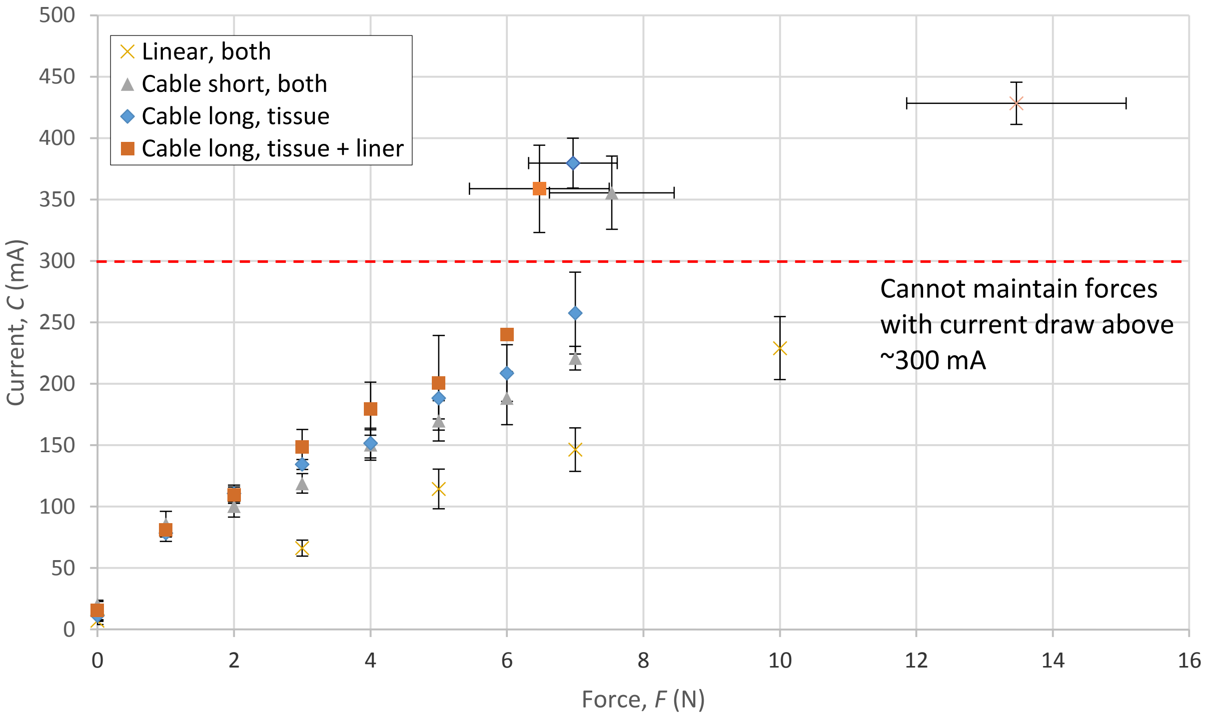

Figure 4.28 Current draw at various static loads for linear tactor, short 75 mm cable-driven tactor, and long 220 mm cable-driven tactor with a single bend of 21 mm from center. Note that different materials are plotted separatly when significantly different

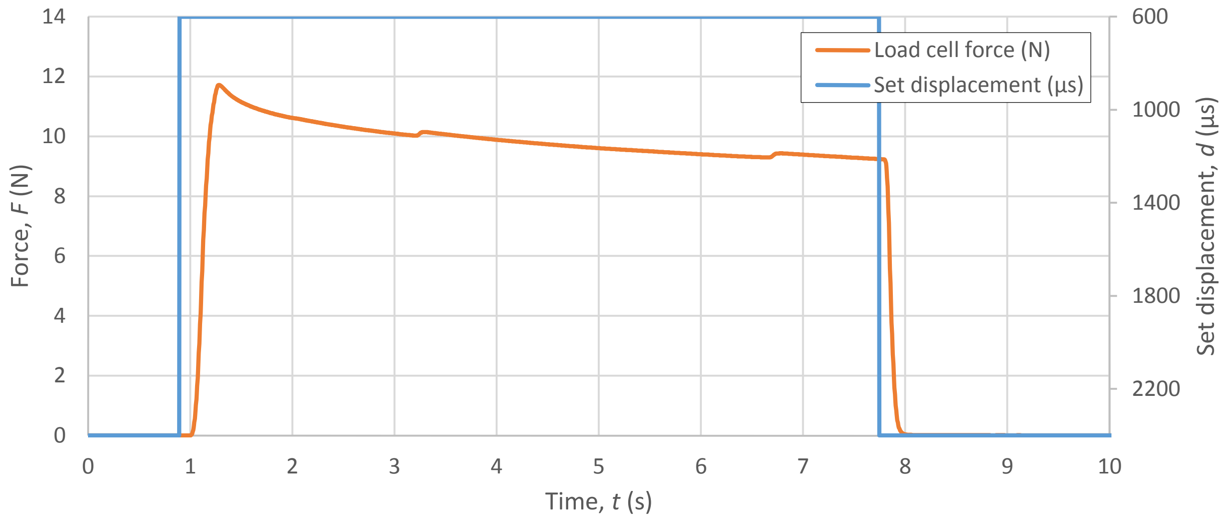

Figure 4.29 Peak applied force measured over time for a single linear tactor

4.6.2 Temperature

The temperature of each motor was measured using a digital thermocouple (Omega, HH506RA), placed on the servo casing, just beneath the motor itself. Both static and cyclical conditions were tested for thirty minute trials; held constant at 5 N and loading up and down to 7 N in a sine wave for the linear tactor and to 5 N for the long cable tactor, respectively. Three different motors were tested by pressing onto two layers of alpha liner. In both cases the cyclical loading did not reach as high of a temperature as the static loading. For the linear tactor, in the 5 N static loading case, after the motors were running for approximately 20 minutes two of the plastic housings began to slowly warp due to the heat produced by the motor (up to an external temperature of 37.6 ± 0.3°C); upon inserting the thermocouple inside of the motor housing the recorded temperature was up to 50°C, which is hot to the touch. The cable-driven tactor reached an external temperature of 43.4 ± 3.4°C, however warping did not occur, as the direction of the rack gear did not push onto the heated plastic resulting in deformation.

This testing suggests that the system should not be used to apply high forces for extended periods of time, as this will cause the motors to exceed the threshold for hot touch temperature requirements of 45°C. This is not expected to occur during normal use; in fact it should be avoided as extended high loads increase the risk of pressure ulcers, as discussed previously.

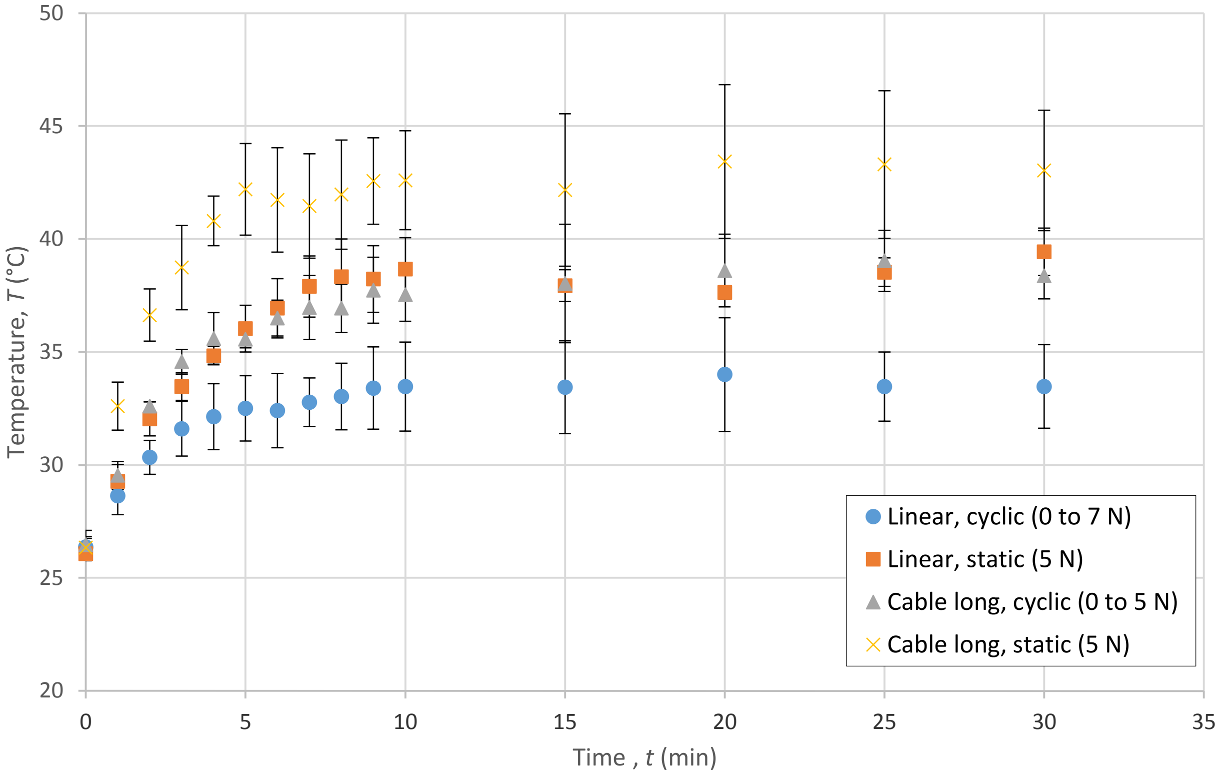

Figure 4.30 Temperature at various loading conditions for linear tactor and long 220 mm cable-driven tactor with a single bend of 21 mm from center

4.7 Conclusion

Several design refinements have been implemented into the tactor designs. These tactors are able to apply forces onto the residual limb, where the linear tactor can reach a larger excursion distance and maintain a higher force than the cable-driven tactor, mainly due to the friction introduced by the Bowden cable. If forces are matched between the linear and cable-driven tactor, the linear tactor will draw less current and therefore maintain a lower temperature. Both tactors can be limited in the maximum force they can apply by including a mechanical stopper onto the rack gear of the system.

The mechanical subsystem for both tactors can be produced for approximately $50 not including engineering design or labour costs (Table 4.4 and Appendix B).

Table 4.4 Comparison of mechanical systems of tactors, see Appendix B for more detailed breakdown of cost, weight, and manufacturing time

Feature	Linear Tactor	Cable-Driven Tactor Minimum length [a] (80 mm)	Maximum length [a] (220 mm with 21 mm deviation)
Footprint in limited real estate region (mm x mm)	21 x 41	25 x 25	25 x 25
Maximum height (mm)	37	20.5	20.5
Weight (g)	9	20	36
Peak applied force (N) [b]	13.5 ± 1.6	7.9 ± 0.7	6.8 ± 0.9
Current draw at 5 N (mA)	114 ± 16	170 ± 16	195 ± 28
External temperature after 20 min at 5 N (°C)	37.6 ± 0.3	N/a	43.4 ± 3.4
Maximum excursion distance (mm)	17	N/a	15
Raw material cost ($CAD)	50	45	50
Approximate rapid prototyping time (min)	38	76	76
Approximate manual labour time (min)	40	60	60

(a) Lengths measured from front of servo motor to center of tactor head, maximum length indicates tested length – a longer cable is possible, but performance will fall outside tested abilities

(b) Peak applied force cannot be sustained, and can be limited as discussed in section 4.5.1.2

The successful clinical deployment of the new simplified inexpensive tactor will help to make sensory feedback for prosthetic sockets practical and financially feasible, however several future improvements are suggested.

4.8 Future Improvements

Based on the evaluation of the cable-driven tactor, it is suggested that the D47 Power Servo motor be integrated where long cable lengths are required to increase the force that can be applied and reduce the overall temperature the motor reaches during heavy use situations. Alternatively, a motor could be designed with the exact system specifications to optimize power draw, current, size, and rotation limits.

It would be beneficial to limit the amount of current that can reach the motor. Despite the safeguards, it is possible that the tactors may apply more than 7 N of force. Limiting the current would reduce the peak force that could be applied to the residual limb, as well as reduce the temperature that the tactor can reach. Static testing suggests that the current could be limited to approximately 300 mA for the cable-driven tactor, though further testing should be conducted to ensure that dynamic loading would not be compromised by this limited current. The linear tactor would need to be limited to an even lower current draw. Therefore current limiting electronics would need to change based on what type of tactor is used and potentially the length of cable and number of bends used. The ability to accurately measure current draw may also be useful for quantifying applied forces, discussed further in Chapter 6.

Another improvement would be to construct the tactor system using a different material with a higher melting point and strength, such as nylon or aluminum. Due to the complex geometry and low required quantity, the selected material for the housing should still be capable of being rapid prototyped. It is also recommended to manufacture or source the gears with higher tolerances to improve meshing.

Options for reducing the temperature of the servo motor should be further investigated. This is especially important as up to 53% of prosthetic users experience heat and/or perspiration discomfort within their prosthesis [81]. Possible avenues to explore include investigating heat sinks, or implementing a shroud to cover the motor and prevent accidental contact, however this would reduce air flow. Another option is to implement software that will pulse the motor if it is reaching a higher temperature to allow it to cool down.

Several of the specifications were out-of-scope for this thesis work due to lack of information regarding system usability. Therefore prior to take-home trials it will be important to conduct a study that determines the typical usage of the tactors to quantify information such as how often tactors are activated, how hard they are pushing onto the skin, and if there are any further limitations such as noise or unexpected wear.

Chapter 5. Above-Elbow Prosthesis Integration

5.1 Introduction

Thus far in literature, integration of tactors onto an above-elbow prosthesis has not been demonstrated. In fact, integrating tactors onto a socket has been largely overlooked in literature, and is therefore a barrier to clinical translation. Acceptance of tactors may be improved by minimizing the changes required to the traditional socket manufacturing process, maintaining the functionality of the socket, and ensuring that the tactors do not interfere with fit and comfort. In order to facilitate clinical translation, integration and use of a tactor system in an above-elbow prosthesis must therefore be demonstrated.

5.2 Background

In order to provide feedback to the user, tactors require access to skin sites on the residual limb. The tactor must be integrated onto and through the prosthetic socket, which is used to attach the prosthesis to the residual limb (Figure 5.1). Therefore an understanding of this socket interface is needed.

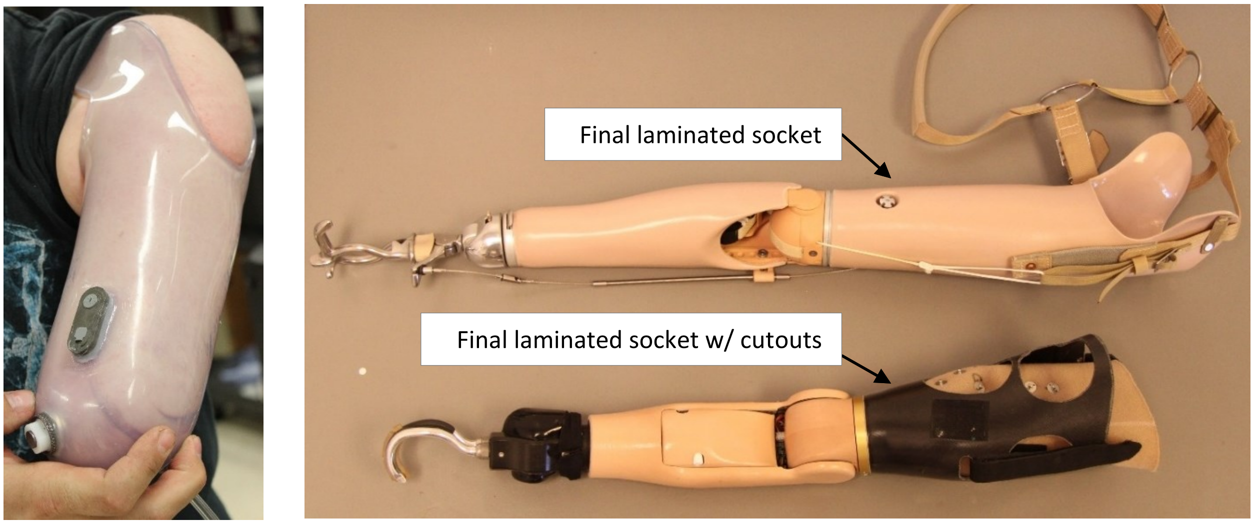

(a) (b)

Figure 5.1 Prosthetic socket examples, (a) temporary, and (b) final laminated

Different socket designs can include combinations of roll-on suction suspension gel liners, locking mechanisms, harnessing, flexible socket construction, and anatomically contoured (self-suspending) sockets [1]. The use of a gel liner is becoming a standard for upper-limb socket designs, as it has been clinically observed to allow a larger range of motion at the remaining joints, increase the comfort and tolerance of aggressive socket design, and protect fragile skin [82, 83]. Sockets are typically constructed from plastics, thermoplastics, and laminates since they are light, flexible, and allow patient-specific contouring [8]. Currently, the main focus of socket design is on appearance, function, control, comfort, and durability [2].

There are many novel socket designs being developed. For example, through the Revolutionizing Prosthetics 2009 DARPA funded project, advances in shoulder microframes, silicone sockets with embedded flexible surface sensors, and hybrid sockets have been investigated [23]. While tactors are mentioned briefly, a plan for their integration is not provided in any detail.

Most papers concerning tactor designs do not address the socket integration issue. One paper demonstrated the integration of several tactors into the forearm of sockets for eight below-elbow amputees using custom moulded prosthetic sockets with access holes drilled into the socket for access to the skin [26]. These arms were kept in a fixed position during testing and passively manipulated by the experimenter. Another paper suggested mounting the tactor in the interface between the user and the prosthetic device, within the socket [47], however no demonstration of this concept was provided.

Thus integrating a tactor system onto an above-elbow myoelectric prosthesis has yet to be thoroughly investigated.

5.3 Temporary Socket Integration

The tactor system was initially integrated onto a rapid prototyped sleeve for able-bodied participant testing, with details presented in Appendix C. This helped to address spacing and alignment challenges. The tactor system was then integrated onto a temporary socket of an above-elbow amputee for evaluating additional challenges associated with interfacing with a socket manufactured using traditional methods. This included integration of the tactors onto the prosthetic socket and design of an electronics enclosure to embed the electronics into the forearm of the prosthesis. A bill of materials is provided in Appendix B.

5.3.1 Tactor Subsystem Attachment

A temporary thermoplastic socket was cast in-house[6] containing a one-way valve (Trulife) and two EMG electrodes (Motion Control, Triad Preamp System) (Figure 5.2 (a)). Tactors were attached to the socket using small screws with blind holes drilled into the socket (Figure 5.2 (b)).

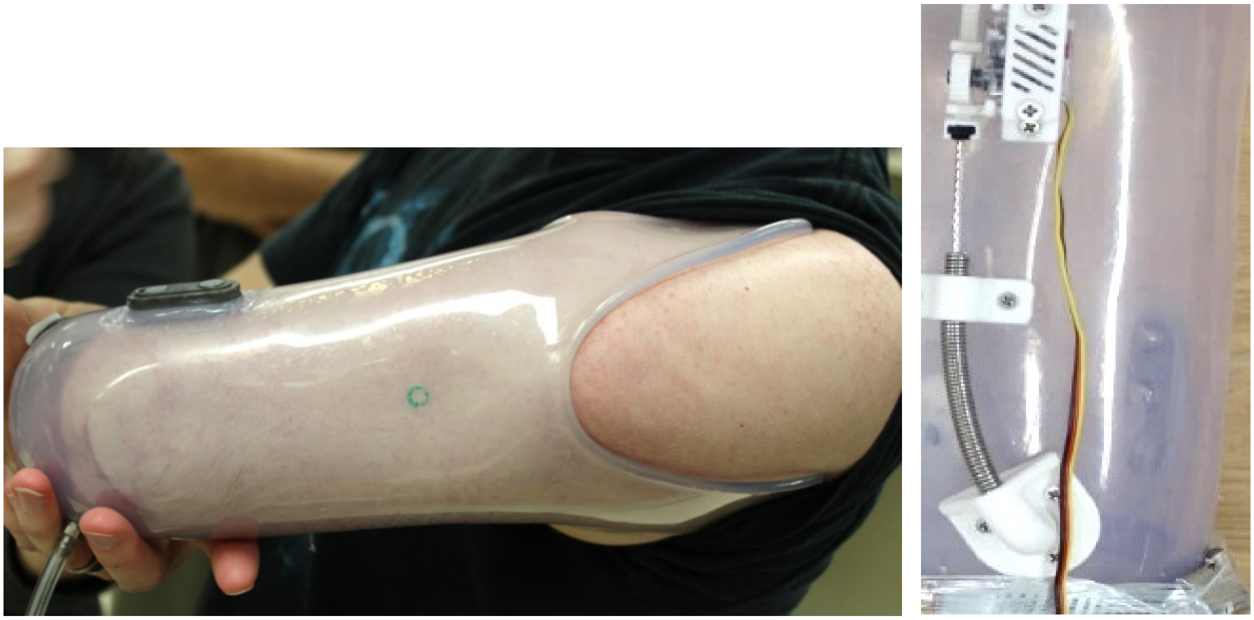

(a) (b)

Figure 5.2 Temporary thermoplastic socket (a) intial, and (b) with integrated tactors

Mouldable glue (Sugru) was used in places of high curvature to adhere the flat tactor components to the curved socket. Future improvements to these parts may involve matching the curvature

---

[6] The temporary socket was manufactured by Michael Stobbe, BLINC lab member and Certified Prosthetist

of the component bases to the curvature of the socket. The tactor head accessed the skin via a 9 mm diameter through hole in the socket. Two tactors were attached, one each on the lateral and medial sides of the arm.

5.3.2 Electronics Subsystem

5.3.2.1 Wearable Tactor Controller

In addition to the tactor components, electronics were required to control the system. Initial prototypes used an Arduino Uno controller (Arduino), however a miniaturized electronics system was developed, the Wearable Tactor Controller (WTC, Figure 5.3). The controller system was developed in-house[7] and can be produced for an approximate additional $54 and two hours of skilled labour to manufacture.

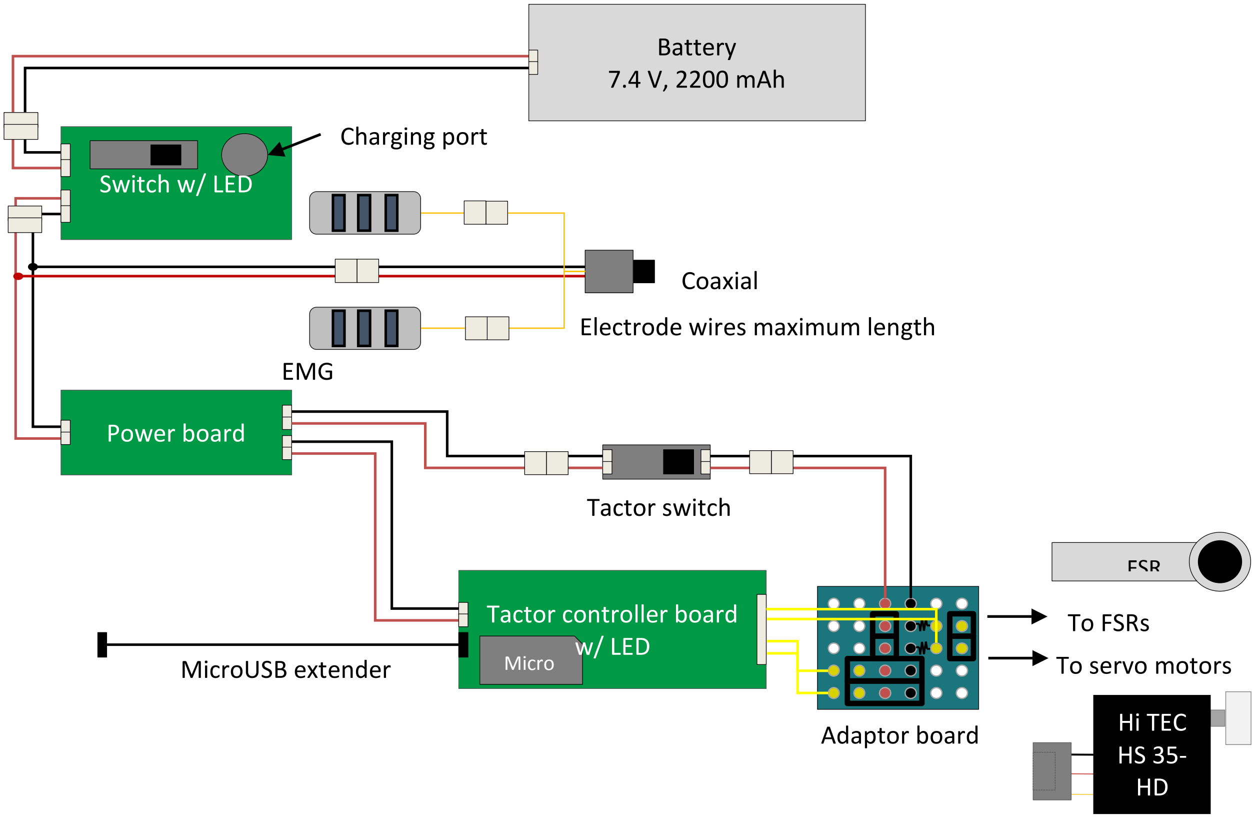

Figure 5.3 WTC components schematic diagram

---

[7] The controller and associated electronics were designed and manufactured in-house by Brodi Roduta Roberts

5.3.2.2 Embedded Enclosure

An enclosure was designed to contain the electronics within the forearm of a commercial prosthesis (Figure 5.4). The enclosure fits into the space within a commercially available prosthetic forearm. The minimum length within the forearm is 98 mm, with an additional protrusion of 8 mm for the wrist adapter; should this space not be available within a prosthetic forearm, the design may be modified so that the batteries are placed in alternate compartments within the forearm. The switches and charging port extend out the top of the forearm, as do the cables for the FSRs. The servo wires, electrode wires, and microUSB adapter extend out the back of the forearm at the elbow joint.

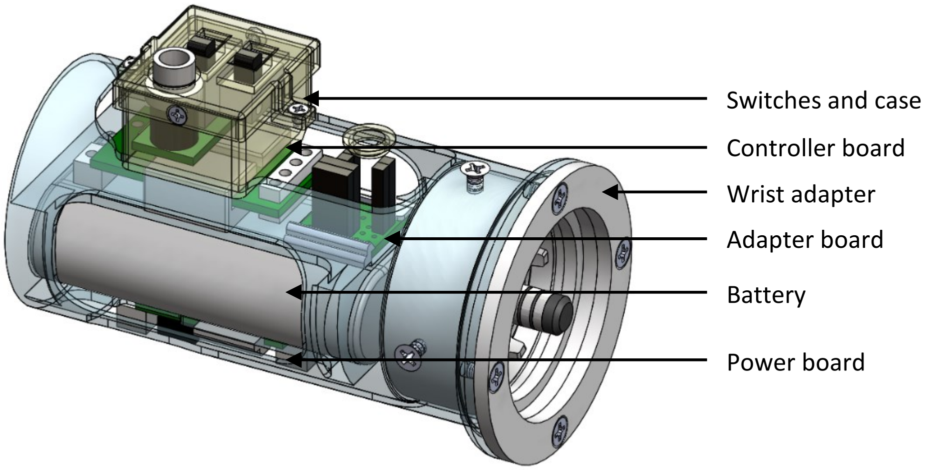

(a)

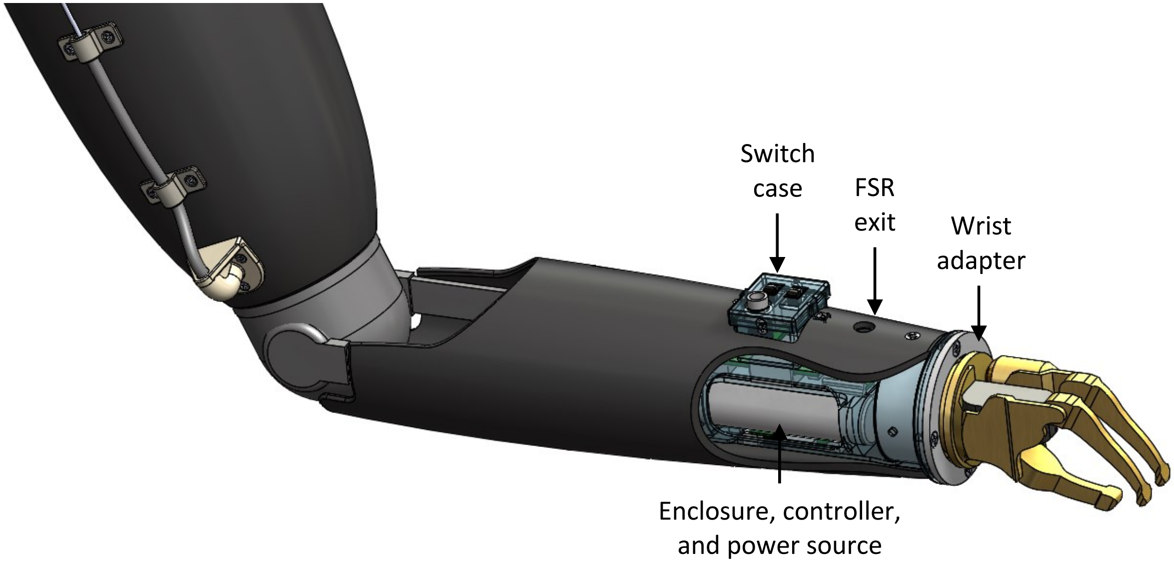

(b)

Figure 5.4 Enclosure for the WTC (a) design, and (b) fit into the forearm of the prosthesis

5.3.2.3 Sensor Selection and Integration

Sensors were integrated onto the terminal device (Figure 5.5), based on accuracy and size constraints of the selected prosthetic system; in this case inexpensive FSRs were adhered to the surface of the prosthetic fingers as recommended in a review paper for sensors in prosthetic applications [19]. While these sensors are not as accurate as load cells, their small size and flexibility make them feasible to attach to a commercial prosthetic finger without extensive modification.

Figure 5.5 FSRs adhered to the index and thumb of the prosthetic hand

5.3.3 Final Integrated Prosthetic Arm

The final assembly[8] included a prosthetic hand (BeBionic, BBHMDLQD – Medium hand with EQD wrist) myoelectrically controlled using two EMG electrodes (Motion Control, Triad Preamp System) over the biceps and triceps muscles, with a body powered elbow with a lift assist (Hosmer, Lift Assist Unit) and electronics housed in the forearm (Hosmer, E400 Forearm Assembly) (Figure 5.6(a)).

---

[8] The commercial components were assembled with assistance from Michael Stobbe, BLINC lab member and Certified Prosthetist

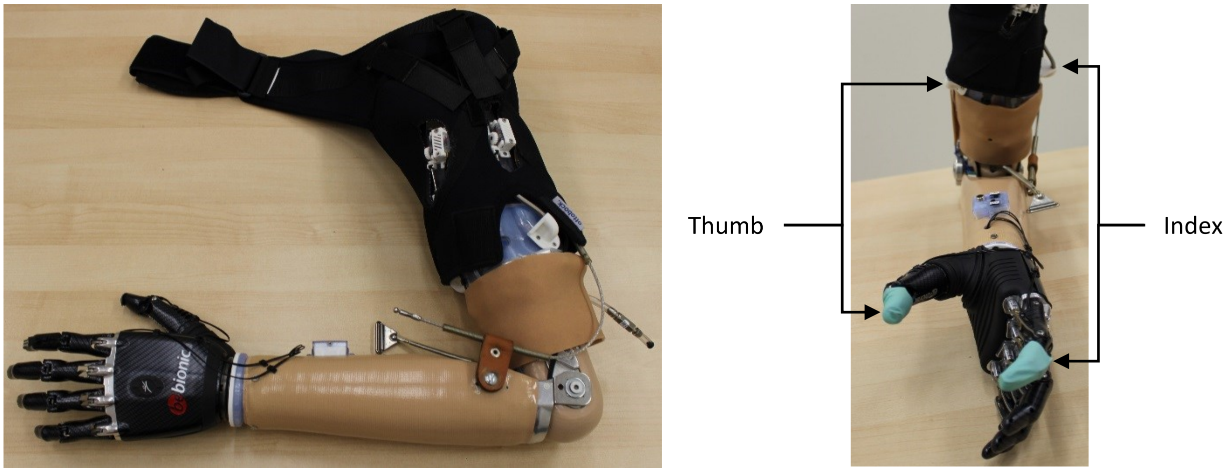

(a) (b)

Figure 5.6 Integrated socket for participant testing (a) overall, and (b) linked tactor components

The tactor on the lateral side of the arm was linked to the FSR placed on the index finger of the prosthetic hand, while the tactor on the medial side of the arm was linked to the thumb (Figure 5.6(b)). This was selected to spatially align the tactors to the prosthetic index and thumb while the hand was in the neutral position with a slight opening. The tactor head position for the lateral tactor was moveable so that it could be placed close to the EMG sensors for evaluation.

5.4 Evaluation

An amputee participant (Table 5.5) was outfitted with the tactor system described in Section 0 and performed several tasks to demonstrate the capabilities of adding mechanotactile feedback to a prosthetic arm. This study was approved by the University's Health Research Ethics Board, and written informed consent was obtained from the participant.

Table 5.5 Participant measurements and prosthetic arm details

Category	Measurement
Gender	Male
Age	29
Height	5'10"
Weight	175 lbs
Days per week prosthesis is worn	4-5
Hours per day prosthesis is worn (on average)	8-14
Time since amputation (years)	2 years and 11 months
Level of amputation	Trans-humeral
Side of amputation	Left
Residual limb length	28 cm
Residual humerus length	26 cm
Diameter at axilla	36 cm
Diameter approx. mid length	27 cm
Prosthetic hand	Bebionic
Prosthetic elbow	Ottobock AF13 12K44
Harness	Ottobock Acro comforT

5.4.1 Participant Set-Up

Participant inclusion criteria were that the participant have an above-elbow amputation, currently operate a myoelectric hand, and have a well-fitting prosthetic socket. The participant was fitted with a temporary socket mounted to similar components he was used to operating, including type of myoelectric hand and control method (Figure 5.7). Tactor placement was determined in a preliminary session, ensuring that tissue compliance was adequate (i.e. no boney prominences or excessive fatty tissue), placement was over areas with no known sensitivity or pain issues, and EMG sites were avoided.

(a) (b)

Figure 5.7 Prosthetic arm with integrated tactors fit to the participant, (a) hand, and (b) socket with harness attachment

Experimental set-up included a table and chair to allow the participant to be seated comfortably with his prosthesis supported when not in use. Noise cancelling headphones playing white noise and a blindfold were applied during test sessions to prevent external stimuli from affecting results. Forces were measured using a load cell (Omega, LCM703-5) reading into Simulink Realtime (Mathworks Inc., 2014).

5.4.2 Methods

5.4.2.1 Sensitivity and Discrimination

Sensitivity and two-point discrimination were measured over the tactor sites at the beginning and end of testing (Figure 5.9), using the staircase method discussed in Chapter 3 to ensure that the participant's sensitivity remained within normal thresholds.

5.4.2.2 Finger Identification

The ability to identify which finger was being stimulated was evaluated through two sessions, similar to [46, 48]. A learning session was conducted where each of the prosthetic fingers was stimulated by the investigator for approximately three seconds (index, thumb, or both), followed by verbal confirmation of the finger(s) being stimulated. This learning session was conducted with vision and hearing intact, up until the participant was comfortable with identification (three presentations of each finger combination). The test session was then conducted with the participant’s vision and hearing occluded. Finger stimulations were applied in a random order (including a “neither” condition) four times each for a total of sixteen stimulations. The participant was queued for his response using a light touch on his shoulder, and his response recorded.

5.4.2.3 Force Level Detection

Force levels applied by each tactor were tested within a comfortable range determined by the participant, taking the most conservative of three repeated measures of maximum comfortable tactor displacement. This was approximately 2.3 and 1.2 N in the corresponding thumb and index locations, respectively. Forces measured on the prosthetic fingers (between 0 and 10 N) were mapped to those applied by the tactor, with the approximate mapping presented in Appendix E. Force levels applied to the prosthetic finger were as follows: none (0 N), low (2 N), medium (6 N), and high (10 N).

The ability to distinguish the level of force being applied was evaluated through two sessions at each force level tested, similar to [46, 48]. A learning session was conducted where forces were applied by hand to the prosthetic finger for approximately three seconds using a load cell to measure force. Forces were applied in order from smallest to largest to demonstrate the levels being tested, up until the participant was comfortable with force identification (between two and four presentations at each level). The test session was conducted with the participant’s vision and hearing occluded. Force stimulations were applied in a random order (including a “no-touch” condition) eight times each, as in [58]. The participant was queued for his response using a light touch on his shoulder, and his response recorded. An additional level was added until participant performance deteriorated to below 75% accuracy. Both tactor locations were evaluated separately.

5.4.2.4 Ball stiffness discrimination

The ability to distinguish balls of different stiffnesses (750 N/m and 235 N/m) was evaluated through two sessions, similar to [58]. A learning session was conducted where balls were grasped alternatively, up until the participant was comfortable with density identification (approximately 5 times each, including ten minutes of free play as in [58]). The test session was conducted with the participant's vision and hearing occluded. Balls were placed in the prosthetic hand in a random order (including a "no-ball" condition) eight times each. The participant was queued for his response using a light touch on his shoulder, and his response recorded.

5.4.2.5 EMG interference

The effect of tactor placement on EMG signal response was evaluated, as placing EMG sensors and tactors close together may reduce control and sensing by the participant [34, 58]. The tactor head was movable so that it could be positioned approximately 2 or 4 cm from the EMG electrode over the bicep muscle (Figure 5.8). The participant was asked to open and close his prosthetic hand around a ball five times, while EMG signals were logged to the prosthetic device software (BeBionic, BeBalance 3.5) under four test conditions (tactor placement close or far, with tactors on or off), replicated for a total of eight trials.

(a) (b)

Figure 5.8 Moveable tactor head test set-up approximately (a) 2 cm from EMG electrode, and (b) 4 cm

5.4.2.6 Qualitative Survey

The participant was given a survey to complete at the end of the test session. He was asked to subjectively rank various aspects of the tactor system using a 5-point Likert scale, as well as respond qualitatively to several questions.

5.4.3 Results and Interpretation

5.4.3.1 Sensitivity and Discrimination

Both tactor sites were measured to be within the normal range of sensitivity (below a monofilament index of 2.8, with the sensitivities of the thumb and index corresponding locations being equivalent), and two-point discrimination values and changes fell within the ranges found in previous testing (between 12 and 66 mm, and up to 30 mm respectively) (Figure 5.9).

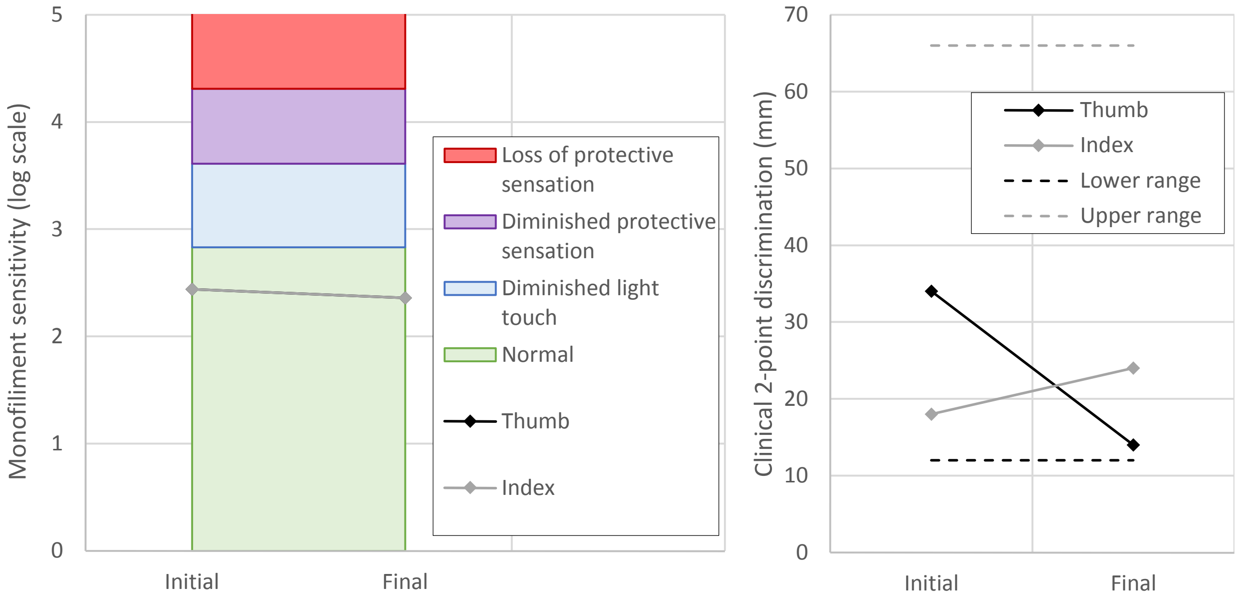

(a) (b)

Figure 5.9 Measurements at beginning and end of testing (a) sensitivity, and (b) two-point discrimination

5.4.3.2 Finger Identification

Finger identification was performed with 100% accuracy, suggesting there was no difficulty in identifying the finger being stimulated.

The participant in this study did not have hand mapping on his residual limb, so substitution was used to identify which digits were indicated by the movement of each tactor. Finger identification was performed with 100% accuracy, suggesting there was no difficulty in identifying the finger being stimulated.

It is expected that with a larger number of tactors that substitution would become more challenging, as found in [46, 48]. It may be valuable to confirm this with a fully integrated tactor system in a prosthetic user, as opposed to tactors being placed on the forearms of able-bodied participants as in [46, 48].

5.4.3.3 Force Level Detection

Analysis of the results indicates that the accuracy of force level identification droped as more levels were added, as would be expected (Figure 5.10). Distinguishing between tactors being on or off was correct 99.3% of the time, with only one error reported as touch when none was applied. Accuracy at three levels (no touch, soft, and hard) was 79 and 88%), and for four levels dropped off to 63 and 66%.

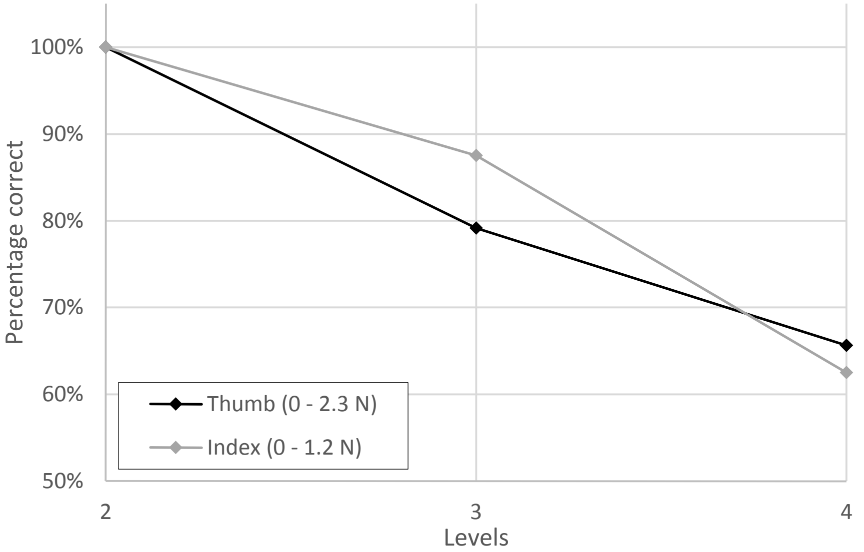

Figure 5.10 Comparison of force discrimination accuracy at different levels

This is poorer than that found in previous studies, where accuracy at four levels in [48] was 93%, in [46] was between 92 and 98%, and in [58] was between 75 and 85%. This may be due to several differences between studies. In these previous studies, larger force ranges were applied (up to 10 N in [46, 48], up to 3 and 5 N in [58], versus up to 1.2 and 2.3 N in this study), which allows larger differences in step sizes between levels. As well, force steps were applied approximately linearly; in this study, input forces were measured by an FSR, and the output from this sensor was linearly mapped to tactor head displacement. As a result, due to FSR response being non-linear, this resulted in a non-linear application of forces to the residual limb. An approximate relationship is shown in Figure 5.11, which was determined by calibrating the FSR and tissue response. This shows that at higher force levels, the differences in forces applied to the residual limb were quite small, which may help to explain the poorer performance. A discussion of this calibration and the associated errors is provided in Appendix E. Finally, in [46, 48], reinforced learning continued through the test session, where the participants were informed if they had correctly identified the force level, which was not done in this study to avoid learning as a confounding variable.

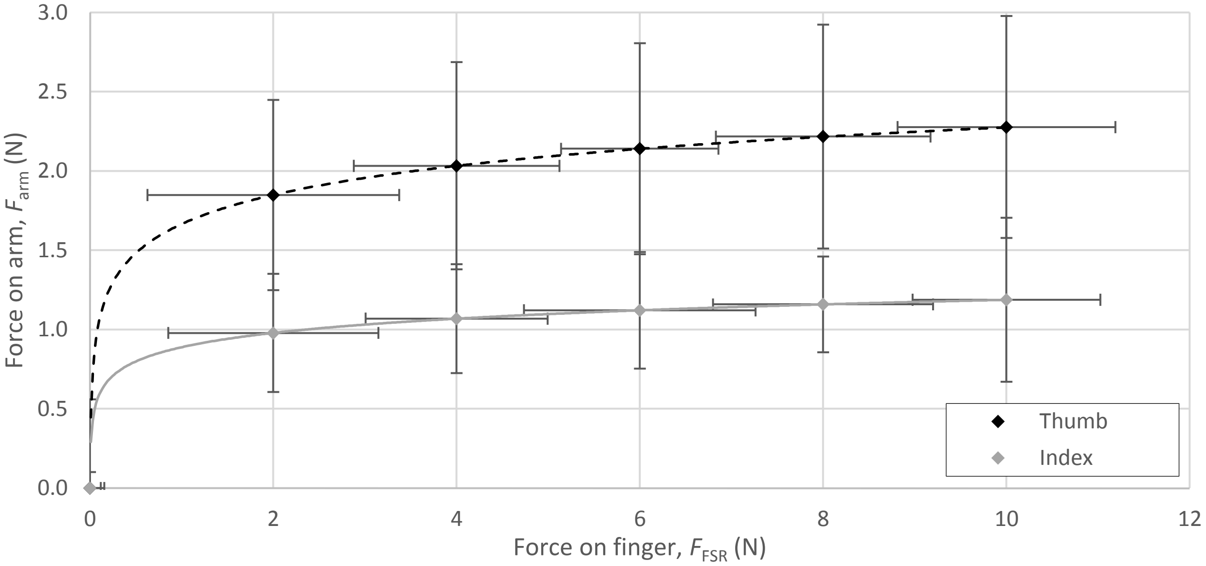

Figure 5.11 Approximate mapping between input force to the prosthetic finger to forces applied by the tactor to the residual limb

Other modalities have found different force level discrimination accuracies. In [84] air filled bulbs were used to display forces to the limb, where discrimination at two levels (without a "zero" case) was between 80 and 90%, which is comparable to the accuracies found in this study, between 79 and 88%.

5.4.3.4 Ball stiffness discrimination

Overall accuracy in distinguishing between no ball, soft, and firm was 67%. Distinguishing between ball and no ball gave an accuracy of 83%. This is poorer than the 100% accuracy found in a previous study [58]. The reduction in accuracy is likely due to differences in test set-up. In [58], the hand was stopped at a given displacement rather than allowing it to close fully (i.e. until the index and thumb contacted each other), and mapping of forces was magnified such that the forces applied by the tactor were as different as possible for each ball squeezed. In this study, the hand was not modified in order to remain pertinent to a real-world application, however this meant that under a constant close signal the hand will close until it stalls, measured to be 18 ± 2 N, so very close attention must be paid to the rate at which the hand closes or the rate at which the tactors apply force. An added complication is that when no ball is placed in the hand, if the index and thumb come into contact the sensors will press against each other and cause the tactors to push onto the arm. Unless the user is paying close attention to the timing of the hand close, which requires very precise control, it is nearly indistinguishable from closing around an object. Towards the end of the trial the participant was experiencing some muscle fatigue making control difficult; this may have influenced his ability to precisely control grip velocity.

5.4.3.5 EMG interference

Raw data could not be exported from the software (Figure 5.12), so maximum signal for each command (open or close) was measured from the graphs. A paired t-test demonstrated a significant difference between the close and open signal magnitudes ($p < 0.05$). This is clear from observation of the graphs, as was the fact that a hand open signal also resulted in co-contraction, suggesting that the close electrode should be repositioned to a better location. These conditions were consistent across all combinations of placement and activation of the tactors.

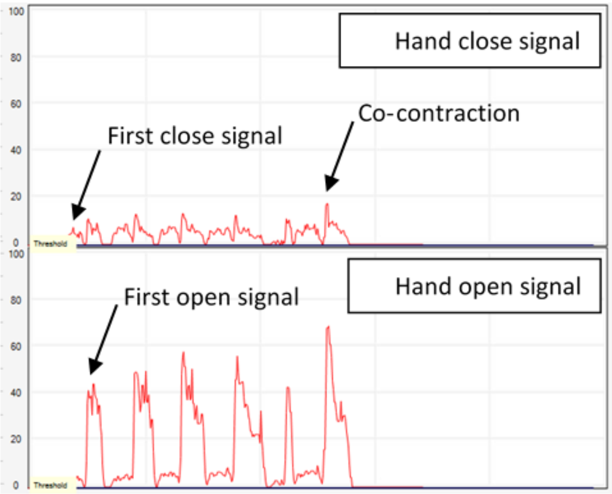

Figure 5.12 Sample EMG data collected (tactors on, positioned 4 cm from EMG sensor)

Two-way analysis of variance (ANOVA) was conducted to investigate the effect of tactor placement (2 or 4 cm from EMG) and activation (on or off) on signal magnitude. There were no significant differences in magnitude of signals under any test conditions ($p < 0.05$) (Figure 5.13).

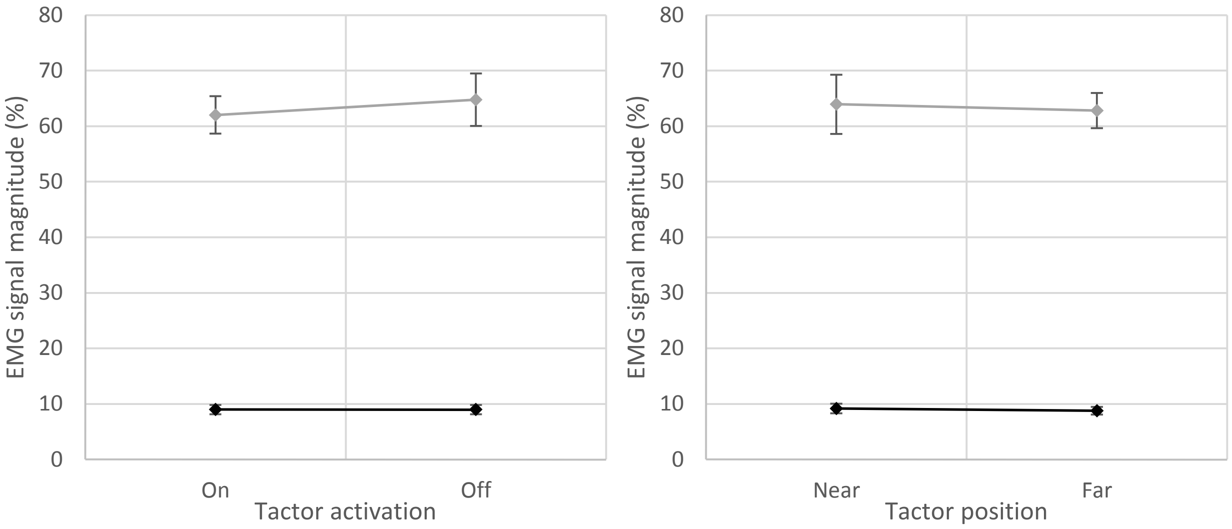

(a) (b)

Figure 5.13 Means plots of EMG signal magnitudes with (a) tactor activation, and (b) tactor position

In prosthetic hand control, commands are sent to the prosthetic hand when signal magnitude passes a set threshold. This testing indicated no significant difference in signal magnitude based on tactor placement and activation, which suggests that there would be no change in the commands being sent to the hand. Qualitatively, no change in control was observed by the participant in any test position. Finally, no motion artefacts were observed, suggesting that tactor operation did not interfere with the measured signals. This is promising in that it suggests that tactors may be placed as close as 2 cm from the EMG electrodes without compromising control of the myoelectric prosthesis.

5.4.3.6 Qualitative Survey

In terms of comfort, the tactors both stationary and moving were ranked as maximally comfortable (5/5). A ranking of 3/5 was given to how useful the tactor force was regarding the grasp force. The feeling of the tactors was minimally distracting (1/5), however the sound was distracting (4/5). It would be desirable to have the tactor system incorporated into his everyday life (5/5).

Qualitatively, the prosthetic arm with the integrated tactor system “did not feel much different from [his] normal prosthesis”. He would wear the system all day, as long as the “sound of the tactors is muffled or tactors could be disabled”. He also recommended that a user “would need time to adapt to the system for it to integrate with [their] senses" and that the system should be further miniaturized.

5.4.4 Discussion

The participant had no trouble distinguishing between tactors and was able to use substitution to correlate each tactor with a single digit on his prosthetic hand, demonstrating 100% accuracy in identifying which digit was stimulated during a blind trial. He was able to distinguish three levels of force with 79 and 88% accuracy, which is not as high as previous studies have shown; this is thought to be a combination of a reduced range of forces being applied, as well as a non-linear mapping between input force to the finger and output displacement to the residual limb. Note that later in the study the participant expressed a desire to increase the forces being applied to his arm to improve the usefulness of the stimulation, so in the future a larger range of forces should be applied, with care taken to ensure comfort of the user throughout the length of the trial. The participant was 67% accurate in distinguishing a stiff ball (750 N/m) from a soft ball (235 N/m) and no ball, likely due to the hand being closed to stall conditions at which it applies a relatively consistent force during normal operation. This also highlighted the difficulties in distinguishing between grasping an object and having the fingers contact each other with no object; in both cases the same forces are measured by the sensors, the main difference being the time it takes to close the hand. Without very good myoelectric control this timing can be difficult to estimate. Finally, in this experiment moving the tactor head from approximately 4 to 2 cm away from the EMG sensor did not degrade myoelectric control.

5.5 Conclusions and Future Work

While promising, this testing points towards future directions of improvement for follow-up studies. Large errors in calibration of the sensors on the terminal device highlight the need for more accurate force sensors, as discussed in [19]. This review paper argues that FSRs, while not ideal, are the best sensors currently available for prosthetic applications; in the interim the FSRs should be individually calibrated to map tactor forces linearly, as this may improve force level discrimination. For this relationship to be linear, it will be important to investigate methods of closed-loop control for controlling the forces applied by the tactor (see Chapter 6).

Additionally, for a suction socket to fit properly the vacuum seal must be maintained; it will be important to investigate methods of making the system air-tight despite the need for access holes in the socket to allow the tactor head to contact the residual limb (see Chapter 7). It is also suggested that more functional tasks be conducted that can evaluate the usefulness of the system in everyday tasks, such as picking up and moving fragile objects. However, there are currently no specific metrics to evaluate the functional performance benefits of sensory feedback so results would mainly be qualitative.

In terms of object stiffness detection, future work into providing a sense of prosthetic hand position should be investigated; understanding the applied force may not be sufficient without understanding the corresponding position of the prosthetic digits. The interplay between tactors and EMG sensors should also be further investigated to include more adjustability of tactor head placement and applied forces. The test should not only investigate the effect on control, but also if muscle contraction affects sensation of the tactors.

This preliminary testing has demonstrated the full integration of a tactor system into an above elbow commercial prosthetic device, which is untethered, lightweight, and inexpensive. To the authors' knowledge, this is the first integration of its kind to be documented. The electronics enclosure fits into the forearm of the prosthesis, with cables routed cleanly between the input sensors on the terminal device to the controller and out to the motors driving the tactor devices. The cable tactors were able to apply forces on two locations on the participant's residual limb, and due to their reduced vertical profile they allowed access to the inside of the arm without pressing uncomfortably into the participant's torso.

Overall this testing has demonstrated a system with potential to provide useful tactile information to an amputee about their grip, and has highlighted some key areas to investigate for future improvements.

Chapter 6. System Measurement and Control

6.1 Introduction

It is desirable to develop a control system that is capable of setting either tactor head displacement or applied force. This system must not greatly increase the overall size or cost of the tactor itself, and should not interfere with the integration onto a prosthetic socket.

6.2 Background

Mechanotactile tactors used in literature can be controlled with an open-loop controller by setting displacement (and often mapping to force) [26, 48, 60], or controlled with a closed-loop controller by setting force [49, 52]. Applied tactor forces range from 3 to 13.3 N [26, 47-49, 52, 60].

In the displacement-controlled (open-loop) studies found, an indenter was pushed onto the skin of two subjects using a force gauge mounted to a vertical slider to plot displacement versus force, and this was used to calibrate the system. For each of the two subjects, the maximum force reached 9 N, corresponding to displacements of 16 and 17 mm [26, 48, 60]. A criticism of this method of calibrating force and displacement is that only two able-bodied participants were tested, and it was not specified where skin compliance was tested. It is expected that skin compliance would vary substantially between subjects (especially those with an amputation), as well as position on arm, making this calibration unreliable. Additionally this cannot likely be translated to upper arm amputees due to different tissue compliances, given that the day-to-day usage of a residual limb is very different from a sound limb resulting in different tissue morphologies.

Methods of force-control (closed-loop) are also used in some studies. Kim *et al.* use a closed-loop system in the design of their tactors, either feeding back information from force sensors in their end effectors or torque sensors between the actuator and mechanism. Overall accuracy and time delays are not specifically quantified, however from their graphs of loading up to 2 N in a sinusoidal pattern the time delay is between 10 to 20 ms and accuracy is within 0.3 N [49]. Meek *et al.* measured force using a small transducer on the tactor head and this was fed back until the desired force was achieved by increasing or decreasing the displacement, however this device is not wearable and accuracy of the system was not quantified [52].

Different mapping schemes between measured force on the prosthetic terminal device and the force applied to the skin have been presented in literature, and can be either linearly mapped such as in Phase 1 of [47], non-linearly mapped such as in Phase 2 of [47], or mapped to discrete levels [26, 48, 60]. Studies have shown that it is most effective to map to three different levels; any more than this and additional levels do not provide useful information [26, 48, 60], however in a vibrational feedback study jumps by multiple levels were recognizable [85].

6.3 Selection of Sensors

6.3.1 Available Sensors

In order to control a closed-loop system, information about the applied force must be fed back to the controller, measured using a sensor. Several types of sensor technologies were considered; displacement measured by a potentiometer, current by a current sensor, strain by a strain gauge, and force by a load cell or force sensitive resistor or capacitor. One key specification was to keep the system low cost, so only inexpensive sensors were considered.

The servo motor used in the tactor (HS-35 HD, HiTec) contains an internal potentiometer that measures displacement. It was hypothesized that this could be used to apply a relatively consistent force given constant conditions, but that differences in compliance would result in large variances in forces applied.

A motor will typically draw more current the harder it is working, so it was hypothesized that current drawn by the servo motor could be related to applied force, regardless of the compliance of the material contacted. For this method, a current sensor was selected (ACS712, Sparkfun). This current sensor could be either be integrated into the Wearable Tactor Controller or distanced from the controller using wires, depending on spacing requirements.

Another method considered was to integrate a force sensor onto the tactor to measure the applied force directly. The sensor could be placed on the tactor head itself, but this would change the head geometry, and complicate the development of an air-tight interface due to the presence of protruding wires. Therefore, the sensor would be integrated in-line with the tactor cable or rack gear. Of utmost importance was the size of the sensor, as this could dramatically increase the overall size of the tactor. Note that force sensitive resistors (FSR) are polymer thick film (PTF) devices, which decrease in resistance with an increase in applied force. While they have similar properties to a load cell, they are not very precise [86]. Of the potential sensors (Figure 6.1), none of the load cells were considered small enough for the application, so the FSR was selected for further evaluation due to its low cost and very small profile.

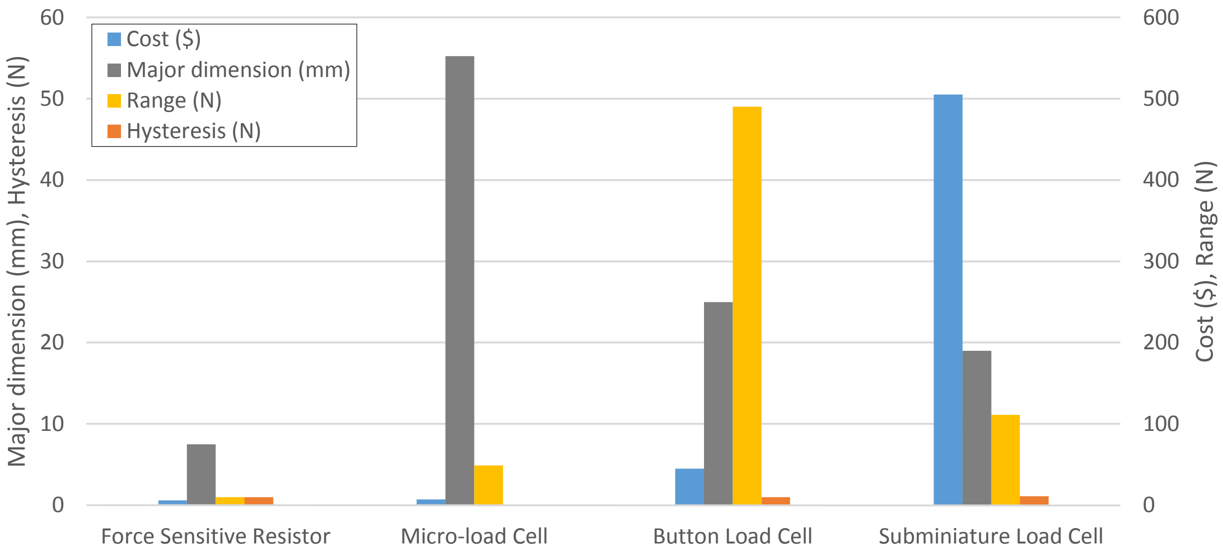

Figure 6.1 Comparison of available force sensors, including FSR (Sparkfun, SEN-09673 ROHS), micro-load cell (Robotshop, RB-Phi-118), button load cell (Robotshop, RB-Phi-121), and subminiature tension and compression load cell (Omega LC201)

Strain gauges were also considered, as it was hypothesized that deformation of the tactor head or rack gear could be correlated to applied force. These have been used in other prosthetic applications previously [19]. Strain gauges were eliminated from the potential methods due to their high cost and relative bulk compared to an FSR. For example, a miniature linear strain gauge (KFH-3-120-C1-11L1M2R, Omega) costs approximately $125.

It was desirable to explore force sensitive capacitor technology, as these can be less susceptible to changing conditions than force sensitive resistors [87]. While there are sensor arrays using this technology, both in research stages [87, 88] and commercially available [89], a small commercially available sensor could not be located for this application. Additionally, these sensors may not work well as expensive electronics are required to produce high sensitivity at the low force ranges required for prosthetic applications [19].

Overall, the FSR was selected as the optimal sensor for this application due to its low cost, small size, and low power consumption. These sensors have been used previously in force sensing prosthetic applications [58, 90, 91], and in a review paper published in 2010 were determined to be the “only device available commercially that has a suitable characteristics and dimensions… for use in an artificial hand” [19]. The current sensor has also been evaluated as an alternative to directly sensing force.

6.3.2 Initial Evaluation of Sensors

6.3.2.1 Set-up

The different materials tested were stiff PLA (MakerBot® Industries), compliant 6 mm thick alpha liner (WillowWood™), and 14 mm thick tissue analog with simulated skin, fat, and muscle (Syndaver™ Labs, Muscular Tissue Plate) (Figure 6.2).

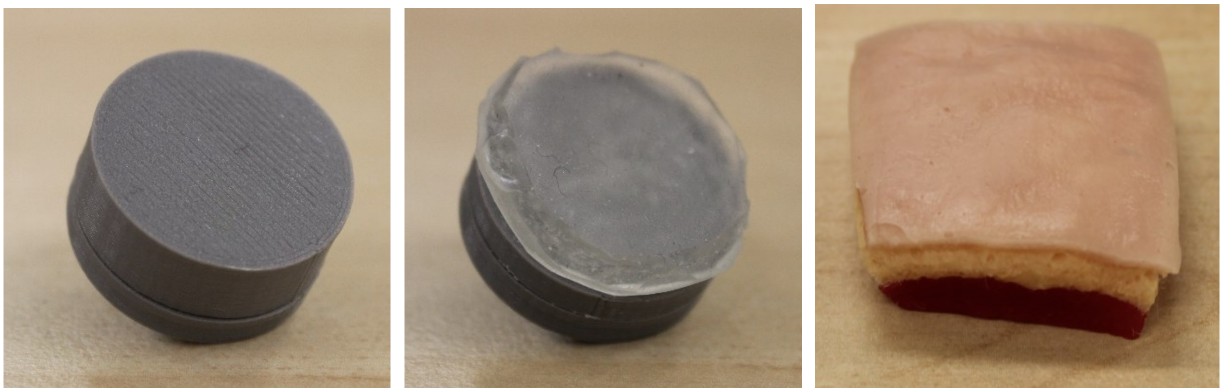
(a) (b) (c)

Figure 6.2 Materials used for testing, including (a) stiff PLA, (b) flexible alpha liner, and (c) tissue analog

In each case, the tactor was pushing into the material attached to the load cell (Figure 6.3). Note that data points were collected once the outputs reached steady-state values.

Displacement was set by the Arduino GUI (Guino), force was measured from the load cell calibrated to ± 0.02 N accuracy (Omega, LCM703-5) using Simulink Realtime (Mathworks Inc., 2014), and actual displacement was measured using digital calipers (Sparkfun, TOL-10997). For current sensor trials, current was read from the servo motor using the current sensor (Sparkfun, ACS712) with the output voltage measured by a multimeter (Fluke, 189). For FSR trials, voltage was read in-line with the tactor head by the FSR (Sparkfun, SEN-09673). All calibrations were conducted under static loading conditions. See Appendix F for interface and GUI explanations, as well as circuit diagrams for the electronic components used.

The servo motor was powered externally, while the current sensor and force sensor were powered through the Arduino board; with multiple tactors being run at once, there is too high of a current demand from the Arduino Uno. Additionally, initial testing indicated a drop in voltage when the servo motor was active, which could introduce non-linearity to the current sensor calibration unless the servo and current sensor were powered independently.

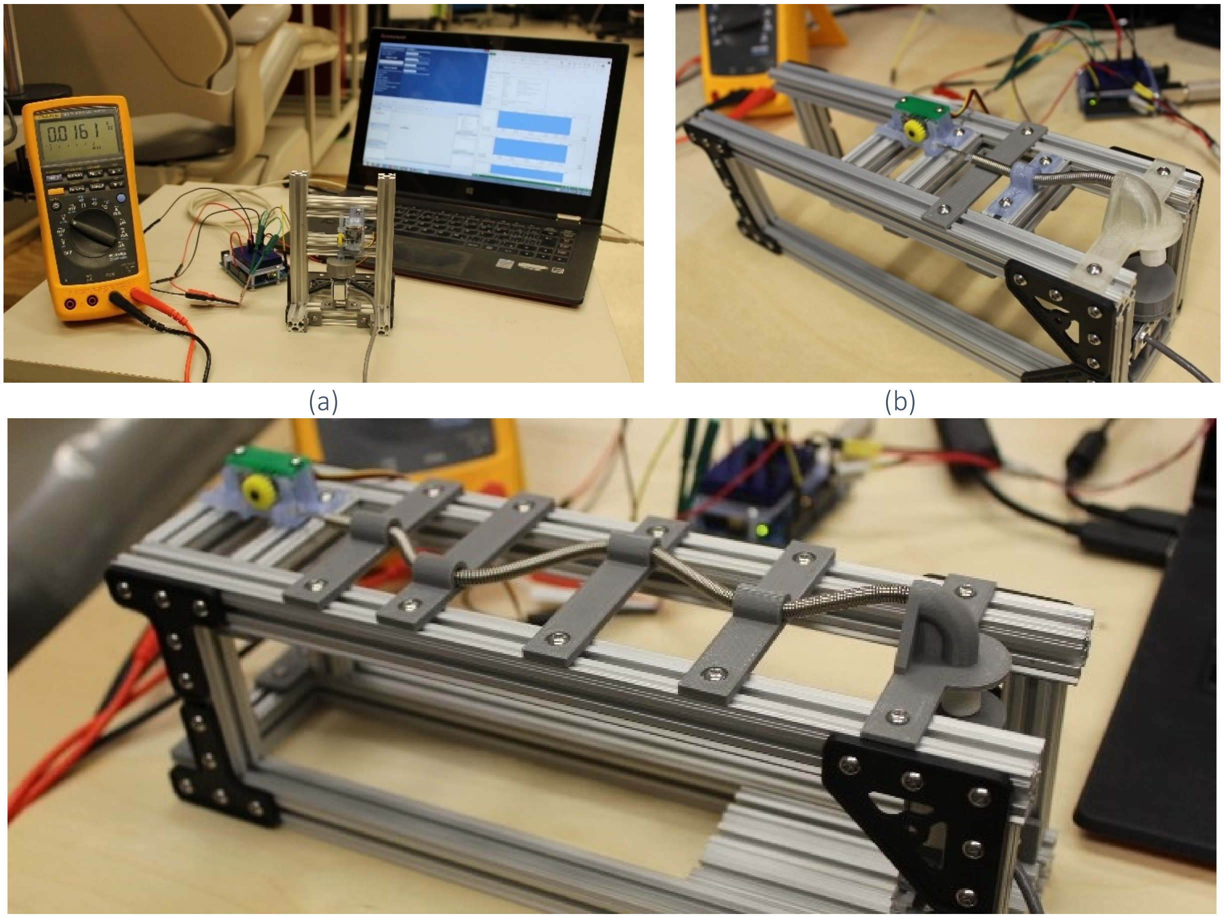

(a) (b)

(c)

Figure 6.3 Set-up for testing for the (a) rack and pinion, (b) short Bowden cable, and (c) long Bowden cable tests (note the tactor pushing onto the platform, which transfers force to the load cell)

6.3.2.2 Evaluation of Internal Potentiometer

The servo motor receives pulse width modulated commands from the Arduino Controller to set displacement, measured by a potentiometer internal to the device (see section 6.6.1.1). First, displacement (in mm) was calibrated against the angle of the motor shaft (in µs) over three consecutive loading cycles in the unloaded case (Figure 6.4 (a)).

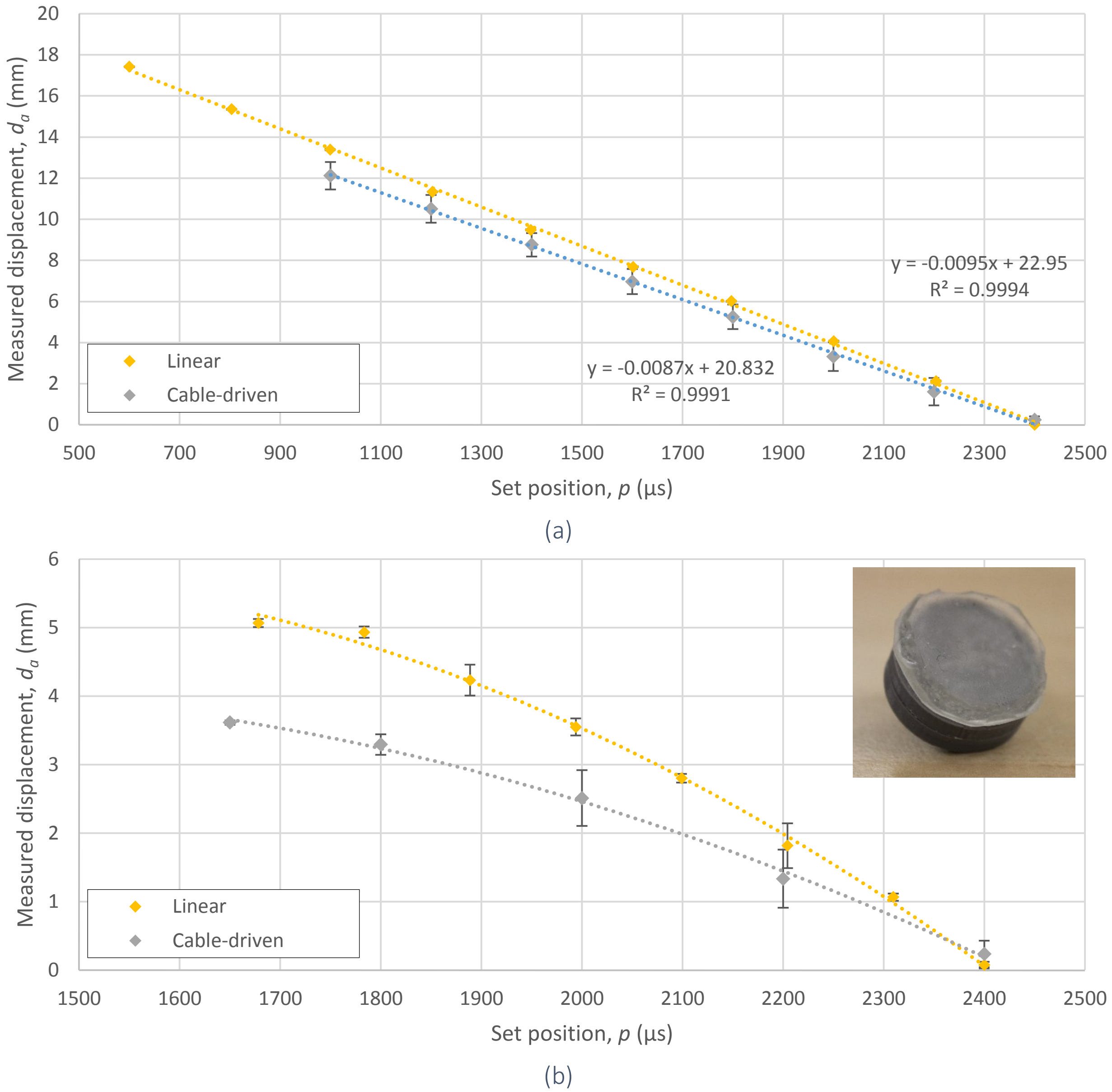

Figure 6.4 Graph of measured displacement versus set position under (a) free loading, and (b) compliant single layer alpha liner material

The calibration is very linear when not in contact with a surface, with an accuracy of ± 0.2 mm for the linear tactor, and ± 0.9 mm for the cable-driven tactor. When pressing onto a material however the calibration curves are no longer linear (Figure 6.4 (b)). As well, the cable-driven tactor does not reach the same displacement as the linear tactor for the same set position, suggesting that there is bending or buckling of the cable within the conduit which reduces the overall displacement of the tactor head.

Attempting to calibrate set displacement against applied force is therefore difficult, as the calibration curve depends heavily on the position of the tactor head relative to the material, the stiffness of the material itself, and the length of cable between the motor and the tactor head.

6.3.2.3 Evaluation of Current Sensor

In calibration of the current sensor using just the rack and pinion, relatively consistent slopes can be obtained for both the stiff and compliant materials. Combining the data together (Figure 6.5) yields average error of 0.5 N and maximum error of 2.1 N.

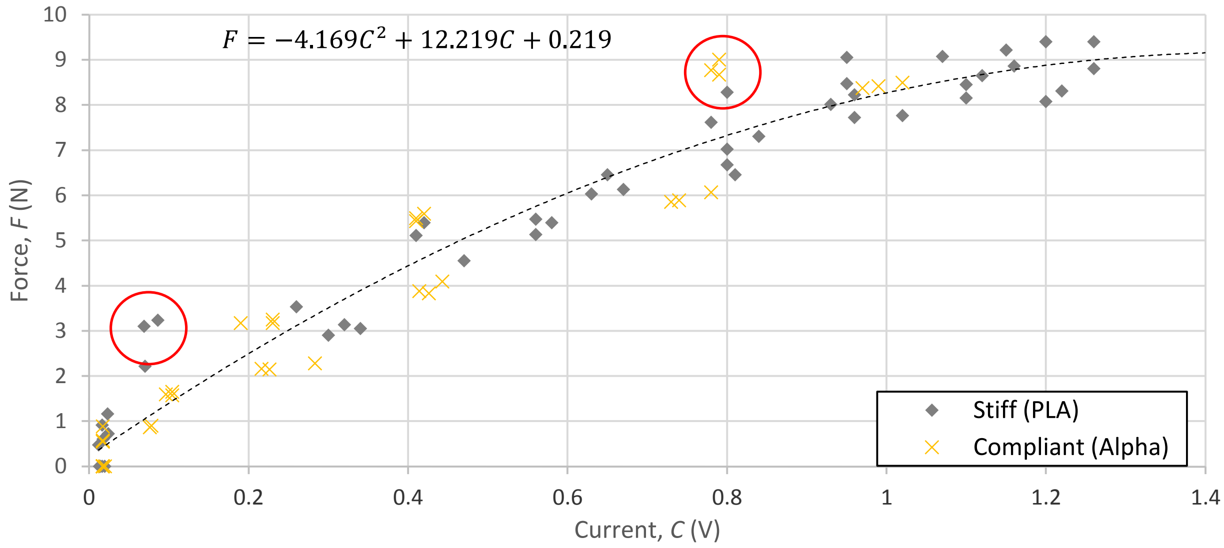

Figure 6.5 Graph of combined stiff and compliant materials for linear tactor, where data points with the highest error are circled in red

The inclusion of the Bowden cable results in significant hysteresis and directionally dependent behavior (Figure 6.6). This is likely due to the increased amount of energy being stored mechanically in the system (i.e. loading upwards gives a relatively consistent calibration, but when unloading the system will maintain a position without needing significant current to hold it in place). This hysteresis and directionally dependent behavior has been cited as problematic for closed-loop control of tendon and sheath systems for other haptic applications [92]. This results in loads as high as 6.8 N, while reading the same current as the no loading condition. Combining the data together yields an average error of 1.6 N and maximum error of 5.2 N.

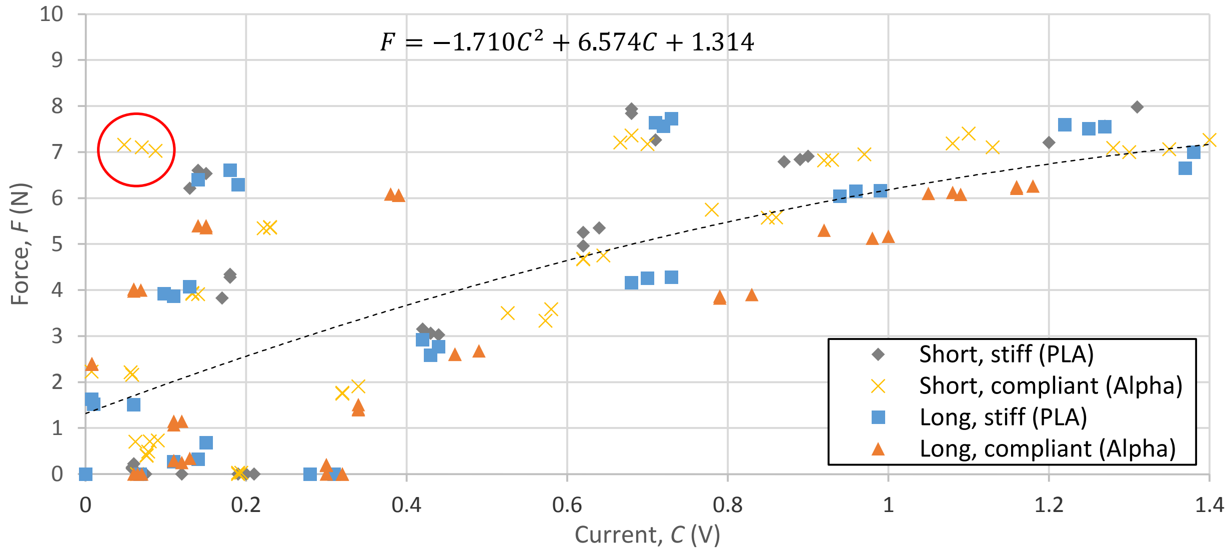

Figure 6.6 Graph of combined stiff and compliant materials for cable-driven tactor, where data points with the highest error are circled in red

It appears that it is not feasible to use the current sensor for force regulation of the cable-driven tactor. It is expected that dynamic loading will further reduce this accuracy. In follow up testing with the current sensor it was found that consistent signal amplification was very difficult to achieve due to the presence of adjustable gain and offset dials on the current sensing board. This suggests that a sensor with a fixed gain should be built into the system to improve repeatability.

Table 6.6 Summary of current sensor calibration at each different test set-up

		Range (N)	x^2 coeff	x coeff	Intercept	Maximum error (N)	Average error (N)
Rack and pinion	Stiff material	9	-3.4	11.1	0.5	1.8	0.5
	Compliant material	9	-4.8	13.2	0.0	1.5	0.5
	Combined	9	-4.2	12.2	0.2	2.1	0.5
Bowden cable	Short cable w/ stiff material	8	-4.4	11.2	0.5	4.6	1.5
	Short cable w/ compliant material	7	-1.4	5.9	1.9	5.0	1.4
	Long cable w/ stiff material	7	-2.0	7.2	1.2	4.2	1.4
	Long cable w/ compliant material	6	0.2	3.2	1.5	3.5	1.5
	Combined	6	-1.7	6.6	1.3	5.5	1.6

6.3.2.4 Evaluation of Force Sensitive Resistor (FSR)

Evaluation of FSR response to temperature, compliance, and curvature was conducted and is under review by the Journal of Biomechanics (Manuscript ID BM-D-15-01253). From this study, it is important to note that a consistent curvature, compliance, and temperature improve overall calibration accuracy. For this reason, the FSR was sandwiched between two rigid pieces of plastic (Figure 6.7); behind the rack gear and in front an indenter on the tactor head (for the linear tactor) or cable (for the cable-driven tactor). This ensured consistent loading conditions on the FSR regardless of the material or geometry the tactor was contacting.

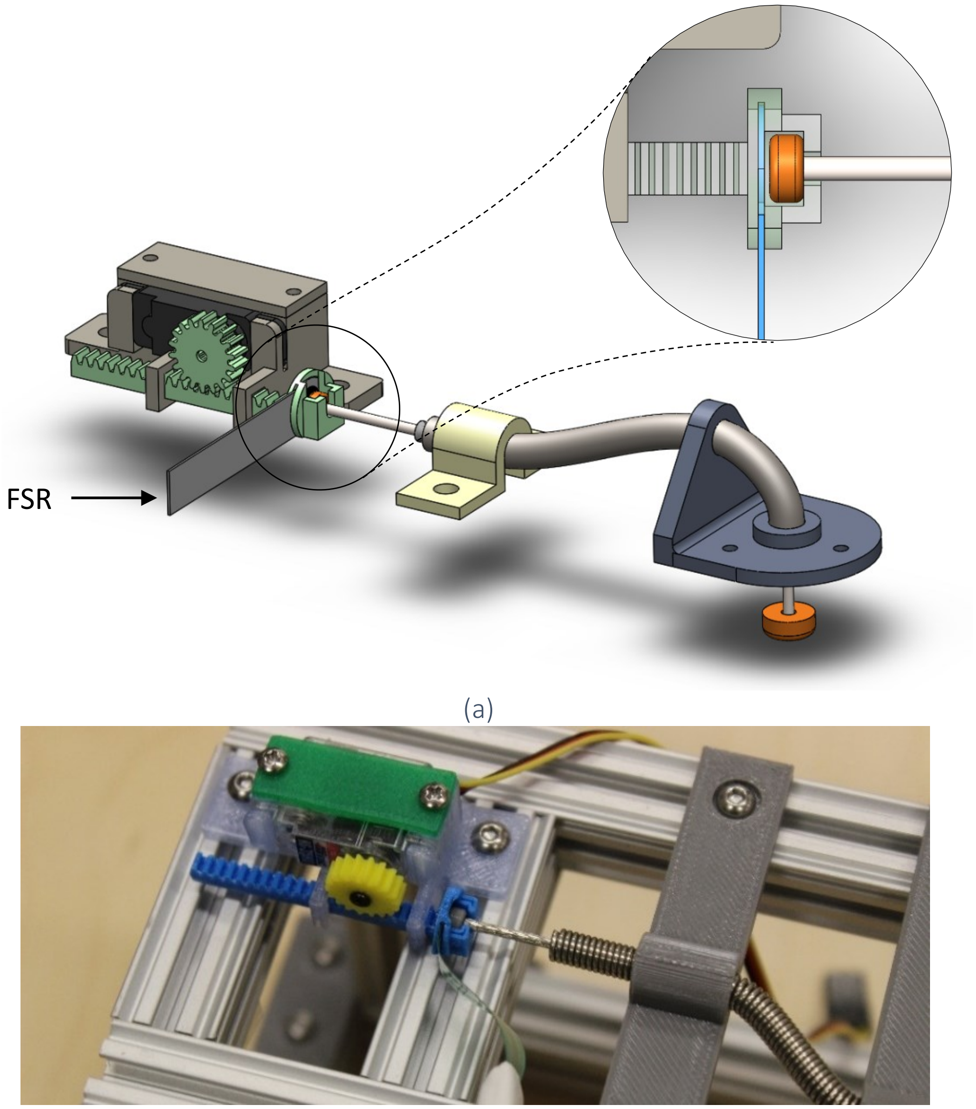

(a)

(b)

Figure 6.7 Incorporating FSR into rack gear, where (a) shows the tactor design, and (b) physical implementation of FSR placement

Using the rack and pinion, relatively consistent slopes were obtained for both the stiff and compliant materials. Combining the data together (Figure 6.8) yields an average error of 0.6 N and maximum error of 2.0 N.

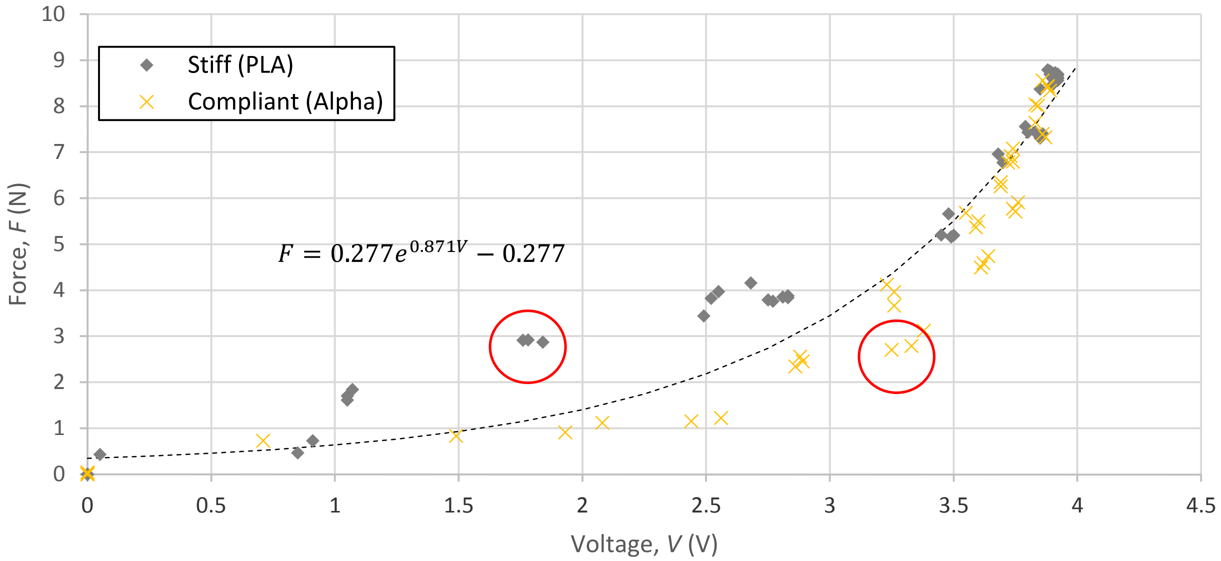

Figure 6.8 Graph of combined stiff and compliant materials for linear tactor, where data points with the highest error are circled in red

The inclusion of the Bowden cable added some hysteresis, although not as much as the current sensor (Figure 6.9). Combining the data together yields an average error of 1.1 N and maximum error of 2.5 N.

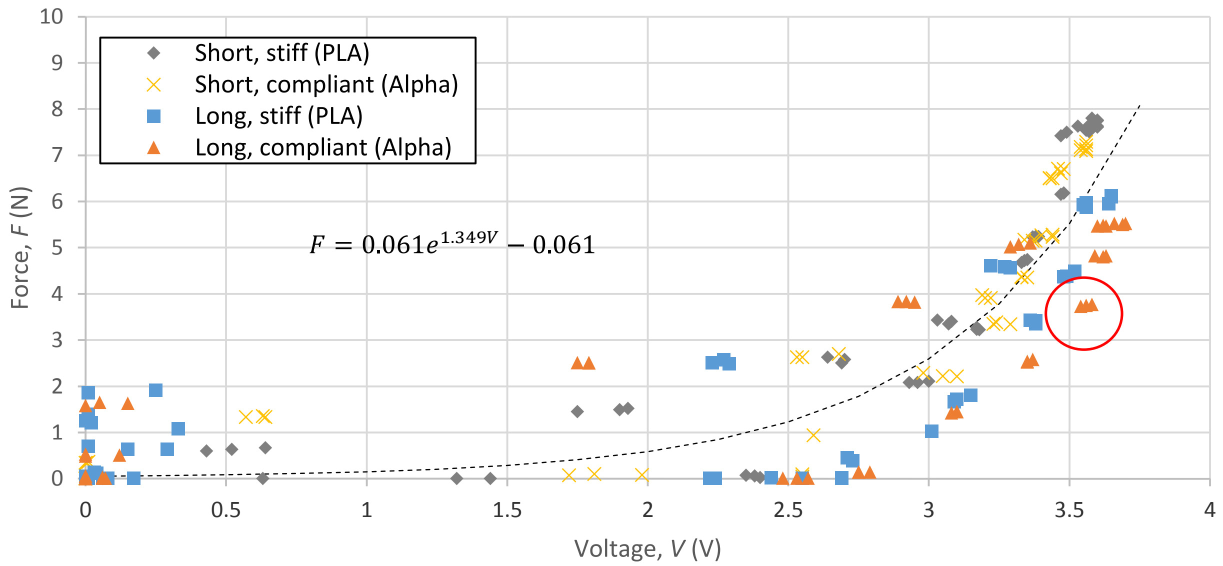

Figure 6.9 Graph of combined stiff and compliant materials for cable-driven tactor, where data points with the highest error are circled in red

Upon further discussion it was determined that a tactor with a single bend (rather than two bends) is more realistic (Figure 6.10 and

Table 6.7). This results in an average error of 0.6 N and a maximum error of 2.2 N. Using the FSR to measure force on the cable-driven tactor results in less hysteresis than the current sensor.

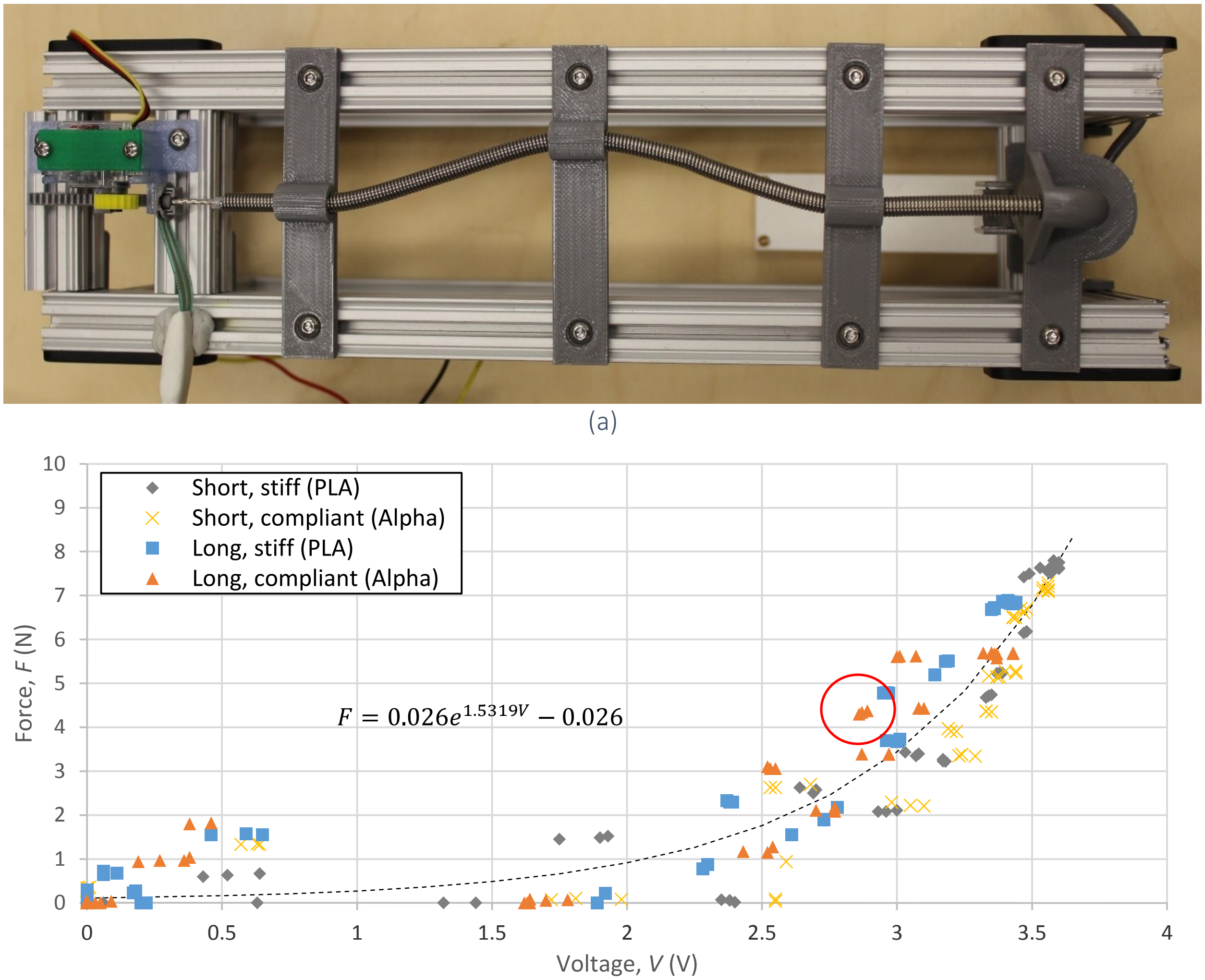

(a)

(b)

Figure 6.10 Calibration with single bend (a) set-up, and (b) graph of calibration curve, where data points with the highest error are circled in red

Table 6.7 Summary of FSR calibration at each different test set-up

		Coefficient	Exponential	Intercept	Maximum error (N)	Average error (N)
Rack and pinion	Stiff material	1.369	0.499	1.369	1.3	0.4
	Compliant material	0.038	1.378	0.038	1.0	0.4
	Combined	0.277	0.871	0.277	2.0	0.6
Bowden cable	Short cable w/ stiff material	0.015	1.747	0.015	1.2	0.4
	Short cable w/ compliant material	0.007	1.944	0.007	1.6	0.5
	Long cable (2 bends) w/ stiff material	0.006	1.897	0.006	2.1	0.6
	Long cable (2 bends) w/ compliant material	0.174	0.979	0.174	2.3	1.0
	Long cable (1 bend) w/ stiff material	0.066	1.368	0.066	1.5	0.5
	Long cable (1 bend) w/ compliant material	0.174	0.979	0.174	1.8	0.7
	Combined (1 bend and short)	0.061	1.349	0.061	2.2	0.6

One potential problem with this method when applied to the cable driven tactor is that, similar to the current sensor, the FSR is measuring not only the force applied by the tactor head, but also the friction forces resisting movement of the cable through the conduit (Figure 6.11). This friction force causes the voltage to plateau at an average of 1.96 ± 0.04 V, 2.1 ± 0.1 V, and 2.9 ± 0.1 V for the short, long curve (single bend) and long curve (double bend), when travelling through empty space. This corresponds to force values of 0.8, 0.9, and 2.0 N, respectively. This phenomenon does not occur with the linear tactor.

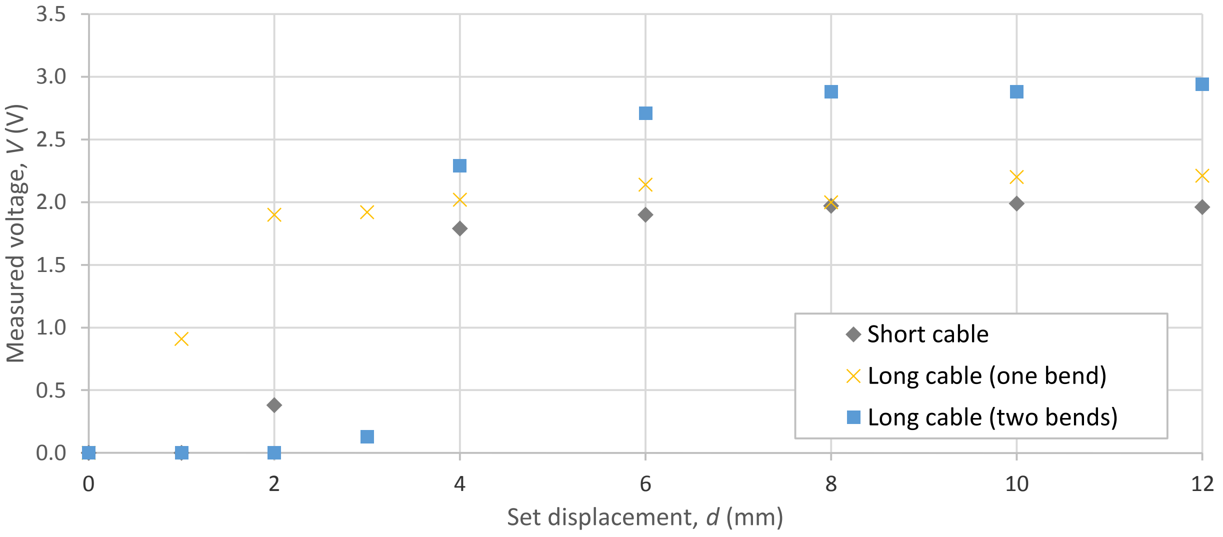

Figure 6.11 Voltages measured as tactor travels through empty space

This suggests that if a longer cable with tighter curvature is desired, the FSR should be placed closer to the tactor head using an in-line cable adapter, rather than attached to the rack gear, (Figure 6.12), to obtain better accuracy of force readings.

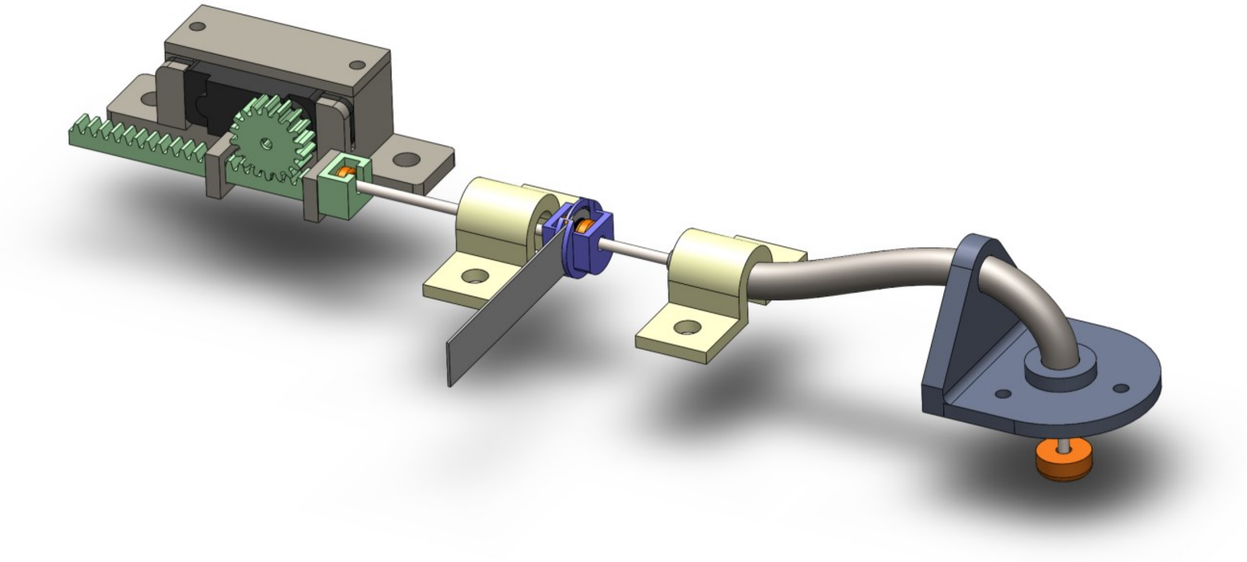

Figure 6.12 Incorporating FSR into cable in-line to reduce measured frictional effects

6.3.2.5 Discussion

With consideration of sensor accuracy and ease of implementation, the cable-driven tactor may be integrated with the FSR to quantify approximate forces, as the FSR can be integrated in-line outside of the socket, however there is significant hysteresis present in the system. It is possible that the linear tactor could be integrated with a current sensor, as this does not require the FSR to be moving in and out of the socket interface, however further testing into consistent signal amplification is required.

6.4 Filtering[9]

An analysis of signal filtering was conducted to remove potential noise from the recorded sensor data.

6.4.1 Collecting Raw Data

6.4.1.1 System Set-Up

Voltage measurements were collected from two FSRs; one on the terminal device (referred to herein as the *reference FSR*) measuring the grip force of the prosthetic terminal device and one in-line with the tactor (*tactor FSR*) measuring the force applied to the residual limb.

The system was set-up with the tactor pushing downwards (Figure 6.13). The computer was used to upload code to the Arduino controller (Arduino UNO) and the Simulink Real-Time (MathWorks, Inc.) Data Acquisition System (DAQ) (National Instruments). The Arduino controller set the displacement of the indenter by controlling the servo motor rotation (Hitec RCD, HS 35-HD). It also powered and read the voltage from the two FSRs (Sparkfun, SEN-09673 ROHS), one would be attached to a prosthetic terminal device as a reference sensor, and another in-line with the rack gear and tactor indenter, which would feedback information about how hard the tactor is pressing onto the residual limb. The load cell (Omega, LCM703-5) measured normal forces being applied to it by the tactor.

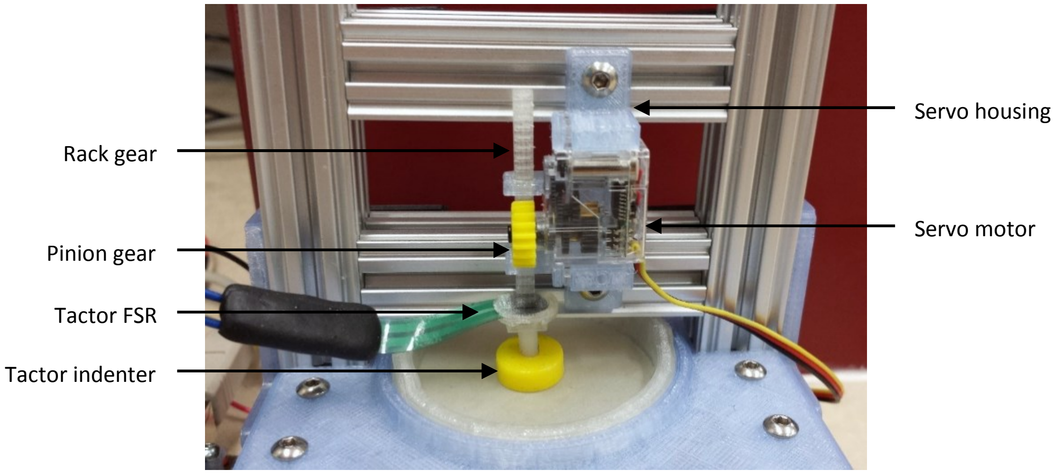

(a)

---

[9] Note that this sub-chapter is adapted from a course project submitted in partial fulfilment of the requirements for Mec E 563: Signal Processing of Time and Spectral Series.

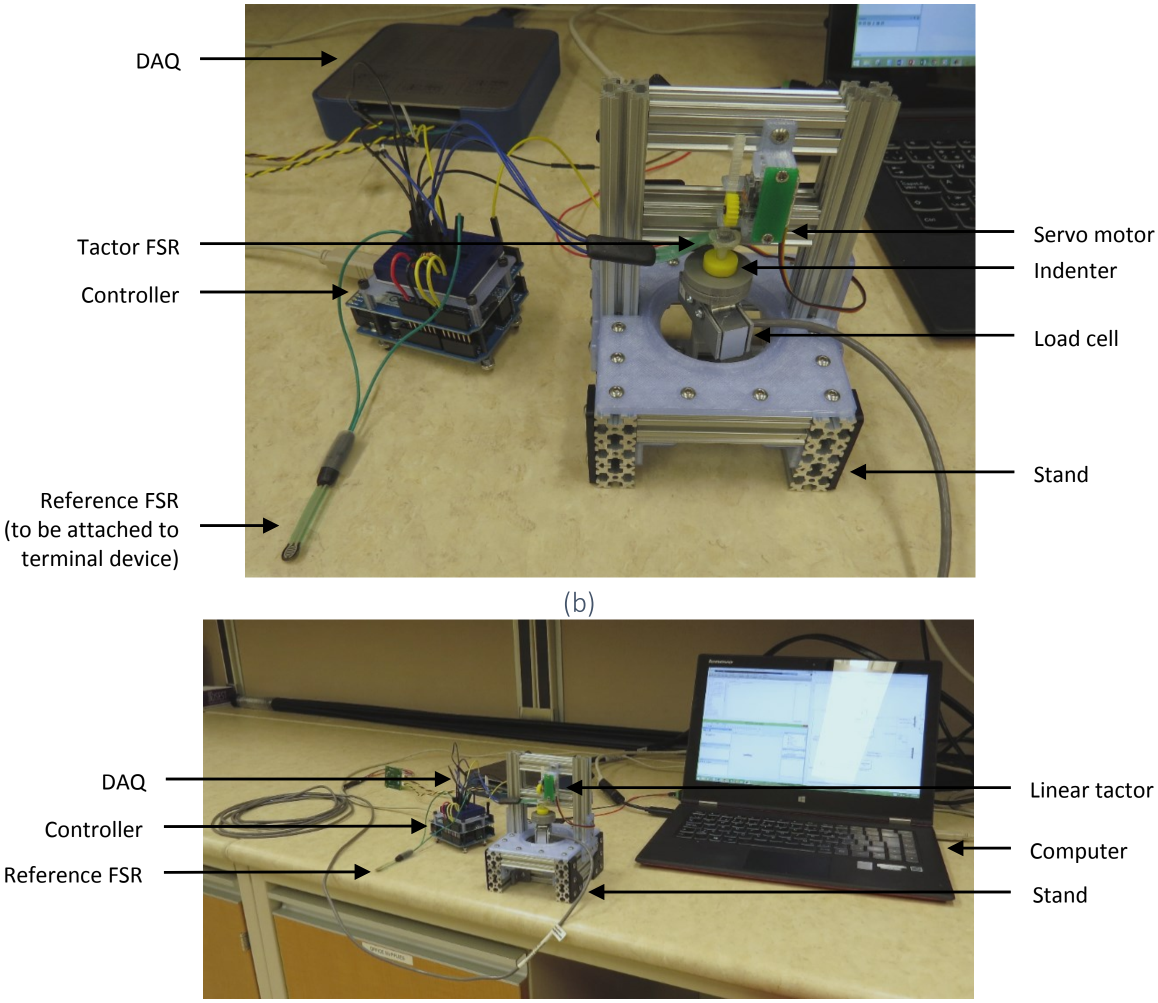

(b)

(c)

Figure 6.13 System set-up showing (a) the in-line FSR, (b) focused on tactor and controller, and (c) overall

Data from the FSRs and the load cell was read into Simulink Real-Time using the DAQ and logged to the computer to allow for further processing (calibration, evaluation of filters, and error quantification). The Arduino controller allowed data to be read from two FSRs, servo motor position to be set, and data logged to a data logger (Ethernet Shield, Arduino) which communicated over a Serial Peripheral Interface (SPI) bus. Additional connections were included which allowed data to be read into the DAQ (but would not be included in the wearable controller design). Simulink control through the DAQ allows a much faster recording speed compared to the logger, and made data alignment easier as all data was recorded to the same place with a single time stamp. See Appendix F for the wiring diagram and Simulink interface.

6.4.1.2 Signal Processing Theory on Data Acquisition

FSRs output a continuous analog signal, with a range spanning the voltage applied to the sensor (0 to 5 V in this case). In typical operation, the recorded signals in this application are random, and can be classified as transient non-periodic; that is they vary over time and cannot be exactly represented mathematically.

Analog-to-digital (A/D) conversion occurs internally within the Arduino controller, where the analog voltage from each FSR is converted to a digital signal using a 10 bit A/D converter. The quantization step (Q_{step}) is therefore:

$$Q_{step} = {}^{R}\!/_{2^N} = {}^{5\ \mathrm{V}}\!/_{2^{10}} = 0.005\ \mathrm{V}$$

Where R is the full scale range of the analog input to the FSR (0 to 5 V) and N is the usable number of bits (10). The resulting quantization error (Q) is half of this step, since the quantization levels are shifted to the midpoint of each analog interval:

$$Q = {}^{Q_{step}}\!/_{2} = 0.0025\ \mathrm{V}$$

This quantization error is fairly low, which provides a decent signal-to-noise ratio (SNR) for most inputs. Therefore quantization noise was not a large concern.

Uniform sampling was used for simplicity, at a sample frequency of 250 Hz (or sampling interval of 0.004 s). This was chosen to ensure that there was ample raw data to filter using a low-pass filter to reduce noise above the Nyquist sampling rate selected for each FSR, while not taxing the Arduino controller with large arrays of data to store. This sampling rate oversamples the signals, to help prevent aliasing from negatively affecting the system. Of a more minor note, it also prevents a significant shift in time during the D/A conversion due to the relatively small zero order hold time. The acquisition time (or amount of time required to sample the data) is very low for the DAQ compared to two Arduino data loggers tested, so the DAQ system was selected to record signals in this project (Appendix F). Note that originally a sample rate of 1000 Hz was used, but this introduced memory limitations for the Arduino controller (Appendix H).

6.4.1.3 Raw Digital Signal Results

FSR data was obtained by attaching the FSR to a finger, and pressing it onto a rigid surface at various rates representative of possible loading situations ranging from a gradual press to rigid fluctuations (Figure 6.14). Upon initial observation of the data it was found that there was not very much noise in the system. However, there is potential for noise at the higher frequency ranges, such as at 60 Hz from the radio frequency interference of fluorescent lighting and power lines [93, 94]. Noise was artificially added to the FSR signal to determine if the filters could remove the noise, should it exist (for example, if the system was used in a different location where interference were more of a concern). From observation in the time domain, the FSR is capable of measuring both gradual and rapidly applied finger loads.

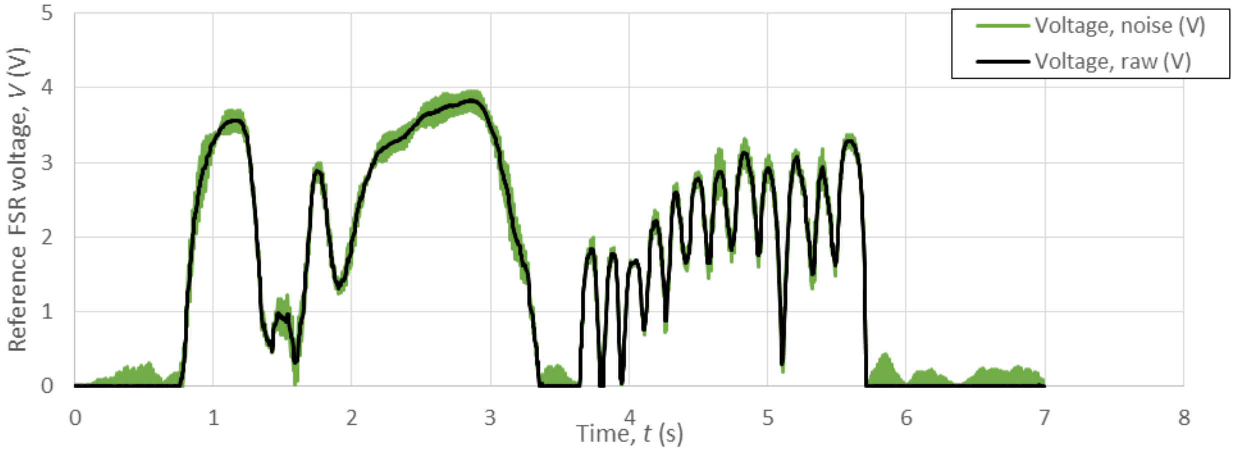

Figure 6.14 Raw signal data from FSR

6.4.1.4 Frequency Domain

Raw sample data was transformed into the frequency domain and the resulting magnitude spectrums are shown below. Discrete Time Fourier Transform (DTFT) would ideally be used to transform data to the digital frequency spectrum because the data is non-periodic.

$$X(\Omega) = \sum_{n=-\infty}^{\infty} x[n] \cdot e^{-jn\Omega}$$

Where Ω is the digital frequency (0 to π), and $x[n]$ are each of the data values collected at time n. Because the data is finite, the Fast Fourier Transform (FFT) function was used, which limits n to the number of samples collected for each signal, N. The magnitude spectrum was determined by taking the magnitude of the resultant complex numbers, $|X(\Omega)|$. The *x*-axes of the frequency plots were converted to show responses at analog frequencies (*f*), based on the following equation:

$$f = \Omega^{f_s}/_{2\pi}$$

Where f_s is sample frequency (250 Hz). Plots are only shown from 0 to 125 Hz (equivalent to a digital frequency of 0 to π) since the spectrum repeats beyond these limits (with a period of 2π), so it does not provide any additional useful information.

From observation of the frequency magnitude plot (Figure 6.15), it is clear that most of the signals occur at low frequencies (implying that they change relatively slowly over time, consistent with observation of the time domain). The DC (average) component of the spectrum is the largest. The FSR signal occurs mainly below 15 Hz, with the artificially created noise appearing around 60 Hz, as designed.

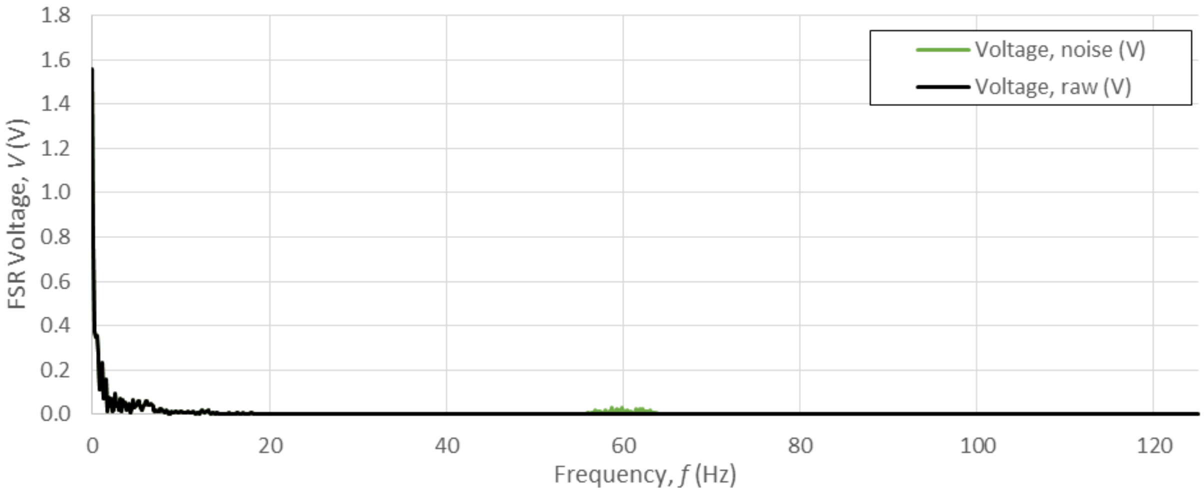

Figure 6.15 Frequency magnitude spectrum, where artificial noise is added to the FSR signals to evaluate filters.

6.4.2 Evaluating Filters

6.4.2.1 General Filter Design

Digital low pass filters were implemented as they are more flexible and simple to use than analog filters, which are more complex and costly. Additionally, analog filters require physical components; for this application the controller is meant to be wearable, so reduction in size and weight is a priority. Non-recursive (causal) filters only depend on present and past inputs, and are classified as finite impulse response filters (FIR). Recursive filters can produce similar filter responses using fewer coefficients, but depend on both present and past inputs as well as past outputs, and are classified as infinite impulse response (IIR) filters. Both FIR and IIR filters have been compared in this study.

6.4.2.2 Parameter Specifications

Different filter parameters were selected for each sensor, based on the observed signals and noise for each specific intended use. For each sensor a low pass filter was designed, since the important information lies within the lower part of the frequency spectrum.

FSRs are not designed to read high frequency signals [86], and Interlink FSR response at various frequencies is not quantified in the data sheet [95]. One study demonstrated that Interlink FSRs are better for measuring relatively higher frequencies than other similar sensors [96], but quantitative data was not provided. From the literature, it is unclear what sorts of frequencies to expect, or what types of filters should be selected. Filter parameters were therefore based on other aspects of the intended application as well as observation of test measurements.

For the reference FSR, a minimum pass band edge frequency of 7 Hz was implemented as this is equal to the average frequency exerted by healthy individuals during fast tapping motions [97]; this should be sufficiently high, as users are not expected to be tapping (but rather grasping objects) and because they will be using a prosthetic terminal device which is not able to move as quickly as a healthy hand. A stop band edge frequency of 21 Hz was selected; while tapping motions may not necessarily be smooth inputs, this low cut-off frequency prevents the system from causing the tactor to move too jarringly, as this could be uncomfortable to the user. Additionally, very abrupt contacts (such as slamming the prosthesis into something) are not deemed useful information for the tactor to convey (as it should already be obvious to the user), so resulting high frequency signals were filtered out in order to avoid discomfort. This stop band also removes any 60 Hz noise from lights and power lines. A cut-off frequency of 14 Hz was applied for filters unable to accommodate both pass and stop band frequencies.

For the tactor FSR, which is interfacing with human anatomy, the types of pressure that can be interpreted by various skin receptors were investigated. Tactile mechanoreceptors are sensory receptors in the skin that detect pressure and distortion, and pass these signals through the nervous system to the brain for interpretation [98, 99]. There are four main types, which are summarized in the table below. Because the tactor is to be used to provide sensations of force, this will mainly involve the Merkel discs; subsequently any frequencies above 15 Hz will not provide very much useful information. To account for possible differences between users, a minimum pass band frequency of 20 Hz was used. This signal does not need to be smoothed as much as the reference signal, so the stop band need only prevent interference from lights and power lines from affecting the signal; it was conservatively set to 40 Hz to ensure any 60 Hz noise would be removed. A cut-off frequency of 30 Hz was applied for filters unable to accommodate both pass and stop band frequencies.

Table 6.8 Tactile mechanoreceptors and their properties [98, 99]

Mechanoreceptor	Sensation	Location	Frequency range	Relevance
Merkel disc	Touch, pressure, texture	In all skin types	5 to 15 Hz	Very
Meissner's corpuscle	Light touch, stroking, fluttering	Mainly glabrous skin	20 to 50 Hz	Slightly
Pacinian corpuscle	Deep pressure, rapid vibratory pressure and touch	Dermis (mainly fingers, mammary glands, external genetalia), superficial and deep fasciae, and joint capsules	60 to 400 Hz, optimal at 250 Hz	Not
Ruffini corpuscle	Skin stretch, linked to kinesthetic sensation	Deep dermis	N/a	Not

The load cell was filtered using the same filter and parameters as the tactor FSR to ensure that the data from both sensors was aligned for calibration, with no significant difference in time delay, phase distortion, or influence from high frequency components.

6.4.2.3 Specific Filter Design

Four different low pass filters were evaluated; Moving Average (FIR), Hanning Window (FIR), Butterworth (IIR), and Chebyshev Type II (IIR), which are all commonly used filters in signal processing applications [100]. The design of the filters is discussed in detail in Appendix I through Appendix L, with code used to apply the filters to the data in Appendix M. A summary of the performance of these filters is shown for the reference FSR case below.

Table 6.9 Summary of filter performance using reference FSR parameter specifications

	Moving average	Hanning	Butterworth	Chebyshev type II
Attenuation at stop band (dB)	-13	-44	-40	-40
Monotonic in pass band	No	No	Yes	Yes
Monotonic in stop band	No	No	Yes	No
Coefficients in difference equation	7	59	11	9
Phase distortion	None	None	Present	Present
Delay from filter (s)	0.012	0.076	0.076 s to 0.052	0.043 to 0.037
Oscillations	None	None	Possible	Possible (less than Butterworth)

The Moving Average filter has the advantage of not causing oscillations or introducing phase distortion, and only uses 7 coefficients in its difference equation. However, it was not clear that an attenuation of -13 dB (Gain = 0.22) would be sufficient to remove noise. The Hanning filter also does not cause oscillations or introduce phase distortion, but uses the most coefficients and produces the longest time delay. The Butterworth filter is the only one to be monotonic in the stop band, but this should not have a large benefit since higher frequency components are being attenuated. This filter may cause oscillations and will introduce phase distortion. The Chebyshev Type II filter has fewer coefficients in the difference equation than the Butterworth filter (and has a lower order), and is also monotonic in the pass band. While phase distortion is still present, it is not as variable as the Butterworth filter, and has the second shortest time delay overall. Oscillations may occur, but because the filter's zeroes are close to its poles, these oscillations will be somewhat mitigated.

6.4.3 Filter Selection

Raw data from the FSR was filtered using each of the designed filters (Figure 6.16). One concern of FIR filters is boundary effects which cause problems for the first set of data points collected. For this application the system is always unloaded when turned on, so the FSRs are reading approximately 0 V. Because the filters extend the input with zeros this does not change the smoothed input, so boundary effects are not a concern (Figure 6.16 (b)). All of the filters seem to follow along with the signal fairly well while still removing the noise, except for the Moving Average filter which still appears to show some of the noise. The Moving Average filter has the shortest delay, followed by the Chebyshev Type II filter, the Butterworth filter, and the Hanning filter. This aligns with the analysis of the filters.

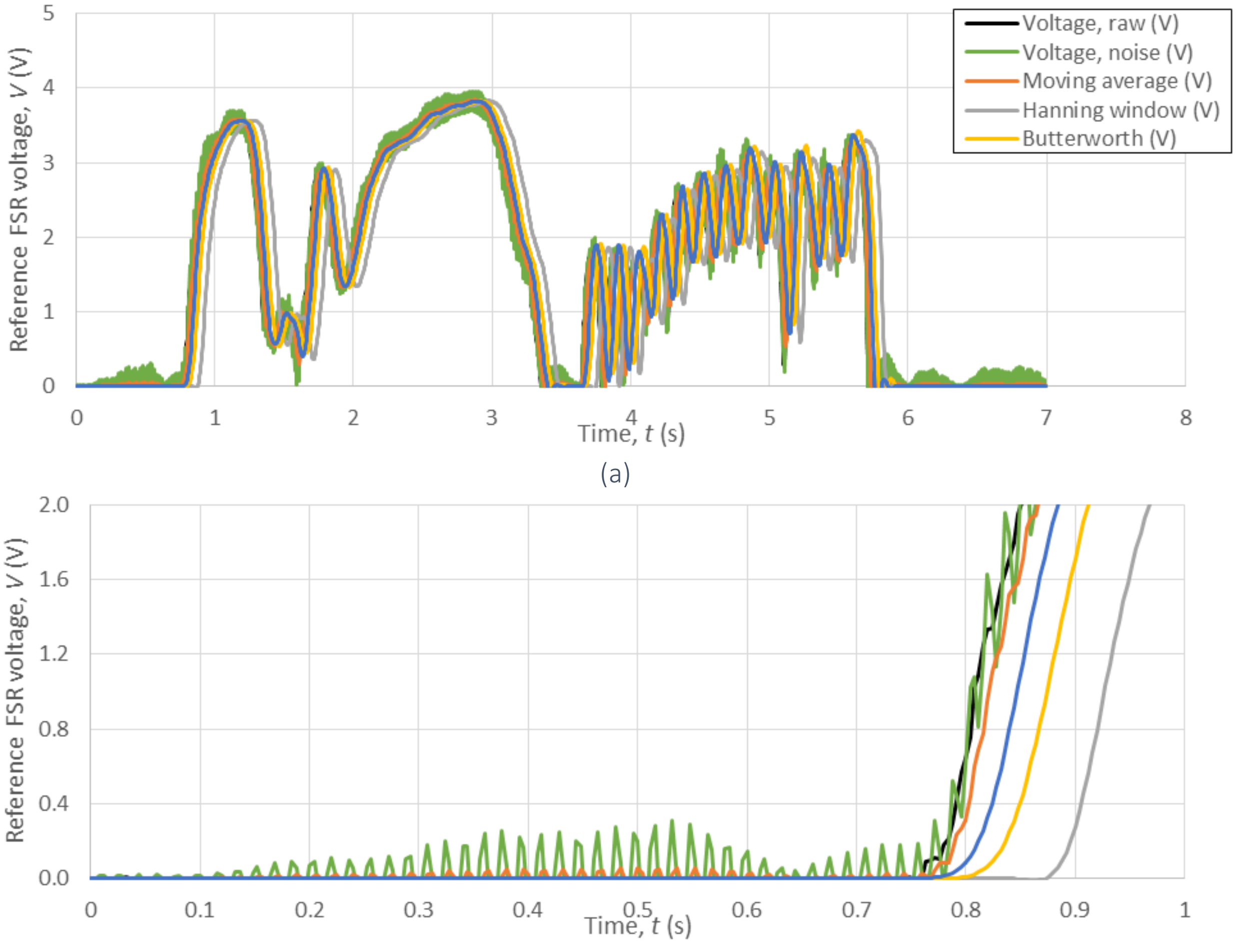

(a)

(b)

Figure 6.16 Raw and filtered signal data from reference FSR (a) entire signal, and (b) beginning

The magnitude spectrums of the filtered data from the FSR demonstrated that none of the filters significantly affect the low frequency components of the signal, as designed (Figure 6.17). The magnitude response at 60 Hz confirms that the Moving Average filter is not able to attenuate the artificial noise, while the other filters are sufficient (Figure 6.17 (b)). The Moving Average filter does not attenuate well above the cut-off frequency (of 14 Hz), but the other filters clearly show some attenuation between the pass and stop band (7 and 21 Hz, respectively), and high attenuation above the stop band frequency (Figure 6.17 (c)).

From this analysis, the optimal filter for the application will depend if there is noise present in the system. If the signal is clean then the moving average filter should be used as it produces the least delay. If there is noise, the Chebyshev Type II filter is sufficient to attenuate the noise without producing a significant time delay.

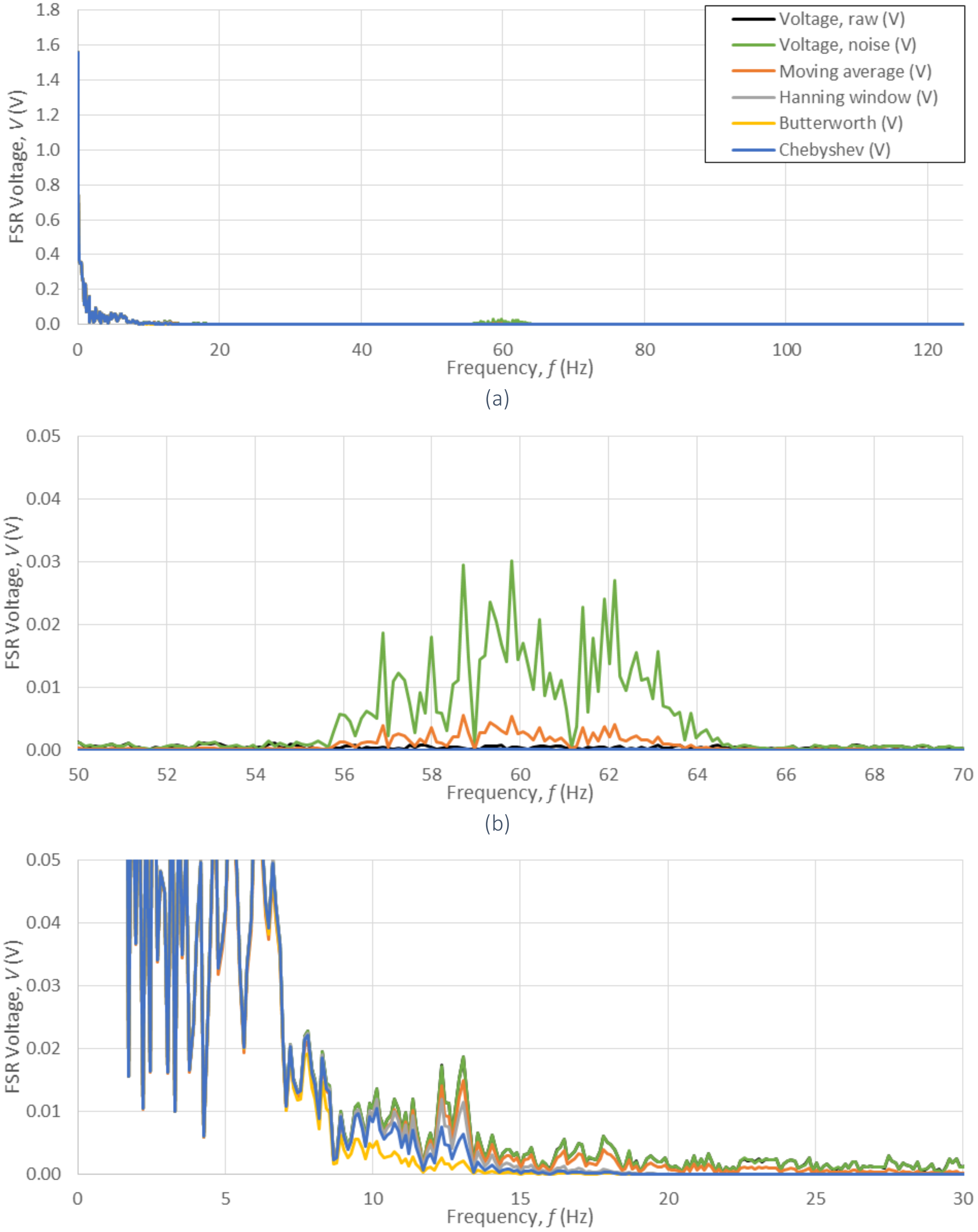

(a)

(b)

(c)

Figure 6.17 Frequency magnitude spectrum from reference FSR showing (a) entire spectrum, (b) range including artificial noise, and (c) low frequency components

6.5 Dynamic Calibration

After initial experimentation with the system, it was found that FSRs respond differently dependent on loading rate, as suggested in [86]. Therefore a dynamic calibration was conducted. The Arduino controller was used to set the displacement of the indenter, with the position for each material set so that the tactor applied approximately 10 N at maximum displacement. Voltage and load readings were automated using the DAQ and Simulink Real Time. Different loading patterns were tested, including a sine wave (period varied) and a stepped pyramid (step size varied).

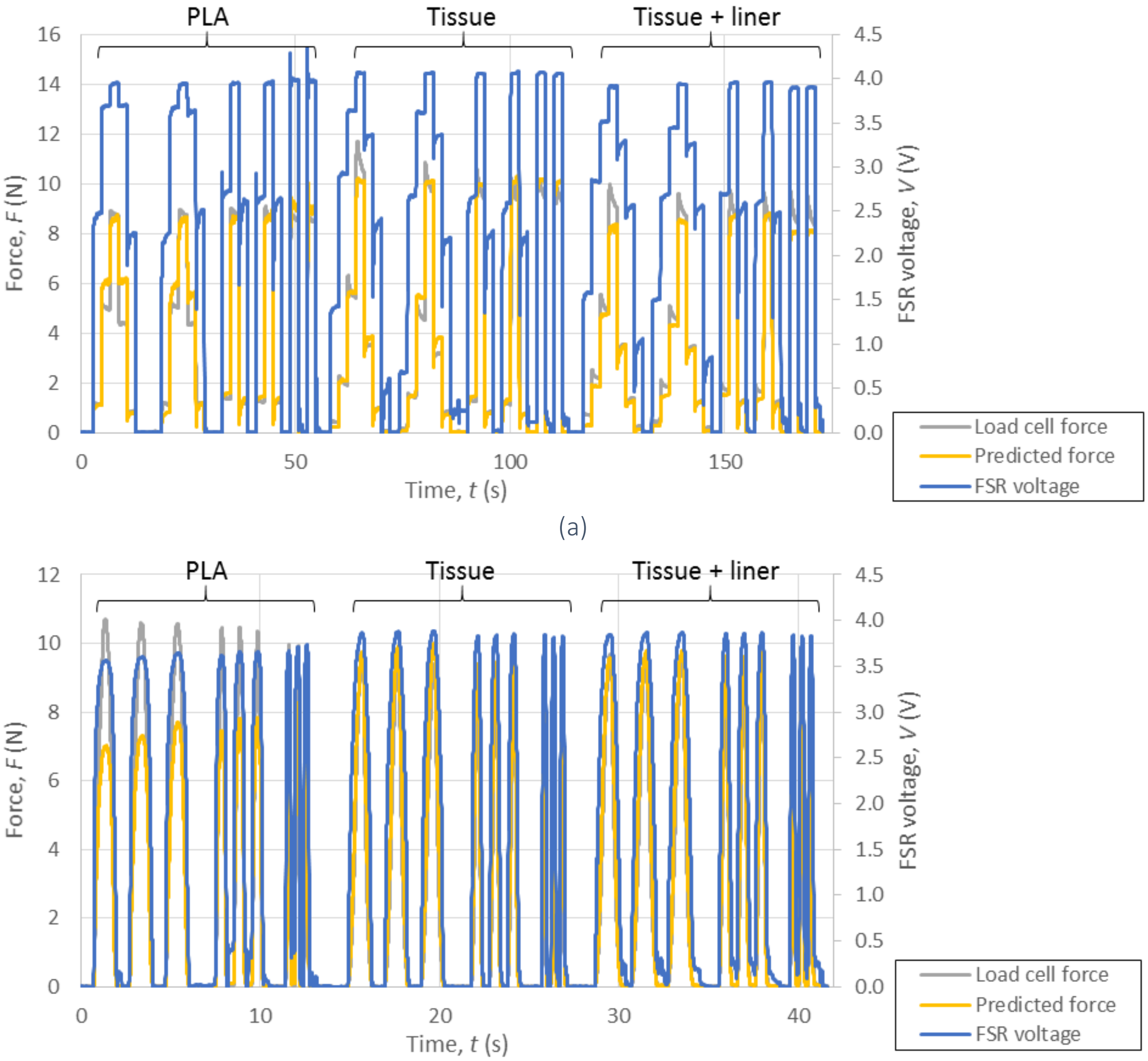

(a)

(b)

Figure 6.18 Transient loading patterns for different materials, (a) stepped loading, and (b) sine loading

It was determined that the calibration curve for pressing into the PLA material was different from that of the tissue or tissue and liner curves, as was found with the steady-state calibration. It presented more hysteresis (likely because the tactor did not need to travel far before the maximum force was applied, so the FSR had little time to relax), and more overshoot at the higher loads. For this reason the PLA data was excluded from further analysis. This means that on average the tactor will push harder than desired when placed directly over bony areas with minimal tissue compliance. This is not considered to be detrimental since the areas of interest likely will not be over bony areas, as pressing onto a bony area would be uncomfortable so should not be chosen.

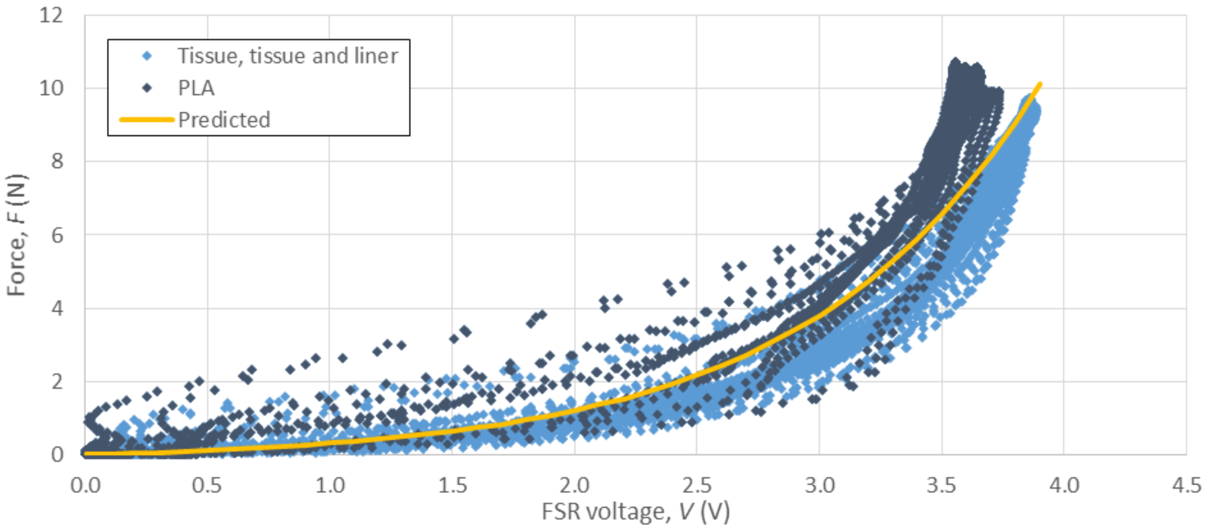

(a)

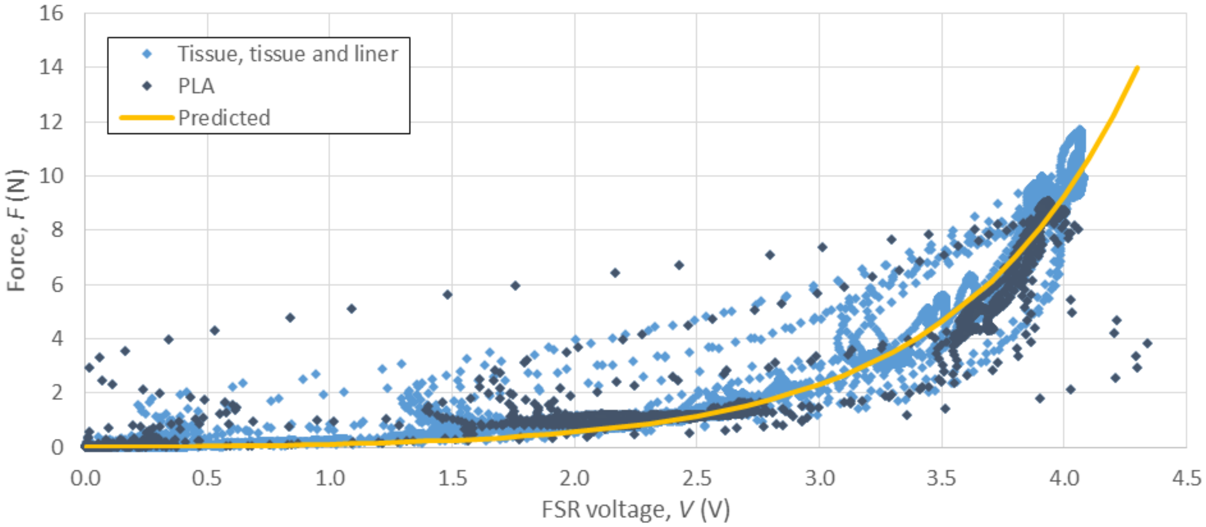

(b)

Figure 6.19 Transient calibration curves, (a) sine loading, and (b) stepped loading

The resultant calibration curve is the combination of the tissue and tissue plus liner runs, over all loading patterns and speeds (Figure 6.20). The best fit curve was determined by numerically minimizing the root mean square error of the fit of the equation to the recorded data.

$$F = 0.056e^{1.286V} - 0.056$$

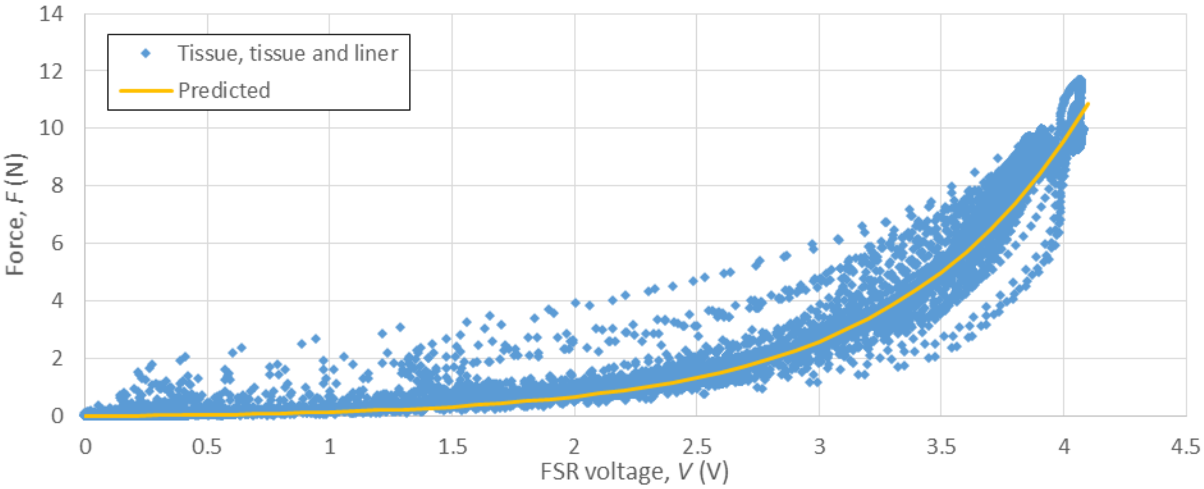

Figure 6.20 Transient calibration curve, all loading patterns

Plotting this fitted curve to the filtered FSR voltage (Figure 6.21) yields a maximum error of 3.5 N, but is generally not higher than 2 N in high loading and rapidly changing cases (Figure 6.21 (c)). The average error is 0.3 N. From the graphs it can be observed that with stable loads the predicted force will typically overestimate the applied force, and for moving loads it will underestimate the loads while the direction is changing.

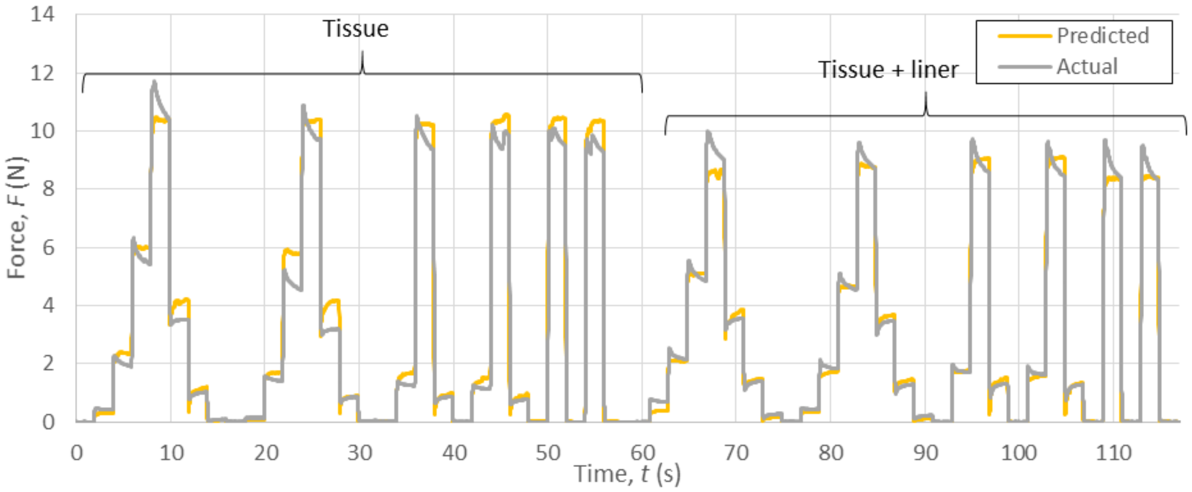

(a)

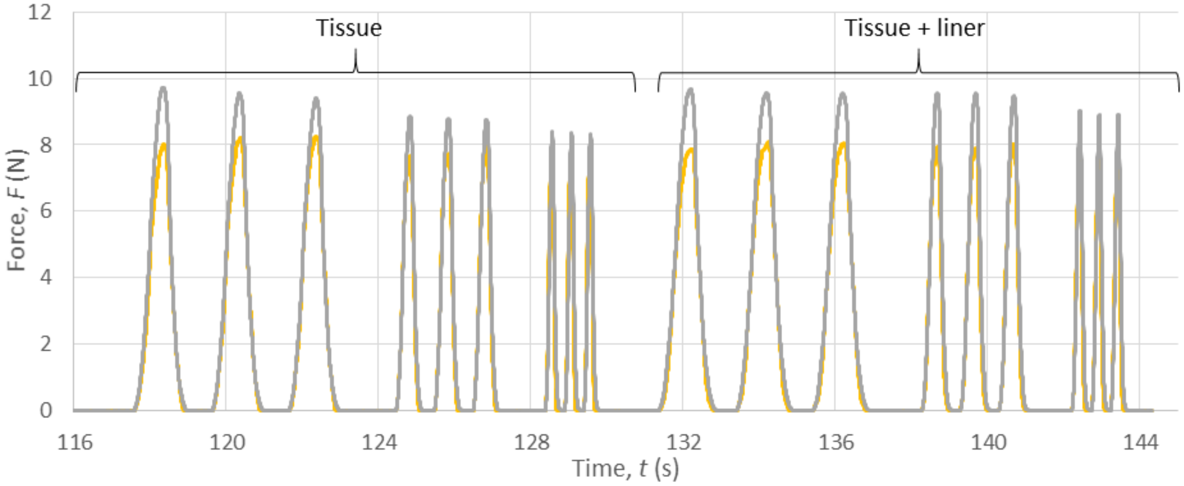

(b)

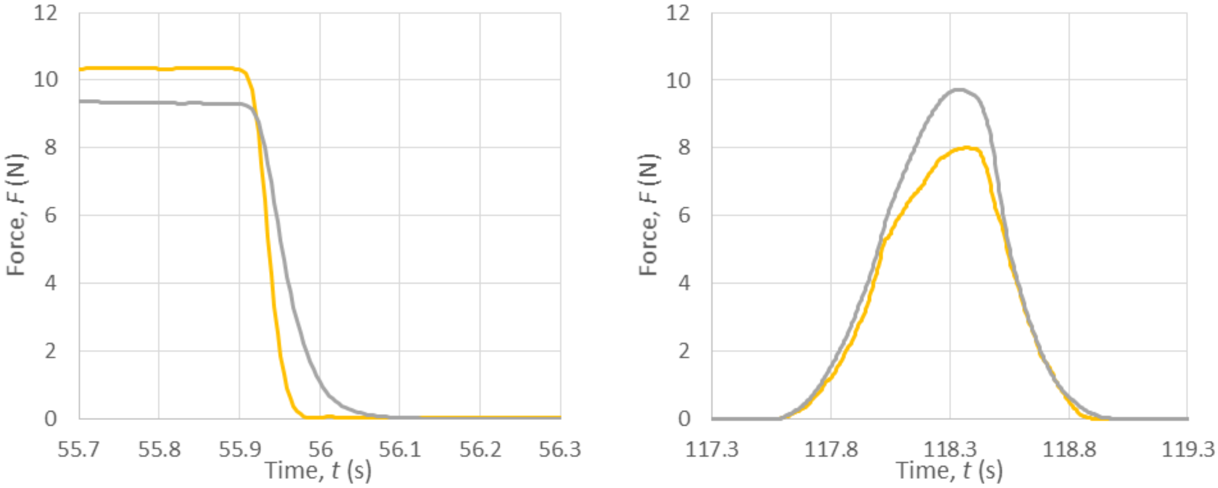

(c)

Figure 6.21 Predicted and actual load (a) stepped loading, (b) sine loading, and (c) high error locations

6.5.1 Stability of Calibration over Time

Repetitive testing was conducted by loading the tactor onto a double layer of Alpha liner (WillowWood^{TM}) to approximately 5 N for 5 seconds, then unloading for 5 seconds, and repeating cyclically for a duration of 24 hours. This time duration was selected as it would easily cover several days of in-lab testing, and would indicate if re-calibration would be needed over the duration of a typical study with several participants.

6.5.2 Repeat calibration

The calibration was conducted the same as with the initial transient calibration (Figure 6.22), and produced a very similar best fit curve. In fact, using the original curve maintains the same average error, and actually reduces the maximum error from 3.6 to 3.3 N. So after testing over a period up to 24 hours, the system should not require a new calibration.

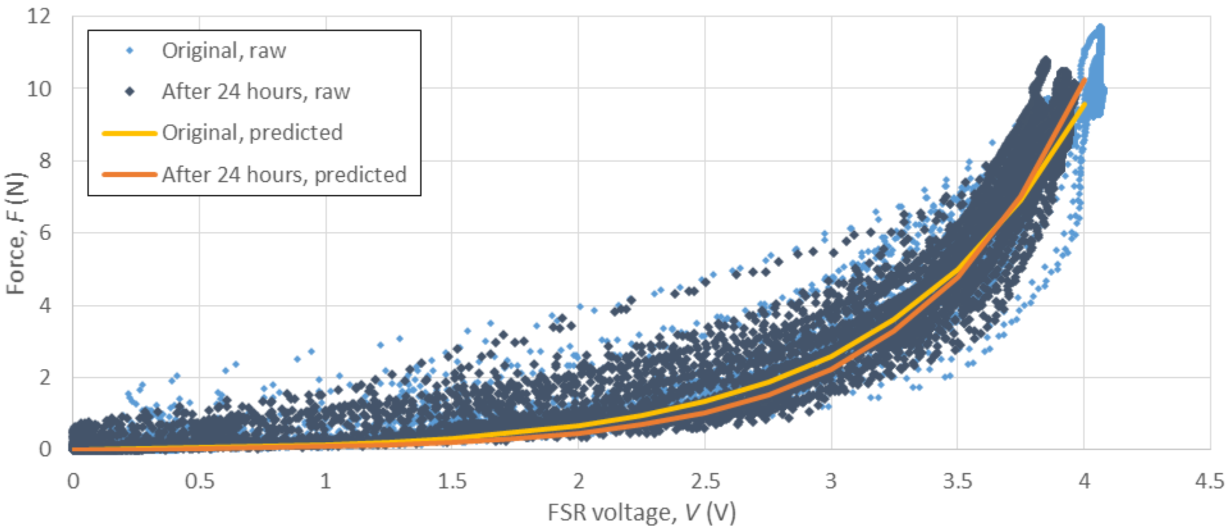

Figure 6.22 Transient calibration curve, all loading patterns, before and after wear test

Table 6.10 Calibration data before and after wear test

	Original data and fit	New data and fit	New data, original fit
Coefficient and offset	0.0561	0.0243	0.0561
Exponential	1.2861	1.5108	1.2861
Maximum error (N)	3.5	3.6	3.3
Average error (N)	0.3	0.3	0.3

6.5.3 Calibration of Cable-Driven Tactor

Calibration of the FSR integrated in-line with the long cable-driven tactor was conducted for comparison (Table 6.11 and Figure 6.23). The cable tactor was calibrated up to 6 N (compared to 10 N for the linear tactor) as higher forces cannot be maintained by the cable-driven tactor. FSRs were placed at two locations; one in-line close to the tactor head (FSR 1) and one in-line on the rack gear (FSR 2). From analysis, both appear to give similar responses, so in future the FSR should be placed on the rack gear as this is simpler to implement and requires fewer additional components and space, unless the length of the cable is sufficiently long. In both cases there is a large amount of hysteresis in the system.

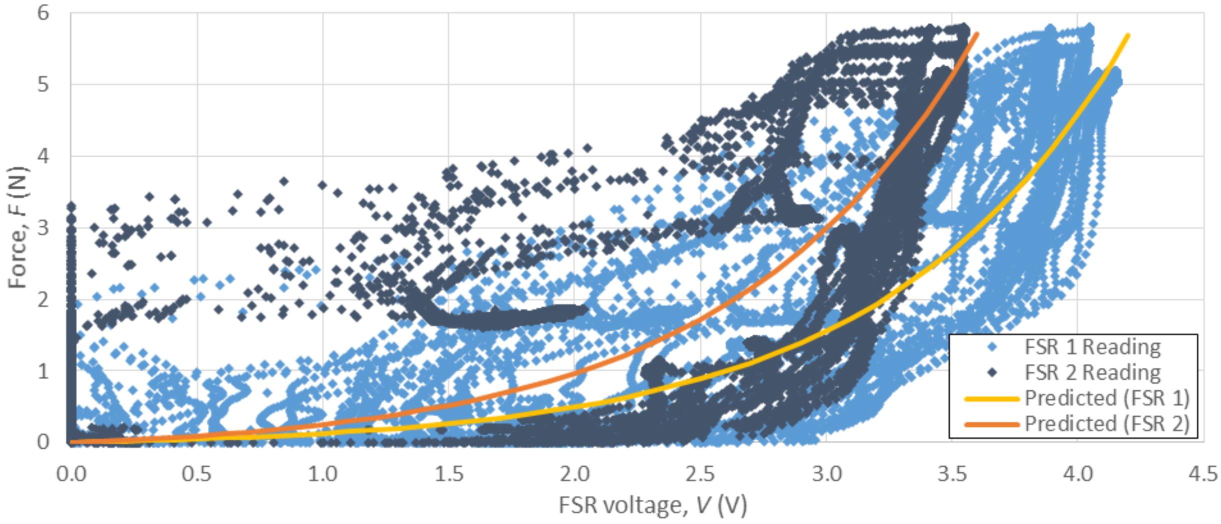

Figure 6.23 Transient calibration curve, all loading patterns

Table 6.11 Calibration data of FSR 1 (close to tactor head) and FSR 2 (on rack gear)

	FSR 1	FSR 2
Coefficient and offset	0.0687	0.1379
Exponential	1.054	1.0409
Maximum error (N)	3.1	2.6
Average error (N)	0.5	0.5

Plotting this fitted curve to the filtered FSR voltage (Figure 6.24) yields a maximum error of 3 N, but is generally not higher than 1.5 N in high loading and rapidly changing cases.

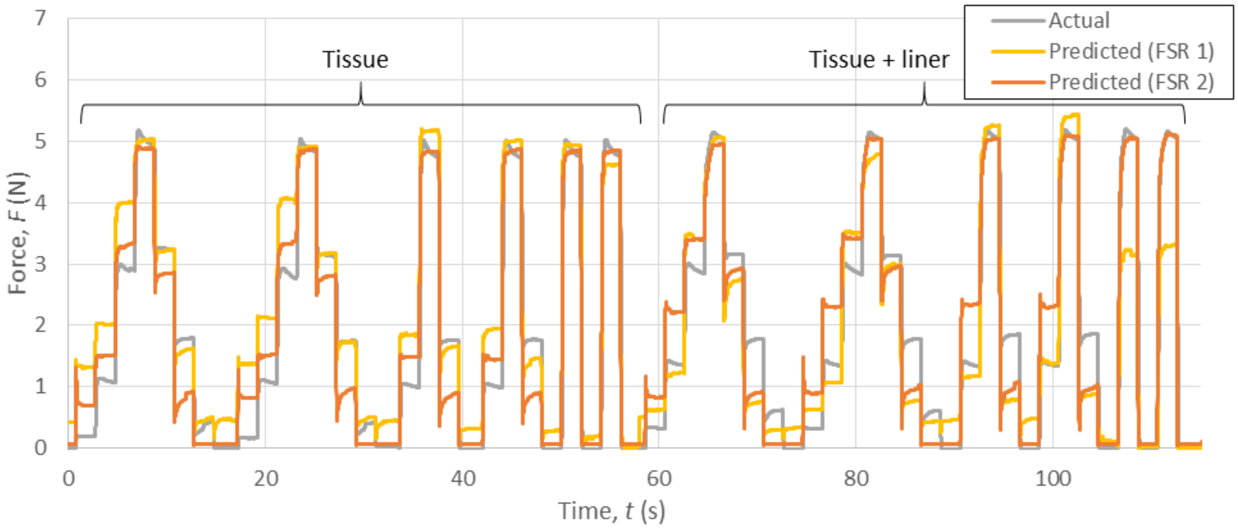

(a)

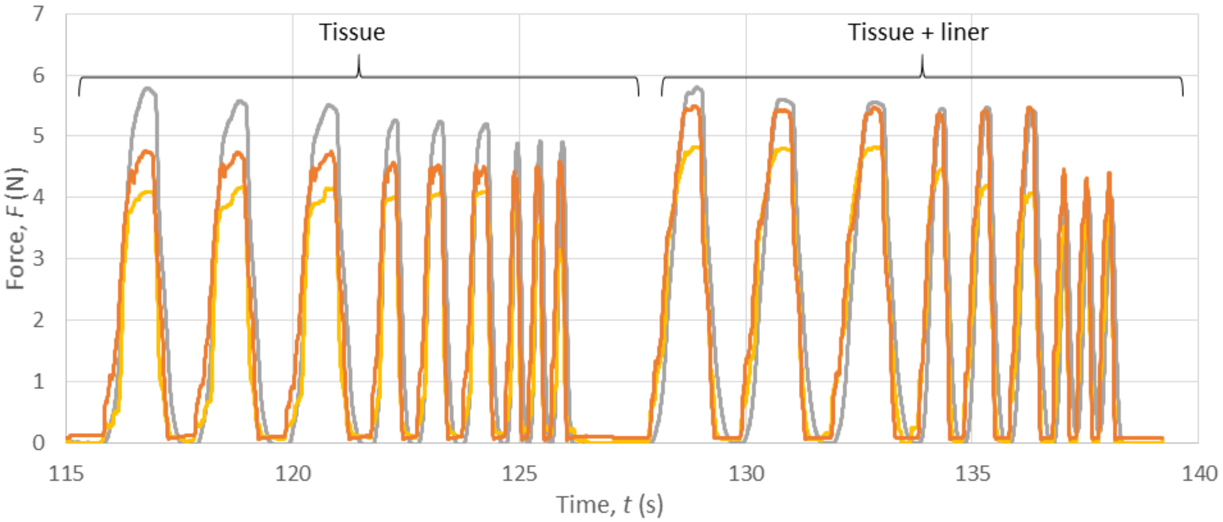

(b)

Figure 6.24 Predicted and actual load (a) stepped loading, and (b) sine loading

It can be observed that the FSR begins to read a change in voltage prior to applying a force; this is likely the FSR measuring friction in the system. Additionally, a dynamic “pulling” force can be observed when the tactor is retracting from the tissue, which rises to a steady-state voltage once the system has stopped moving. The effects of friction are thought to be responsible for the observed hysteresis.

This suggests that while the FSR may be sufficient to measure approximate forces applied by the tactor, the hysteresis inherent to the cable-tactor may prevent it from being used as accurate feedback to a closed loop control system.

6.6 Control

6.6.1 Background

6.6.1.1 System Commands

The servo motor is a direct current (DC) stepper motor controlled with pulse width modulation (PWM), where a digital signal is sent to the motor of various length pulses, which indicates the angular position of the motor (Figure 6.25).

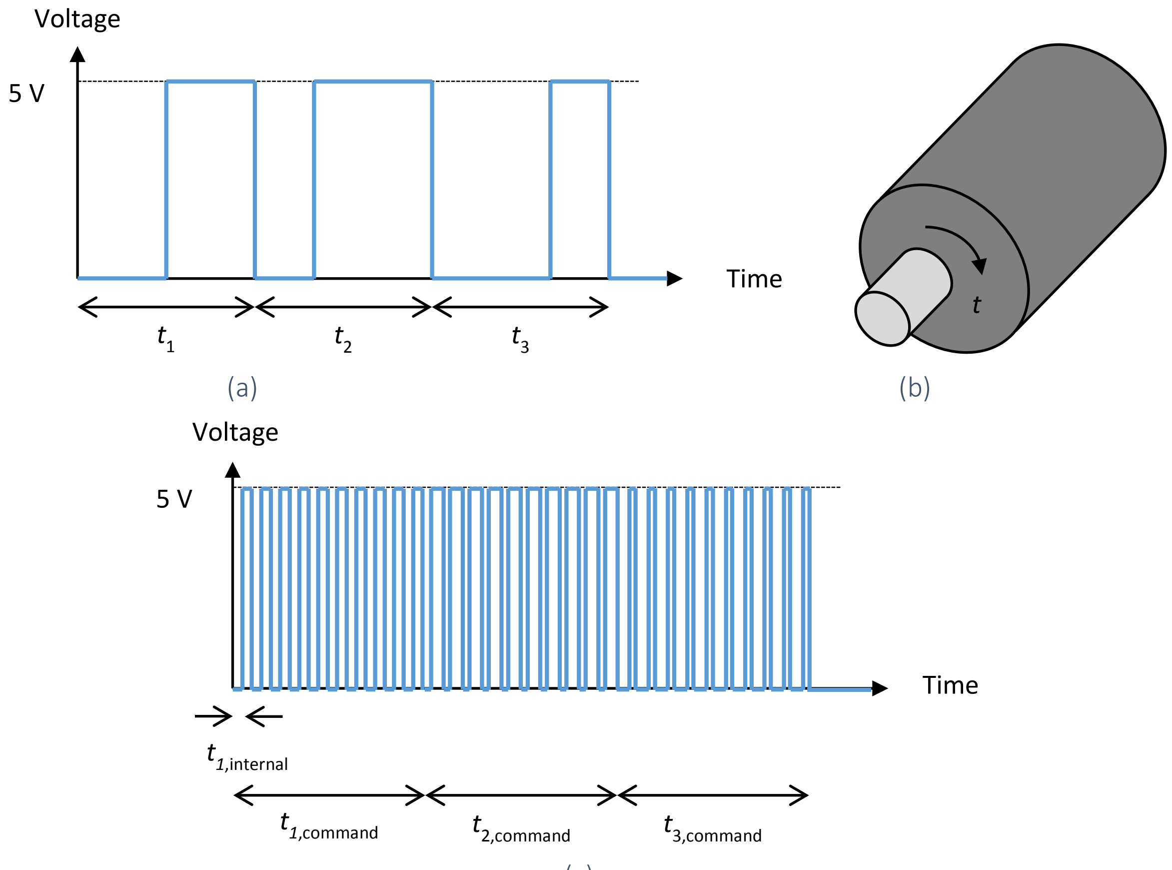

(a) (b)

(c)

Figure 6.25 Pulse width modulation of a servo motor, where (a) the width of the pulse per unit of time corresponds to the (b) position of the motor, and (c) shows a motor updating at a higher internal PWM frequency

Internally within the servo motor, a closed-loop system operates to set the angular displacement using a potentiometer (Figure 6.26). Both digital and analog servo motors receive PWM commands at 50 Hz, however a digital motor contains a microprocessor which internally translates signals to 300 Hz, allowing the motor to respond with increased acceleration and reduced deadband [101] (Figure 6.25 (c)).

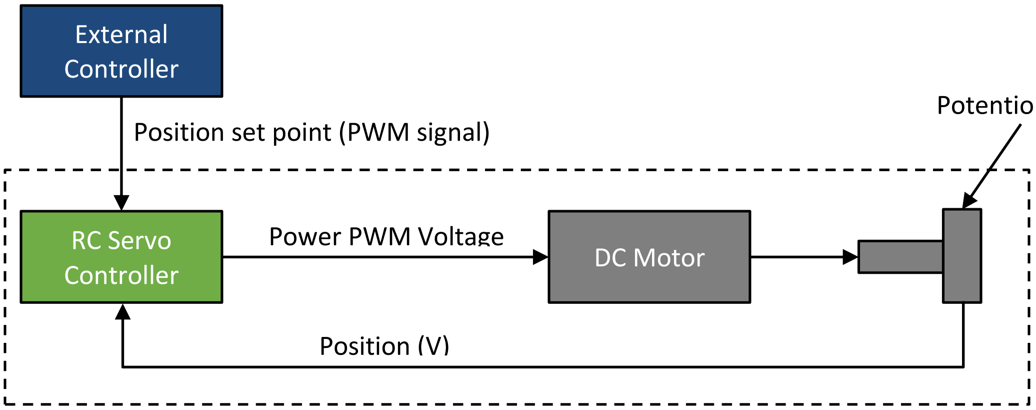

Figure 6.26 Internal closed-loop system within servo motor

The signal sent to the servo motor from the external controller may be either open or closed-loop, depending on the application or desired response (Figure 6.27). The advantages of open and closed-loop control will be evaluated, in terms of their accuracy, time delay, and overall use in this tactor control application.

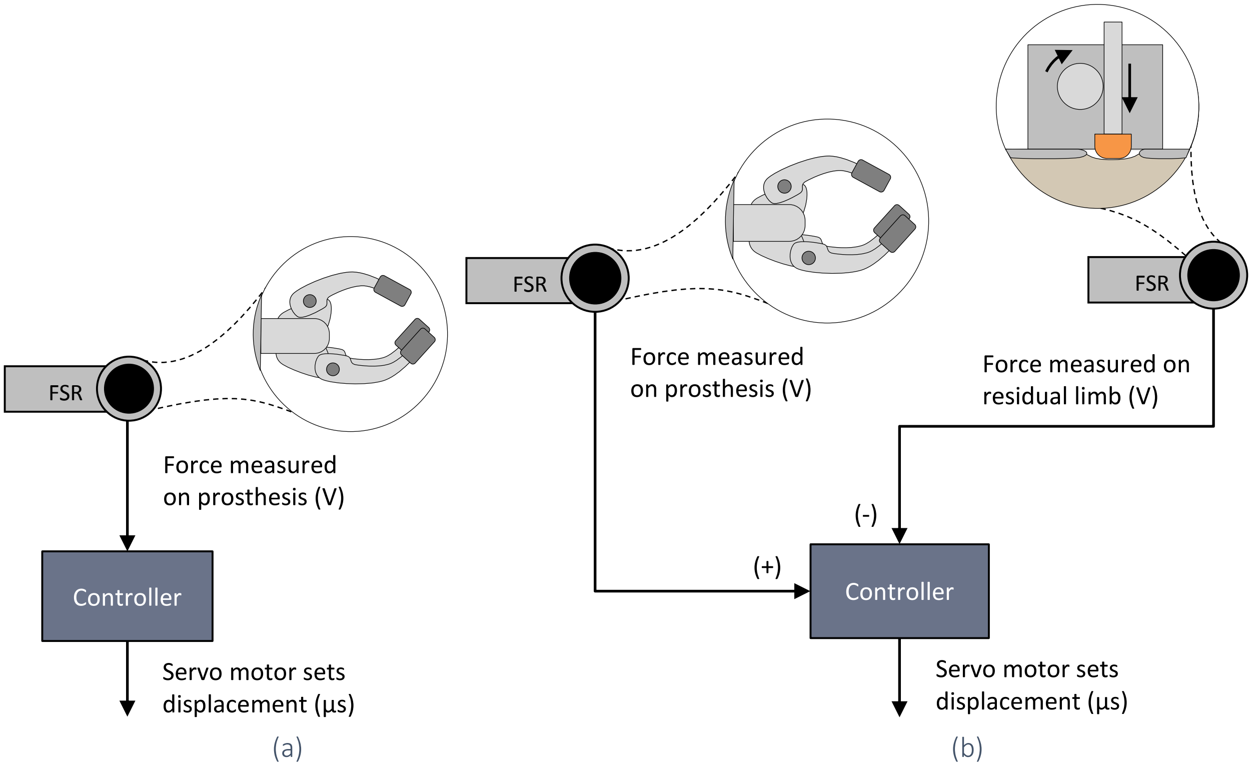

Figure 6.27 Control of tactor system using (a) open-loop, and (b) closed-loop control

6.6.1.2 Time Delay

In the human system, tactile information reaches the brain in 14 to 28 ms [102]. One article makes the case that feedback should be provided with a delay that is a fraction of this amount to avoid increasing the overall time substantially, suggesting a goal of delays less than 5 ms [5]. This may be an overly conservative value. While noticeable delay thresholds have not been studied for tactor responses specifically, studies have been conducted for similar applications. In haptic feedback applications, time delays may be noticed when they exceed 200 ms [103], and may alter the perception of grip forces being applied [104, 105]. The noticeable delay threshold for the control of a myoelectric prosthetic arm has been measured to be between 50 and 400 ms [106]. For the rubber hand illusion to work, in which the user begins to embody the device, the delay must be less than 300 ms [107]. It is therefore important that the overall time delay not substantially exceed 200 ms.

6.6.2 Open-Loop Control

6.6.2.1 Procedure

A linear fit was used to set the displacement for any given force, and was evaluated using step inputs as well as inputs from the reference FSR applied by hand under different loading conditions, including: applied to tissue, applied to tissue with a starting offset of 0.5 cm, and applied to tissue covered with alpha liner.

6.6.2.2 Evaluation of Linear Tactor

The linear tactor system was calibrated against the tissue analog using a linear fit from 0 N at a displacement of 0 µs to 10 N at a set displacement of 950 µs, yielding the following equation.

$$F = 0.0105d$$

Where *F* is the force (in N) applied and *d* is the set displacement (in µs). Note that better accuracy could be obtained using a non-linear fit, however a linear fit was used for a simple demonstration of the concept of open-loop control.

When calibrated to the tissue, error was up to approximately 1.5 N, however when displaced from the tissue error was as high as 5.2 N (Figure 6.28). When a liner covers the tissue and changes the compliance, error at high loads increases to 3.1 N. In all cases the time delay between the input signal from the reference FSR to the output applied force is less than 0.15 s.

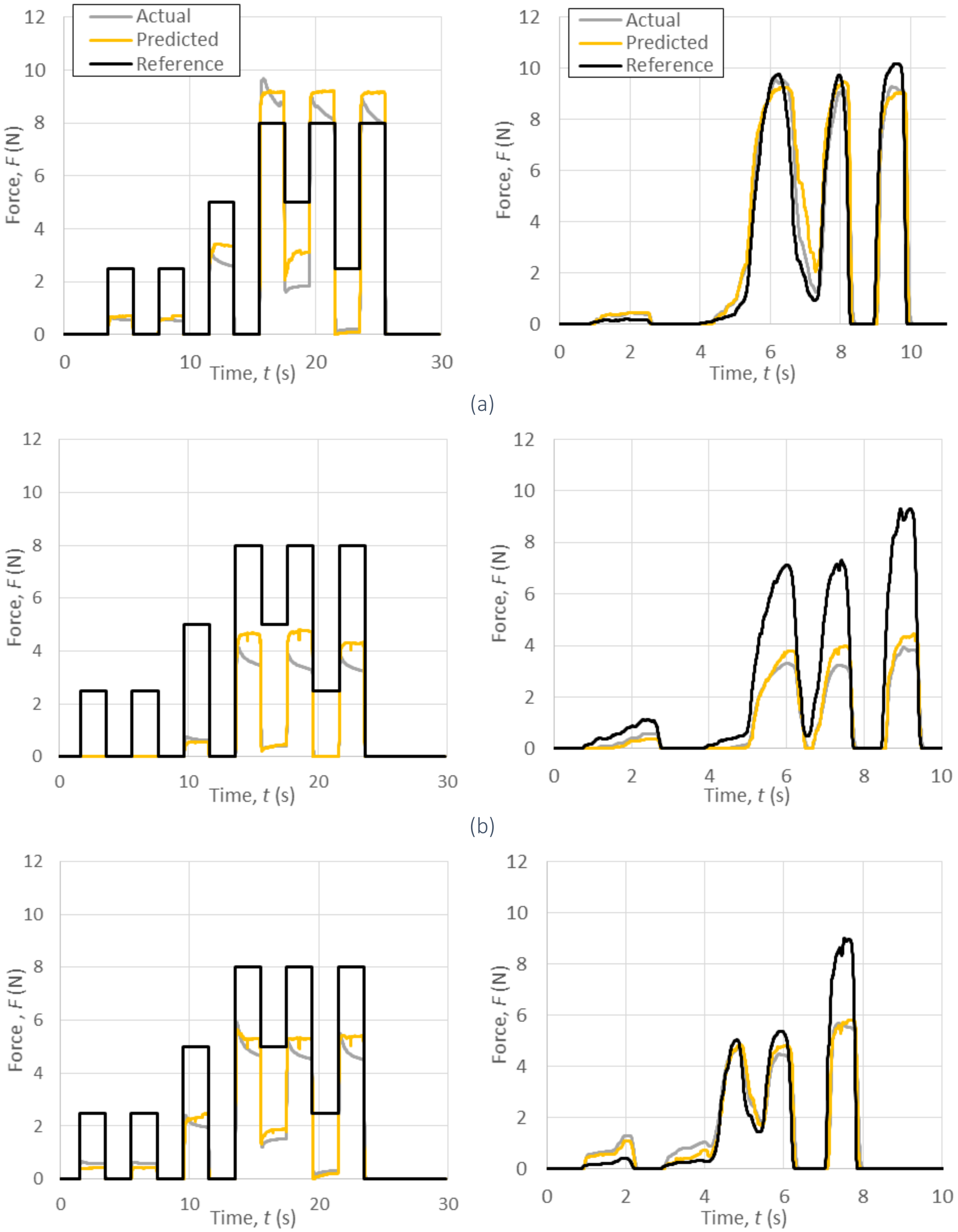

(a)

(b)

(c)

Figure 6.28 Evaluation of open-loop control on (a) tissue analog, (b) with 0.5 cm gap, and (c) tissue analog covered with alpha liner

6.6.2.3 Evaluation of Cable-Driven Tactor

Using the same procedure, the cable-driven tactor system was calibrated against the tissue analog using a linear fit from 0 N at a displacement of 0 µs to 6 N at a set displacement of 1100 µs, yielding the following equation. This differs from the linear tactor calibration, likely due to internal buckling of the cable within the conduit.

$$F = 0.00545d$$

Where *F* is the force (in N) applied and *d* is the set displacement (in µs).

When calibrated to the tissue, error is up to approximately 1.5 N (Figure 6.29). The time delay between the input signal from the reference FSR to the output applied force is less than 0.3 s, longer than the time delay from the open-loop linear tactor.

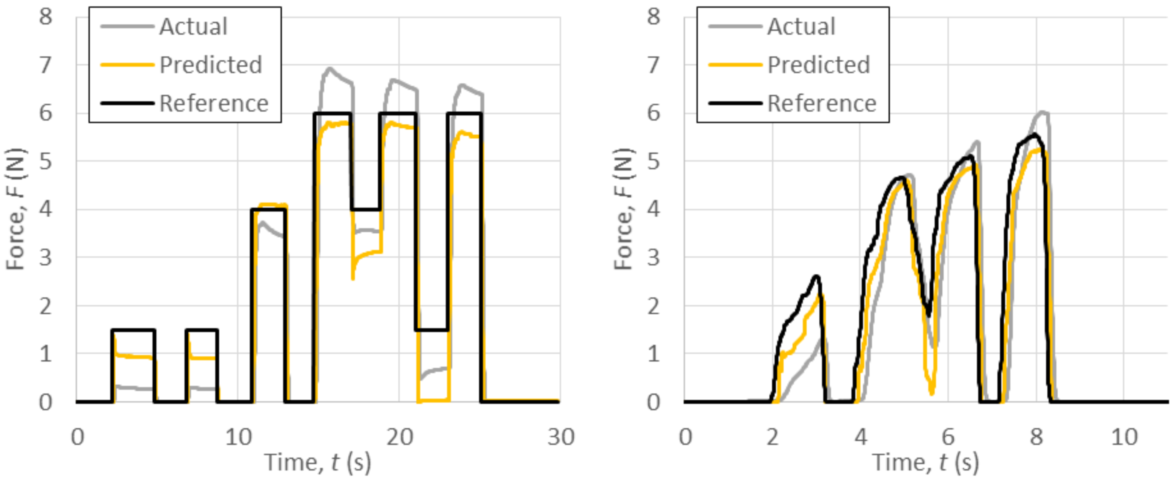

Figure 6.29 Evaluation of open-loop control on tissue analog

6.6.3 Closed-Loop Proportional Integral Derivative (PID) Control

6.6.3.1 Theory

A closed loop system is one in which a target set-point is chosen, where a sensor measures the process variable and provides feedback to the system in order to make adjustments to compensate for any difference between the set-point and the process variable [108, 109]. Several commonly used metrics include percent overshoot, rise time, settling time, and steady state-error, as shown pictorially below.

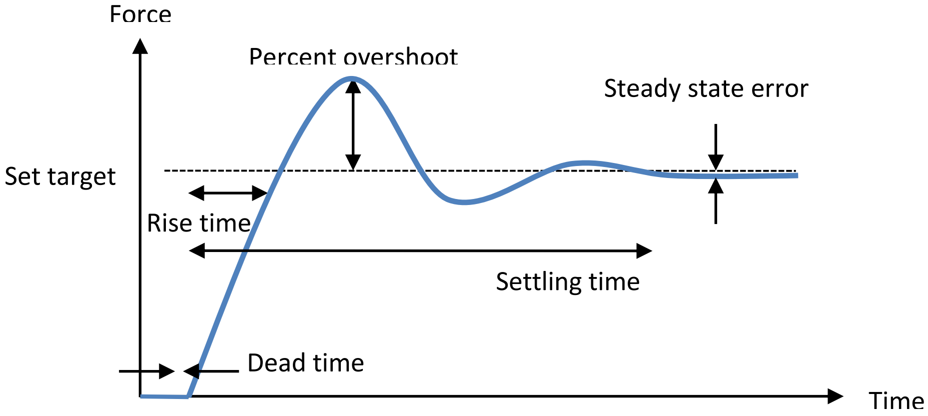

Figure 6.30 Response of a PID closed loop system, adapted from [108, 109]

Proportional-Integral-Derivative (PID) control uses three different coefficients, each varied to operate the response of the system, as shown in the equation below for controller output, *u(t)*.

$$u(t) = K_p e(t) + K_i \int_0^t e(\tau) d\tau + K_d \frac{d}{dt} e(t)$$

Where K_p is proportional gain, K_i is integral gain, K_d is derivative gain, and *e(t)* is error.

6.6.3.1.1 Proportional response

The proportional term depends on the overall error, the difference between the measured response and the set-point. Increasing this term will increase the speed of the response, but if too large will cause the system to oscillate out of control.

6.6.3.1.2 Integral response

The integral term sums the error over time, so that a small error will cause a small change in response. It will slowly result in the system moving to zero steady state error. Integral windup will occur if the term is too large, where a large change in set-point will accumulate a large error, causing the system to overshoot until the accumulated error eventually returns to zero.

6.6.3.1.3 Derivative response

The derivative term causes the system to decrease its output if the process variable is quickly increasing, and is proportional to the rate of change of the process variable. This term is highly sensitive to noise, so is typically set quite small, otherwise the system can become unstable.

6.6.3.1.4 Tuning

Tuning of the system may be accomplished through trial and error, where first the K_p term is increased until the system begins to oscillate. Then the K_i term is increased to stop the oscillations and obtain a minimal steady state error. Finally the K_d term is increased until the system reaches the set point in an acceptable amount of time.

An overview of the tactor system is shown in Figure 6.31, using closed-loop control.

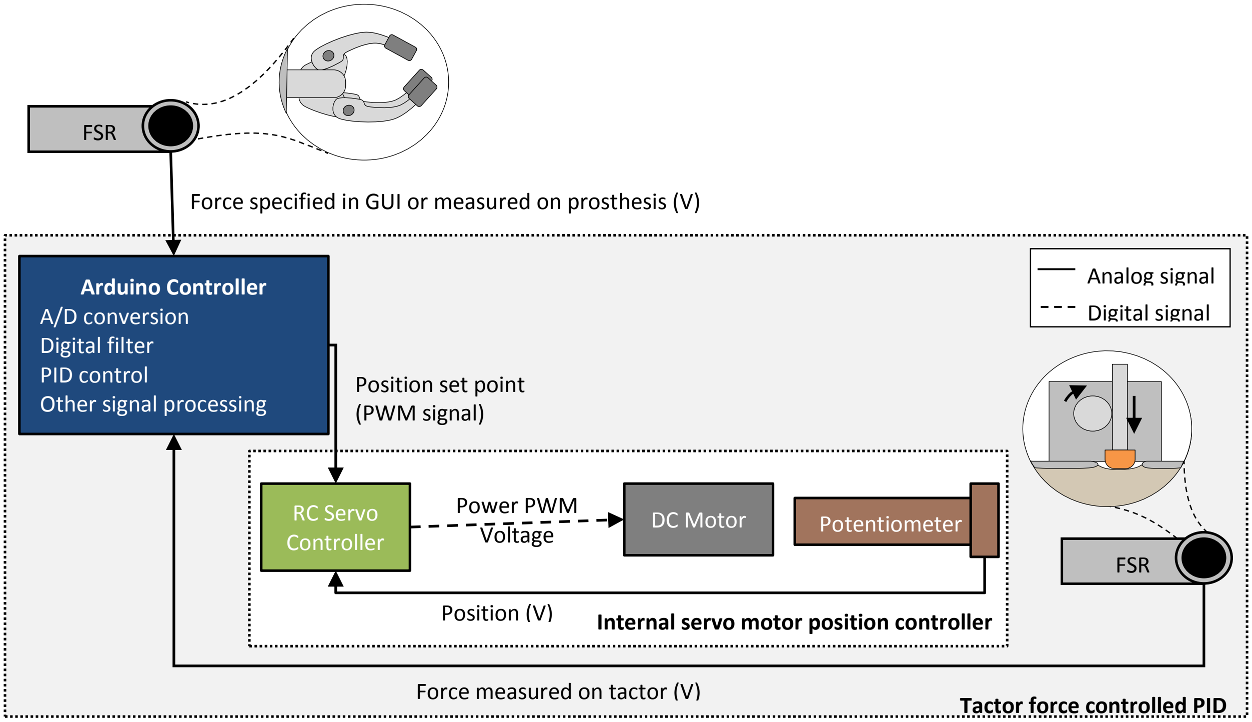

Figure 6.31 Overview of system operation

6.6.3.2 Procedure

The PID controller was tuned against the same materials as with open-loop control, with the caveat being that minimal overshoot and little oscillations could be allowed, as this may be confusing to the user [110]. Error was quantified by setting both step set points and set points applied by hand, and measuring the difference from the force applied to the load cell.

6.6.3.3 Evaluation of Linear Tactor

After several iterations of tuning parameters, the final parameters selected were $K_p = 1.0$, $K_i = 0.05$, and $K_d = 0.05$ (Figure 6.32). This produces a delay of approximately 0.3 to 0.4 s, with a maximum error of 2.0 N, however the error did not typically exceed 1.0 N. A faster response could be achieved by increasing the K_p term, however it was decided that a slower response was preferable to oscillations, which could be very confusing to the user.

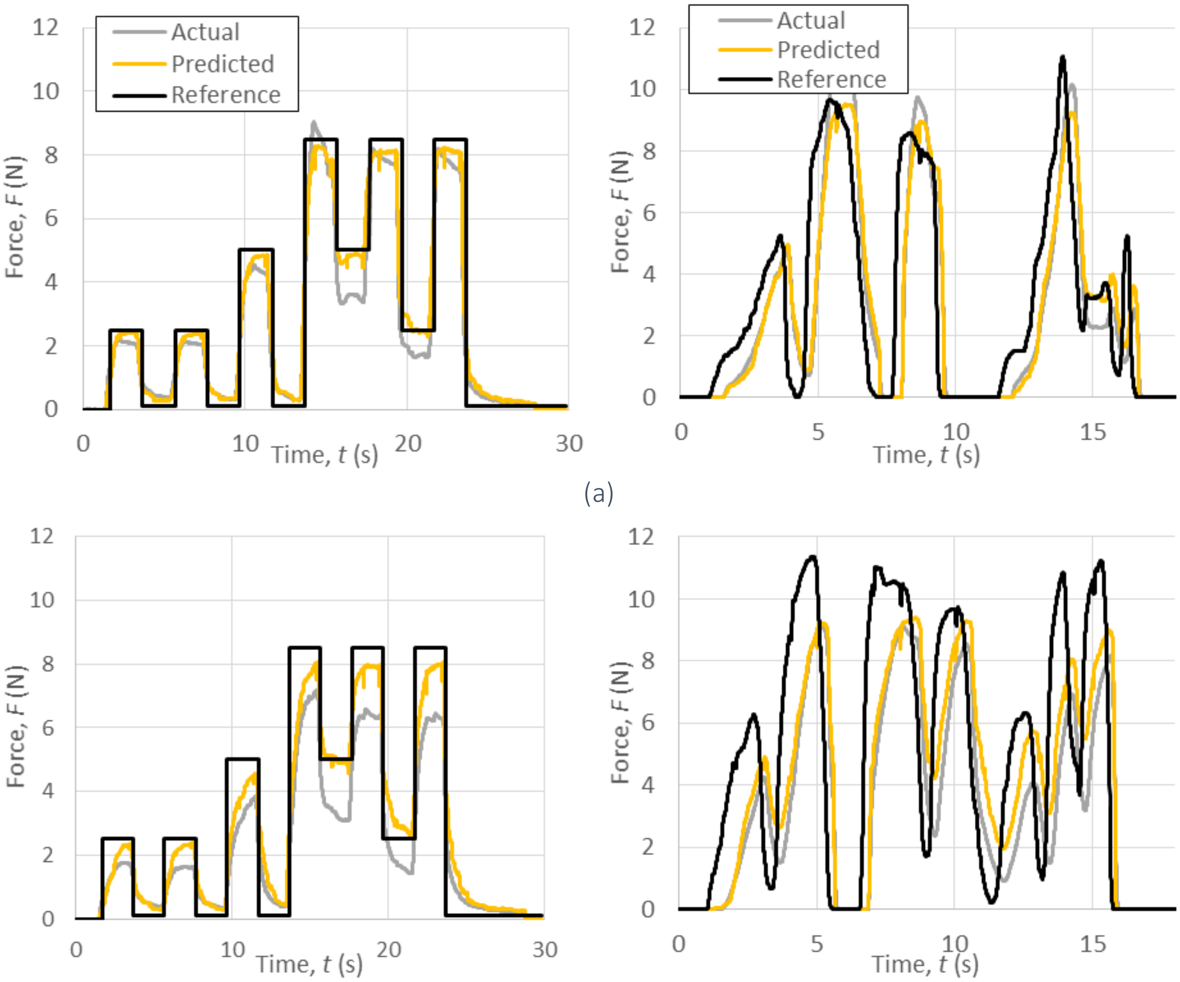

(a)

(b)

Figure 6.32 Evaluation of closed-loop control of linear tactor on (a) tissue analog, and (b) covered with alpha liner

An issue was observed where the tactor was distanced from the skin by 0.5 cm and a small load was applied; this meant that the tactor traveled very slowly and took time to apply a load, up to 3 seconds. This was remedied by adapting the tuning parameters so that $K_p = 50$ if the tactor FSR is reading zero applied force and adjusting the set point to 0.1 N to prevent significant overshoot. In this case the tactor typically moves quickly to 0.5 N, which may help to distinguish between the no-touch and touch case. Once the FSR reads a force the tuning parameters are adjusted back to their original values. This substantially reduces the time to contact (Figure 6.33) from 3 s to

0.4 s when there is a separation distance of 0.5 cm. When the tactor is placed close to the skin this drops to 0.3 s of delay.

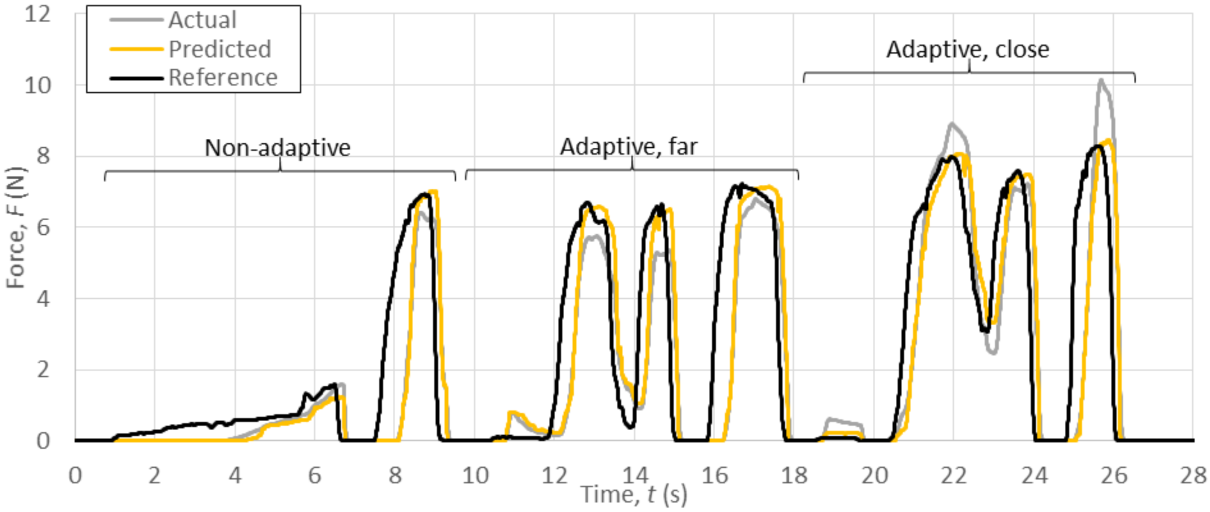

Figure 6.33 Graph of PID control using non-adaptive and adaptive tuning parameters pressing into tissue analog

The FSR has a dead band of approximately 0.1 N, which means that it could be touching the skin but not registering a force. Further investigation into preloading the sensors is warranted, as this may help to reduce the deadband. In order to ensure that the touch and no touch conditions are satisfied, the system could move to a zero position when the set point is 0 N. In this case, it would be important that the zero position of the tactor head is close to the skin in order to avoid introducing a substantial time delay.

PID control was also tested using a load cell in place of the FSR, shown in Appendix P. Response time was fairly similar, with typical time delays between 0.3 and 0.4 s, however error was reduced substantially, to a typical maximum of 0.3 N. Oscillations were of larger concern at the higher forces when step loads were applied, so the K_p term was reduced yielding a slower responding system. One potential way to reduce oscillations would be to improve meshing between the rack and pinion gears, as some play in the gears was observed during oscillations. Another is to change the tuning parameters as the tactor pushes onto the material, as the non-linear response of the tissue analog results in different effective stiffnesses depending on the compression applied.

6.6.3.4 Evaluation of Cable-Driven Tactor

The gains were retuned for the cable-driven tactor to $K_p = 1.9$, $K_i = 0.05$, and $K_d = 0.05$. This produced a delay of approximately 0.3 to 0.4 s, with a maximum error of 1.6 N (Figure 6.34), so approximately equivalent to the linear tactor.

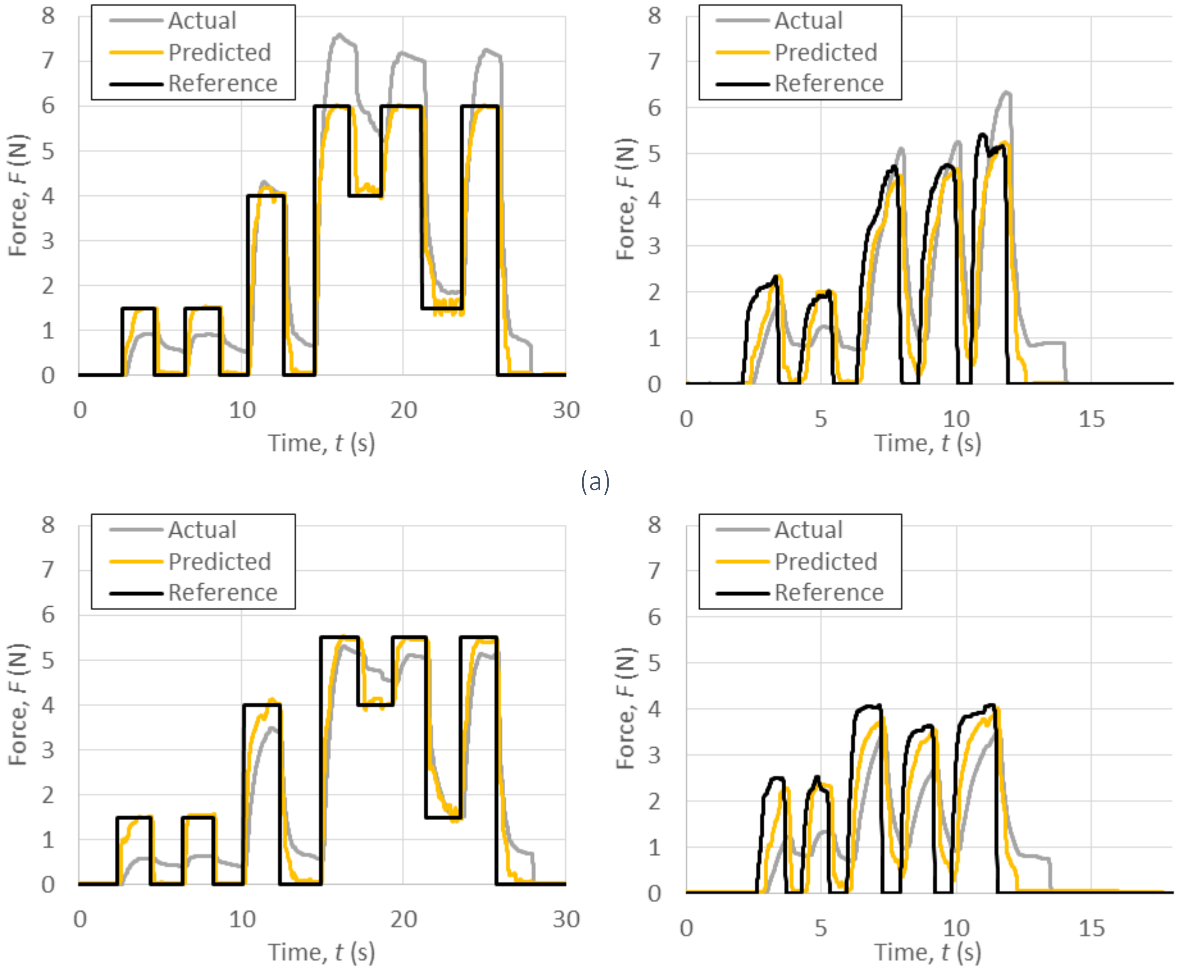

(a)

(b)

Figure 6.34 Evaluation of closed-loop control of cable-driven tactor on (a) tissue analog, and (b) covered with alpha liner

One major problem with the cable-tactor is the increased deadband; applied forces as high as 1 N can be read in as a predicted force of 0 N. This is likely a consequence of the frictional forces in the cable “pulling” away from the FSR as the tactor is retracted. As with the linear tactor, to ensure that the touch and no touch conditions are satisfied, the system should move to a zero position when the set point is 0 N.

6.6.4 Comparison of Control Methods

6.6.4.1 Accuracy and Adaptability

Using open-loop control, calibration at each particular stiffness can yield an error as high as 2.5 N, but applying a calibration from one curve to another gives errors up to 5.2 N (Figure 6.35). This confirms the hypothesis that this methods may work well under constant conditions, but would need to be recalibrated at different locations, and would not be able to adapt to changing conditions such as rotational movement of the socket or muscle contractions. For the linear tactor, the maximum time delay measured from open-loop control was 0.15 s, but is generally less than 0.1 s. The cable-driven tactor is slightly slower to respond, where the maximum time delay measured was 0.3 s, but is generally less than 0.15 s.

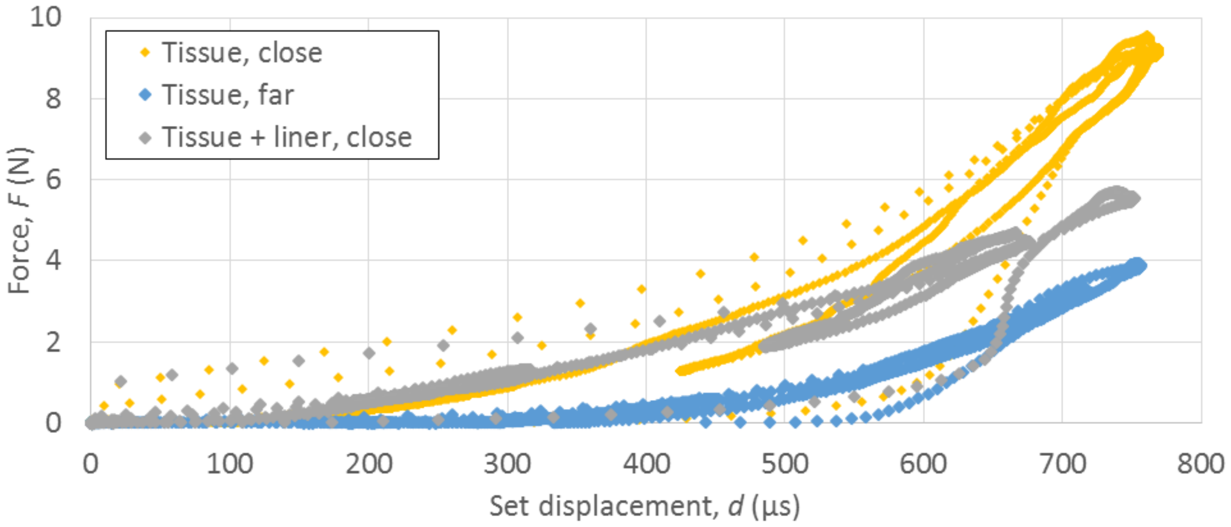

Figure 6.35 Graph of set displacement versus force under various loading conditions using the linear tactor

Closed-loop control is able to reduce the effect of changing conditions when compared to calibration against displacement (Figure 6.36), although the delay in the system is longer. A maximum error of 2.1 N was observed across changing conditions for the linear tactor, however typical error is less than 1 N. Using adaptive control to account for travel through empty space, the maximum delay observed was 0.5 s, however it is typically between 0.3 and 0.4 s.

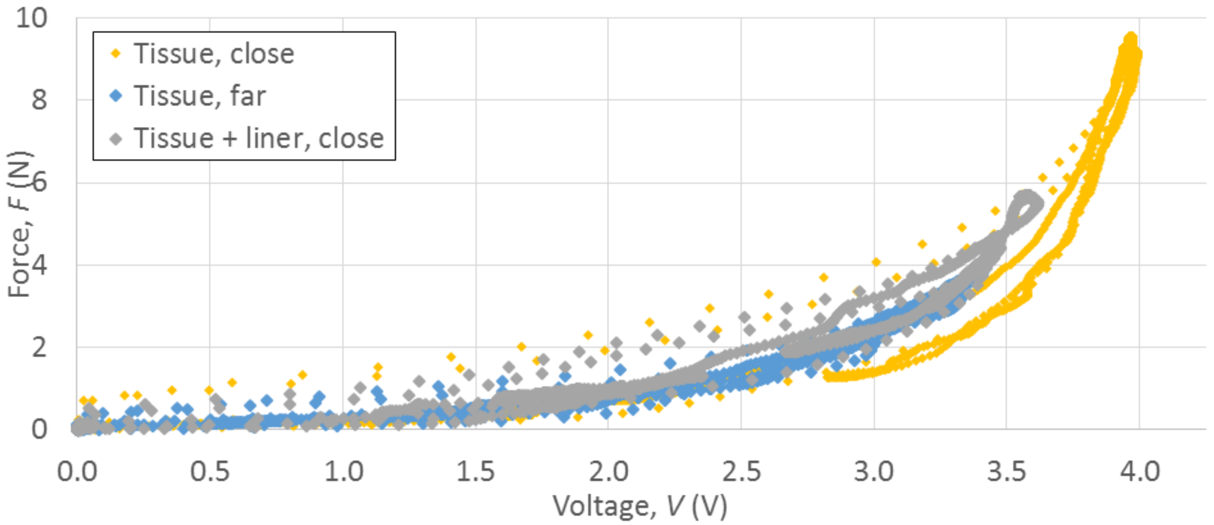

Figure 6.36 Graph of FSR voltage versus force under various loading conditions using the linear tactor

A maximum error of 1.6 N was observed across changing conditions for the cable-driven tactor, with similar delays between 0.3 and 0.4 s. The deadband is as high as 1 N, meaning that forces below this cannot be applied reliably. Further investigation into preloading the sensors is warranted, as this may help to reduce the deadband.

6.6.4.2 Total System Delay

The total perceived time delay of the system is assumed to equal the time between when the analog signal is measured with the reference FSR, up to when the analog signal is measured with the tactor FSR (Figure 6.37 and Table 6.12).

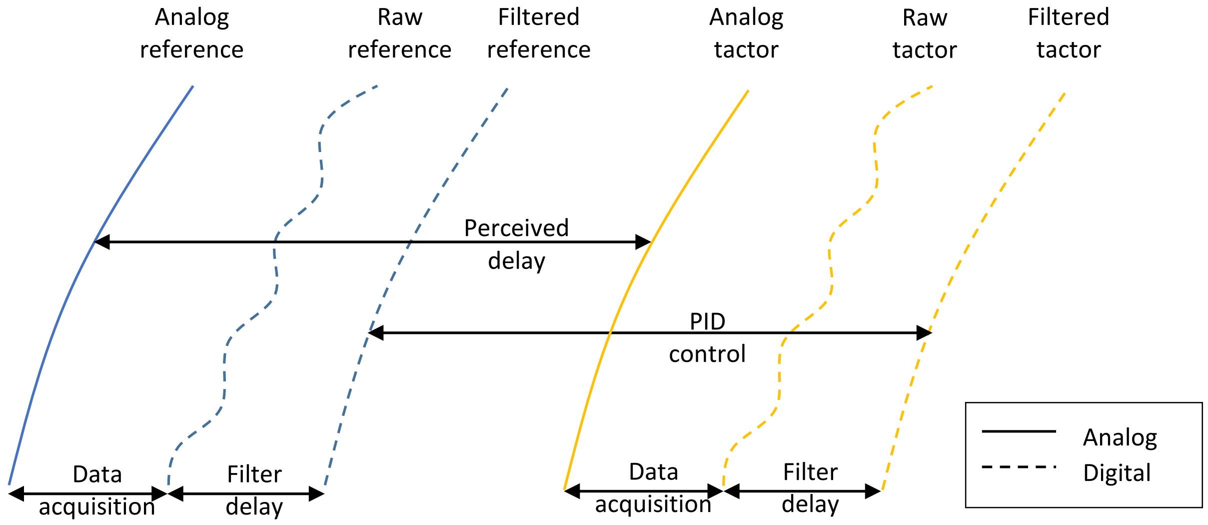

Figure 6.37 Components leading to time delay in system

Table 6.12 Delay contribution from each step in control methods

	Open-loop control		Closed-loop control	
	Linear	Cable-driven	Linear	Cable-driven
Data acquisition (s)	< 0.001	< 0.001	< 0.001	< 0.001
Inherent max filter delay (s): Reference	0.043	0.043	0.043	0.043
Tactor	n/a	n/a	0.016	0.016
Implement filter calculation (s): Reference	< 0.001	< 0.001	< 0.001	< 0.001
Tactor	n/a	n/a	< 0.001	< 0.001
Total perceived delay (s)	0.05 to 0.15	0.1 to 0.3	0.3 to 0.5	0.3 to 0.5

The duration of the data acquisition and calculations were measured using timers embedded into the Arduino script, all of which were completed in under 0.001 s (the resolution of the timer). The open-loop delay for the linear tactor should not be noticeable as it is less than the 200 ms estimated to define noticeable haptic feedback [103], however the cable tactor and the closed-loop linear tactor system delays may be noticeable to some users.

6.7 Conclusions and Future Directions

Several different sensors have been evaluated under static conditions, including a potentiometer, a current sensor, and an FSR. The FSR was selected as the optimal sensor for measurement of forces applied by the cable-driven tactor, and it was calibrated under dynamic loading conditions. In general the accuracy of the cable-driven tactor is lower than for the linear tactor, due mainly to the friction present in the system resulting in substantial hysteresis.

Two methods of tactor system control have been developed; open-loop control where the displacement of the tactor head is set, and closed-loop control where the applied force is measured and fed back such that the system can reach a target force.

System evaluation has indicated that open-loop control for both the linear and cable-driven tactor may be within the threshold required for a user to interpret tactile sensations as simultaneous (i.e. the user may not notice a delay between force applied to the prosthetic finger and force applied to their residual limb). However, without calibration of the compliance in the residual limb, or under changing conditions, open-loop control may result in large inaccuracies in the forces applied.

Closed-loop control using an in-line FSR has shown some promise in improving the accuracy of applied forces, however this is difficult to integrate into the linear tactor without compromising socket integration, and demonstrates some deadband with the cable driven tactor due to friction in the system. The response is slower than open-loop control, and may be outside of the threshold for detection of asynchronous tactile inputs (i.e. the user may notice a delay between force applied to the prosthetic finger and force applied to their residual limb).

If a closed-loop tactor system is to be further pursued, it will be important to reduce the deadband to ensure that the touch/no-touch case can be applied reliably by the tactor, as well as reduce the time delay to ensure that it is not noticeable to the user. The dead band may be reduced by preloading the sensor, however care should be taken to ensure that the range of the sensor is not substantially reduced. One way to reduce the overall delay could be to reduce the amount of filtering applied to the input signal to a cut-off frequency of 100 Hz, as suggested in [19], as this would reduce the delay introduced by the filter. However, it will be important to verify that there is no noise below this cut-off frequency interfering with the signal, and that the inputs to the controller do not result in significant overshoot of applied tactor forces.

Another way to improve response time would be to select a motor that can receive commands faster than at 50 Hz from the controller. While the servo motors in the tactor designs may be overdriven at higher PWM frequencies, this is not suggested by the manufacturer. The analog motor tested (Hitec HS35-HD) updates at 50 Hz, while the digital version of the motor (Hitec HS5035-HD) updates internally at 300 Hz. Preliminary testing did not show an improved time response over the analog motor; despite an improved internal response, the system still receives commands at 50 Hz from the controller, which limits the overall speed of the system. The digital motor also draws more current and heats up faster, so is not recommended in this case. It may be possible to access the internal control loop within the digital motor, which would allow for faster commands to be read from the controller. Another possible option to reduce system delay would be to develop a more sophisticated controller, such as that proposed in [110] which uses optimization criteria to settle quickly with little overshoot.

It is recommended that current draw be further investigated as a method of quantifying forces applied by the linear tactor, particularly using a fixed and optimal amplification of the signal, and observing current draw during dynamic loading.

Once the control for the linear tactor has been optimized, an attempt should be made to implement this control system with the cable-driven tactor using a different sensor, as an FSR implemented onto the rack gear of the tactor introduces too much deadband to the system. Alternate methods of integrating a sensor onto the tactor head itself may be explored to eliminate the hysteresis introduced by the cable and conduit, however sensor selection and wire routing must be taking into consideration.

In the future, it would be useful to experiment with time delays in mechanotactile prosthetic feedback applications, to understand what delays can be detrimental to system functionality in terms of perceived usefulness as well as force estimation. An experiment to determine optimal mapping between measured and applied forces would also be useful to understand how tactile information can be best communicated to the user.

Chapter 7. Sealing Methods

7.1 Introduction

Evaluation of the tactor-integrated prosthetic arm (Chapter 5) highlighted the importance of maintaining an airtight seal when integrating a tactor onto a prosthetic socket, in the case that a suction attachment method is used. Maintaining this seal has been largely overlooked in literature, so further investigation is needed before tactor systems can be widely implemented in the clinic.

7.2 Background

Lower-limb sockets are commonly attached to the body with a suction seal, which helps to maintain the attachment of the prosthetic socket. They may even use an elevated pressure pump to increase the vacuum pressure differential in the socket. These elevated vacuum sockets are commonly prescribed to help prevent volume loss and improve overall limb health [111-115].

Suction attachments are used particularly in the case of myoelectric arms, as opposed to body-powered arms, which typically use harnesses for attachment [13, 116]. Elevated vacuums in upper-limb prostheses are not commonly used, however they are mentioned in a review paper on DARPA socket development [23]. Additionally, two studies have tested an elevated vacuum in transradial amputees, and have shown promising anecdotal results [117, 118].

It is therefore important to consider the effect of a vacuum attachment on tactor integration to ensure that these devices are applicable across users. While some groups have looked at integrating tactors into a socket [26, 47], none have yet addressed the suction seal issue, nor provided specific details of tactor integration.

Generally, electrodes for myoelectric control are kept in contact with the body either by embedding them in a socket which is worn directly on the skin, or by embedding them into a fabric liner that fits between the socket and the body [23]. In this way, the vacuum seal needed to maintain connection to the residual limb is not compromised. This concept is extended to apply to tactors in a paper from the Applied Physics Laboratory at Johns Hopkins that mentions mounting the tactor in the interface between the user and the prosthetic device, within the socket [47].

While this concept may work well for small components such as electrodes, there is an added challenge in that tactors are generally larger and contain moving components. In the case of the cable-driven tactor, which has a relatively long horizontal profile, other sealing methods must to be considered.

7.3 Potential Sealing Methods

Three different methods of sealing the socket were considered, all isolating the tactor from the residual limb at different points along the device and socket.

7.3.1 Compartmentalizing Limb Segments

One method is to isolate the tactor at the surface of the residual limb (Figure 7.1), where a portion of skin under the tactor is isolated from the remainder of the interface using an O-ring attached to the inner wall of the socket. This would compartmentalize any potential broken seals formed as the tactor pushes the skin away from the hole in the socket by localizing loss of vacuum pressure to a small segment of the arm. A possible drawback is that this may be uncomfortable to the user, as it places localized compressive loads on the residual limb in addition to the compression already induced on the limb by the socket itself. It could also potentially cause tissue edema due to differences in pressure between adjacent locations. Further exploration would be required prior to attempting to implement this concept to ensure that it is safe and comfortable over long durations of socket wear.

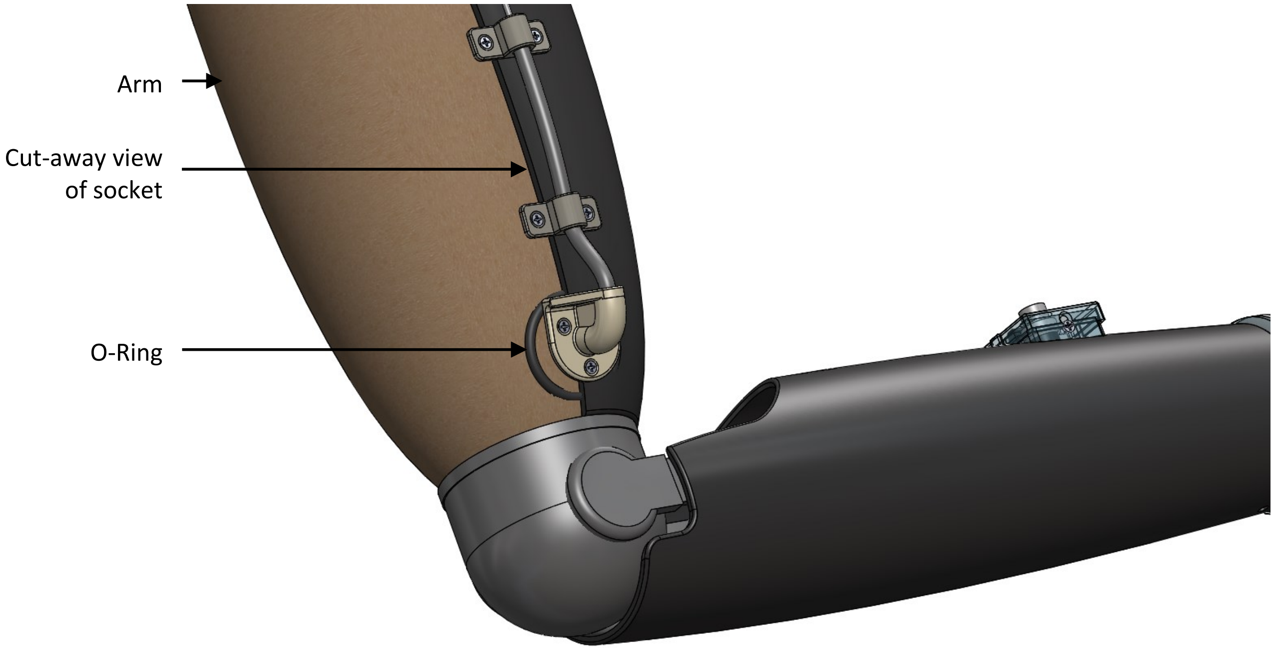

Figure 7.1 Limb compartmentalization showing cut-away view of limb compartment under tactor

As a potential extension, the limb could be segmented into several different compartments, with areas of high and low vacuum pressure cycling between segments to promote blood flow and maintain a sufficient vacuum pressure to hold the socket to the arm. If explored further, the influence of cycling vacuum pressures on tissue edema would need to be evaluated, as well as overall comfort of the system and other potential health issues.

7.3.2 Enclosing Entire Tactor

The second concept is to enclose the entire tactor within a layer of thermoplastic (i.e. integrated within the socket wall itself), a sealed chamber, or membrane cover (Figure 7.2). Enclosing the tactor within the socket is the only method currently published in literature, without specific details provided [47].

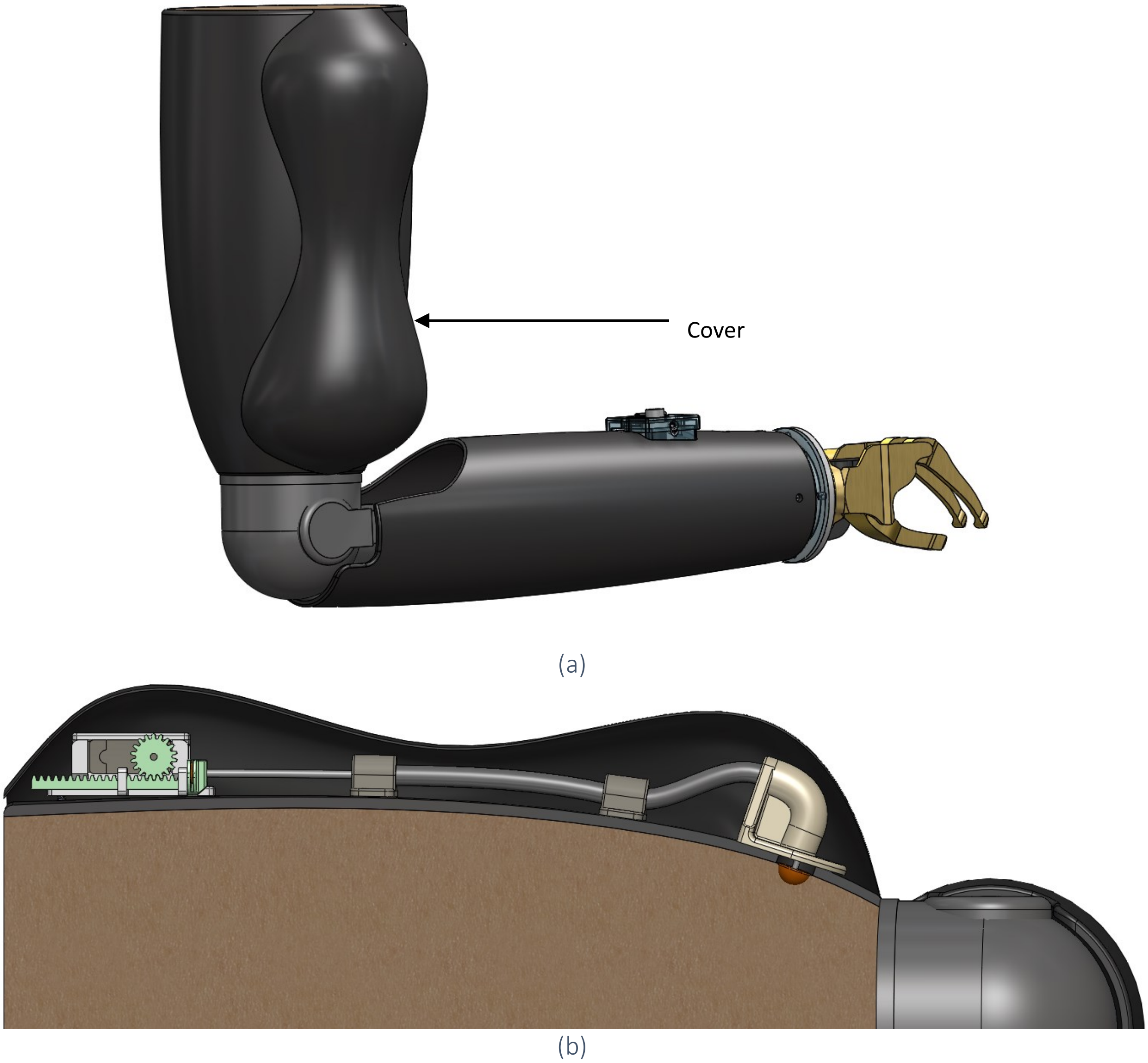

Figure 7.2 Enclosed tactor (a) entire arm, and (b) cut-away view

This concept yields the benefits of eliminating pinch points and ensuring that tactor remains clean while offering some protection from damage. However, it would add significant bulk to the overall size and weight of each tactor. For the cable-driven tactor this would be particularly difficult to implement, as either a large area would need to be covered, or the cables would need to be routed through the socket itself. This would increase manufacturing time significantly, likely increase the weight of the socket, and make it difficult to perform any required maintenance on the system.

7.3.3 Interface of Socket and Limb

Another option is to isolate the limb at the socket interface using a flexible membrane inserted between the socket and liner or skin (Figure 7.3). The tactor head would either press through the membrane if the membrane were compliant enough to maintain the tactor head shape, or be connected to either side of the membrane so that it directly contacts the skin. The advantage of this concept is that it requires minimal redesign of the tactor system, does not increase weight substantially, and does not pose a significant risk for edema compared to a system open to atmospheric pressure.

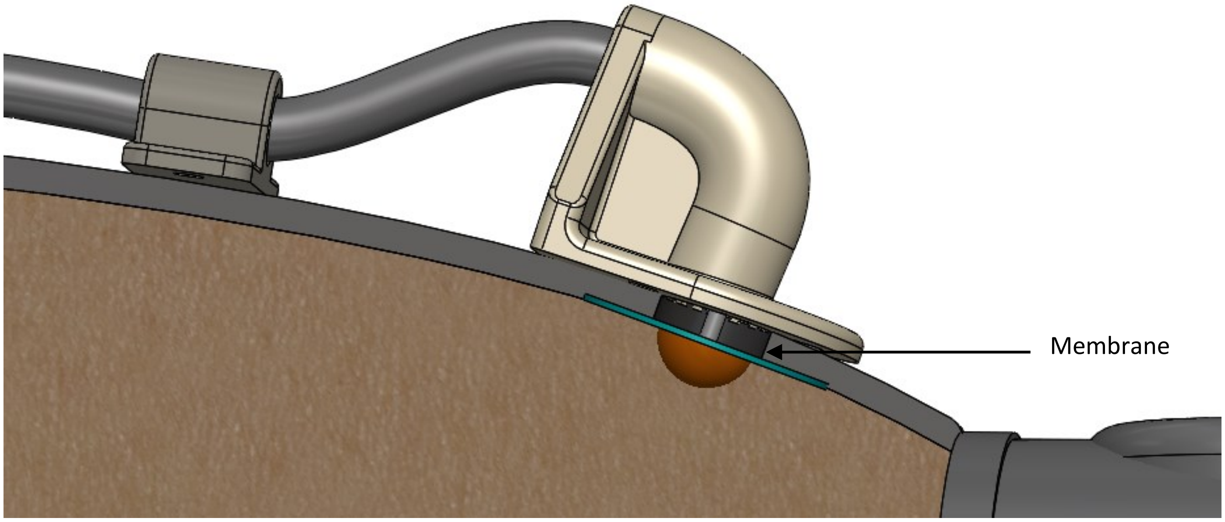

Figure 7.3 Separation of arm from socket using membrane interface

A potential complication is that it may increase the current draw from the tactor given that the head must press through the additional membrane. It also has the potential to reduce the overall throw of the tactor. For this reason, the membrane must be quite compliant, or be shaped so that it is not required to stretch but rather displace, such as a contoured rather than flat seal (Figure 7.4). In order to avoid pinch points, a cup-shaped seal may be preferable to a bellows seal. The material must also be strong enough to maintain an air-tight seal under the potential vacuum conditions applied in socket attachment.

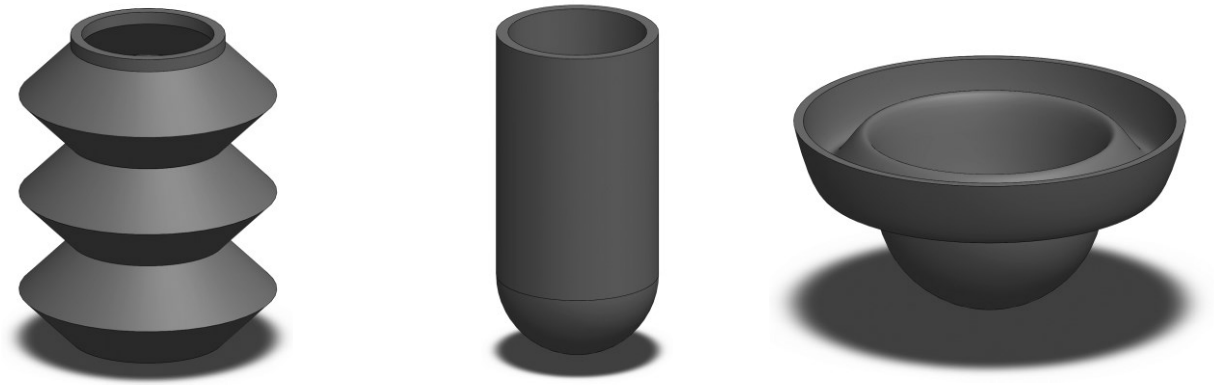

(a) (b) (c)

Figure 7.4 Rendering of membrane geometries, (a) bellows, (b) extended cup, and (c) retracted cup

7.3.4 Method Selection

A decision matrix was utilized in order to select the best method to pursue, based on design specification requirements (Appendix Q). The membrane concept was chosen to investigate further for its simplicity, ease of implementation, and reduced bulk compared to the other methods. In order to develop this method, an understanding of the interactions of pressures in the socket, characteristics of various membranes, and loading on the interface by the tactor is needed.

7.4 Membrane Testing

7.4.1 Background

7.4.1.1 Anticipated Pressures

Specific information on typical prosthetic socket suction pressures was not found for upper limb sockets literature [23, 117, 118], so an estimate of vacuum pressures to anticipate was required.

Vacuum pressures in lower-limb sockets range across studies (Table 3.1). Previous in-lab testing involved measuring the vacuum pressures applied using the Harmony e-Pulse elevated vacuum system (Ottobock, Duderstadt, Germany). This device is designed to maintain the pressure of a lower-limb socket at a specific level; when the pressure rises above a threshold (measured to be -42 kPa) the pump activates until the pressure is restored (-62 kPa).

Table 7.13 Elevated vacuum pressures tested in lower-limb studies.

Author(s)	Year	Elevated vacuum pressures tested [kPa]
Board et. al [114]	2001	-78
Street [115]	2006	-78
Gerschutz [112, 113]	2010	-27 to -51
Komolafe et. al [111]	2013	-58
Gerschutz [119]	Not provided	-27 to -68

Negative Pressure Wound Therapy (NPWT) involves placing a wound under vacuum pressure with the goal to promote healing. Typical vacuum pressures range from -6 to -27 kPa [120, 121]. In the 1960s, a team of researchers studied suctions of 1 cm diameter applied at various pressures to their lower lateral abdominal skin, ranging from -13 to -95 kPa. Observations included measuring time to blistering of skin on the abdomen of five participants [122]. At -27 kPa, the average time to blistering was 55 ± 15 minutes. It is worth noting that the experimental test setup differs from the case of a hole within a socket, as areas of vacuum and free tissue are reversed, so this may not directly transfer to tactor integration.

The lower limit of vacuum pressures in elevated lower-limb sockets is -27 kPa, and this is also the upper limit for NPWT. Higher vacuum pressures should not be used, as this caused blistering in a test of vacuum pressures applied to small areas of the skin. Therefore this pressure was used as a conservative estimate for subsequent testing; if the membranes are sufficient at -27 kPa they should be sufficient for typical suction attachments in the upper limb.

The pressures mentioned up to this point have been listed as gauge pressures (i.e. relative to atmospheric pressure). For reporting purposes, pressures will be reported as absolute pressure. The atmospheric pressure (p) in Edmonton is:

$$p \approx p_o \left(1 - \frac{gh}{c_p T_0}\right)^{\frac{c_p M}{R}} = 101.3169 \text{ KPa} \approx 101.3 \text{ KPa}$$

Where p_0 is the atmospheric pressure at sea level (101.325 kPa), g is the acceleration due to gravity (9.80665 m/s^2), h is the altitude of Edmonton (671 m), c_p is the constant pressure specific heat capacity of dry air (1007 J/kg·K), T_0 is the standard temperature at sea level (288.15 K), M is the molar mass of dry air (0.0289665 m/s^2) and R is the universal gas constant (8.31447 J/mol·K).

The calculated pressure of 101.3 kPa is close to the pressure of 101.5 kPa measured by the University of Alberta's Department of Earth & Atmospheric Science on the day that initial testing was conducted [123]. Therefore the actual testing pressure must be as low as 74.3 kPa. For simplicity, a gauge pressure of -30 kPa was applied, or an absolute pressure of 71.3 kPa.

7.4.1.2 Nervous System Adaption

It is important to maintain sensitivity of the skin to applied tactor forces, and with the potential to cover the skin with a membrane, it is necessary to understand how the nerves in the skin function and adapt. Adaption involves a reduced sensitivity to a constant stimulus, and is characteristic of fast-adapting receptors. Meissner corpuscles are responsible for fine touch and pressure as well as low frequency vibration, and adapt within one second of contact. Pacinian corpuscles are sensitive to deep pressure, and are also fast-acting [99]. Therefore the activity of both of these receptors should not be reduced by a membrane that is in contact with and stationary relative to the skin. However, Merkel discs which sense fine touch and pressure and Ruffini corpuscles which sense pressure and distortion of the skin are both tonic receptors, meaning they do not adapt to a constant stimulus. In this case, adaption occurs through peripheral adaption (within the peripheral nervous system, PNS) and central adaption (within the central nervous system, CNS), and is the reason that one typically does not pay conscious attention to the sensation of their clothing unless it is moving relative to the skin [99].

Based on the adaption of some of the key receptors involved in sensation as well as the adaption of the CNS and PNS, a stationary membrane covering the skin is not expected to reduce sensitivity to applied tactor forces noticeably, as the body will adapt to the continuous contact of the membrane.

7.4.1.3 Membrane Response

A consideration in using rubber materials is the *Mullins effect*, where large strains applied to the material result in large hysteresis loops and stress softening over time. The stress drop is typically larger during the first few cycles, and becomes negligible after approximately 10 cycles. Some of the deformation can be permanent, although much of it can be recovered over time, depending on the elongation and material properties. Recovery is enhanced at high temperatures (such as 100°C) but does not typically occur at room temperature [124].

7.4.2 Previous Development[10]

A membrane placed over the tactor head was hypothesized previously to ensure an airtight seal could be maintained (Figure 7.5). Repetitive testing demonstrated that a smooth surface helps to reduce wear over time, but further material and geometry testing was required.

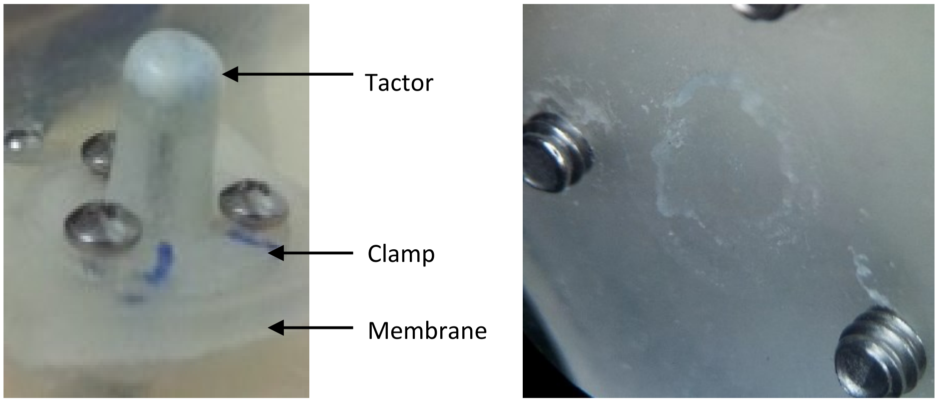

(a) (b)

Figure 7.5 Image of of (a) tactor extended through membrane, and (b) wear on membrane

---

[10] This preliminary membrane testing was conducted by Kent Herrick during a summer work term

7.4.3 Membrane Selection

Several prosthetic liner materials were tested, including a thermoplastic elastomer, a silicone gel, and a silicone elastomer (Table 2). Silicone elastomers are highly cross-linked and contain little free polydimethylsiloxane (PDMS), where silicone gels are lightly cross-linked and swollen with PDMS (allowing it to bleed out of the gel). Stiffness of the silicone liners is documented as being linear, where the gel has lower stiffness than the elastomer, and stiffness are comparable when the fabric backing is removed [125]. Data about the thermoplastic elastomer has not been specified in the data sheet [126].

Table 7.14 Material data of liners tested

Liner	Location	Classification	Thickness	Stiffness (kPa)
Alpha Liner [126]	Willow Wood: Mt. Sterling, Ohio	Thermoplastic elastomer	2.15	Unspecified
SiloLiner [125]	Silipos: New York, New York	Silicone gel	3.0	41
Iceross [125]	Ossur USA.: Columbia, Maryland	Silicone elastomer	4.0	195

Additional materials were investigated, all within the rubber and polyurethane families (Table 7.15). Rubber is often used for sealing applications, is strong, stretches, and tends to bounce back to its original shape. Polyurethane acts similar to rubber, with improved tear and abrasion resistance [127].

Table 7.15 Material properties, determined using McMaster Carr and Matweb [127, 128].

Possible Materials	Cost* (\$/ft^{2})	Thickness (mm)	Durometer Hardness	Ultimate tensile strength (MPa)	Elongation at break (%)	Service temperature (°C)	Possible Allergen
Polyurethane	76	1.0	40 OO (extra soft)	0.7	40 - 950	-29 to 71	Uncommon
	76	1.0	50 OO (soft)	0.8			
Buna-N (nitrile)	4**	0.10	40A (medium soft)	10.3	400 - 600	-29 to 93	Uncommon
	4**	0.18					
Latex	2	0.15	40A (medium soft)	26.5	~1000	-34 to 70	Possible
	2	0.25					
	3	0.36					
Silicone	17	0.79	10A (soft)	1.4	5 - 4460	-29 to 82	Uncommon
EPDM	9	0.79	40A (medium soft)	5.5	~600	-40 to 104	Uncommon
Neoprene	6	0.79	30A (soft)	6.9	100 - 800	-29 to 93	Possible

* Normalized

** Cut from nitrile gloves, so cost is approximated assuming 3”x3” piece can be obtained per glove

The EPDM and Neoprene were removed from consideration as they were too thick and stiff. The following materials were therefore evaluated: Alpha liner, Siloliner, and Iceross (very compliant, stretchy, seems to return to original shape, somewhat tacky so may collect dust, but may also help with sealing), polyurethane and silicone (similar properties to liners, though thinner overall), and latex and nitrile (very compliant, thin, and stretchy). Finally, a thin layer (0.6 mm) of Ninja Flex 3D printable material (Fenner Drives, Inc.) was tested. While not as flexible as other materials, it can be printed in various shapes such as the bellows seal.

7.4.4 Membrane Evaluation

7.4.4.1 Stationary Testing

Stationary testing incorporated a cap to seal the membrane in place (Figure 7.6). The membrane was sealed on top of the lid around its edges with a nitrile O-ring, and the screws were sealed on the bottom of the lid with miniature attached O-rings. A plastic insert was placed over the sharp metal edge to prevent tearing of the membranes, and better represent the contact that would occur when mounted to a socket.

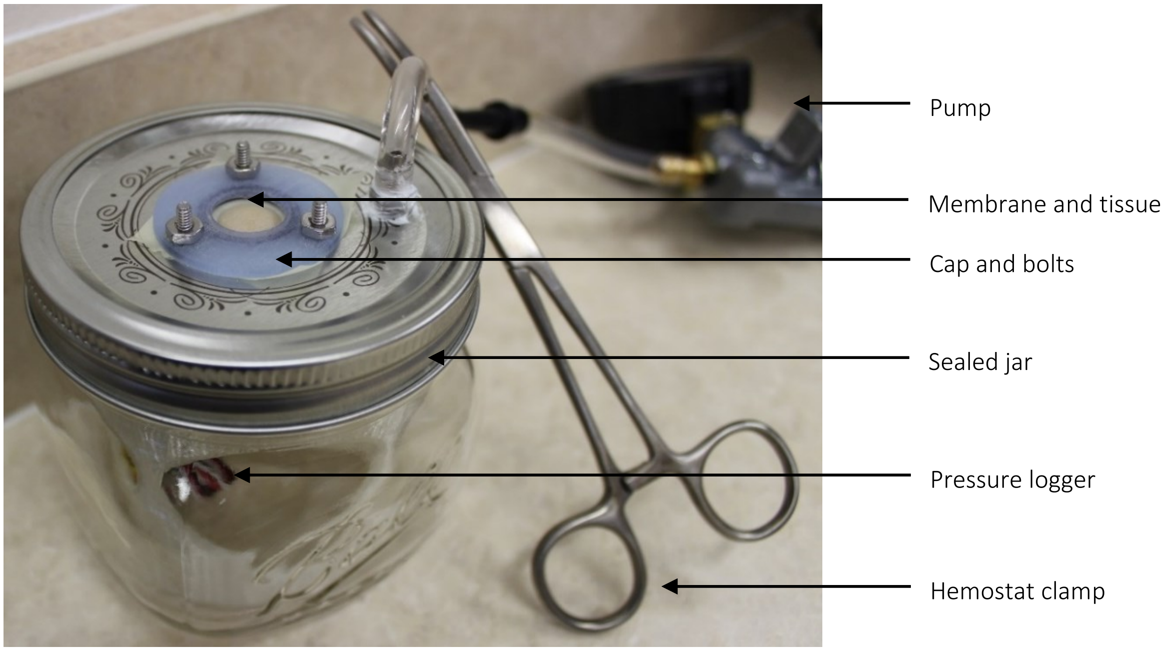

Figure 7.6 Stationary test set-up

The stationary membrane tests involved two stages of evaluation. First was an empty chamber test where membranes were loaded to -60 kPa gauge, or until failure, while the jar was empty.

Next was a tissue support test, where membranes were loaded to -30 kPa gauge and pressure maintained for one hour, or until failure. Tissue was supported with a PLA spacer and a layer of foam covered with alpha liner to simulate the compliance of fatty tissue and skin (Figure 7.7). There was a 5 mm gap between the alpha liner and the membrane to simulate a worst case scenario where the residual limb is offset from the socket.

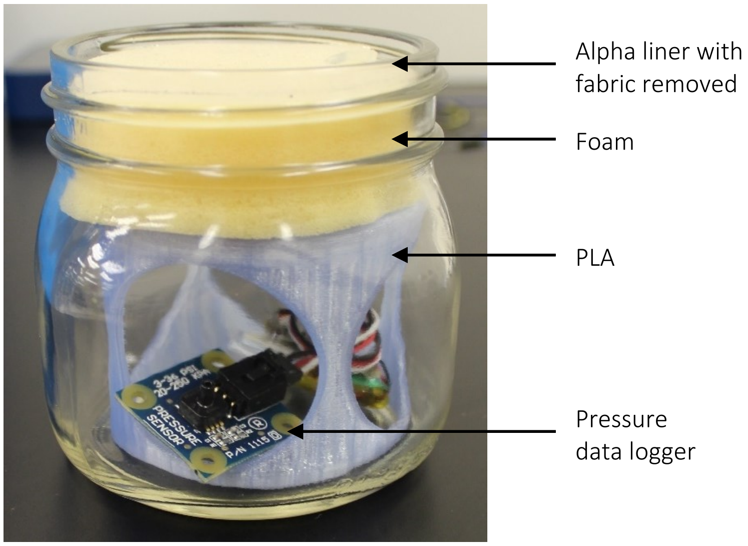

Figure 7.7 Tissue support materials.

During the stationary membrane tests, membranes failed at various pressures and times under constant pressure (Table 7.16). An optimal membrane would fail above the cut-off pressure of -27 kPa and would not fail during the constant pressure testing period (Figure 7.8).

Table 7.16 Pressure at failure at (relatively) consistent loading rate and time to failure at -30 kPa gauge

Membrane	Thickness (mm)	Empty chamber pressure at vacuum loss (gauge, kPa)	Tissue support time to vacuum loss (s)
Alpha Liner	2.15	-8*	234
SiloLiner	3.0	-24*	346
Iceross	4.0	-54*	>3600
Polyurethane (40)	1.0	-36	>3600
Polyurethane (50)	1.0	<-60*	>3600
Silicone	0.8	-49	>3600
Latex	0.15	-25*	697
	0.25	-50	>3600
	0.36	<-60	>3600
Nitrile	0.10	<-60*	>3600
	0.18	<-60	>3600
Ninja Flex	0.6	N/A	0

*Expanded significantly

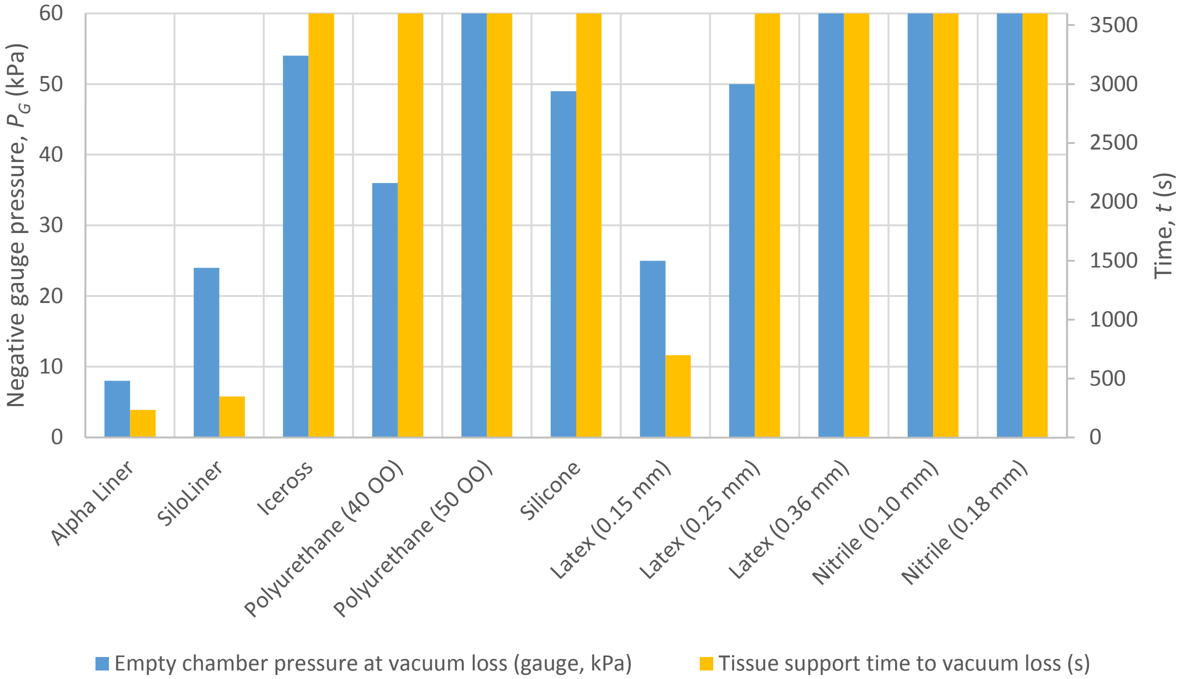

Figure 7.8 Pressure at failure at (relatively) consistent loading rate and time to failure at -30 kPa gauge

An example of the pressure data is shown for the silicone testing which failed at -49 kPa gauge, giving a safety factor of 1.8 (Figure 7.9).

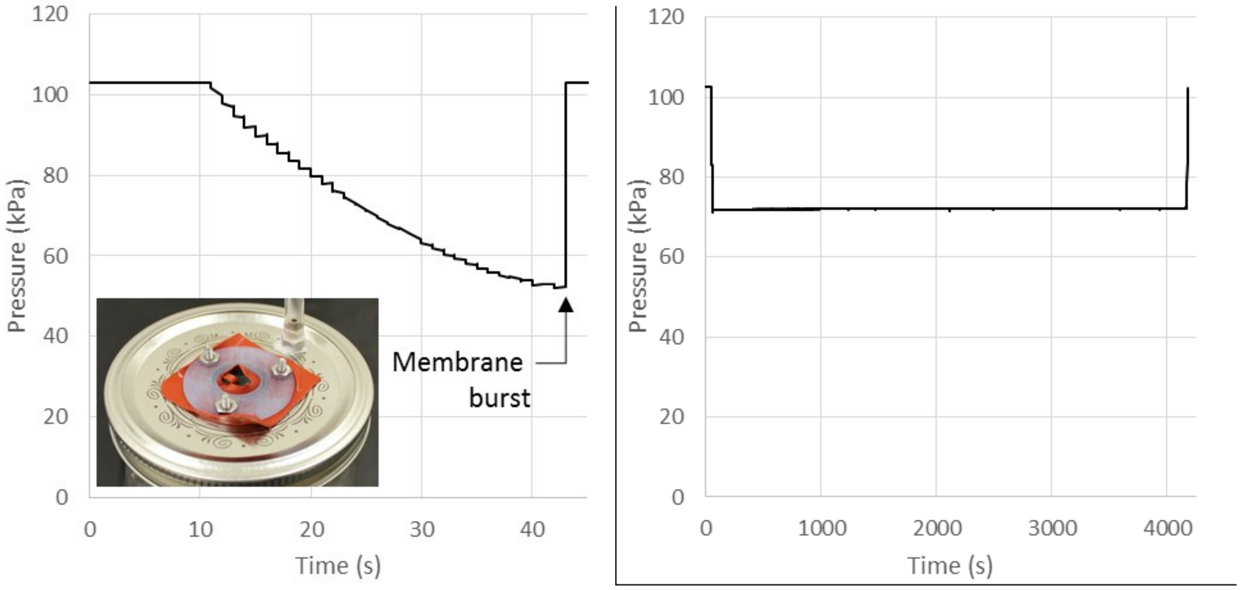

(a) (b)

Figure 7.9 Silicone test data collected (a) increasing pressure until bursting, and (b) with tissue support

7.4.4.2 Force Profiling

After eliminating several membranes based on the stationary membrane tests, the remaining membranes were evaluated for their force properties under loading.

Each membrane is a different thickness and stiffness. An ideal membrane would not require much force to press through, so that the membrane does not reduce the maximum force output or significantly change the calibration of the tactor. Each membrane was tested using the linear tactor modified to be in series with a load cell (accuracy ± 0.02 N) with open-loop control allowing displacement to be set.

Membranes were loaded without support to a maximum set displacement of 600 µs (corresponding to an unloaded displacement of 17 mm), at atmospheric pressure (Figure 7.10). Loads were applied in the upwards and downwards directions three times and force recorded at each 2 mm step (Table 7.17). Actual displacement was measured at the end of the third loading cycle using calipers.

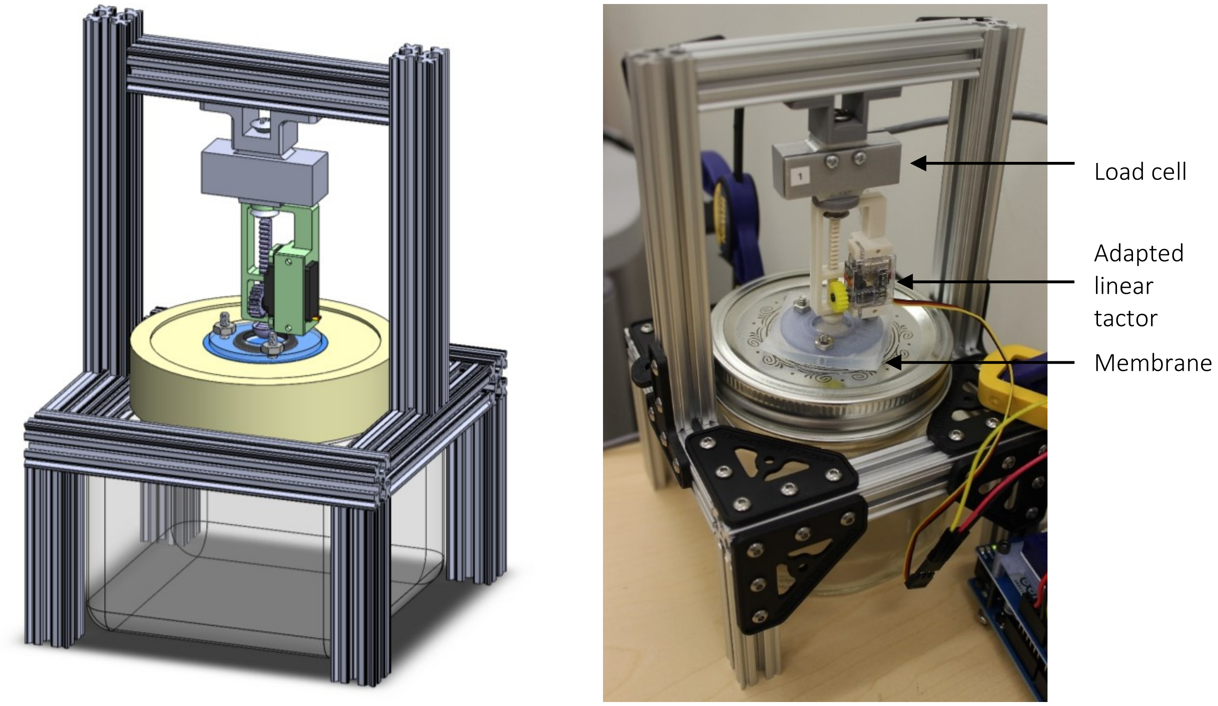

(a) (b)

Figure 7.10 Force profiling test set-up, (a) modeled, and (b) physical

Table 7.17 Measured force and displacement at maximum set displacement (600 µs)

Membrane	Thickness (mm)	Force applied at maximum set displacement (N)	Measured displacement (mm)	Force/displacement (N/mm)
Iceross	4.0	5.8	15.5	0.35
Polyurethane (40)	1.0	6.7	16.5	0.54
Polyurethane (50)	1.0	5.7	16.5	0.48
Silicone	0.8	4.4	16.5	0.32
Latex	0.25	6.4	16.5	0.55
	0.36	8.7	16.5	0.74
Nitrile	0.10	3.8	16.5	0.34
	0.18	4.8	16.5	0.43

An optimal membrane would require little force to displace to the maximum displacement (Figure 7.11).

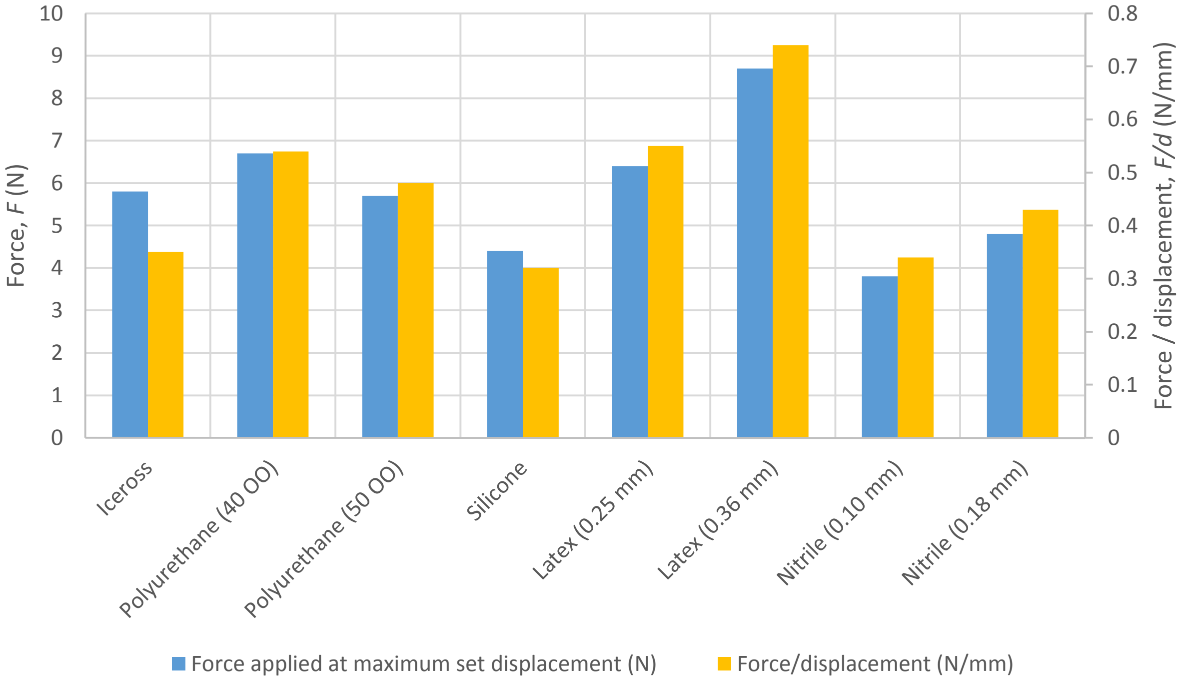

Figure 7.11 Measured force and displacement at maximum set displacement (600 µs)

Silicone and nitrile required the least force to displace, however the graphs of their loading characteristics show some evidence of permanent deformation over the three cycles tested (Figure 7.12). It was therefore important to confirm that they could maintain a seal over repeated loading cycles.

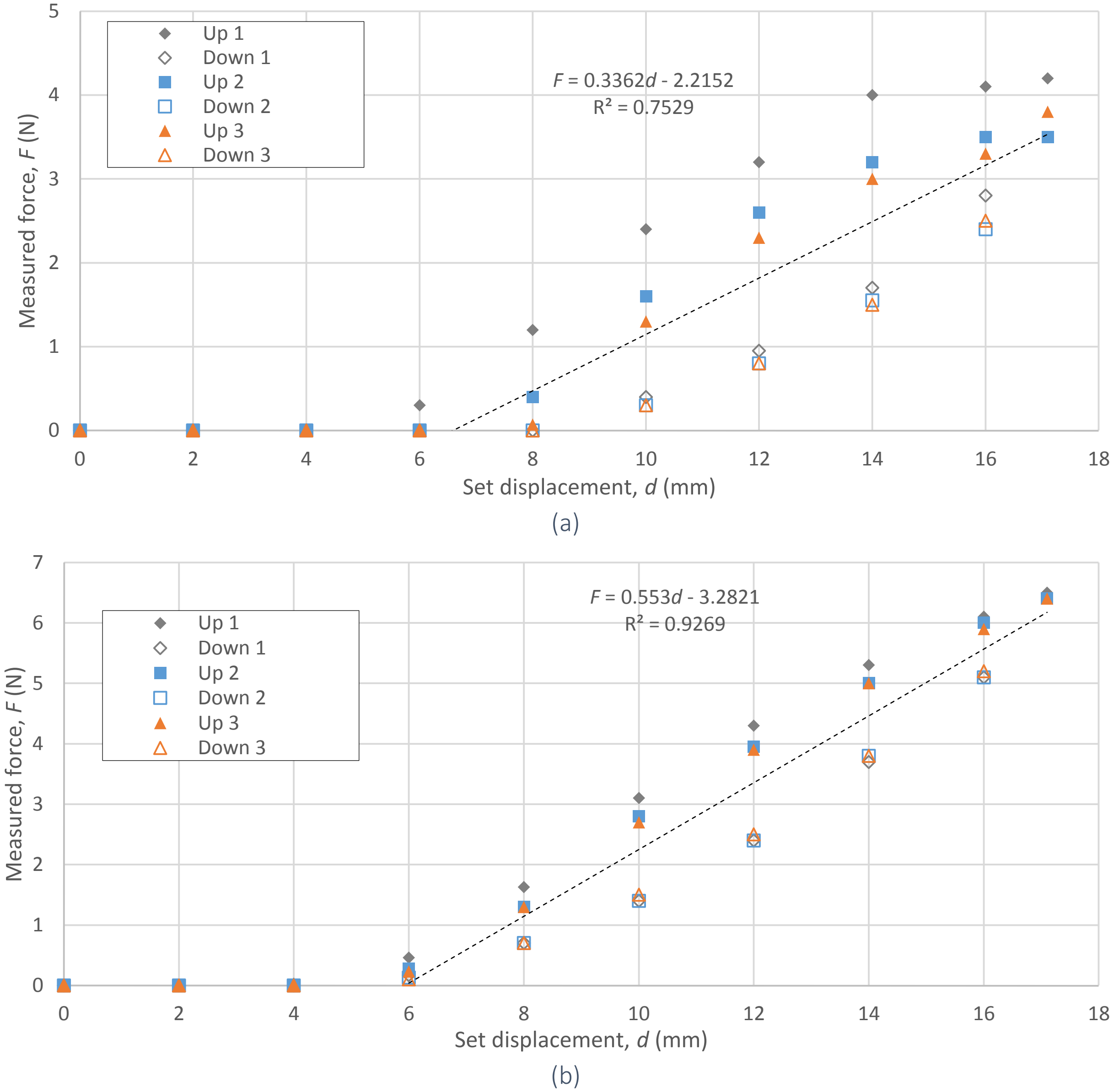

Figure 7.12 Force profiling of (a) nitrile (0.10 mm), showing possible stretching over time, and (b) latex (0.25 mm thick), showing limited stretching over time

7.4.5 Shaped Membrane Evaluation

7.4.5.1 Membrane Shaping

Based on the force profiling, it was found that flat membranes require a significant amount of force to deform (Figure 7.13 (a)), so alternate methods to reduce the elongation of the membrane were developed. Two options were determined; a larger diameter membrane (Figure 7.13 (b)) or a pre-shaped membrane (Figure 7.13 (c)) requiring less elongation.

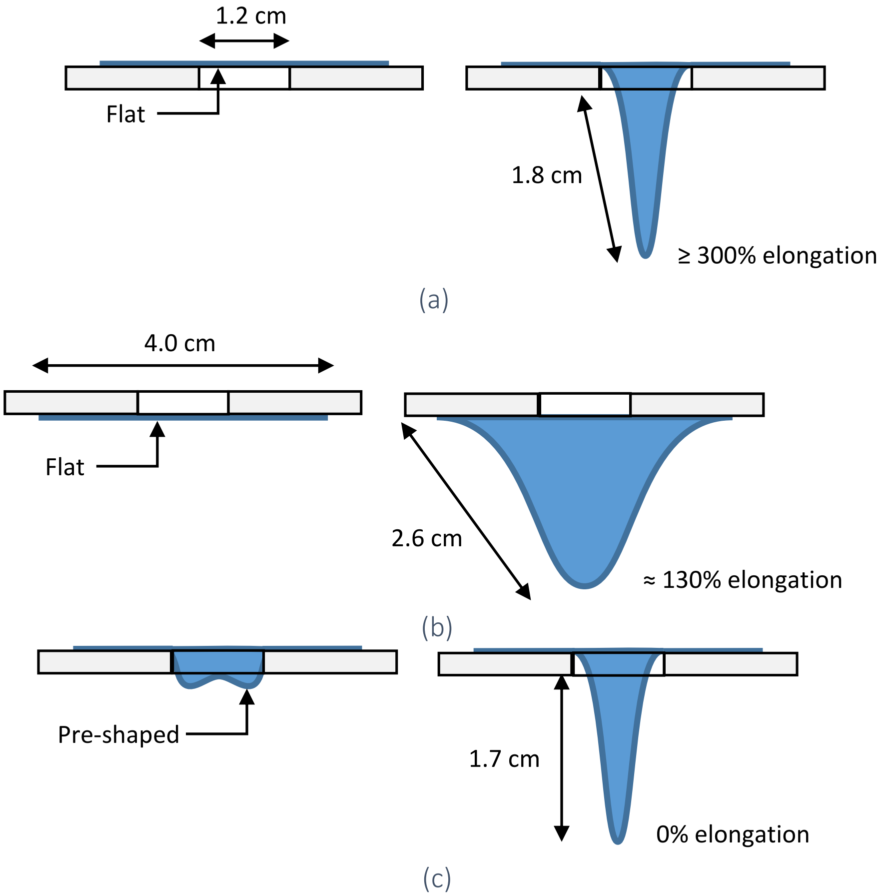

Figure 7.13 Membrane shapes (a) flat, (b) large diameter, and (c) pre-shaped

A shaped nitrile seal was manufactured using the pinky of a nitrile glove, as it is already contoured (Figure 7.14). The nitrile fingertip was wrapped and glued around the O-ring so that it protruded from the base of the socket. The length of the protrusion was dictated by the maximum displacement required of the tactor.

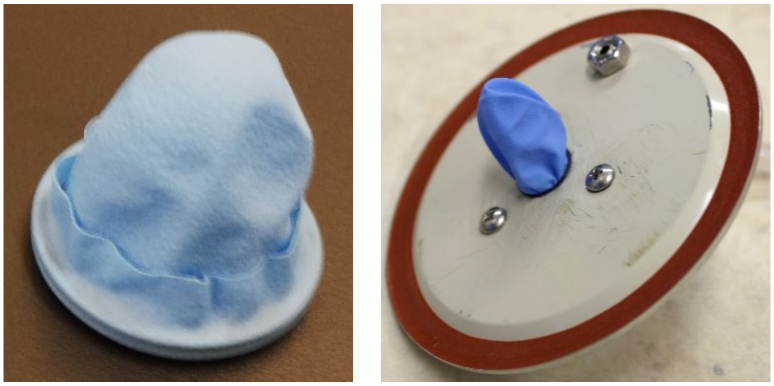

(a) (b)

Figure 7.14 Nitrile finger (a) insert, and (b) bottom view of attachment

Finally, the tactor head was attached outside of the membrane so that it could directly contact the skin (Figure 7.15).

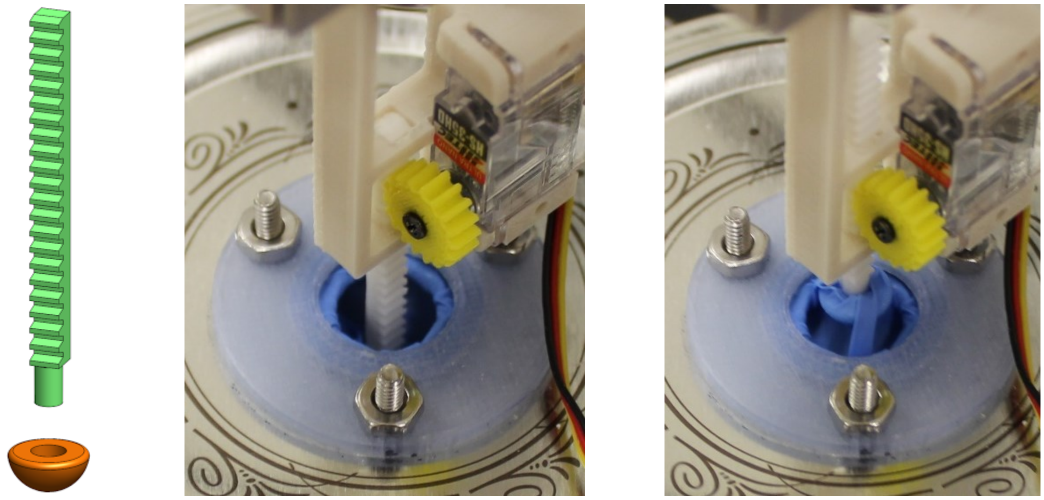
(a) (b) (c)

Figure 7.15 Tactor through membrane (a) model, (b) prototype at bottom of throw, and (c) top of throw

An attempt was made to shape the silicone material, however more sophisticated manufacturing techniques are needed (Appendix R).

7.4.5.2 Dynamic Testing

The remaining membranes were evaluated for their response to continuous cyclical loading under vacuum.

7.4.5.2.1 Initial Testing

Membranes were loaded cyclically between 0 and the maximum set displacement of 17 mm with a period of 5 s for a duration of one hour (720 cycles total), using the tissue support set-up discussed previously, at -30 kPa gauge pressure. Pressure was logged with the data logger and force recorded with the load cell through Simulink Realtime.

The flat silicone membrane demonstrated a slow leak, as the pressure returned to atmospheric over the duration of the test (Figure 7.16 (a)). Of the through tactor membranes manufactured, two out of three did not seal from the beginning, suggesting that this method was not reliable. The third tactor was found to leak after 45 minutes of testing. Additionally, the tactor required a negative force to retract from the skin, which would be detrimental to closed-loop control (Figure

7.16 (b)). Both the flat and shaped nitrile membranes were able to withstand initial loading tests for the full hour duration.

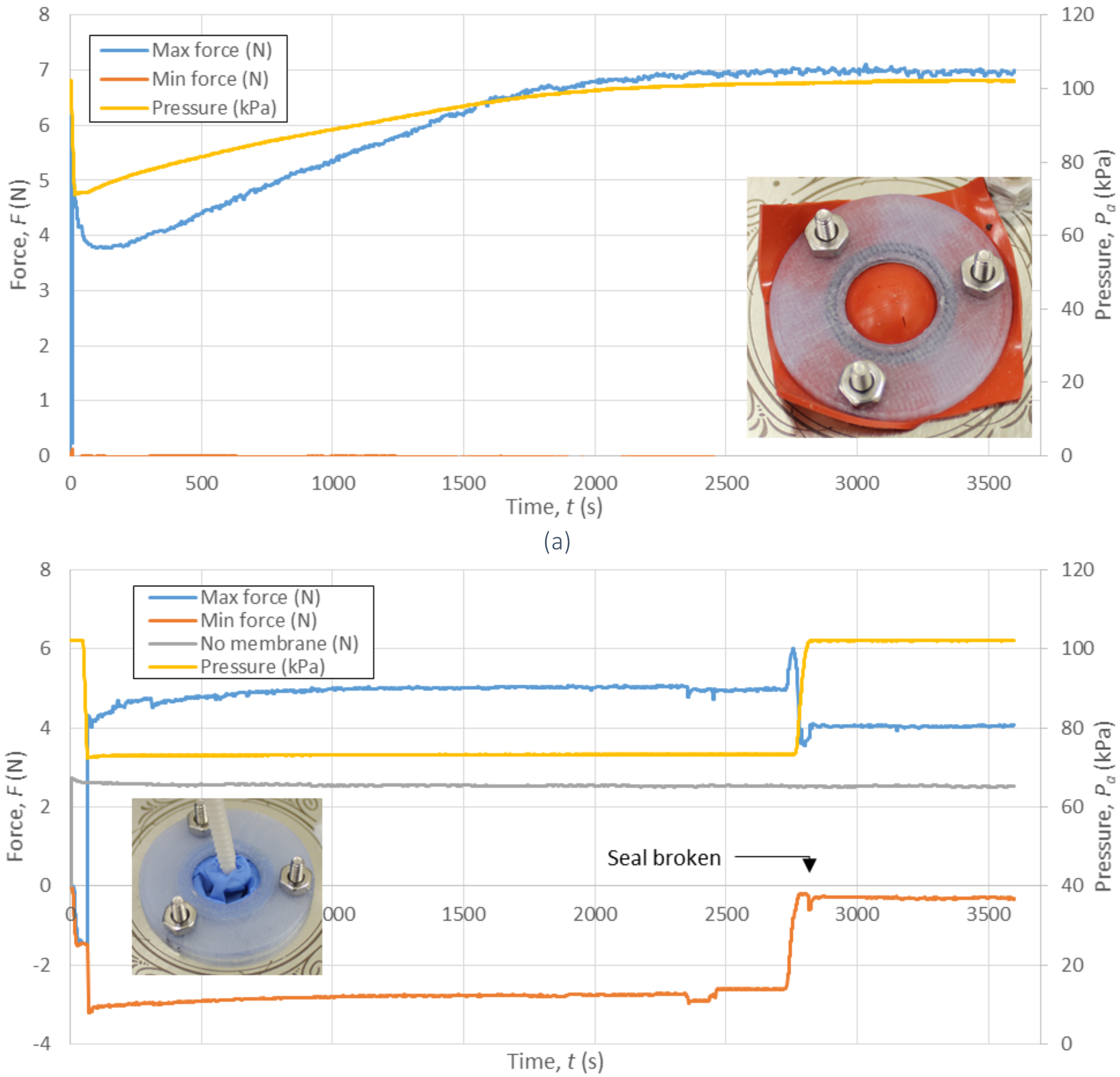

(a)

(b)

Figure 7.16 Response over time of (a) silicone flat membrane showing slow loss of pressure, and (b) nitrile with through tactor, showing sudden loss of pressure and negative force required to retract tactor

7.4.5.2.2 Final Testing

Membranes were loaded cyclically between 0 and a set displacement of 17 mm with a period of 5 s for a total duration of 10 minutes (120 cycles total), at -30 kPa gauge pressure. Pressure was logged with the data logger, and force recorded with the load cell through Simulink Realtime.

The set-up was modified to more accurately mimic realistic conditions. It was determined that over time, the tissue analog in the previous set-up would slowly deform around the tactor, likely due to its porous nature. Realistically, the vacuum should only be applied to the small gap between the tissue and the socket (not to the tissue itself), so the set-up was modified to include an added layer of liner (Alps-SFR38-3HP, OrtoPed) between the tissue and lid (sealed at the edge of the jar lid) in order to isolate the tissue from the vacuum. It was verified that the pressure on the tissue remained at atmospheric levels while the tests were conducted. The pressure data logger was placed in a second jar and connected with a three-way open valve to the pump.

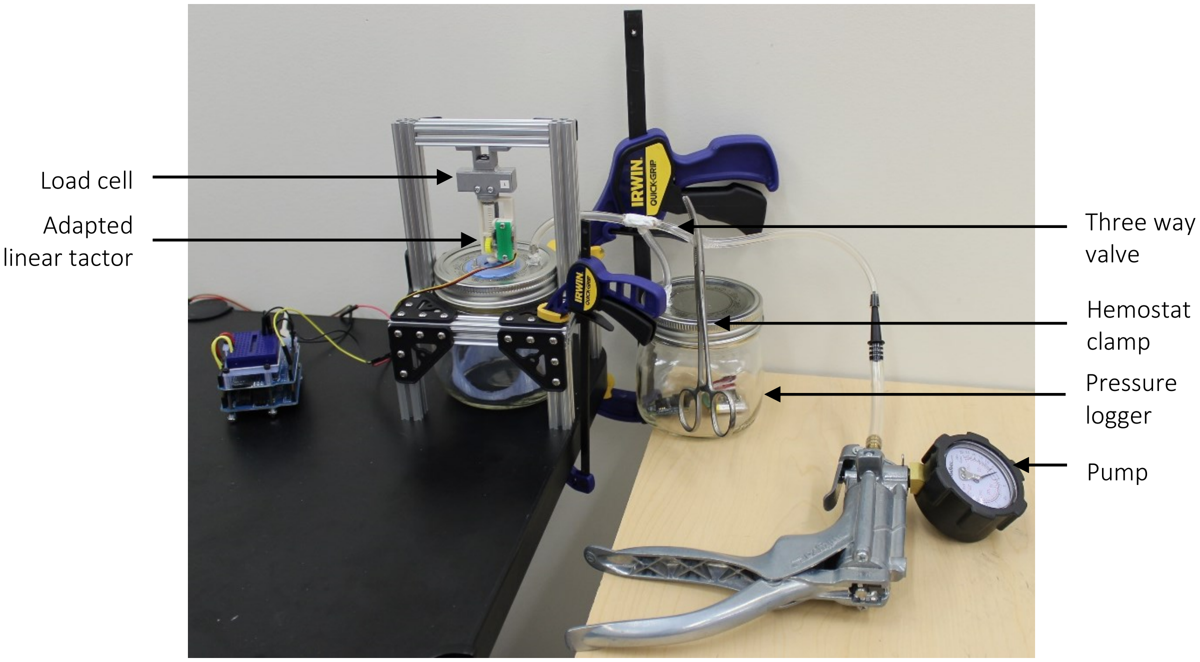

Figure 7.17 Loading membrane test set-up with tissue excluded from vacuum pressures.

Results for each membrane configuration is shown below. Note that repeatability of the set-up was confirmed by testing an identical set-up five times, disassembling between tests, and comparing the average maximum force applied over ten cycles. Repeatability was found to be ± 0.3 N, and was deemed acceptable.

In all cases, adding the membrane increased the force required to reach the same set displacement, although by varying amounts.

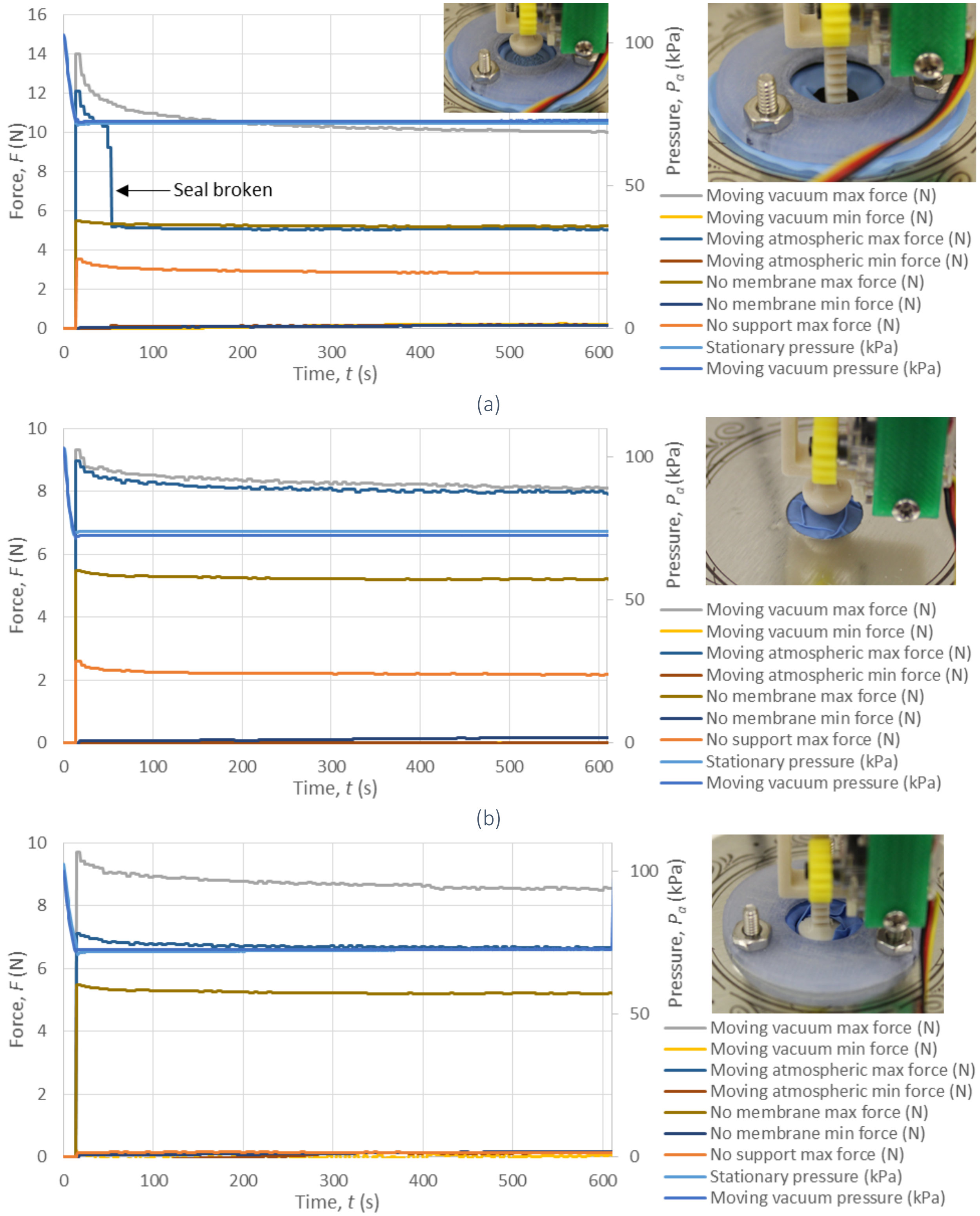

(a)

(b)

(c)

Figure 7.18 General loading response over time for (a) clamped flat nitrile, showing large increase in force with membrane use, (b) glued large flat nitrile, showing increase in force with membrane use, and (c) shaped nitrile, showing little increase in force with membrane use

The clamped 12 mm diameter flat nitrile membrane was able to maintain an airtight seal for the duration of a single test, however upon further testing the membrane burst, so this method is deemed unacceptable (Figure 7.18 (a)). In addition, adding the membrane and vacuum increased the maximum force applied substantially (~ 5 N).

The glued 40 mm diameter flat membrane was able to maintain an airtight seal during all tests (Figure 7.18 (b)). The addition of the membrane at atmospheric pressure did not increase the maximum applied force as substantially as the smaller diameter membrane (~ 3 N), meaning less power would be required to reach the same displacement. Adding a vacuum to the system did not greatly increase the maximum force (~ 0.2 N), likely because the change in pressure did not change the geometry of the membrane substantially.

The shaped nitrile was able to maintain an airtight seal during all tests (Figure 7.18 (c)). The addition of the membrane at atmospheric pressure did not increase the maximum applied force as substantially as other membrane configurations (~1.5 N), meaning less power would be required to reach the same displacement. Adding a vacuum to the system however did increase the maximum force (~2 N), likely because the membrane bunches together under vacuum so that it must stretch rather than deform as intended.

Observing the specific loading response (Figure 7.19) it is shown that the small flat clamped membrane requires higher force to reach the same displacement, while the shaped and large flat membranes are similar. The shaped membrane has a slightly negative force at the base of extension, likely because the membrane is slightly wrapped around the tactor head, pulling it downwards. This may complicate closed-loop control.

Based on these results, the glued large flat membrane is selected as the optimal membrane configuration, however if open-loop control is being used or if the large membrane interferes with other socket components the shaped membrane can be substituted.

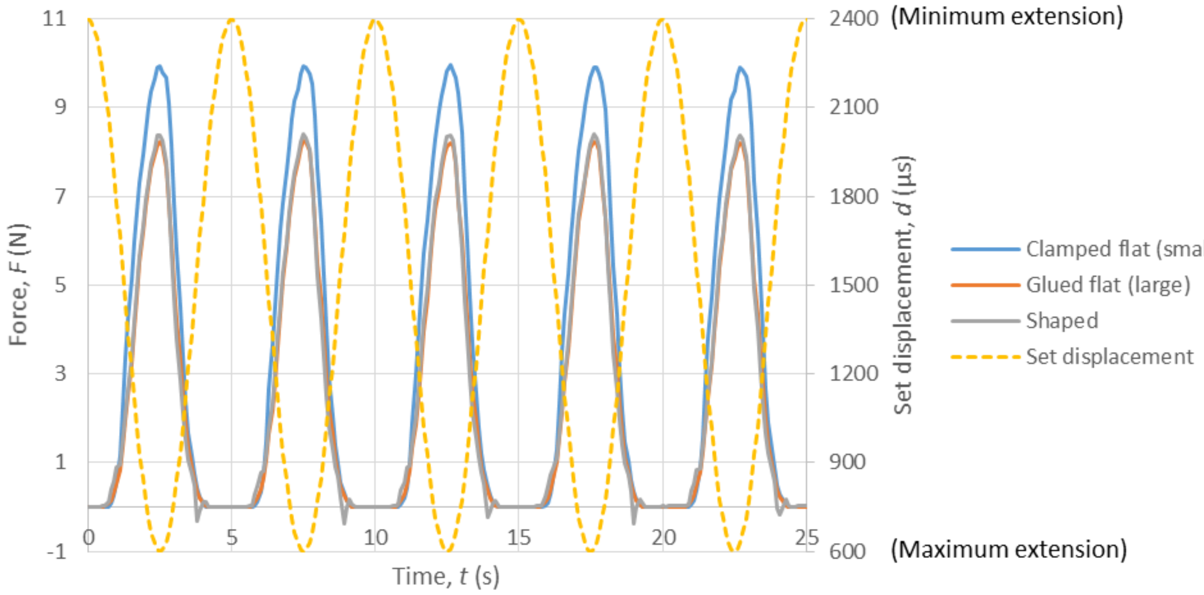

Figure 7.19 Loading response at plateau under vacuum for each membrane

7.4.6 Long Term Evaluation

The large flat membrane was loaded cyclically between 0 and a set displacement of 17 mm with a period of 10 s for a total duration of 7 hours (2520 cycles total), at -30 kPa gauge pressure, using the modified tissue support set-up discussed previously (Section 7.4.5.2.2). Pressure was logged with the data logger, and force recorded with the load cell through Simulink Realtime.

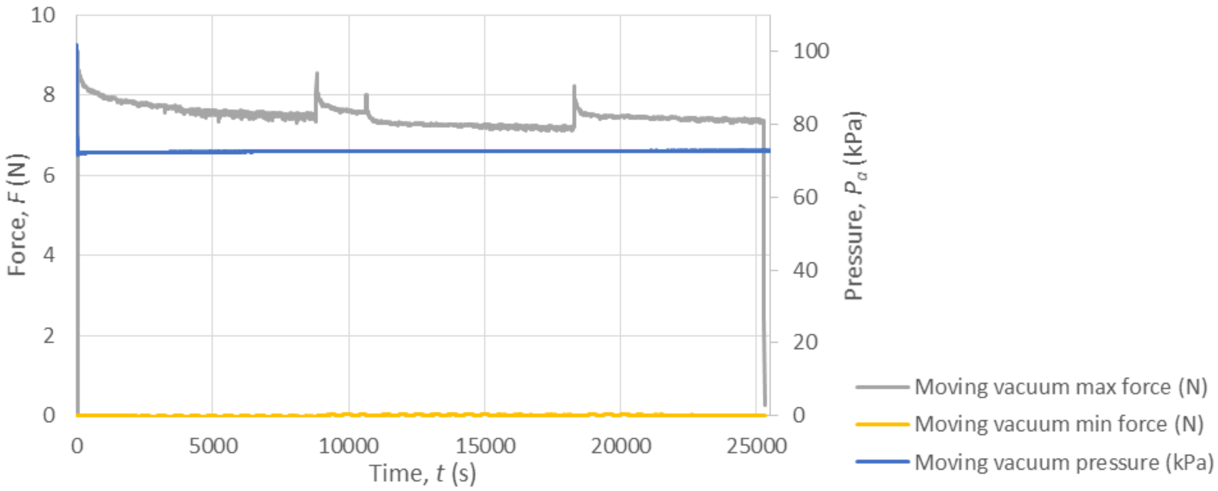

Figure 7.20 General loading response over time for long therm test, glued large flat membrane

Note that over time the tactor periodically stopped moving and needed to be restarted, likely due to overheating as it was being loaded cyclically to a high force continuously; this is the reason for the spikes in the graph as the test was restarted. Overall the system showed a loss of pressure of only 0.8 kPa and membrane force response properties did not change substantially. Therefore this sealing method is considered sufficient and should be tested further within an actual socket under more realistic loading cases.

7.5 Conclusions and Future Work

Based on the analysis, nitrile is the ideal material for sealing of the tactor system. It is inexpensive, readily available, and is not a common allergenic material. A large flat membrane glued to the inside of the socket is optimal, where a 40 mm diameter is sufficient.

The addition of a vacuum does not substantially change the force response, therefore calibration at atmospheric pressure will be acceptable and resulting force curves would not be dependent on the variable vacuum pressure in the socket. Gluing the membrane directly to the inside of the socket requires less components than other attachment methods tested, however it is more permanent so is not very easy to replace if damaged. For this reason it is recommended that a thin reinforcement material be attached over the edges of the membrane to prevent shear forces from tearing the membrane. This could be accomplished using a thin ring shaped component such as ShearBan (Tamarack Habilitation Technologies Inc.) (Figure 7.21).

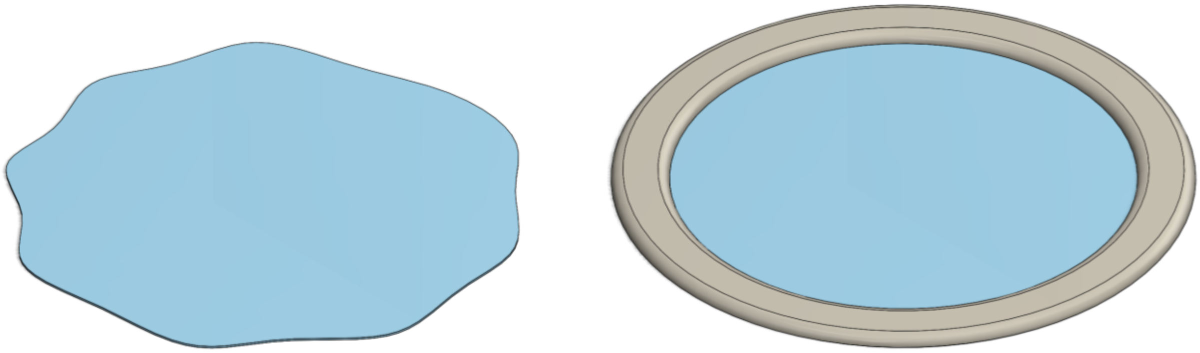
(a) (b)

Figure 7.21 Large membrane (a) uncovered, and (b) flexible material covering edge

Further testing may be conducted to determine the relationship between membrane diameter and additional force requirements, although curvature of the socket would also need to be considered. Finally, further testing is required to determine the durability and comfort of this method through trials on an actual prosthetic socket.

Chapter 8. Conclusion

Myoelectric prostheses are becoming increasingly complex and dexterous. However these devices are currently lacking a means of providing sensory feedback to the user. The goal of including sensory feedback in these robotic arms is to improve their control and overall acceptance. To date, no sensory feedback systems for upper-limb prosthetic devices are available commercially or clinically.

The main objective of this thesis was to develop a tactile sensory feedback system for use by upper-limb amputees, and address specific aspects of the design that have traditionally been barriers to clinical translation. This document outlines the rationale behind selecting a mechanotactile tactor, improvements to existing designs, bench-top testing, and evaluation of the integrated prosthetic sensory feedback system with a single above-elbow amputee participant. A summary of the findings and contributions is presented below.

In literature, a large range of tactor head shapes and sizes have been used with little justification. To address this shortcoming, an optimization study was conducted to determine optimal tactor head geometry and diameter in regards to improving two-point discrimination and comfort. Ten participants were recruited; eight able-bodied and two with trans-humeral amputations. Response parameters were shown to change over time, by participant, and by location on the arm. The study demonstrated that the optimal tactor head shape should be domed (8 or 12 mm) or triangular (12 mm), and that spacing between tactors may be determined using a standard clinical two-point discrimination device and adding a factor of 5 mm. These results will be useful for clinicians and prosthetists in locating tactors on the arm for clinical translation.

Several different mechanotactile tactors have been detailed in the literature, yet the designs are either bulky, move non-linearly, or are expensive. Initial prototypes of a linear and cable-driven tactor were developed by the BLINC lab, where the cable-driven tactor allows the bulky motor to be distanced from the tactor head to conserve space on the residual limb. These tactors were manufactured using 3D printing techniques and off-the-shelf components, and are therefore inexpensive and simple to translate to other institutions. This thesis work focused on evaluating and improving these designs through various bench-top tests. Improvements include implementing additional safety constraints, mitigating temperature rise, investigating alternative motor options, evaluating friction in the cable-driven tactor, and quantifying capabilities of the tactors. Both the linear and cable-driven tactor systems met the majority of the design requirements; however there is a need for information from usability trials to collect usage data for the tactors and refine the design specifications. Recommendations for improvements have been provided, which may include using a different material for the housing and gears to improve durability, implementing further methods to dissipate temperature from the motor, and integrating a stronger yet bulkier motor into the cable-driven tactor to overcome the additional friction introduced by the Bowden cable.

The tactor system was implemented onto both a rigid tactor cuff as well as a temporary prosthetic socket. The rigid tactor cuff will allow future usability testing to be conducted with able-bodied participants. The temporary prosthetic socket was used to conduct a preliminary evaluation of the system with an above-elbow amputee participant. This testing revealed that distinguishing between two tactors was no trouble, and that placing a tactor as close as 2 cm from an EMG sensor does not degrade signal magnitude or device control, within the ranges tested. More importantly, the testing highlighted the need for improvements to several aspects of the integration. Namely, better measurement and control of the forces applied by the tactor should be investigated (Chapter 6) and sealing of the socket to improve attachment to the arm is required (Chapter 7). As well, distinguishing between different object stiffnesses was shown to be difficult when using a commercial prosthesis; tactile feedback is not sufficient, as an understanding of hand position or closing speed is also needed. Despite these limitations, the participant expressed a strong desire for the system to be integrated into his everyday prosthesis, a testament to the importance of providing sensory feedback.

From the literature, several different sensors have been investigated for measuring forces in prosthetic systems, all with various drawbacks. Control of tactor movement differs across systems, with some being open-loop (where force on the terminal device is mapped to displacement of the tactor) and others closed-loop (mapped to force measured on the residual limb). An attempt was made to implement closed-loop control using inexpensive off-the-shelf sensors into both the linear and cable-driven tactor systems. Several different sensors were investigated, including a potentiometer, a current sensor, and a force sensitive resistor (FSR). The FSR was selected as it demonstrated the greatest accuracy and least hysteresis. Several filters were investigated to reduce noise in the recorded signals, and a Chebyshev Type II filter was selected. Open- and closed-loop control were evaluated in terms of time delay and accuracy. Open-loop systems were found to respond faster (up to 0.2 s for the linear tactor, 0.3 s for the cable-driven tactor), but could not adapt to changes in compliance or positioning (error up to 5 N when system displaced by 5 mm). Closed-loop systems using proportional, integral, derivative (PID) control responded slower (up to 0.5 s) but provided higher accuracy under changing conditions (up to 2 N, but generally less than 1 N). Adding a cable to the system did not substantially impact the overall time delay but did introduce hysteresis to the system and a deadband of 1 N, meaning that force below this cannot be applied reliably, likely due to the friction in the cabling system. Recommendations for reducing the time delay include reducing filtering, increasing the rate of position commands sent to the servo motor, or using a different method of control. Improving accuracy would require a more accurate sensor, and the effects of the friction in the cabling could be eliminated by integrating the sensor onto the tactor head. There do not appear to be off-the-shelf sensors that meet the size and accuracy requirements of this system, so custom sensors may need to be further investigated.

The final study involved investigating methods of tactor integration without compromising the suction seal between the residual limb and socket. This integration challenge has been largely overlooked in literature and limits the applicability of tactors across all types of socket attachment. Bench top testing was conducted to investigate different membrane responses under vacuum pressure in regards to material selection and geometry specification. A flat nitrile membrane of 40 mm diameter was selected as the optimal design, however future investigation of how this method performs within an actual prosthetic socket is required.

In summary, an inexpensive and practical mechanotactile sensory feedback system has been designed and integrated onto the socket of a temporary prosthesis. While there are many improvements to the system that may be further investigated, this system allows for pilot data to be collected. Overall, it has been demonstrated that this inexpensive tactor system can be used to provide useful tactile feedback to an amputee user. It is expected that this work will feed into other branches of the BLINC Lab mandate in creating integrated sensory motor prostheses to improve the function and quality of life of patients living with the loss of an upper limb.

References

[1] C. Lake and R. Dodson. Progressive upper limb prosthetics. *Phys. Med. Rehabil. Clin. N. Am 17(1),* pp. 49-72. 2006.

[2] E. A. Biddiss and T. T. Chau. Upper limb prosthesis use and abandonment: A survey of the last 25 years. *Prosthet. Orthot. Int. 31(3),* pp. 236-257. 2007.

[3] E. A. Biddiss and T. T. Chau. Upper-limb prosthetics: Critical factors in device abandonment. *Am. J. Phys. Med. Rehabil. 86(12),* pp. 977-987. 2007.

[4] J. S. Schofield, K. R. Evans, J. P. Carey and J. S. Hebert. Applications of sensory feedback in motorized upper extremity prosthesis: A review. *Expert Rev. Med. Devices* pp. 1-13. 2014.

[5] C. Antfolk, M. D'Alonzo, B. Rosen, G. Lundborg, F. Sebelius and C. Cipriani. Sensory feedback in upper limb prosthetics. *Expert Rev. Med. Devices 10(1),* pp. 45-54. 2013.

[6] K. Ziegler-Graham, E. J. MacKenzie, P. L. Ephraim, T. G. Travison and R. Brookmeyer. Estimating the prevalence of limb loss in the united states: 2005 to 2050. *Arch. Phys. Med. Rehabil. 89(3),* pp. 422-429. 2008.

[7] L. E. Pezzin, T. R. Dillingham, E. J. Mackenzie, P. Ephraim and P. Rossbach. Use and satisfaction with prosthetic limb devices and related services. *Arch. Phys. Med. Rehabil. 85(5),* pp. 723-729. 2004.

[8] C. Lake. The evolution of upper limb prosthetic socket design. *J. Prosthet. Orthot. 20(3),* pp. 85-92. 2008.

[9] C. Behrend, W. Reizner, J. A. Marchessault and W. C. Hammert. Update on advances in upper extremity prosthetics. *J. Hand Surg. 36(10),* pp. 1711-1717. 2011.

[10] A. J. Thurston. Pare and prosthetics: The early history of artificial limbs. *ANZ J. Surg. 77(12),* pp. 1114-1119. 2007.

[11] P. Hernigou. Ambroise paré IV: The early history of artificial limbs (from robotic to prostheses). *Int. Orthop. 37(6),* pp. 1195-1197. 2013.

[12] P. J. Sauerborn. Advances in upper extremity prosthetics in the united states during world war II and early post-world war II era. *J. Facial Somato Prosthet. 4(2),* pp. 93-104. 1998.

[13] D. A. Zlotolow and S. H. Kozin. Advances in upper extremity prosthetics. *Hand Clin. 28(4),* pp. 587-593. 2012.

[14] M. S. Johannes, J. D. Bigelow, J. M. Burck, S. D. Harshbarger, M. V. Kozlowski and T. Van Doren. An overview of the developmental process for the modular prosthetic limb. *Johns Hopkins APL Technical Digest 30(3),* pp. 207-216. 2011.

[15] L. Resnik, S. L. Klinger and K. Etter. The DEKA arm: Its features, functionality, and evolution during the veterans affairs study to optimize the DEKA arm. *Prosthet. Orthot. Int. 38(6),* pp. 492-504. 2014.

[16] I. Gibson, *Advanced Manufacturing Technology for Medical Applications: Reverse Engineering, Software Conversion and Rapid Prototyping.* John Wiley & Sons, 2006.

[17] R. Narayan. *Rapid Prototyping of Biomaterials : Principles and Applications* 2014.

[18] (July 7, 2015). *Enabling the Future*. Available: http://enablingthefuture.org/.

[19] P. H. Chappell. Making sense of artificial hands. *J. Med. Eng. Technol. 35(1),* pp. 1-18. 2011.

[20] J. Davidson. A survey of the satisfaction of upper limb amputees with their prostheses, their lifestyles, and their abilities. *J. Hand Ther. 15(1),* pp. 62-70. 2002.

[21] L. V. McFarland, S. L. Hubbard Winkler, A. W. Heinemann, M. Jones and A. Esquenazi. Unilateral upper-limb loss: Satisfaction and prosthetic-device use in veterans and servicemembers from vietnam and OIF/OEF conflicts. *J. Rehabil. Res. Dev. 47(4),* pp. 299-316. 2010.

[22] A. E. Schultz, S. P. Baade and T. A. Kuiken. Expert opinions on success factors for upper-limb prostheses. *J. Rehabil. Res. Dev. 44(4),* pp. 483-489. 2007.

[23] C. W. Moran. Revolutionizing prosthetics 2009 modular prosthetic limb-body interface: Overview of the prosthetic socket development. *Johns Hopkins APL Technical Digest 30(3),* pp. 240-249. 2011.

[24] T. W. Wright, A. D. Hagen and M. B. Wood. Prosthetic usage in major upper extremity amputations. *J. Hand Surg. Am. 20(4),* pp. 619-622. 1995.

[25] S. Lewis, M. F. Russold, H. Dietl and E. Kaniusas. User demands for sensory feedback in upper extremity prostheses. Presented at IEEE Symposium on Medical Measurements and Applications. 2012, .

[26] C. Antfolk, M. D'Alonzo, M. Controzzi, G. Lundborg, B. Rosen, F. Sebelius and C. Cipriani. Artificial redirection of sensation from prosthetic fingers to the phantom hand map on transradial amputees: Vibrotactile versus mechanotactile sensory feedback. *IEEE Trans. Neural Syst. Rehabil. Eng. 21(1),* pp. 112-120. 2013.

[27] C. E. Stepp and Y. Matsuoka. Vibrotactile sensory substitution for object manipulation: Amplitude versus pulse train frequency modulation. *IEEE Trans. Neural Syst. Rehabil. Eng. 20(1),* pp. 31-37. 2012.

[28] P. D. Marasco, K. Kim, J. E. Colgate, M. A. Peshkin and T. A. Kuiken. Robotic touch shifts perception of embodiment to a prosthesis in targeted reinnervation amputees. *Brain 134(Pt 3),* pp. 747-758. 2011.

[29] C. Cipriani, F. Zaccone, S. Micera and M. C. Carrozza. On the shared control of an EMG-controlled prosthetic hand: Analysis of user-prosthesis interaction. *IEEE Trans. Robot. 24(1),* pp. 170-184. 2008.

[30] C. Pylatiuk, A. Kargov and S. Schulz. Design and evaluation of a low-cost force feedback system for myoelectric prosthetic hands. *J. Prosthet. Orthot. 18(2),* pp. 57-61. 2006.

[31] P. E. Patterson and J. A. Katz. Design and evaluation of a sensory feedback system that provides grasping pressure in a myoelectric hand. *J. Rehabil. Res. Dev. 29(1),* pp. 1-8. 1992.

[32] G. F. Shannon. A comparison of alternative means of providing sensory feedback on upper limb prostheses. *Med. Biol. Engineering 14(3),* pp. 289-294. 1976.

[33] J. D. Brown, A. Paek, M. Syed, M. K. O'Malley, P. A. Shewokis, J. L. Contreras-Vidal, A. J. Davis and R. B. Gillespie. Understanding the role of haptic feedback in a teleoperated/prosthetic grasp and lift task. Presented at World Haptics Conference. 2013, .

[34] K. Kim and J. E. Colgate. Haptic feedback enhances grip force control of sEMG-controlled prosthetic hands in targeted reinnervation amputees. *IEEE Trans. Neural Syst. Rehabil. Eng. 20(6),* pp. 798-805. 2012.

[35] C. Tejeiro, C. E. Stepp, M. Malhotra, E. Rombokas and Y. Matsuoka. Comparison of remote pressure and vibrotactile feedback for prosthetic hand control. Presented at Proceedings of the IEEE RAS and EMBS International Conference on Biomedical Robotics and Biomechatronics. 2012, .

[36] A. Benvenuto, S. Raspopovic, K. P. Hoffmann, J. Carpaneto, G. Cavallo, G. Di Pino, E. Guglielmelli, L. Rossini, P. M. Rossini, M. Tombini and S. Micera. Intrafascicular thin-film multichannel electrodes for sensory feedback: Evidences on a human amputee. Presented at IEEE Engineering in Medicine and Biology Society. 2010, .

[37] M. R. Mulvey, H. J. Fawkner, H. Radford and M. I. Johnson. The use of transcutaneous electrical nerve stimulation (TENS) to aid perceptual embodiment of prosthetic limbs. *Med. Hypotheses 72(2),* pp. 140-142. 2009.

[38] T. A. Kuiken, P. D. Marasco, B. A. Lock, R. N. Harden and J. P. Dewald. Redirection of cutaneous sensation from the hand to the chest skin of human amputees with targeted reinnervation. Presented at National Academy of Science of the United States of America. 2007, .

[39] G. F. Shannon. A myoelectrically-controlled prosthesis with sensory feedback. *Med. Biol. Eng. Comput. 17(1),* pp. 73-80. 1979.

[40] T. A. Rohland. Sensory feedback for powered limb prostheses. *Med. Biol. Engineering 13(2),* pp. 300-301. 1975.

[41] T. W. Beeker, J. During and A. Den Hertog. Artificial touch in a hand-prosthesis. *Med. Biol. Engineering 5(1),* pp. 47-49. 1967.

[42] C. Dietrich, K. Walter-Walsh, S. Preissler, G. O. Hofmann, O. W. Witte, W. H. Miltner and T. Weiss. Sensory feedback prosthesis reduces phantom limb pain: Proof of a principle. *Neurosci. Lett. 507(2),* pp. 97-100. 2012.

[43] J. Gonzalez, H. Soma, M. Sekine and W. Yu. Psycho-physiological assessment of a prosthetic hand sensory feedback system based on an auditory display: A preliminary study. *J. Neuroeng. Rehabil. 9(1),* 2012.

[44] J. Wheeler, K. Bark, J. Savall and M. Cutkosky. Investigation of rotational skin stretch for proprioceptive feedback with application to myoelectric systems. *IEEE Trans. Neural Syst. Rehabil. Eng. 18(1),* pp. 58-66. 2010.

[45] R. B. Gillespie, J. L. Contreras-Vidal, P. A. Shewokis, M. K. O'Malley, J. D. Brown, H. Agashe, R. Gentili and A. Davis. Toward improved sensorimotor integration and learning using upper-limb prosthetic devices. Presented at IEEE Engineering in Medicine and Biology Society. 2010, .

[46] C. Antfolk, C. Cipriani, M. C. Carrozza, C. Balkenius, A. Bjorkman, G. Lundborg, B. Rosen and F. Sebelius. Transfer of tactile input from an artificial hand to the forearm: Experiments in amputees and able-bodied volunteers. *Disabil. Rehabil. Assist. Technol. 8(3),* pp. 249-254. 2013.

[47] R. S. Armiger, F. V. Tenore, K. D. Katyal, M. S. Johannes, A. Makhlin, M. L. Natter, J. E. Colgate, S. J. Bensmaia and R. J. Vogelstein. Enabling closed-loop control of the modular prosthetic limb through haptic feedback. *Johns Hopkins APL Technical Digest 31(4),* pp. 345-353. 2013.

[48] C. Antfolk, C. Balkenius, G. Lundborg, B. Rosén and F. Sebelius. A tactile display system for hand prostheses to discriminate pressure and individual finger localization. *Med. Biol. Engineering 30(6),* pp. 355-360. 2010.

[49] K. Kim, J. E. Colgate, J. J. Santos-Munné, A. Makhlin and M. A. Peshkin. On the design of miniature haptic devices for upper extremity prosthetics. *IEEE/ASME Trans. Mechatronics 15(1),* pp. 27-39. 2010.

[50] R. E. Fan, C. Wottawa, A. Mulgaonkar, R. J. Boryk, T. C. Sander, M. P. Wyatt, E. Dutson, W. S. Grundfest and M. O. Culjat. Pilot testing of a haptic feedback rehabilitation system on a lower-limb amputee. Presented at ICME International Conference on Complex Medical Engineering. 2009, .

[51] M. O. Culjat, R. E. Fan and W. S. Grundfest. Optimization of a tactile feedback system to aid the rehabilitation of lower-limb amputees. Presented at 2008 Virtual Rehabilitation, IWVR. 2008, .

[52] S. G. Meek, S. C. Jacobsen and P. P. Goulding. Extended physiologic taction: Design and evaluation of a proportional force feedback system. *J. Rehabil. Res. Dev. 26(3),* pp. 53-62. 1989.

[53] K. Kim, J. E. Colgate, M. A. Peshkin, J. J. Santos-Munné and A. Makhlin. A miniature tactor design for upper extremity prosthesis. 2007, .

[54] P. M. Rossini, S. Micera, A. Benvenuto, J. Carpaneto, G. Cavallo, L. Citi, C. Cipriani, L. Denaro, V. Denaro, G. Di Pino, F. Ferreri, E. Guglielmelli, K. -. Hoffmann, S. Raspopovic, J. Rigosa, L. Rossini, M. Tombini and P. Dario. Double nerve intraneural interface implant on a human amputee for robotic hand control. *J. Clin. Neurophysiol. 121(5),* pp. 777-783. 2010.

[55] J. B. Hijjawi, T. A. Kuiken, R. D. Lipschutz, L. A. Miller, K. A. Stubblefield and G. A. Dumanian. Improved myoelectric prosthesis control accomplished using multiple nerve transfers. *Plast. Reconstr. Surg. 118(7),* pp. 1573-1578. 2006.

[56] T. A. Kuiken, G. A. Dumanian, R. D. Lipschutz, L. A. Miller and K. A. Stubblefield. The use of targeted muscle reinnervation for improved myoelectric prosthesis control in a bilateral shoulder disarticulation amputee. *Prosthet. Orthot. Int. 28(3),* pp. 245-253. 2004.

[57] T. A. Kuiken, L. A. Miller, R. D. Lipschutz, B. A. Lock, K. Stubblefield, P. D. Marasco, P. Zhou and G. A. Dumanian. Targeted reinnervation for enhanced prosthetic arm function in a woman with a proximal amputation: A case study. *Lancet (London) (9559),* pp. 371. 2007.

[58] J. S. Hebert, J. L. Olson, M. J. Marhart, M. R. Dawson, P. D. Marasco, T. A. Kuiken and K. M. Chan. Novel targeted sensory reinnervation technique to restore functional hand sensation after transhumeral amputation. *IEEE Trans. Neural Syst. Rehabil. Eng. (1558-0210),* 2013.

[59] J. S. Hebert, J. L. Olson, M. Morhart, M. R. Dawson, P. D. Marasco, T. A. Kuiken and K. M. Chan, "Targeted sensory reinnervation to enhance sensory feedback after upper limb amputation," in *NATO Science and Technology Organization Human Factors and Medicine Panel Symposium,* Milan, Italy, 2013, .

[60] C. Antfolk, C. Balkenius, G. Lundborg, B. Rosén and F. Sebelius. Design and technical construction of a tactile display for sensory feedback in a hand prosthesis system. *Biomed Eng. Online 9*2010.

[61] N. Garcia-Hernandez, F. Bertolotto, F. Cannella, N. G. Tsagarakis and D. G. Caldwell. How tactor size and density of normal indentation tactile displays affects grating discrimination tasks. *IEEE Trans. Haptics 7(3),* pp. 356-366. 2014.

[62] N. Garcia-Hernandez, N. G. Tsagarakis and D. G. Caldwell. Feeling through tactile displays: A study on the effect of the array density and size on the discrimination of tactile patterns. *IEEE Trans. Haptics 4(2),* pp. 100-110. 2011.

[63] H. E. Ross and D. J. Murray, *E. H. Weber on the Tactile Senses.* Erlbaum: Taylor & Francis, 1996.

[64] T. Skirven, A. Osterman, J. Fedorczyk and P. Amadio. *Rehabilitation of the Hand and Upper Extremity* 2011.

[65] D. Sinclair, *Cutaneous Sensation.* Oxford: Oxford University Press, 1967.

[66] S. Weinstein, "Intensive and extensive aspects of tactile sensitivity as a function of body part, sex, and laterality," in *International Symposium on Skin Senses,* Florida State University, 1968, pp. 195-222.

[67] K. Myles and M. S. Binseel, "The Tactile Modality: A Review of Tactile Sensitivity and Human Tactile Interfaces," *ARL,* 2007.

[68] J. Bear-Lehman, S. M. Albert and A. Burkhardt. Cutaneous sensitivity and functional limitation. *Top. Geriatr. Rehabil. 22(1),* pp. 61-69. 2006.

[69] M. R. Longo and P. Haggard. Weber's illusion and body shape: Anisotropy of tactile size perception on the hand. *J. Exp. Psychol. Hum. Percept. Perform. 37(3),* pp. 720-726. 2011.

[70] J. P. Hunter, J. Katz and K. D. Davis. Dissociation of phantom limb phenomena from stump tactile spatial acuity and sensory thresholds. *Brain 128(2),* pp. 308-320. 2005.

[71] D. Yarnitsky. Quantitative sensory testing. *Muscle Nerve 20(2),* pp. 198-204. 1997.

[72] W. Van Gils, H. A. Reinders-Messelink, F. Smit-Klaij, R. M. Bongers, P. U. Dijkstra and C. K. Van Der Sluis. Sensibility of the stump in adults with an acquired major upper extremity amputation. *Arch. Phys. Med. Rehabil. 94(11),* pp. 2179-2185. 2013.

[73] D. C. Montgomery. *Design and Analysis of Experiments* (7th ed.) 2008.

[74] G. Lundborg and B. Rosen. The two-point discrimination test-time for a re-appraisal? *J. Hand Surg. Br. 29(5),* pp. 418-422. 2004.

[75] E. M. Halar, M. C. Hammond, E. C. LaCava, C. Camann and J. Ward. Sensory perception threshold measurement: An evaluation of semiobjective testing devices. *Arch. Phys. Med. Rehabil. 68(8),* pp. 499-507. 1987.

[76] W. L. Chang and A. A. Seigreg. Prediction of ulcer formation on the skin. *Med. Hypotheses 53(2),* pp. 141-144. 1999.

[77] M. Kosiak. Etiology of decubitus ulcers. *Arch. Phys. Med. Rehabil. 42*pp. 19-29. 1961.

[78] A. Gefen, B. van Nierop, D. L. Bader and C. W. Oomens. Strain-time cell-death threshold for skeletal muscle in a tissue-engineered model system for deep tissue injury. *J. Biomech. 41(9),* pp. 2003-2012. 2008.

[79] E. Ungar, "A New Approach to Defining Human Touch Temperature Standards," *NASA,* .

[80] R. Weir, "Design of artificial arms and hands for prosthetic applications," in *Standard Handbook of Biomedical Engineering and Design*Anonymous The McGraw-Hill Companies, 2004, pp. 32.1-32.61.

[81] K. Ghoseiri and M. R. Safari. Prevalence of heat and perspiration discomfort inside prostheses: Literature review. *J. Rehabil. Res. Dev. 51(6),* pp. 855-868. 2014.

[82] R. J. Dodson and B. Jowid. The clinical application of an upper limb custom silicone interface: Observations of a case study. *J. Prosthet. Orthot. 21(2),* pp. 120-124. 2009.

[83] M. Heim, M. Wershavski, S. T. Zwas, I. Siev-Ner, H. Nadvorna and M. Azaria. Silicone suspension of external prostheses. A new era in artificial limb usage. *J. Bone Joint Surg. B. 79(4),* pp. 638-640. 1997.

[84] C. Antfolk, A. Björkman, S. -. Frank, F. Sebelius, G. Lundborg and B. Rosen. Sensory feedback from a prosthetic hand based on airmediate d pressure from the hand to the forearm skin. *J. Rehabil. Med. 44(8),* pp. 702-707. 2012.

[85] D. D. Damian, M. Ludersdorfer, Y. Kim, A. Hernandez Arieta, R. Pfeifer and A. M. Okamura. Wearable haptic device for cutaneous force and slip speed display. Presented at Proceedings - IEEE International Conference on Robotics and Automation. 2012, .

[86] Interlink Electronics, "Force sensing resistor integration guide and evaluation parts catalog," VersaPoint Technology, Camarillo, CA, .

[87] H. K. Lee, J. Chung, S. I. Chang and E. Yoon. Normal and shear force measurement using a flexible polymer tactile sensor with embedded multiple capacitors. *J. Microelectromech. Syst. 17(4),* pp. 934-942. 2008.

[88] J. A. Dobrzynska and M. A. M. Gijs. Polymer-based flexible capacitive sensor for three-axial force measurements. *J. Micromech. Microengineering 23(1),* 2013.

[89] XSensor Technology Corporation, "XSensor X3 LX100 Sensor Series," 2014.

[90] A. B. Junaid, S. Tahir, T. Rasheed, S. Ahmed, M. Sohail, M. R. Afzal, M. Ali and Y. Kim. Low-cost design and fabrication of an anthropomorphic robotic hand. *J. Nanosci. Nanotechnol. 14(10),* pp. 7427-7431. 2014.

[91] X. Wang, J. Zhao, D. Yang, N. Li, C. Sun and H. Liu. Biomechatronic approach to a multi-fingered hand prosthesis. Presented at IEEE RAS and EMBS International Conference on Biomedical Robotics and Biomechatronics. 2010, .

[92] Low Soon Chiang, Phee Soo Jay, P. Valdastri, A. Menciassi and P. Dario. Tendon sheath analysis for estimation of distal end force and elongation. Presented at IEEE/ASME International Conference on Advanced Intelligent Mechatronics. 2009, .

[93] V. A. Godyak. Bright idea: Radio-frequency light sources. *IEEE Ind. Appl. Mag. 8(3),* pp. 42-49. 2002.

[94] Anonymous "Radio Frequency Interference - And What to Do About It," *Radio-Sky Journal,* vol. 4, 2001.

[95] Interlink Electronics, "FSR 400 Data Sheet," Accessed: 2015.

[96] A. Hollinger and M. M. Wanderley. Evaluation of commercial force-sensing resistors. Presented at Proceedings of International Conference on New Interfaces for Musical Expression. 2006, .

[97] P. Arias, V. Robles-García, N. Espinosa, Y. Corral and J. Cudeiro. Validity of the finger tapping test in parkinson's disease, elderly and young healthy subjects: Is there a role for central fatigue? *Clinical Neurophysiology 123(10),* pp. 2034-2041. 2012.

[98] E. P. Gardner, J. H. Martin and T. M. Jessell, "The bodily senses," in *Principles of Neural Science*, 5th ed., E. R. Kandel, J. H. Schwartz, T. M. Jessell, S. A. Siegelbaum and A. J. Hudspeth, Eds. McGraw-Hill, 2012, .

[99] F. H. Martini, *Fundamentals of Anatomy and Physiology.* San Francisco: Pearson Education Inc., 2006.

[100] R. A. Losada, "Data Filters with Matlab," *The MathWorks, Inc.,* 2008.

[101] Ripmax, "Digital FET servos," Futaba, Enfield, England, .

[102] R. S. Johansson and J. R. Flanagan. Coding and use of tactile signals from the fingertips in object manipulation tasks. *Nat. Rev. Neurosci. 10(5),* pp. 345-359. 2009.

[103] C. Jay and R. Hubbold. Delayed visual and haptic feedback in a reciprocal tapping task. Presented at Joint Eurohaptics Conference and Symposium on Haptic Interfaces for Virtual Environment and Teleoperator Systems. 2005, .

[104] R. Leib, A. Karniel and I. Nisky. The effect of force feedback delay on stiffness perception and grip force modulation during tool-mediated interaction with elastic force fields. *J. Neurophysiol. 113(9),* pp. 3076-3089. 2015.

[105] M. Tavakoli. Hand haptic perception. *Springer Tracts in Advanced Robotics 95*pp. 189-200. 2014.

[106] T. R. Farrell and R. F. Weir. The optimal controller delay for myoelectric prostheses. *IEEE Trans. Neural Syst. Rehabil. Eng. 15(1),* pp. 111-118. 2007.

[107] S. Shimada, K. Fukuda and K. Hiraki. Rubber hand illusion under delayed visual feedback. *PloS One 4(7),* pp. e6185. 2009.

[108] (March 29, 2011). *PID Theory Explained*. Available: http://www.ni.com/white-paper/3782/en/.

[109] G. F. Franklin, J. D. Powel and A. Emami-Naeini, *Feedback Control of Dynamic Systems.* Upper Saddle River, NJ: Pearson, 2009.

[110] T. Hulin, R. Gonzalez Camarero and A. Albu-Schaffer. Optimal control for haptic rendering: Fast energy dissipation and minimum overshoot. Presented at IEEE/RSJ International Conference on Intelligent Robots and Systems. 2013, .

[111] O. Komolafe, S. Wood, R. Caldwell, A. Hansen and S. Fatone. Methods for characterization of mechanical and electrical prosthetic vacuum pumps. *J. Rehabil. Res. Dev. 50(8),* pp. 1069-1078. 2013.

[112] M. Gerschutz. Elevated vacuum suspension: Evaluation of residual limb movement in a prosthetic socket. Presented at Proceedings of the 36th Annual Meeting and Scientific Symposium of the American Academy of Orthotists and Prosthetists. 2010, .

[113] M. J. Gerschutz. Elevated vacuum suspension: The effects on an amputees residual limb volume. Presented at Am. Acad. Orthot. Prosthet. 36th Annual Meeting and Scientific Symposium Chicago, IL, USA. 2010, .

[114] W. J. Board, G. M. Street and C. Caspers. A comparison of trans-tibial amputee suction and vacuum socket conditions. *Prosthet. Orthot. Int. 25(3),* pp. 202-209. 2001.

[115] G. M. Street, "Vacuum suspension and its effects on the limb," *The Orthopadie Technik,* vol. 4, pp. 1-4, 2006.

[116] W. Daly. Upper extremity socket design options. *Phys. Med. Rehabil. Clin. N. Am. 11(3),* pp. 627-638. 2000.

[117] J. Miguelez, D. Conyers, M. Lang, R. Dodson and K. Gulick. Transradial and wrist disarticulation socket considerations: Case studies. *J. Prosthet. Orthot. 20(3),* pp. 118-125. 2008.

[118] M. Lang and D. Conyers. Utilization of negative pressure for socket suspension in upper extremity prosthetics . 2008, .

[119] M. J. Gerschutz, J. A. Denune, J. M. Colvin, G. Schober, M. L. Haynes and D. Nixon, "Technical Notes on Elevated Vacuum Suspension: Amputee Patient Outcomes Evaluating Patient Verbal Opinion and Pressure Data ," *Ohio Willow Wood,* .

[120] M. M. Baharestani. Use of negative pressure wound therapy in the treatment of neonatal and pediatric wounds: A retrospective examination of clinical outcomes. *Ostomy Wound. Manage. 53(6),* pp. 75-85. 2007.

[121] G. C. Murphey, B. R. Macias and A. R. Hargens. Depth of penetration of negative pressure wound therapy into underlying tissues. *Wound Repair Regen. 17(1),* pp. 113-117. 2009.

[122] L. Lowe Jr B. and J. van der Leun C. Suction blisters and dermal-epidermal adherence. *J. Invest. Dermatol. 50(4),* pp. 308-314. 1968.

[123] (May 6, 2015). *Weather Stations: Edmonton, Alberta, Canada*. Available: http://easweb.eas.ualberta.ca/page/weather_stations.

[124] J. Diani, B. Fayolle and P. Gilormini. A review on the mullins effect. *Eur. Polym. J. 45(3),* pp. 601-612. 2009.

[125] J. E. Sanders, B. S. Nicholson, S. G. Zachariah, D. V. Cassisi, A. Karchin and J. R. Fergason. Testing of elastomeric liners used in limb prosthetics: Classification of 15 products by mechanical performance. *J. Rehabil. Res. Dev. 41(2),* pp. 175-186. 2004.

[126] Anonymous "Willow Wood Instruction Manual," *Willow Wood,* 2015.

[127] (2015). *About Rubber and Polyurethane*. Available: http://www.mcmaster.com/#about-rubber/=x2cmlw.

[128] (2015). *Material Property Data*. Available: http://www.matweb.com/.

[129] (2015). *Memory*. Available: http://arduino.cc/en/Tutorial/Memory.

[130] (2015). *Double*. Available: http://arduino.cc/en/Reference/Double.

Appendices

Appendix A. Design Compliance Matrix

The design compliance matrix for the cable-driven tactor is given below.

Table A.1 Design compliance matrix for cable-driven tactor

Item #	Component / system description	Design specification / requirement	Design authority	Design importance (1-5)	Design compliance (1-10)	Notes
1.00	**Overall**					
1.10	**Total size (max)**					
1.11	Controller	5.3 x 3.5 x 1.7 cm (includes enclosure and battery)	BLINC	2	2	Sits within forearm of prosthesis, ø50 mm tube of 105 mm length, with protruding switches; contains wrist adapter. Scope creep: more requirements from controller and battery than anticipated.
1.12	Tactor	2.0 x 2.0 x 2.0 cm (tactor bend size)	BLINC	2	7	2.5 x 2.5 x 2.05 cm
1.20	**Total weight (max)**					
1.21	Controller	< 60 g (includes enclosure and battery)	BLINC	2	1	Approximately 145 g. Scope creep: more requirements from controller and battery than anticipated.
1.22	Tactor	< 50 g per tactor	BLINC	2	10	Tactor with long cable length (25 cm) weighs 36 g
1.30	**Total cost**	**< $1250 (includes enclosure, controller, 6 tactors, battery, charger)**	**BLINC**	**2**	**10**	**Approximately $425 for raw materials, not including assembly time for electronics or tactors**
	Controller	< $400	BLINC	2	10	Approximately $55 of components
	Electronics enclosure	< $100	BLINC	2	10	Approximately $3
	Tactor	< $200	BLINC	2	10	Approximately $50 of components

Item #	Component / system description	Design specification / requirement	Design authority	Design importance (1-5)	Design compliance (1-10)	Notes
1.40	Manufacturability					
1.41	Off-the-shelf components	Components should be purchased off-the-shelf where possible	BLINC	2	8	Motors, cables, fasteners purchased
1.42	In-house manufacturing	Components should be easily manufactured with available equipment	BLINC	3	8	Components manufactured predominantly using 3D printing and traditional manufacturing methods, outside of electronics PCBs
1.50	Timing					
1.51	Development time	8 months or less	BLINC	3	5	2.5 years development due to part time development (across multiple students)
1.52	Device lifetime	Able to last up to 1 month of intermittent testing	BLINC	3		Follow up required to determine typical usage and evaluate appropriately.
1.60	Materials allowed	Biocompatible with no cytotoxicity, irritation, and sensitization	ISO-22523	5	8	Materials that are not in direct contact with skin are non-toxic according to MSDS, but are not classified as medical grade. Materials in direct contact with skin (Nitrile and Shear Ban) are medical grade
1.70	Noise and vibration	No requirements on noise or vibration levels	ISO-22523	1	6	Makes some noise during operation, especially at higher force levels. Future usability trials should investigate if noise is a concern
1.80	Surface temperature					
1.81	Maximum temperature allowed	Should not exceed 45°C	NASA	5	8	Should not occur during normal use (under extended 5 N loading for 30 minutes temperature reached 43.4 ± 3.4°C). Further usability trials should investigate if heat is a concern during typical usage

Item #	Component / system description	Design specification / requirement	Design authority	Design importance (1-5)	Design compliance (1-10)	Notes
1.82	Means to reduce temperature	Means of protection to remove or minimize rises in temperature,	ISO-22523	2	6	Housing open on two sides, includes vents
1.90	**Supported pressure/force sensors**					
1.91	FSR	0-5 V output, 0-20 N range	BLINC	1	5	Selected FSRs have range of 0-10 N, could source higher if needed
1.92	Load cell	0-5 V output, 0-20 N range	BLINC	1	10	Load cells available at this range, integration out of scope
2.00	**Mechanical Requirements**					
2.10	**Electronics enclosure**	**Houses and protects controller**				
2.11	Size (max)	5.3 x 3.5 x 1.2 cm	BLINC	2	2	Sits within forearm of prosthesis, ø50 mm tube of 105 mm length, with protruding switches, also contains wrist adapter
2.12	Weight (max)	30 g	BLINC	2	7	Approximately 46 g
2.13	Mounting method	Internally inside prosthesis or externally via wrist-watch style mount	BLINC	1	9	Internally within forearm, switches extending out top of forearm
2.14	Environmental isolation	Sealed around connectors to prevent contamination of electronics	BLINC	5	8	Electronics placed within forearm with Sugru to seal edges. May need to use sealed enclosure for future take-home trials in case of exposure
2.20	**Tactor head**	**Component that contacts skin**				
2.21	Head diameter	Between 8 and 12 mm	Optimization study	5	10	8 mm head diameter
2.22	Edging	Rounded edges, for minimized sharpness concentrations	BLINC	5	10	Edges rounded
2.23	Shape	Domed (8 – 12 mm) or triangular (12 mm)	Optimization study	2	10	Domed head shape
2.24	Material	Metallic or high thermal conductivity or smooth plastic	BLINC	4	10	Printed tactor head, smoothed, coated with clear polish

Item #	Component / system description	Design specification / requirement	Design authority	Design importance (1-5)	Design compliance (1-10)	Notes
2.30	**Tactor size**					
2.31	Maximum total height	2 cm maximum offset from the skin	BLINC	4	5	2.05 cm above socket
2.32	Translational depth (throw)	Must be able to push skin in between 1.7 and 2.0 cm	BLINC	5	8	Linear tactor pushes up to 1.7 cm, cable-driven tactor pushes up to 1.5 cm, within normal limits of the device
2.33	Spacing	Capable of a 2 cm center-to-center distance between two tactor heads	BLINC	5	8	Elbow can be modified to achieve this by combining two tactor bends together
2.40	**Skin interaction**					
2.41	Minimized risk to skin	Reduce unacceptable pressure on and stress levels to body tissue	ISO-22523	5	8	Maximum displacement limited. Future usability trials should include visual testing and reporting during breaks to check arm for bruising and redness
2.42	Moving parts	Remove risk of trapping or damaging skin, hair, clothing, during normal usage	ISO-22523	5	8	Moving components (servo, gear train) to be covered for take-home trials
2.43	Skin fatigue	Prevent tissue breakdown from continuous skin fatigue	BLINC	5	8	Maximum displacement limited. Future usability trials should include visual testing and reporting during breaks to check arm for bruising and redness
2.44	Skin abrasions	Prevent the penetration of the skin	BLINC	5	9	Smooth tactor head used, attached well to cable, membrane covers head, and forces should not exceed set limits

Item #	Component / system description	Design specification / requirement	Design authority	Design importance (1-5)	Design compliance (1-10)	Notes
2.45	Maximum allowable force	7 N maximum	BLINC	4	9	Can apply above this range (for short pulse linear up to 15 N, cable up to 8.3 N), but motor will overheat over time. Software prevents applying excessive force, mechanical stop on the rack gear to prevent over-extension
2.50	**Socket integration**					
2.51	Vacuum seal	Must be maintained	BLINC	5	10	Seal is maintained by isolating at the tactor-skin interface
2.52	Interference with tactor	Minimal interference with applied force of tactor	BLINC	3	8	Slight reduction in applied tactor force
2.53	Skin protrusion	Prevent skin from bulging out of socket	BLINC	3	8	Membrane prevents skin from protruding significantly from hole in socket
3.00	**Electrical Subsystem**					
3.10	**Controller**					Scope creep: more requirements from controller and battery than anticipated.
3.11	Size (max)	5.1 x 3.3 x 1.0 cm	BLINC	2	5	Switch board: 2.7 x 1.3 x 2.0 cm Power board: 3.9 x 1.6 x 0.9 cm Controller board: 4.4 x 2.2 x 0.9 cm Pin board (2 tactors): 1.6 x 1.5 x 0.9 cm
3.12	Weight (max)	10 g	BLINC	2	5	Switch board: 8 g Power board: 4 g Controller board: 5 g Pin board (2 tactors): 4 g Wiring and connectors: 10 g Total: 31 g
3.13	Number of tactor PWM channels	6	BLINC	2	10	8 channels maximum (require pin board)
3.14	Number of input sensor channels	6	BLINC	2	10	8 channels (require pin board)

Item #	Component / system description	Design specification / requirement	Design authority	Design importance (1-5)	Design compliance (1-10)	Notes
3.15	Output voltage for tactor channels	3.3 or 5 V individually selectable	BLINC	3	10	Power to servo motors is sent via the adapter board which can be 3.3 or 5 V
3.16	External controls/buttons	Control upper and lower limits for each channel	BLINC	1	10	May adjust from starting point using GUI
3.17	External channel display	LED's to indicate active channels and which upper and lower limits are currently being adjusted	BLINC	5	1	Must observe active tactors
3.18	External battery display	Control indicator LED's and indicate when battery is low	BLINC	5	1	Charge can be gauged using fuel gauge IC. Several backup batteries are available which should be kept fully charged
3.19	Programmable system	Designed to ensure repeatability, reliability, and performance	IEC 60601-1	5	7	Device sufficient based on preliminary testing. Future usability trials will provide more insight
3.101	Circuit protection	If the power supply can be overloaded in use and the overload can cause a risk to the user, that device must be protected against the overload	ISO-22523 8.3, IEC 6061-1-4	5	10	There is a 5 V regulator to the servo motors. If system overloads (i.e. current above 2.6 A is drawn) a PTC fuse on the Lipo switch board will go to high impedance and effectively cut the power to the system.
3.102	EMG protection	Designed to prevent leakage current from travelling backwards into the patient through the EMG sensors	IEC 60601-1	5	8	Mains power to system limits amount of current that can leak back to the patient. Electrode-skin interface provides high impedance. High-level safety management will be implemented; only used by trained staff, electrodes unplugged during programming, wall/battery charger physically disconnects mains ground from the rest of the circuit while charging

Item #	Component / system description	Design specification / requirement	Design authority	Design importance (1-5)	Design compliance (1-10)	Notes
3.20	**Tactor**					
3.21	Power consumption	200 mA or less at 5 V (1 W) per 3-4 N poke for a single actuator	BLINC	5	10	Long cable-tactor (220 mm with a single bend of 21 mm from center) able to apply 4 N of force while drawing 166 ± 22 mA current
3.22	Interference	Must not interfere with electrode response (both motion artifacts and EMF interference)	BLINC	5	5	Tactor approximately 2 cm from an EMG sensor pressing up to 1.2 N anecdotally not shown to interfere with measured response or control, however further testing required
3.30	**Battery**					
3.31	Size (max)	5.3 x 3.5 x 0.5 cm	BLINC	2	1	7.1 x 3.7 x 1.9 cm
3.32	Weight (max)	20 g	BLINC	2	1	97 g
3.33	Runtime (min)	14 hours	BLINC	2		Five long cable-tactors (220 mm with a single bend of 21 mm from center) operating at 5 N at 50% duty cycle could operate for 4.5 hours. Future usability trials should evaluate more realistic estimate
3.34	Adaptable	Can run off dedicated battery or existing prosthesis battery	BLINC	1	5	Currently set-up to run off of dedicated battery, but could run off of prosthesis battery with slight modifications to connectors or adaptor circuitry
3.40	**Charger**					
3.41	Charge time (max)	8 hours	BLINC	1	10	Maximum calculated charging time of 4.4 hours (battery capacity of 2.2 Ah, charging current of 0.5 A)

Item #	Component / system description	Design specification / requirement	Design authority	Design importance (1-5)	Design compliance (1-10)	Notes
3.50	Wiring and connectors					
3.51	Aesthetics	Wiring routed cleanly with snap in polar connectors on the exterior of the electronics enclosure	BLINC	3	6	Internal components are snap fit, external sensors and motors are plug connections for in-lab testing. Future usability trials should utilize entirely snap fit connections
3.52	Safety	Connectors and terminals that the user is required to handle should be designed to minimize risk to the user	ISO-22523	3	10	The user interacts with charger only. Charger cannot operate while system is turned on
3.00	Software Subsystem					
4.10	Map from pressure to tactor output		BLINC			
4.11	Map to applied displacement	Map measured force to set displacement of tactor	BLINC	5	10	Simplest to implement
4.12	Map to applied force	Map measured force to applied force of tactor	BLINC	3	8	Error and time delay introduced
4.13	Configurable mappings	Map linearly, non-linear, etc.	BLINC	1	5	Maps linearly, can be updated in software (*out-of-scope*)
4.20	Filtering signals	Mitigate possible interference from the electromagnetic environment	ISO-22523	1	10	Filters implemented into the software to remove potential noise produced by overhead transmission lines

Appendix B. Bill of Materials

Table B.1 Bill of Materials for linear tactor mechanical subsystem

Component	Manufacturer	Supplier / part number / part file	Printing / cleaning time (min)	Cost per part ($CAD) [(a)]	Estimated mass per part (g)	Quantity	Total cost ($CAD)	Total mass (g)
Servo mount	In-house	Servo mount.x3g (PLA)	17 / 15	$0.11	2.3	1	$0.11	2.3
Servo mount cover	In-house	Servo mount cover.x3g (PLA)	4 / 1	$0.02	0.5	1	$0.02	0.5
Rack gear	In-house	Rack with 8 mm dome.x3g (PLA)	4 / 5	$0.03	0.6	1	$0.03	0.6
Pinion gear	In-house	18 tooth gear assembly.x3g (PLA)	3 / 1	$0.01	0.3	1	$0.01	0.3
Mechanical stop	In-house	Mechanical stop.x3g (PLA)	1 / 1	$0.00	0.0	1	$0.00	0.0
Membrane rim	In-house	Membrane rim.x3g (Ninjaflex)	9 / 1	$0.06	0.7	1	$0.06	0.7
Latex membrane	In-house	McMaster Carr / 6072T83	0 / 1	$24.98 per 400	0.0	1	$0.06	0.0
Servo motor	Hitec	Servo City / HS-35HD		$33.90	4.5	1	$33.90	4.5
Screws (2-56, 1/8 in.)	McMaster Carr	McMaster Carr / 91771A074		$6.20 per 100	0.0	4	$0.25	0.0
Current sensor (optional)	Interlink Electronics	Sparkfun / ACS712		$15.72	0.5	1	$15.72	0.5
Total			38 / 25				$50.17	9.4

(a) Conversions made using 1.31 CAD to 1.00 USD, as of August 6, 2015, costs do not include shipping, taxes, or fees

(b) Note that an approximate additional 15 minutes is required to assemble the components and attach them to the socket, increasing the total manual labour required to approximately 40 minutes per tactor.

Table B.2 Bill of Materials for cable-driven tactor mechanical subsystem

Component	Manufacturer	Supplier / part number / part file	Printing / cleaning time (min)	Cost per part ($CAD) [(a)]	Estimated mass per part (g)	Quantity	Total cost ($CAD)	Total mass (g)
Servo Mount	In-house	Servo mount 2.x3g (PLA)	17 / 15	$0.11	2.3	1	$0.11	2.3
Servo mount cover	In-house	Servo mount cover.x3g (PLA)	4 / 1	$0.02	0.5	1	$0.02	0.5
Rack gear	In-house	Rack and adapter.x3g (PLA)	4 / 5	$0.02	0.5	1	$0.02	0.5
Pinion gear	In-house	18 tooth gear assembly.x3g (PLA)	3 / 1	$0.01	0.3	1	$0.01	0.3
Mechanical stop	In-house	Mechanical stop.x3g (PLA)	1 / 1	$0.00	0.0	1	$0.00	0.0
Adapter	In-house	Cable adapter.x3g (PLA)	1 / 1	$0.00	0.0	1	$0.00	0.0
Cable support	In-house	Cable support.x3g (PLA)	9 / 1	$0.04	0.9	2	$0.08	1.7
Elbow	In-house	Sleeve elbow.x3g (PLA)	22 / 1	$0.15	3.1	1	$0.15	3.1
Tactor head	In-house	Tactor head.x3g (PLA)	2 / 1	$0.01	0.1	2	$0.01	0.3
Membrane rim	In-house	Membrane rim.x3g (Ninjaflex)	9 / 1	$0.06	0.7	1	$0.06	0.7
Latex membrane	In-house	McMaster Carr / 6072T83	0 / 1	$24.98 per 400	0.0	1	$0.06	0.0
Servo motor	Hitec	Servo City / HS-35HD		$33.90	4.5	1	$33.90	4.5
Screws (2-56, 1/8 in.)	McMaster Carr	McMaster Carr / 91771A074		$6.20 per 100	0.0	11	$0.68	0.1
Inner cable	Hosmur	Cascade		$134 per 100 ft.	7.0	1 ft.	$1.34	7.0
Teflon liner	Hosmur	Cascade		$66 per 25 ft.	3.5	1 ft.	$2.64	3.5
Flexible conduit	Hosmur	Cascade		$112 per 25 ft.	10.5	1 ft.	$4.48	10.5
FSR (optional)	Interlink Electronics	Sparkfun / SEN-09673 ROHS		$7.83	0.5	1	$7.83	0.5
FSR adapter (optional)	In-house	FSR inline adapter.x3g (PLA)	4 / 1	$0.01	0.2	1	$0.01	0.2
Total		**250 mm tactor cable**	76 / 30 [(b)]				$49.90	35.7
		75 mm tactor cable					$45.05	20.0

(a) Conversions made using 1.31 CAD to 1.00 USD, as of August 6, 2015, costs do not include shipping, taxes, or fees

(b) Note that an approximate additional 30 minutes is required to assemble the components and attach them to the socket, increasing the total manual labour required to approximately 1 hour per tactor.

Appendix C. Tactor Sleeve Integration

Figure C.1 Image of the prototype tactor sleeve

A preliminary prototype[11] was constructed by mounting the cable-driven tactor onto a wearable plastic sleeve controlled by an Arduino microcontroller and a force sensitive resistor (FSR) to provide proportional control. It was found that the tactor lifted the sleeve away from the skin, suggesting that a rigid socket should be developed to resist these forces and more accurately mimic a prosthetic socket.

The initial design incorporated five cable-driven tactors onto a rigid sleeve to simulate the rigidity of a prosthetic socket. It contains two rapid prototyped halves connected by adjustable straps, with a controller and five tactor systems mounted on top. Inside is a removable liner. Inner studs would be placed between the skin and the liner to improve force transmission.

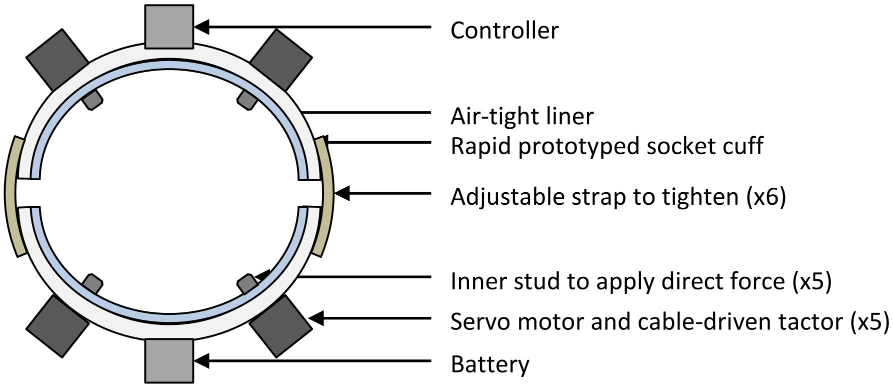

(a)

---

[11] The cable-driven tactor flexible prototype sleeve was initially designed by Kent Herrick during a summer work term

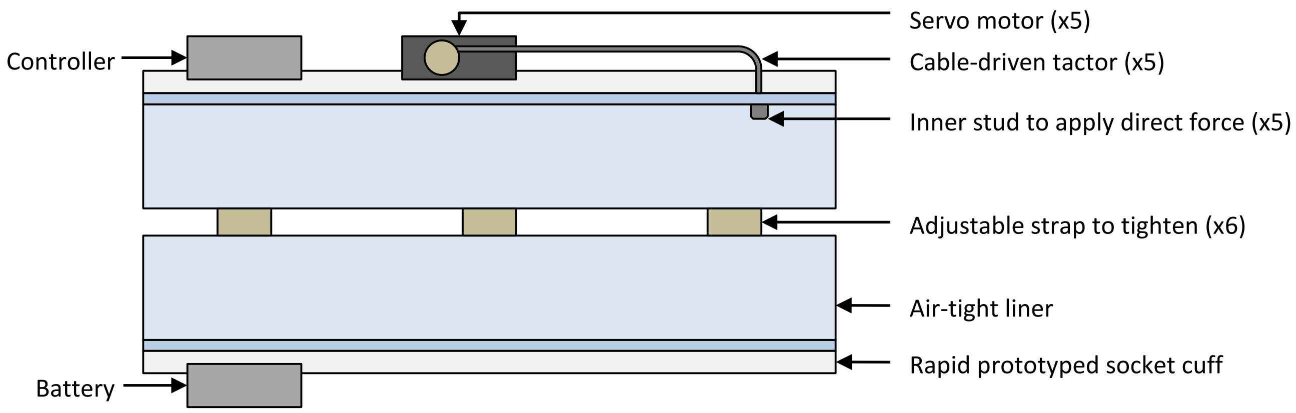

(b)

Figure C.2 Preliminary diagram of socket cuff from (a) front view and (b) cut-away side view

The prototype design for the rigid sleeve included a hinge and clamping method of attachment (rather than straps) to provide rigidity, three cable-driven tactors were incorporated due to space limitations, with no studs through the liner for initial testing. The prototype was slightly curved to allow for changes in the diameter of the upper arm, where sleeve diameters could be altered for different arm geometries.

This prototype sleeve demonstrated the feasibility of integrating the cable-driven tactors onto a rigid surface. In the future, this design may be used for able-bodied usability trials where tactors are placed on the upper arm to simulate the set up for an amputee prosthetic user.

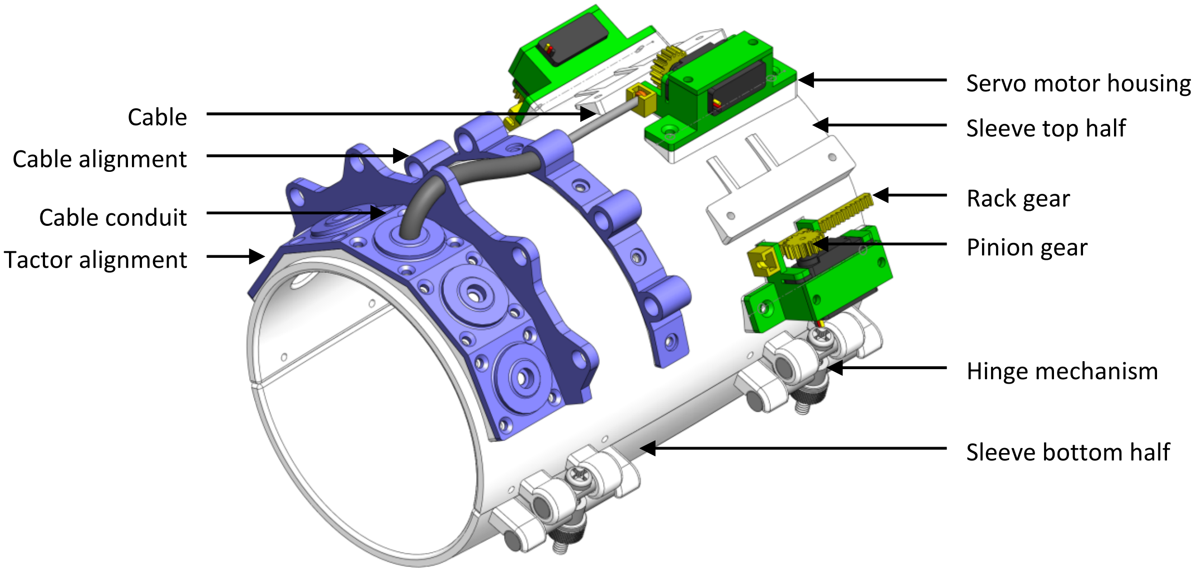

(a)

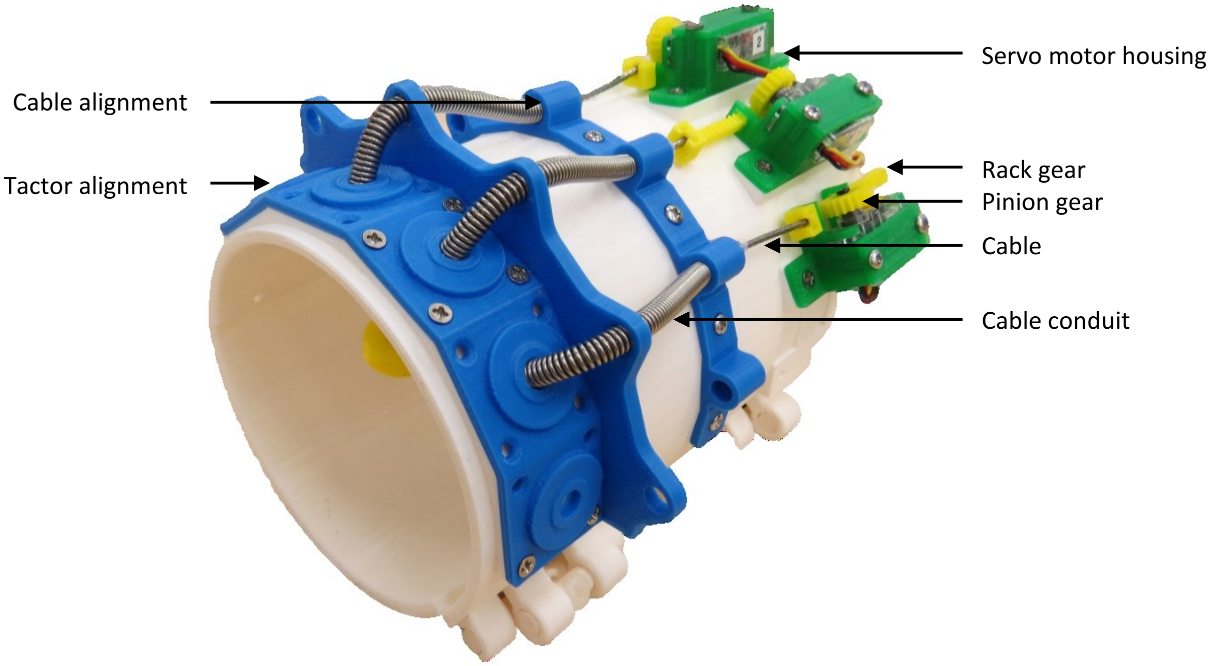

Figure C.3 Prototype of socket cuff (a) design, and (b) printed and assembled

One limitation with this integration is that both the tactors and sleeve are rapid prototyped to complement each other; in a real prosthetic socket, the surface is less geometric, due to the draping process used to manufacture the socket.

Appendix D. Bill of Materials

Table D.1 Bill of Materials for electronics subsystem

Component	Manufacturer	Supplier / part number / part file	Printing / cleaning time (min)	Cost per part ($CAD) (a)	Estimated mass per part (g)	Quantity	Total cost ($CAD)	Total mass (g)
Switch board(b)	In-house	N/a		$53.74	8	1	$53.74	8
Power board(b)	In-house	N/a			4	1		4
Tactor controller(b)	In-house	N/a			5	1		5
Pin board(b)	In-house	N/a			4	1		4
Wiring and connectors(b)	In-house	N/a			10	1		10
Battery	Tenergy	Li-Ion 18650 7.4V 2200mAh Rechargeable Battery Module w/ PCB Protection		$14.00	94	1	$14.00	94
Tactor switch(b)	E-Switch	Digikey / CKN5001-ND		$5.55	1	1	$5.55	1
Micro USB adapter	Qualprors	Amazon / B00KKW4C4I		$2.73	13	1	$2.73	13
Enclosure	In-house	Enclosure.x3g	132 / 5	$1.58	33	1	$1.58	33
Board holders	In-house	Ninjaflex holders.x3g	41 / 1	$1.32	10	1	$1.32	10
Terminal device sensors (FSR) (a)	Interlink Electronics	Sparkfun / SEN-09673 ROHS		$7.89	1	5	$39.45	5
Total			173 / 6				$118.37	187

(a) Conversions made using 1.31 CAD to 1.00 USD, as of August 24, 2015, costs do not include shipping, taxes, or fees

(b) Combined total of approximately 2 skilled hours to assemble

Table D.2 Bill of Materials for temporary prosthetic arm

Component	Manufacturer	Supplier / part number / part file	Printing / cleaning time (min)	Cost per part ($CAD) (a)	Estimated mass per part (g)	Quantity	Total cost ($CAD)	Total mass (g)
Forearm	Hosmer	E400 Forearm Assembly 50 mm		$704.26	650	1	$704.26	650
Lift assist	Hosmer	Lift Assist Unit		$177.86	20	1	$177.86	20
Lamination ring	Otto Bock	10S1		$153.00	15	1	$153.00	15
One-way air valve	Trulife	P190000006		$100.00	5	1	$100.00	5
Shoulder brace	Otto Bock	Acro ComfortT / 5055		$87.50	500	1	$87.50	500
Wrist adapter	In-house	Wrist adapter.x3g	86 / 1	$1.06	22	1	$1.06	22
Coaxial plug	Otto Bock	9E169		$200 (b)	3	1	$200	3
EMG electrodes	Motion Control	Triad Preamp System		$1600 (b)	5	2	$3200	10
EMG wires	Otto Bock	13E129=G		$84.66	1	2	$169.32	2
Temporary socket(c)	In-house	N/a		$100	355	1	$100.00	355
Battery charger	Tenergy	Tenergy Smart Universal TLP-2000 Li-Ion/Li-Po Battery Pack Charger: 3.7V-14.8V		$52.00	N/a	1	$52.00	N/a
Total							$4945	1582

(a) Conversions made using 1.31 CAD to 1.00 USD, as of August 24, 2015, costs do not include shipping, taxes, or fees

(b) Approximate costs

(c) Approximately 4 skilled hours to manufacture

Appendix E. Calibration of Applied Tactor Forces

First maximum grip force of the BeBionic hand was measured by maximally closing the prosthetic hand around the load cell, with both stiff (PLA) and compliant (Alpha liner) materials over the contact areas. It was found to be 18 ± 2 N.

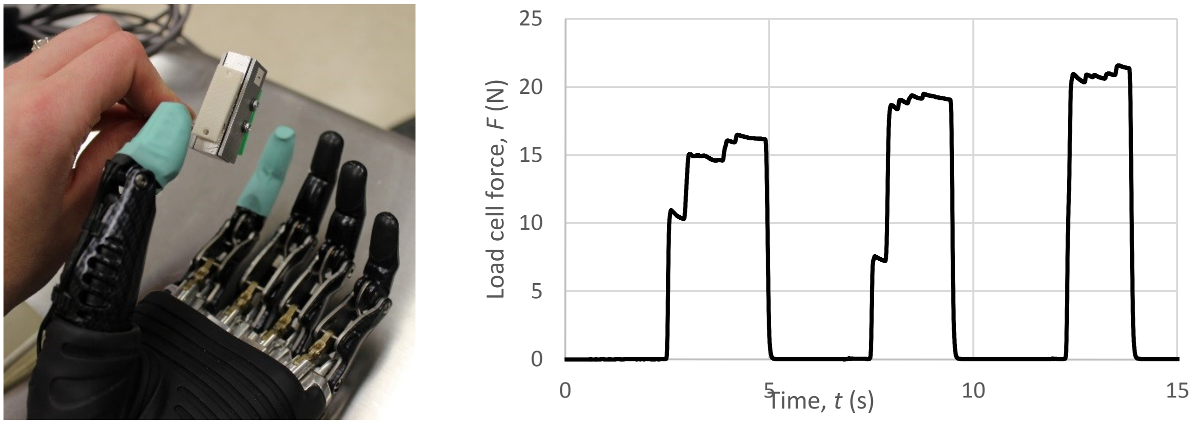

(a) (b)

Figure E.1 Maximual force measurement of the BeBionic hand (a) test set-up, and (b) raw data

The relationship between applied forces to the fingers and measured FSR response was determined by pressing onto each digit by hand with a load cell up to 20 N, with a layer of Alpha liner to provide compliance on the contact area. The resultant calibrations have a mean average error between 0.8 and 0.9 N. Note that FSR error may increase as a result of factors such as differences in compliance, loading rate, and contact area [86], so this calibration may not be valid for cases outside of the calibration.

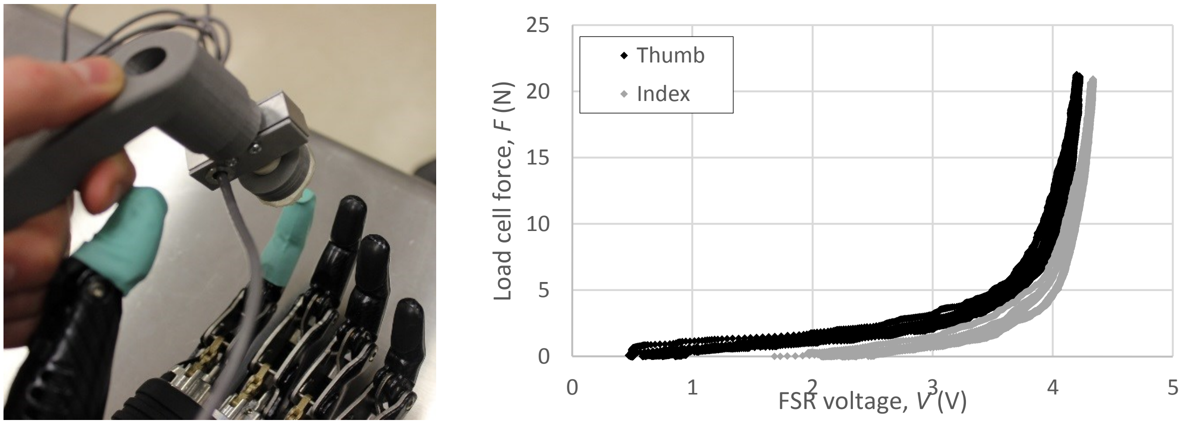

(a) (b)

Figure E.2 Calibration for FSRs (a) test set-up, and (b) raw data

Displacement ranges were determined by loading the participant's arm at each location up to his reported maximal comfort three times, and taking the conservative (lowest) range for mapping displacement for the remainder of the trial.

Finally, calibration of the tissue compliance was determined by loading a linear tactor onto the skin at three different loading rates (sine wave with period of 2, 1, and 0.5 s), with forces measured by the in-line load cell.

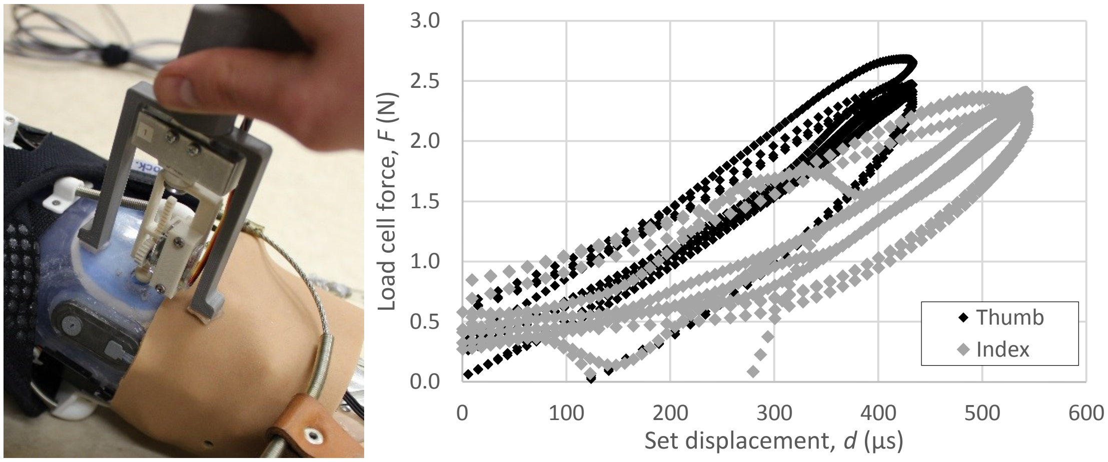

(a) (b)

Figure E.3 Calibration for FSRs (a) test set-up, and (b) raw data

Combining these calibrations produce the approximate curve shown below. Errors not accounted for in the displayed error bars include differences in FSR response based on compliance, loading rate, and contact area of applied forces, as well as differences in forces applied to the arm based on changes to tissue compliance over time and with muscle contraction or shifting of the arm relative to the tactor. There may also be some error resulting from differences between displacement outputs from the linear tactor (used in calibration) to the cable-driven tactor (used in application). These large errors indicate that investigation into a higher accuracy input sensor more accurate method of applying forces to the arm are warranted.

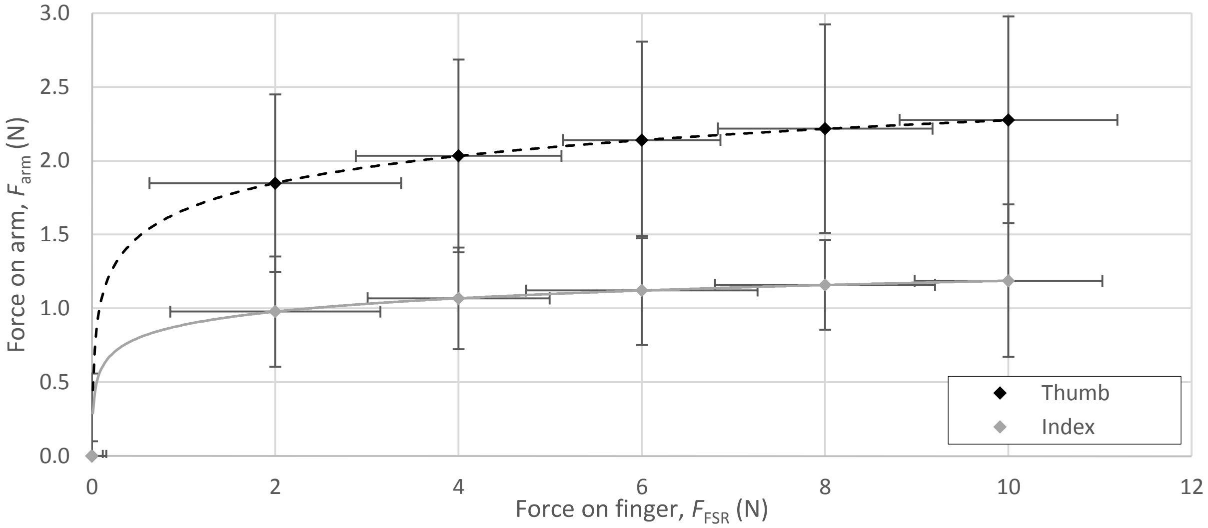

Figure E.4 Approximate mapping between input force to the prosthetic finger to forces applied by the tactor to the residual limb

Appendix F. Interfaces and Circuit Diagrams

The interfaces and circuit diagrams used for initial evaluation of sensors are shown below.

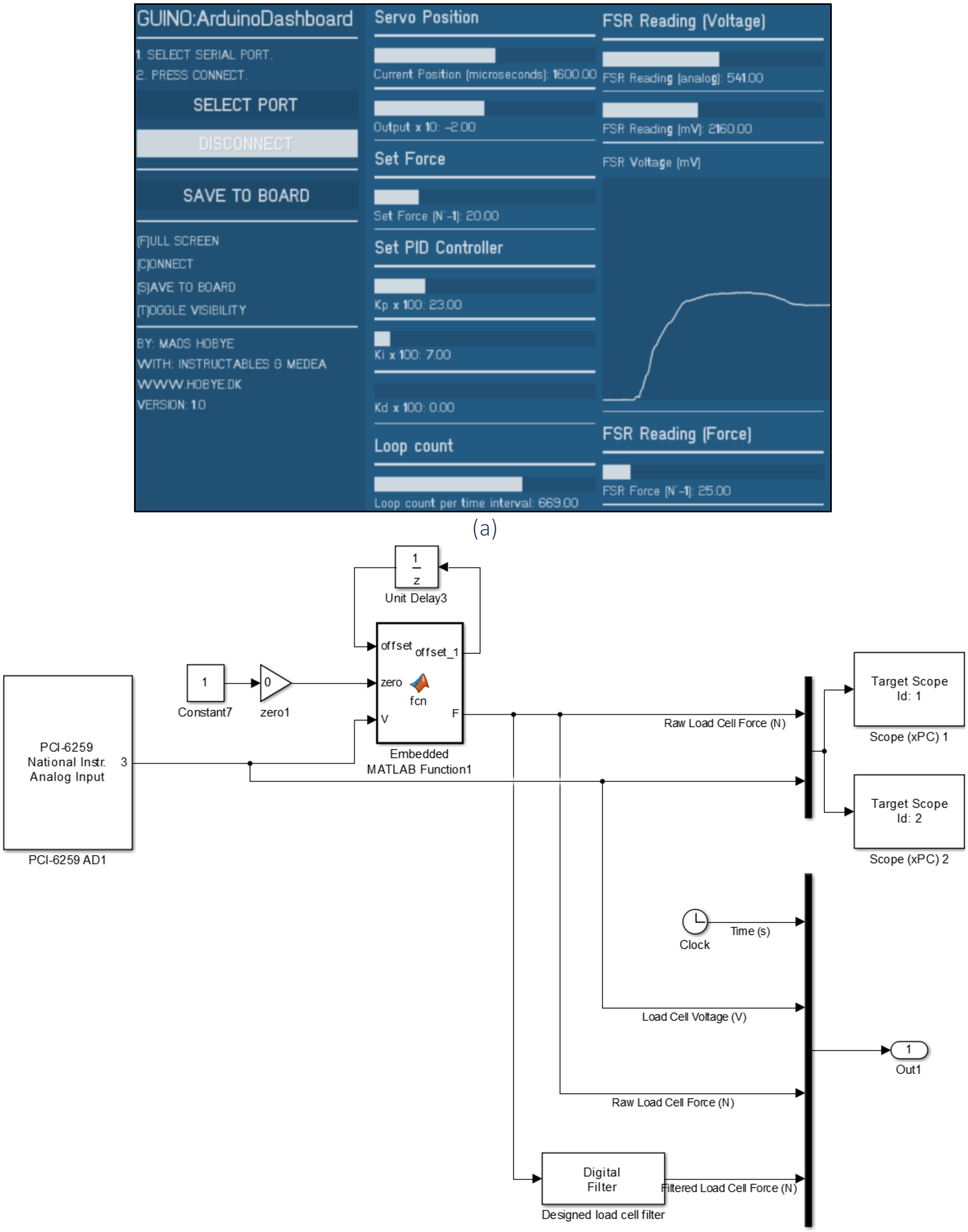

Current Position (microseconds): 1600.00

Output x 10: -2.00

Set Force (N^-1): 20.00

Kp x 100: 23.00

Ki x 100: 7.00

Kd x 100: 0.00

Loop count per time interval: 669.00

FSR Reading (analog): 541.00

FSR Reading (mV): 2160.00

FSR Force (N^-1): 25.00

BY: MADS HOBYE
WITH: INSTRUCTABLES & MEDEA
WWW.HOBYE.DK
VERSION: 1.0

(b)

Figure F.1 Sensor control (a) Arduino GUI and (b) Simulink Real Time interface

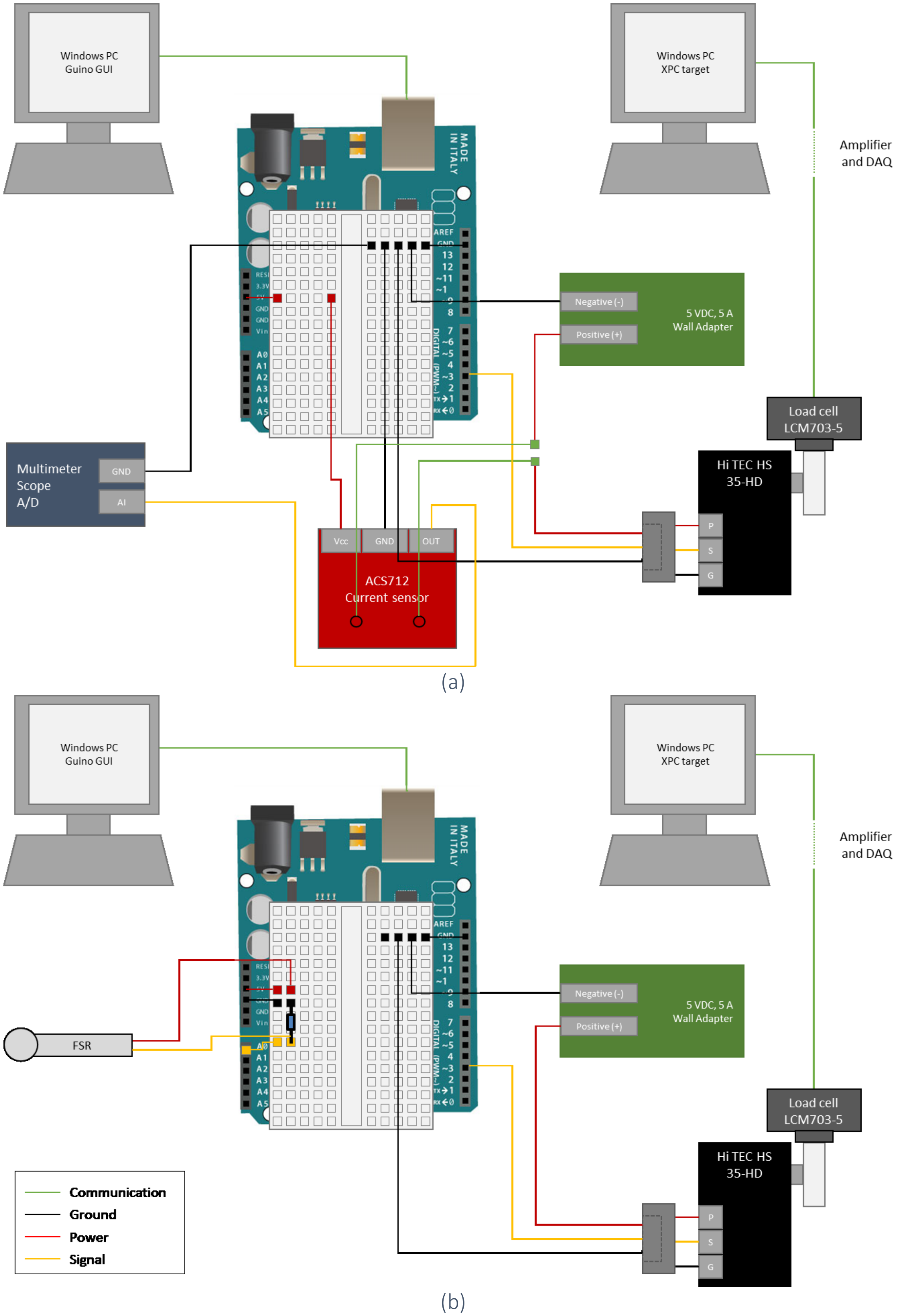

Figure F.2 Circuit diagram of (a) current sensor calibration and (b) FSR calibration

The interface and wiring diagram for the filtering analysis is shown below.

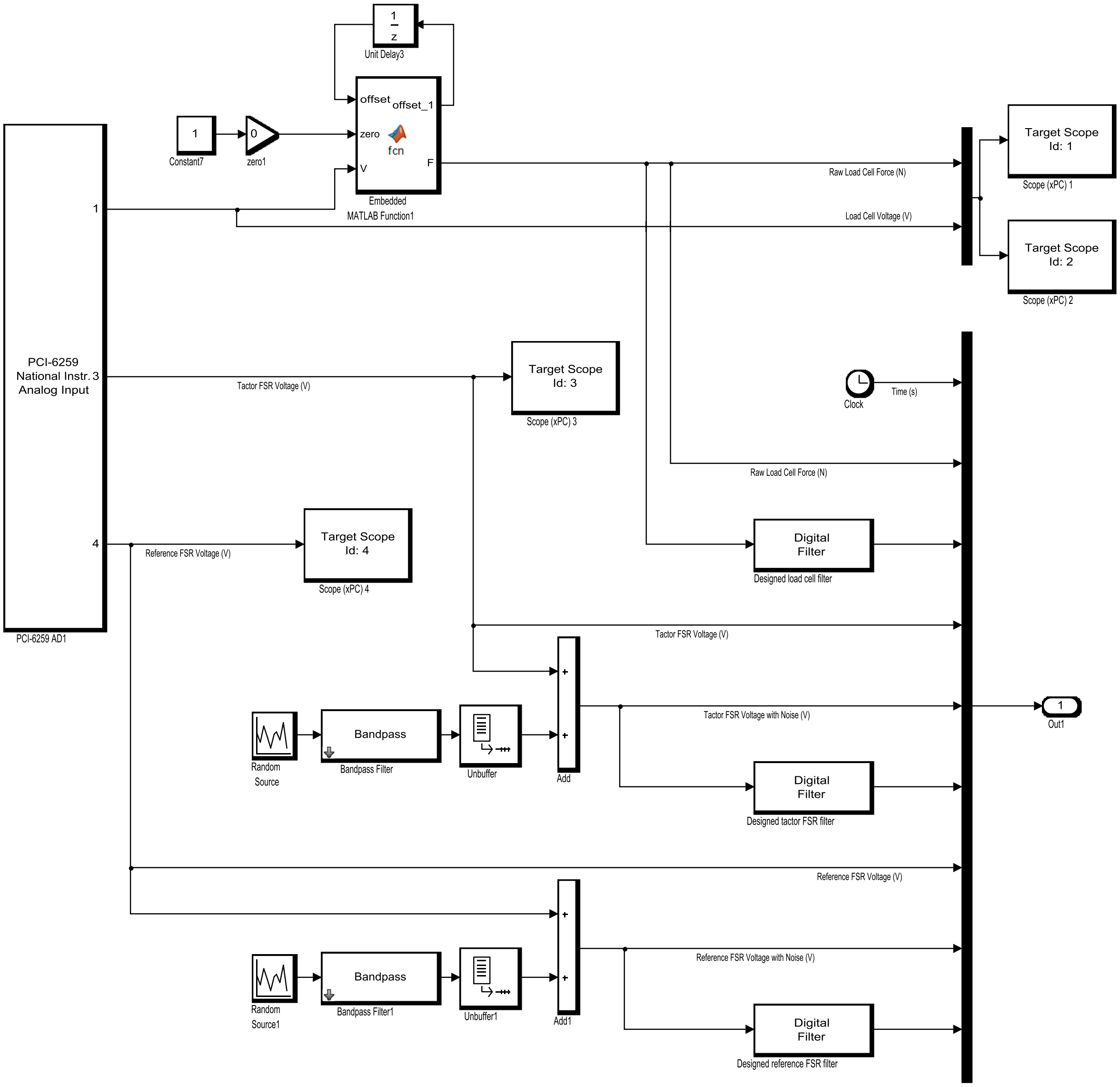

Figure F.3 Schematic of Simulink Real Time interface

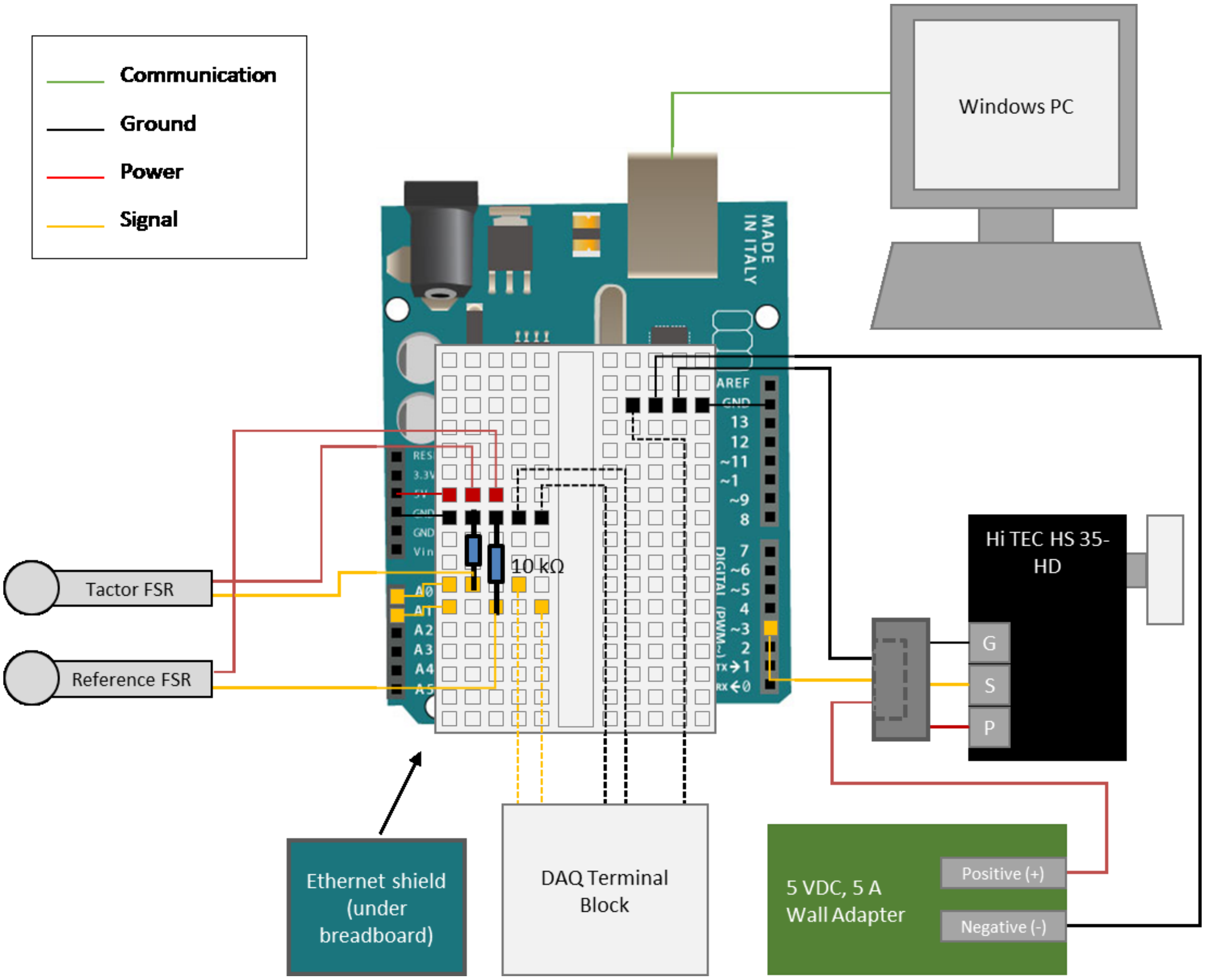

Figure F.4 Wiring diagram of Arduino controller, where dotted lines indicate temporary connections used to communicate with the DAQ terminal block

Appendix G. Interface and Data Logging

An open source graphical user interface (Guino, by Madshobye) was used for initial testing, as this allowed real time adjustment of PID tuning parameters and observation of the results. There were several drawbacks that led to the abandonment of this GUI: data could not be logged (only displayed), the graphs could not be made to show axes (so time response and overshoot could not be quantified), and the serial communication between the Arduino controller and the computer significantly slowed down cycle frequency. This resulted in a slow response time of the controller which was very different to the response time when the GUI wasn't being used (so different tuning parameters would be required, defeating the purpose of being able to adjust them in real-time in the first place).

Next an attempt was made to integrate a data logger (OpenLog, SparkFun) into the system, which would log data internally via one way transmission of serial data to a microSD card, which could then be downloaded after each test was complete. It was found that this significantly slowed the system, more so than the GUI. Attempts were made to minimize the amount of data being transferred, but this did not result in a noticeable change. In addition, the OpenLog tended to create multiple files, and output garbage data (particularly at high rates of data transfer), so it was deemed unacceptable for this application.

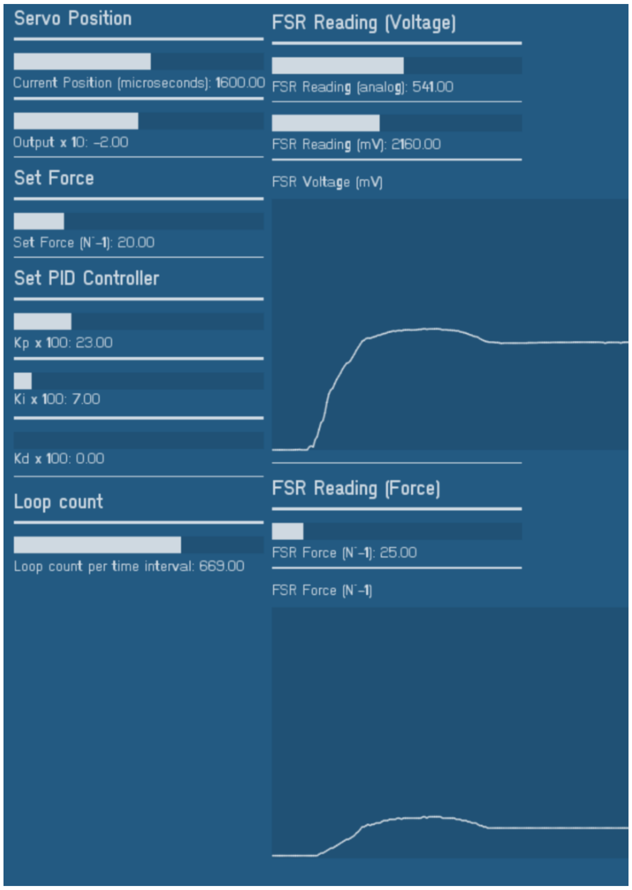

Servo Position

Current Position (microseconds): 1600.00

Output x 10: -2.00

Set Force

Set Force (N^-1): 20.00

Set PID Controller

Kp x 100: 23.00

Ki x 100: 7.00

Kd x 100: 0.00

Loop count

Loop count per time interval: 669.00

FSR Reading (Voltage)

FSR Reading (analog): 541.00

FSR Reading (mV): 2160.00

FSR Voltage (mV)

FSR Reading (Force)

FSR Force (N^-1): 25.00

FSR Force (N^-1)

Figure G.1 Sample GUI of tactor control system

A different method of data logging was also attempted, instead using the Ardino Ethernet Shield, which logs data to the microSD via a Serial Peripheral Interface (SPI) bus. This did not have as much of a problem outputting multiple logs or sending garbage data. The communication speed was adjusted to maximum. Even so, at the high cycle frequency being used, the controller was unable to log data fast enough, which resulted in slowing down the system overall. An optimization was conducted to understand how often data could be sent to the logger without substantially slowing down the loop cycle time, and it was found that sampling every 100 loops would not slow the response substantially.

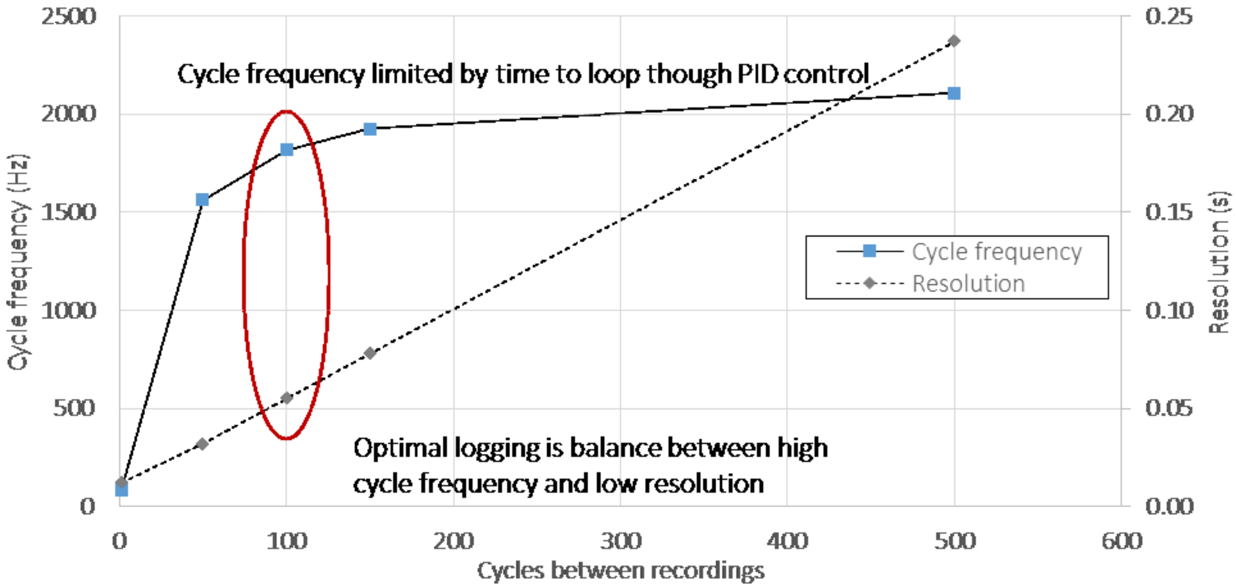

Figure G.2 Optimization of data logger to select recording frequency

After working with the system to calibrate the tactor FSR, it was determined that logging load cell data to the DAQ and FSR data to the microSD card was not efficient, as data from both sources needed to be aligned manually, and differences in timing (as well as some dropped data) made this very difficult. It was decided that moving forward all data would be logged to the DAQ, as this would allow for all of the data to be collected (rather than every 100 cycles, with some information lost), output all data synced together (which would make post-processing much more efficient), and would not slow down the controller cycle frequency (representative of the final controller).

The data logger will be used in the future to get an idea of what forces are being measured by the FSR on the prosthesis and applied to the residual limb, but not at the high frequencies required for accurate calibration and tuning.

Appendix H. Sample Rate Selection and Memory

Based on the initial testing with the data logger, a maximum loop frequency for the PID controller was determined to be approximately 2100 Hz. The servo motor receives signals at a frequency of 50 Hz. A sample rate of 1000 Hz was initially selected as it was within the systems capabilities. A frequency plot of sample data is shown below.

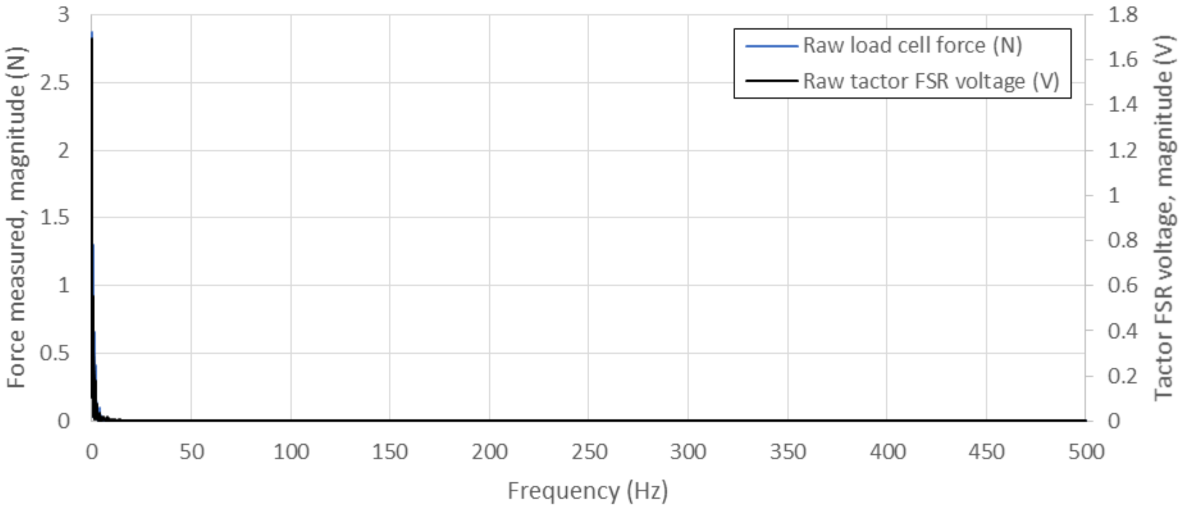

Figure H.1 Frequency magnitude data from load cell and FSR.

There do not appear to be any frequency components above approximately 20 Hz, which suggests that the data was being oversampled. After the initial design of several FIR filters, it was determined that a 1000 Hz sample frequency was too high, as it required a large storage of coefficients and inputs (up to 31 terms for a moving average filter and 237 for a Hanning window filter). Further information about the available memory on the controller was investigated.

The Arduino UNO has three different types of memory. Flash memory stores the sketch. Static random access memory (SRAM) is where variables are created and manipulated, and is volatile (lost when the power is turned off). Electrically erasable programmable read-only memory (EEPROM) holds long-term information that needs to be accessed periodically, and is non-volatile. Each type of memory is allocated a different amount of bytes of memory on the ATmega328 chip on the Arduino Uno, as given below [129].

Flash: 32 kB
SRAM: 2 kB
EEPROM: 1 kB

For filtering parameters, information should be stored as SRAM, since it is called in each loop (so there is no benefit to storing it long term, since it would need to be read in each loop). Therefore there is a total of 2000 Bytes with which to store all of the parameters related to the sketch (including reading in values, filtering, controlling, and logging). Without filtering, the following memory is in use for a single PID controlled tactor:

```
Sketch uses 19,906 bytes (61%) of program storage space. Maximum is 32,256 bytes.
Global variables use 1,295 bytes (63%) of dynamic memory, leaving 753 bytes for local variables.
Maximum is 2,048 bytes.
```

And for two PID controlled tactors:

```
Sketch uses 21,094 bytes (65%) of program storage space. Maximum is 32,256 bytes.
Global variables use 1,395 bytes (68%) of dynamic memory, leaving 653 bytes for local variables.
Maximum is 2,048 bytes.
```

And for three PID controlled tactors:

```
Sketch uses 22,244 bytes (68%) of program storage space. Maximum is 32,256 bytes.
Global variables use 1,499 bytes (73%) of dynamic memory, leaving 549 bytes for local variables.
Maximum is 2,048 bytes.
```

Therefore each additional PID controlled tactor adds approximately 100 Bytes of SRAM memory to operate. A double value on an Arduino Uno requires 4 Bytes of space [130]. Using this information the table below was determined.

Table H.1 Memory requirements for varying numbers of PID controlled tactors and remaining memory

Number of PID controlled tactors	SRAM in code without filtering (Bytes)	SRAM remaining (Bytes)	Maximum coefficients per filter*
1	1295	753	44
2	1395	653	25
3	1499	549	15
4	1599*	449*	10
5	1699*	349*	6

*Estimated

A minimum of two tactors will be used for this system, so for this reason a maximum of 25 coefficients can be used in the final filter selected. In future controller designs, a larger memory space is necessary, such as on the ATmega32U4 chip found on the Arduino Leonardo (which has 2.5 kB of SRAM, which would allow for 16-term coefficient filters when 5 PID controlled tactors are operated).

Appendix I. Design of a Moving Average Filter

The Moving Average filter was developed manually for the case of the reference tactor with the following specifications:

Cut-off frequency, f_c: 14 Hz
Sampling frequency, f_s: 250 Hz

The digital cut-off frequency is:

$$\Omega = 2\pi \, {}^{f}\!/_{f_s} = 0.352$$

Then the number of terms, M, is given by:

$$M = \frac{\pi}{0.352} = 8.9$$

Because the cut-off should not be lower than 14 Hz, and the number of terms should be odd (so that the window is symmetrical) a window size of 7 was selected, as shown below.

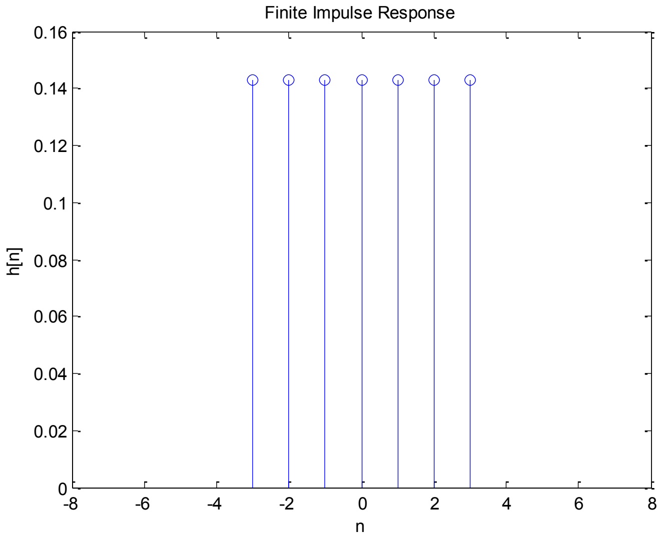

Figure I.1 Filter shape for Moving Average filter

This gives the following 7 term transfer function (only first few terms included):

$$H(z) = 0.1428 + 0.1428z^{-1} + 0.1428z^{-2} + 0.1428z^{-3} + \cdots$$

Which yields the pole zero map below.

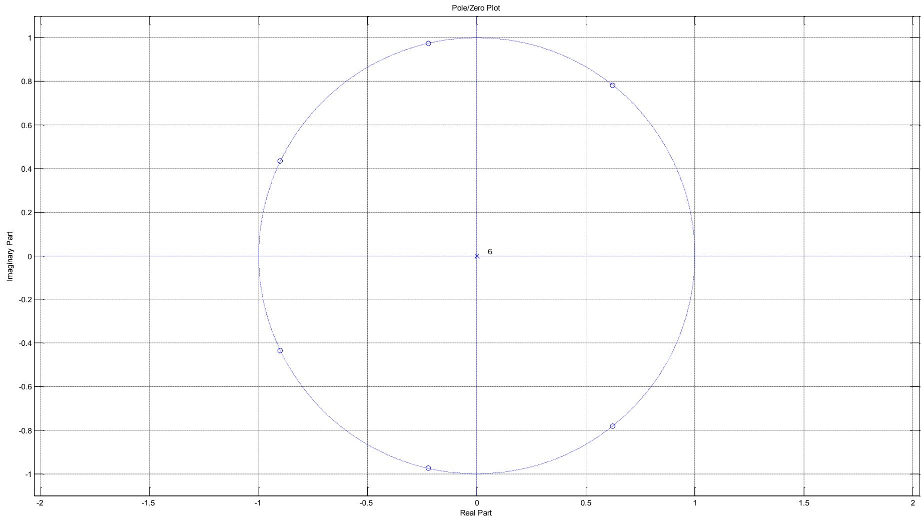

Figure I.2 Pole zero map for Moving Average filter

Because this is a FIR filter, all of the poles are located at the origin, so this is a stable filter. There are zeros on the unit circle, suggesting that there are very small filter magnitudes associated with some frequencies.

The 7 term difference equation is given below (again truncated for space):

$$y[n] = 0.1428x[n] + 0.1428x[n-1] + 0.1428x[n-2] + 0.1428x[n-3] + \cdots$$

Or represented as a non-recursive difference equation diagram:

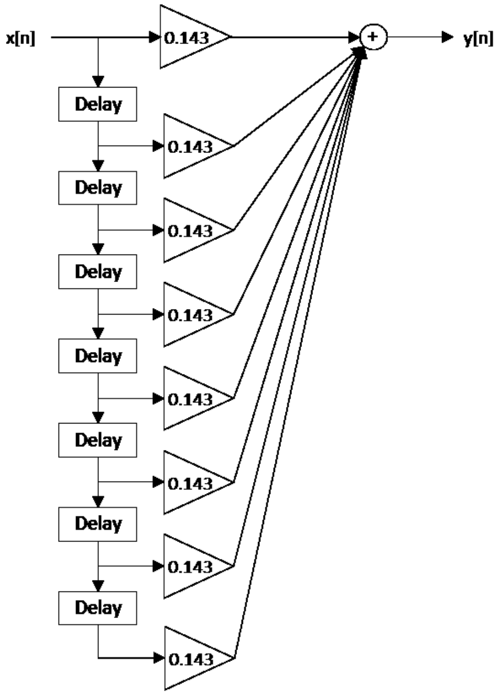

With the frequency response:

$$H(\Omega) = 0.1428 + 0.1428e^{-j\Omega} + 0.1428e^{-j2\Omega} + 0.1428e^{-j3\Omega} + \cdots$$

Which yields the filter shape and phase response:

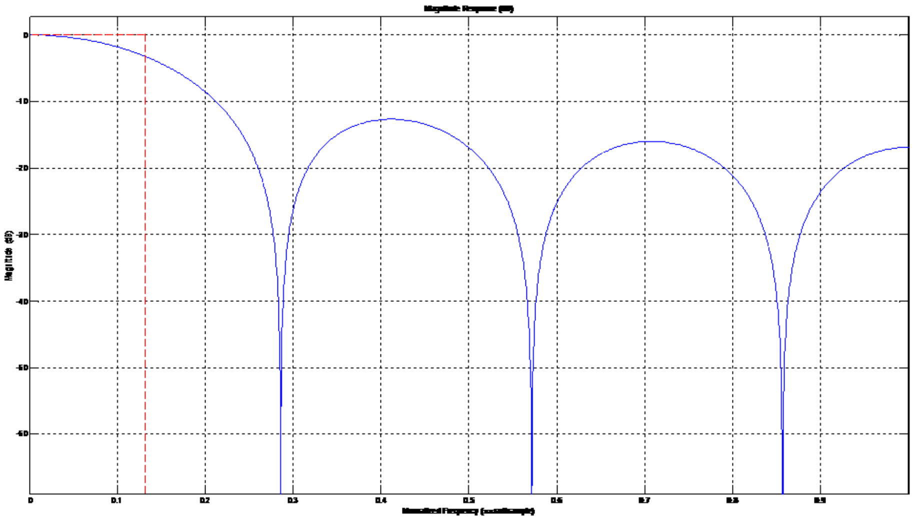

Figure I.3 Filter shape for Moving Average filter.

From this, the stop band attenuation is approximately 13 dB, or a gain of 0.224

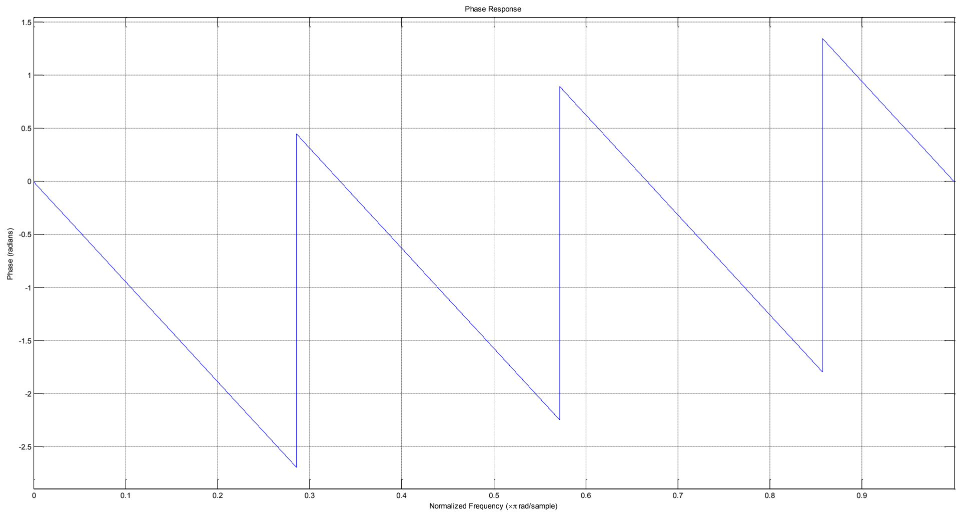

Figure I.4 Phase response for Moving Average filter

There is no non-linearity in the pass band, suggesting that phase distortion will not occur, although there will be a lag for all data points. In this case, looking for example at $\Omega_0 = 0.1\pi$, the phase delay (*n*) is:

$$n = -\frac{\theta(\Omega_0)}{\Omega_0} = -\frac{-0.9}{0.1\pi} = 2.87 \approx 3 \text{ samples}$$

At a sampling frequency of 250 Hz, this corresponds to a dealy of 0.012 s.

The filter for the tactor FSR was designed in the same way, only with slightly different specifications:

Cut-off frequency, f_c: 30 Hz

This resulted in a window size of 3, with the following difference equation:

$$y[n] = 0.3333x[n] + 0.3333x[n-1] + 0.3333[n-2]$$

The code developed in matlab is given below.

```
windowSize = 7;
Mov_avg = (1/windowSize)*ones(1, windowSize);

N = windowSize;
n=[];
for j = 1:N
n(j)=j-(N+1)/2;
end

stem(n,Mov_avg);
title('Finite Impulse Response'); xlabel('n'); ylabel('h[n]');
axis([-8,8,0,0.16]);

fvtool(Mov_avg)
```

Appendix J. Design of a Hanning Window Filter

The Hanning Window filter was first developed manually to better understand the process of designing a digital filter, for the case of the reference tactor with the following specifications:

Pass band, *PB*: 7 Hz
Stop band, *SB*: 21 Hz
Sampling frequency, f_s: 250 Hz

The pass band edge frequency (f_1) was then calculated:

$$f_1 = PB + \frac{SB - PB}{2} = 14 \text{ Hz}$$

The digital pass band edge frequency (Ω_1) was then calculated:

$$\Omega_1 = 2\pi \frac{f_1}{f_s} = 0.3519$$

The infinite impulse response for an ideal low-pass filter was then represented by:

$$h_1[n] = \frac{\sin(0.3519n)}{\pi n}$$

Which is presented graphically below:

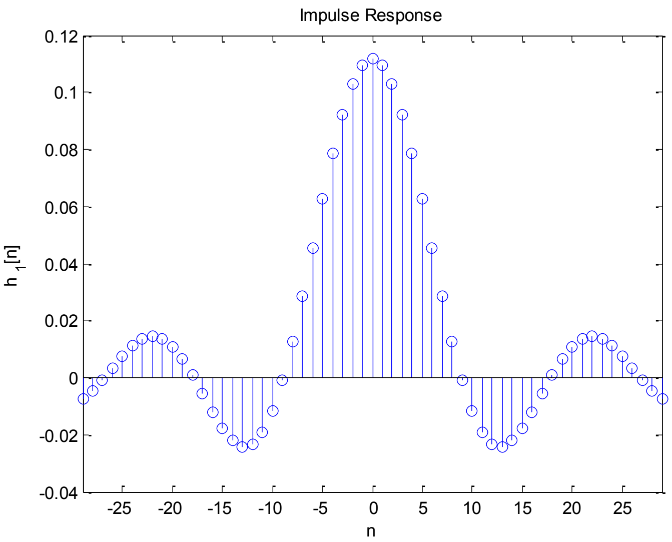

Figure J.1 Infinite impulse response for ideal low-pass filter

For a Hanning Window, the number of terms is given by:

$$N^* = 3.32\frac{f_s}{SB - PB} = 59.2857$$

Then rounding to the nearest odd integer gives a number of terms (*N*) equal to 59.

The Window function is then given by the equation:

$$w[n] = 0.5 + 0.5\cos\left(\frac{2\pi n}{N-1}\right) \qquad \text{for } |n| \leq \frac{N-1}{2}$$

Which is presented graphically below:

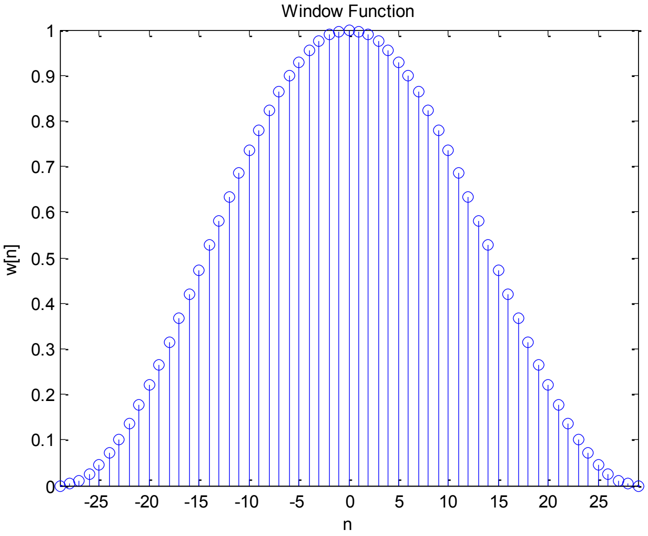

Figure J.2 Window function for Hanning Window of specified width

Calculating the finite impulse response by multiplying the infinite impulse response by the Window gives the following:

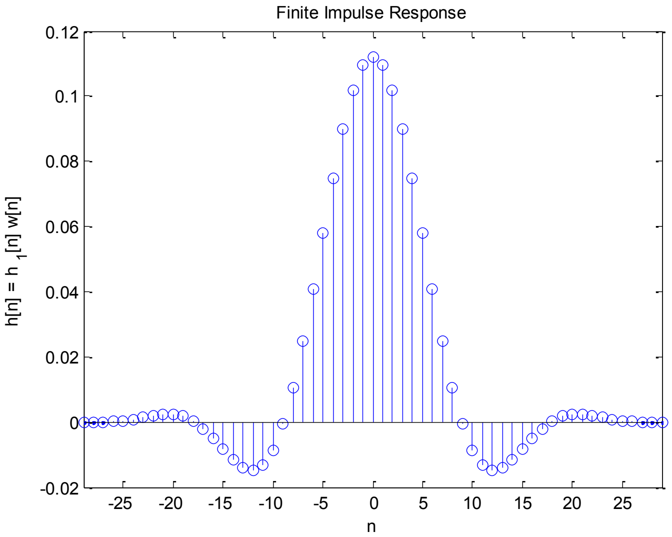

Figure J.3 Finite impulse response for Hanning filter

This gives the following 59 term transfer function (equation truncated for space):

$$H(z) = -0.000014z^{-1} - 0.0000104z^{-2} + 0.0000875z^{-3} + \cdots$$

Which yields the pole zero map below.

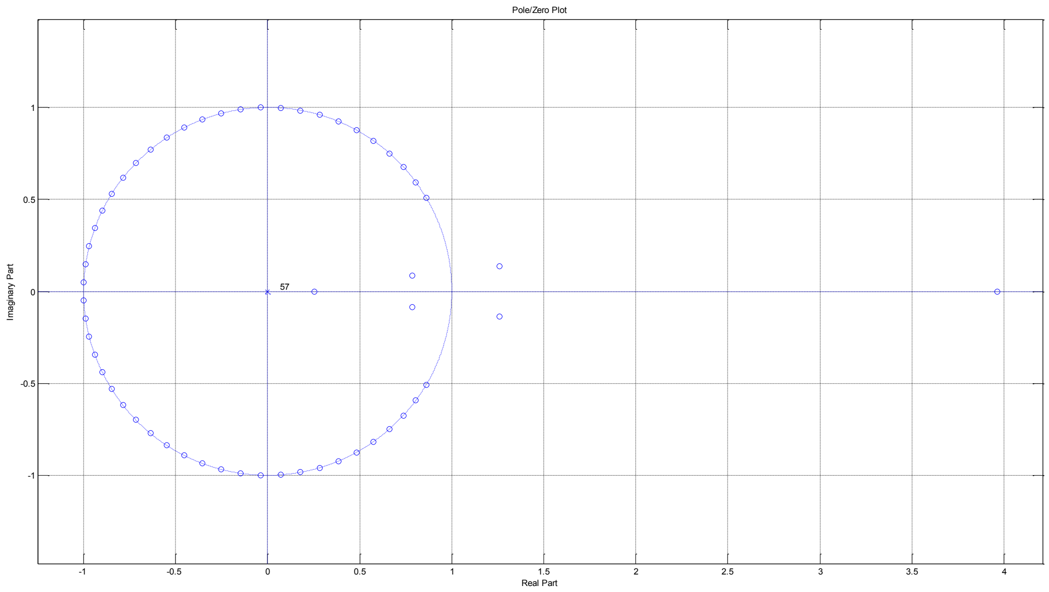

Figure J.4 Pole zero map for Hanning filter

Because this is a FIR filter, all of the poles are located at the origin, so this is a stable filter. There are many zeros on the unit circle, suggesting that there are very small filter magnitudes associated with some frequencies.

The 59 term difference equation is given below (again truncated for space):

$$y(n) = -0.000014x[n-1] - 0.0000104x[n-2] + 0.0000875x[n-3] + \cdots$$

Or represented as a non-recursive difference equation diagram:

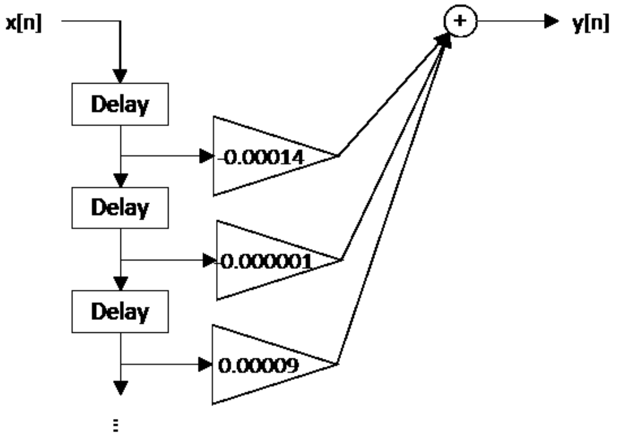

With the frequency response:

$$H(\Omega) = -0.000014e^{-j\Omega} - 0.0000104e^{-j2\Omega} + 0.0000875e^{-j3\Omega} + \cdots$$

Which yields the filter shape:

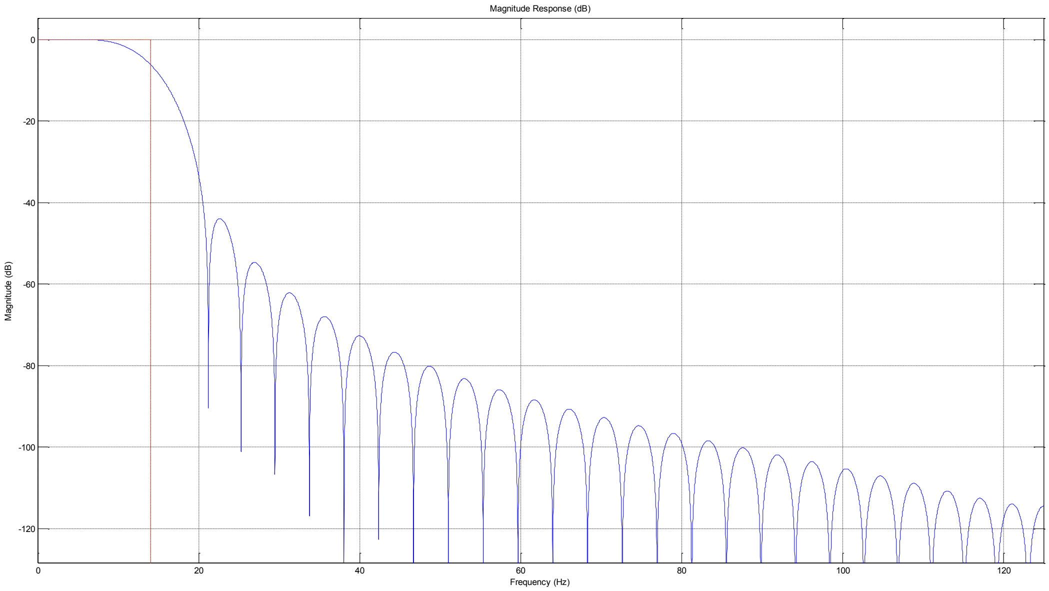

Figure J.5 Filter shape for Hanning filter

From this, the stop band attenuation is approximately 44 dB, or a gain of 0.006.

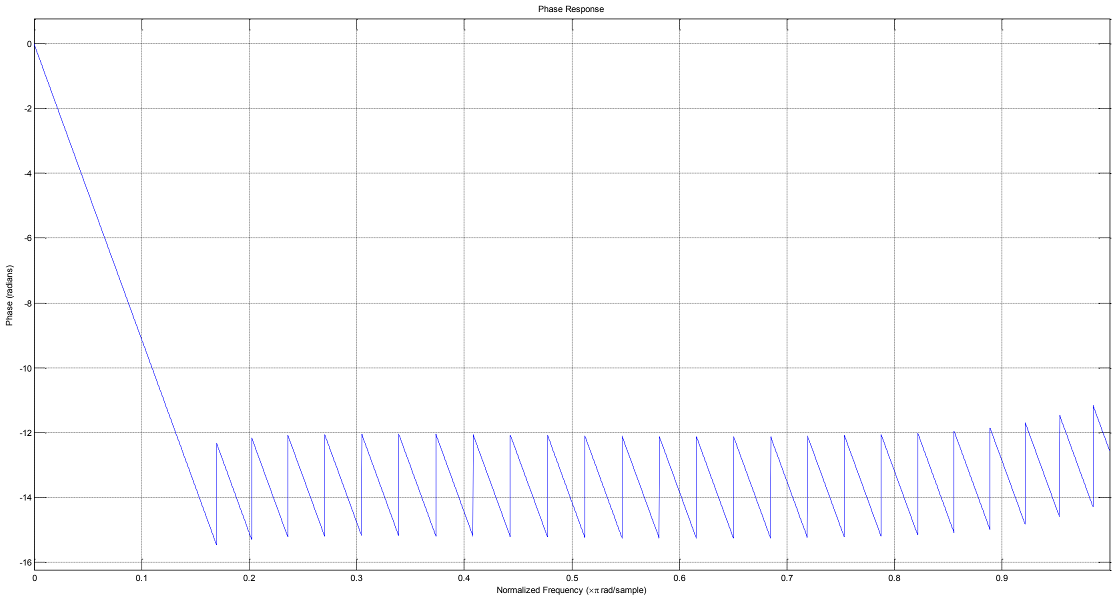

Figure J.6 Phase response for Hanning filter

There is no non-linearity in the pass band, suggesting that phase distortion will not occur. In this case, looking for example at $\Omega_0 = 0.1\pi$, the phase delay (*n*) is:

$$n = -\frac{\theta(\Omega_0)}{\Omega_0} = -\frac{-6}{0.1\pi} = 19.1 \approx 19 \text{ samples}$$

At a sampling frequency of 250 Hz, this corresponds to a dealy of 0.076 s.

The code developed in matlab is given below.

```
PB = 7;
SB = 21;
fs = 250;

TW = SB - PB;
f1 = PB + TW/2;
omega1 = 2*pi*f1/fs;
Nstar = 3.32*fs/TW;
N = fix((Nstar + 1)/2)*2 - 1;

n=[];
for j = 1:N
n(j)=j-(N+1)/2;
end

h1  = [];
for i = 1:N
h1(i) = sin(n(i)*omega1)/(n(i)*pi);
end
h1((N-1)/2+1) = omega1/pi;
```

```
stem(n,h1);
title('Impulse Response'); xlabel('n'); ylabel('h _{1}[n]');
xlim([-(N-1)/2,(N-1)/2]);

w=[];
for i = 1:N
w(i) = 0.5 + 0.5*cos(2*pi* n(i)/(N-1));
end

stem(n,w);
title('Window Function'); xlabel('n'); ylabel('w[n]');
xlim([-(N-1)/2,(N-1)/2]);

h = h1.*w;

stem(n,h);
title('Finite Impulse Response'); xlabel('n'); ylabel('h[n] = h _{1}[n] w[n]');
xlim([-(N-1)/2,(N-1)/2]);

fvtool(h)
```

Note that this filter can also be designed using the designfilt() function, as shown below. It has a filter order of 57.

```
Hann = designfilt('lowpassfir','FilterOrder',N-
1,'CutoffFrequency',f1,'DesignMethod','window','window',hann(N),'SampleRate',250);
```

The filter for the tactor FSR was designed in the same way, only with slightly different specifications:

Pass band, *PB*: 20 Hz
Stop band, *SB*: 40 Hz

Appendix K. Design of Butterworth Filter

A Butterworth filter was investigated since it is monotonic through the pass band and stop band, and is a simple IIR filter to design.

The filter was developed, for the case of the reference tactor, with the following specifications:

Pass band edge frequency, f_{p1}: 7 Hz
Stop band edge frequency, f_{s1}: 21 Hz
Sampling frequency, f_s: 250 Hz
Pass band ripple: 1 dB
Stop band attenuation: 40 dB

These can be converted to digital frequencies using:

$$\Omega = 2\pi \frac{f}{f_s}$$

Resulting in Ω_{p1} being equal to 0.176 rad and Ω_{s1} being equal to 0.528 rad. Next the pre-warped analog frequencies are calculated using:

$$\omega = 2f_s \cdot \tan\left({}^{\Omega}/_{2}\right)$$

Resulting in ω_{p1} being equal to 44.1 rad/s and ω_{s1} being equal to 135.1 rad/s. Then the attenuation is calculated:

$$\delta_s = 10^{-40/20} = 0.01$$

So finally the order required is calculated:

$$n \geq \frac{\log\left({}^{1}/_{{\delta_s}^2} - 1\right)}{2\log\left({}^{\omega_{s1}}/_{\omega_{p1}}\right)} = 4.11$$

Therefore the minimum order of this Butterworth filter is 5. Because the order is greater than 2, the designfilt() function in Matlab was used to develop the Butterworth filter using the code below. This function creates a digital filter object, in place of determining the transfer function, H(s), and performing the bilinear transformation to obtain the digital transfer function, H(z), by hand.

```
Butter = designfilt('lowpassiir','PassbandFrequency',PB,'StopbandFrequency',SB,'PassbandRipple',1,
'StopbandAttenuation',40,'DesignMethod','butter','SampleRate',fs);
```

The coefficients of the transfer function were determined using the function:

```
[b,a] = tf(Butter);
```

The filter was designed to have a minimum order, which was determined to be 5, and is consistent with theory. The filter shape is therefore given by:

$$|H(\omega)| = \frac{1}{\sqrt{\left({}^{\omega}/_{\omega_p}\right)^{2\cdot 5} + 1}}$$

Which produces the plot below.

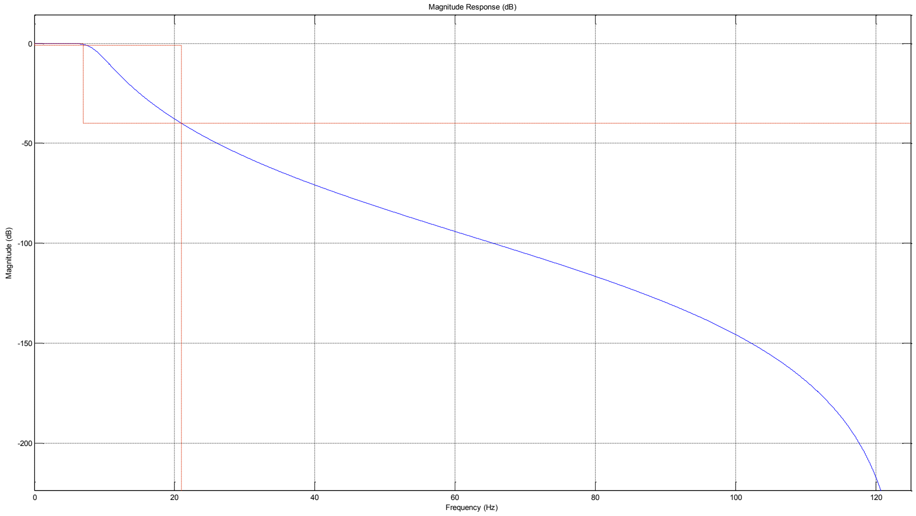

Figure K.1 Filter shape for Butterworth filter

The pole-zero plot was determined in Matlab, and is shown below.

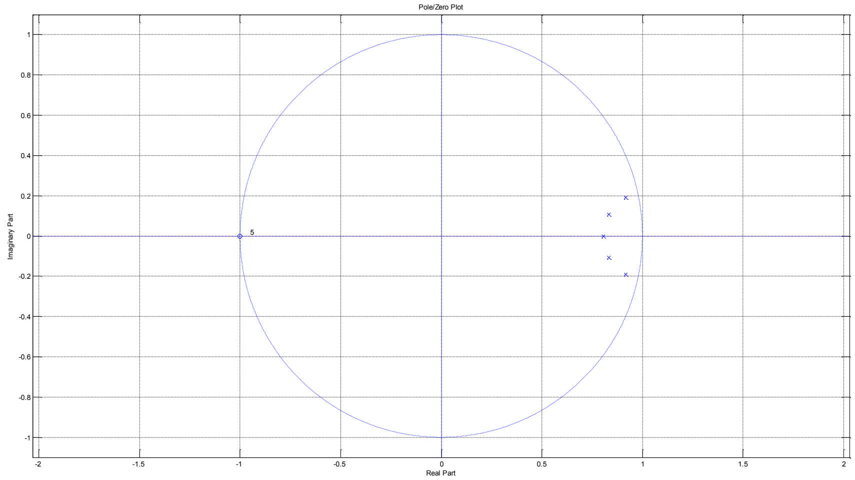

Figure K.2 Pole zero map for Butterworth filter

The poles are located within the unit circle, so the filter is stable. They are all on the right hand side so the filter should not result in alternating between positive and negative values. All but one pole are off of the real axis, suggesting that the filter may result in oscillations. Because the poles are close to the unit circle this is a very selective filter shape. The zeros are very far away from the poles, so they will not reduce the oscillations. In fact these zeros are located on the unit circle, suggesting that there are very small filter magnitudes associated with some frequencies.

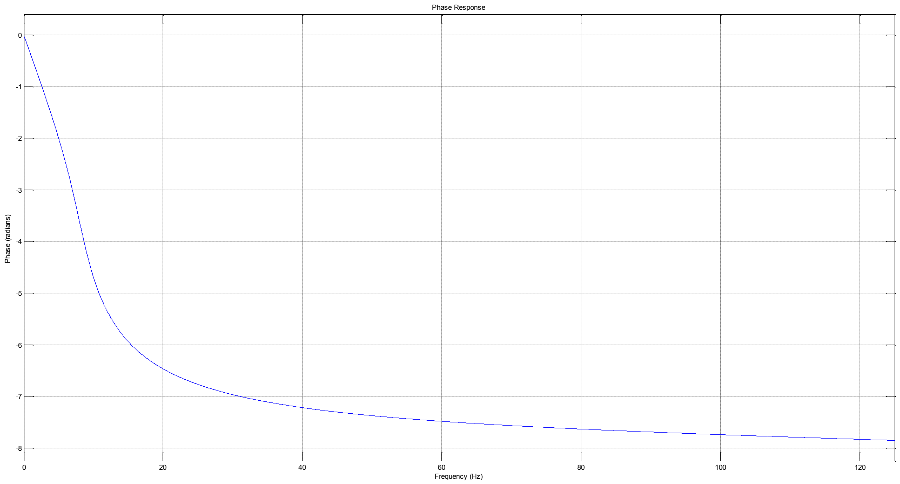

Figure K.3 Phase response for Butterworth filter

The phase response was determined in Matlab. There is some non-linearity in the pass-band, suggesting that phase distortion may occur. In this case, looking for example at Ω_0 = 10 Hz = 0.08π, the phase delay (*n*) is:

$$n = -\frac{\theta(\Omega_0)}{\Omega_0} = -\frac{-4.8}{0.08\pi} = 19.1 \approx 19 \text{ samples}$$

Compared to a phase dealy at Ω_0 = 20 Hz = 0.16π:

$$n = -\frac{\theta(\Omega_0)}{\Omega_0} = -\frac{-6.4}{0.16\pi} = 12.7 \approx 13 \text{ samples}$$

At a sampling frequency of 250 Hz, these correspond to a dealy of 0.076 s and 0.052 s, respectively.

The difference equation is given below:

$$\begin{aligned} y_{Butterworth}[n] & \\ = {} & 0.000001x[n] + 0.00005x[n-1] + 0.0001x[n-2] + 0.0001x[n-3] \\ & + 0.00005x[n-4] + 0.000001x[n-5] + 4.3069y[n-1] - 7.4616y[n-2] \\ & + 6.4962y[n-3] - 2.8408y[n-4] + 0.4990y[n-5] \end{aligned}$$

Or represented as a non-recursive difference equation diagram (Direct Form I Realization):

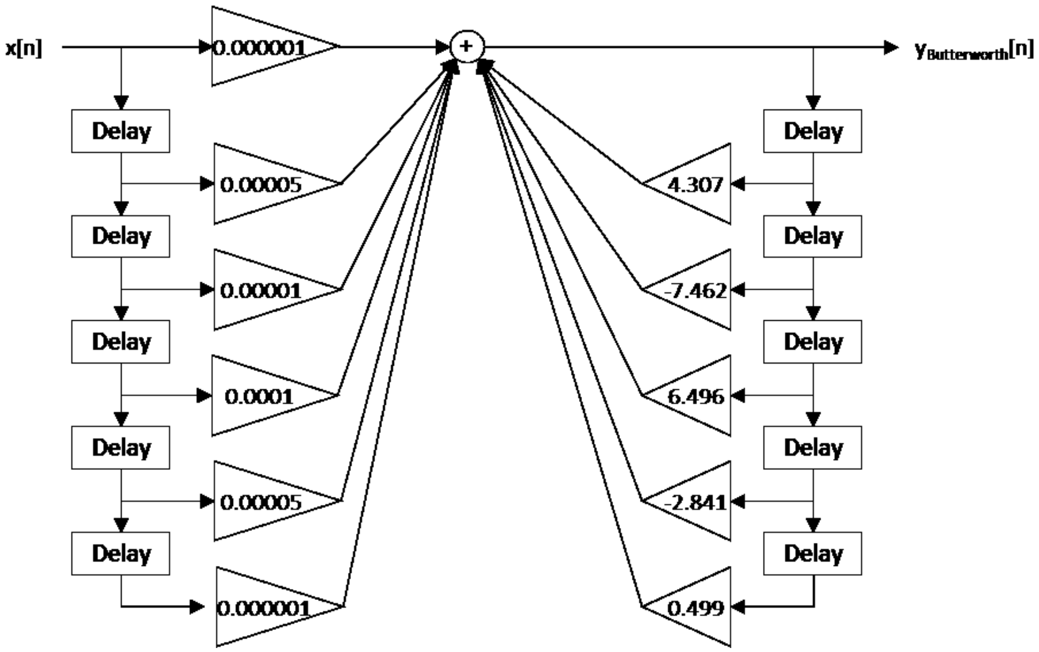

The filter for the tactor FSR was designed in the same way, only with slightly different specifications:

Pass band edge frequency, f_{p1}: 20 Hz
Stop band edge frequency, f_{s1}: 40 Hz

Appendix L. Design of Chebyshev Type II Filter

A Chebyshev Type II filter was investigated since it is monotonic through the pass band and can obtain a sharper roll-off than a Butterworth filter given the same filter order. The ripple in the stop band should not affect the data substantially, since it is being filtered out.

The filter was developed, for the case of the reference tactor, with the following specifications:

Pass band edge frequency, f_{p1}: 7 Hz
Stop band edge frequency, f_{s1}: 21 Hz
Sampling frequency, f_s: 250 Hz
Pass band ripple: 1 dB
Stop band attenuation: 40 dB

These can be converted to digital frequencies using:

$$\Omega = 2\pi \frac{f}{f_s}$$

Resulting in Ω_{p1} being equal to 0.176 rad and Ω_{s1} being equal to 0.528 rad. Next the pre-warped analog frequencies are calculated using:

$$\omega = 2f_s \cdot \tan\left({}^{\Omega}/_{2}\right)$$

Resulting in ω_{p1} being equal to 44.1 rad/s and ω_{s1} being equal to 135.1 rad/s. Then the attenuation is calculated:

$$\delta_P = 10^{-20/20} = 0.1$$

$$\delta_s = 10^{-40/20} = 0.01$$

Then the following parameters are determined:

$$\varepsilon = \sqrt{\frac{1}{(1-\delta_P)^2} - 1} = 0.484$$

$$\delta = \sqrt{\frac{1}{{\delta_s}^2} - 1} = 99.995$$

So finally the order required is calculated:

$$n \geq \frac{\cosh^{-1}\left({}^{\delta}/_{\varepsilon}\right)}{\cosh^{-1}\left({}^{\omega_{s1}}/_{\omega_{p1}}\right)} = 3.37$$

Therefore the minimum order of this Chebyshev Type II filter is 4. Because the transfer function is quite complex, the designfilt() function in Matlab was used to develop the Chebyshev Type II filter using the code below. This function creates a digital filter object, in place of determining the transfer function, H(s), and performing the bilinear transformation to obtain the digital transfer function, H(z), by hand.

```
Cheby = designfilt('lowpassiir','PassbandFrequency',PB,'StopbandFrequency',SB,'PassbandRipple',1,
'StopbandAttenuation',40,'DesignMethod','cheby2','SampleRate',fs);
```

The filter was designed to have a minimum order, which was determined to be 4, and is consistent with theory. The filter shape is therefore given by:

$$|H(\omega)| = \frac{1}{1 + \varepsilon^2 \left[\frac{{C_4}^2\left({}^{\omega_{s1}}/_{\omega_{p1}}\right)}{{C_4}^2\left({}^{\omega_{s1}}/_{\omega}\right)}\right]}$$

where $C_4(x) = \cos(4 \cdot \cos^{-1}(x))$ if $|x| \leq 1$

$C_4(x) = \cosh(4 \cdot \cosh^{-1}(x))$ if $|x| > 1$

Which produces the plot below.

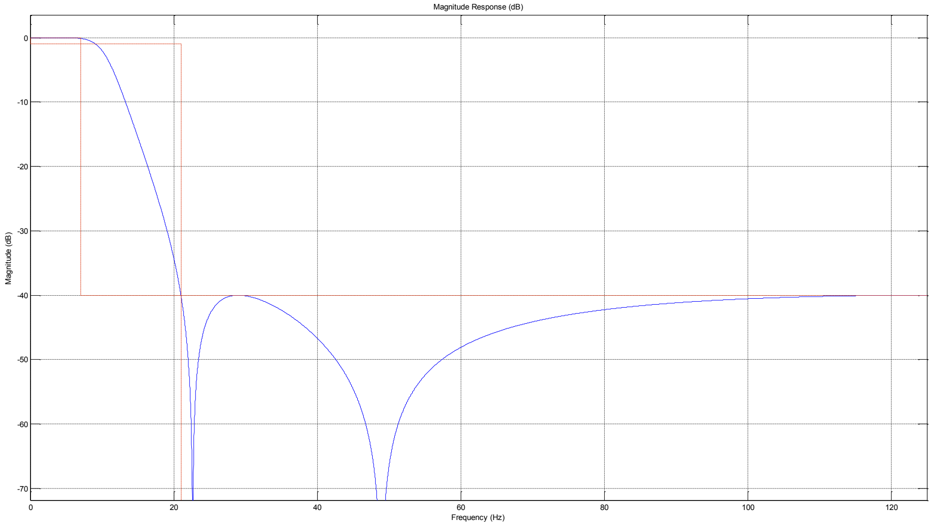

Figure L.1 Filter shape for Chebyshev Type II filter

The pole-zero plot was determined in Matlab, and is shown below.

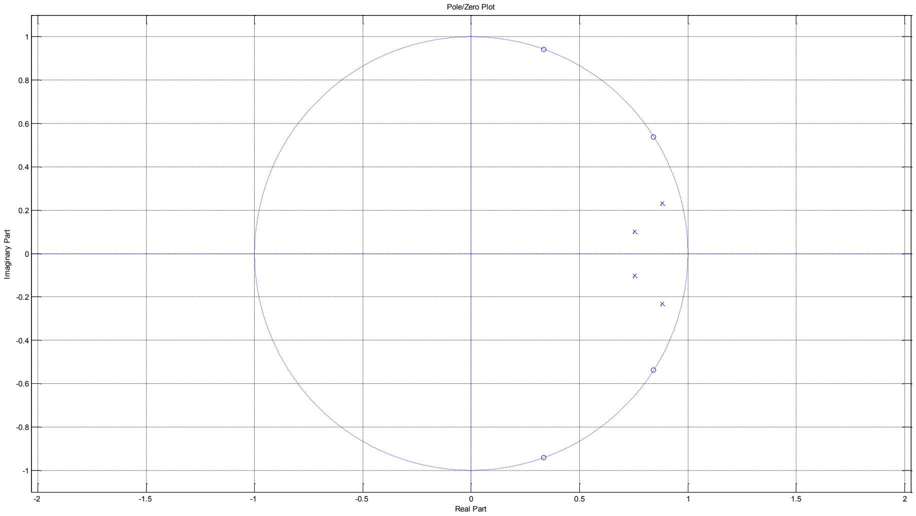

Figure L.2 Pole zero map for Chebyshev Type II filter

The poles are located within the unit circle, so the filter is stable. They are all on the right hand side so the filter should not result in alternating between positive and negative values. All are off of the real axis, suggesting that the filter may result in oscillations. Because the poles are close to the unit circle this is a very selective filter shape. The zeros are fairly close to the poles, so they will may help to reduce the oscillations.

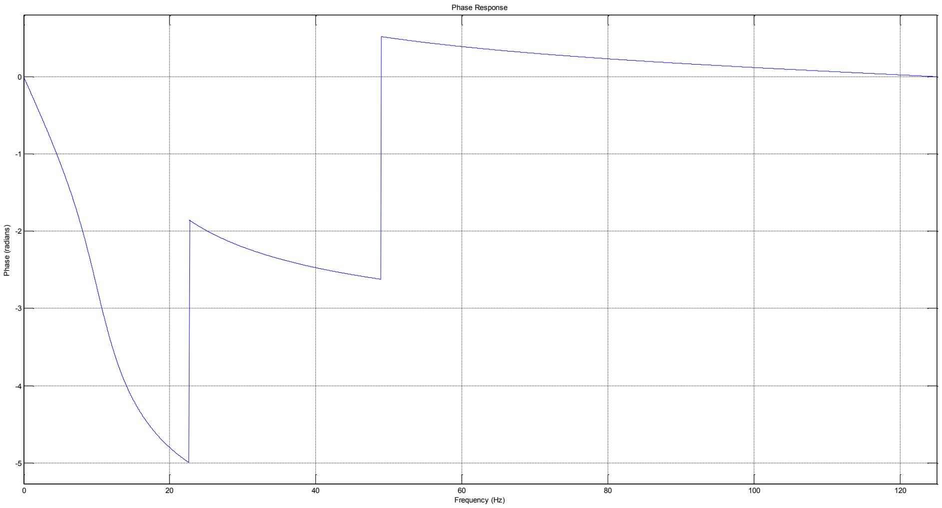

Figure L.3 Phase response for Chebyshev Type II filter

The phase response was determined in Matlab. There is some non-linearity in the pass-band, suggesting that phase distortion may occur. In this case, looking for example at Ω_0 = 10 Hz = 0.08π, the phase delay (*n*) is:

$$n = -\frac{\theta(\Omega_0)}{\Omega_0} = -\frac{-2.7}{0.08\pi} = 10.7 \approx 11 \text{ samples}$$

Compared to a phase dealy at Ω_0 = 20 Hz = 0.16π:

$$n = -\frac{\theta(\Omega_0)}{\Omega_0} = -\frac{-4.7}{0.16\pi} = 9.4 \approx 9 \text{ samples}$$

At a sampling frequency of 250 Hz, these correspond to a dealy of 0.043 s and 0.037 s, respectively.

The coefficients of the transfer function were determined using the function:

```
[b,a] = tf(Cheby);
```

The difference equation is given below:

$$\begin{aligned} y_{Chebyshev\ II}[n] \\ &= 0.0113x[n] - 0.0266x[n-1] + 0.0353x[n-2] - 0.0266x[n-3] \\ &+ 0.0113x[n-4] + 3.2749y[n-1] - 4.0772y[n-2] + 2.2803y[n-3] \\ &- 0.4827y[n-4] \end{aligned}$$

Or represented as a non-recursive difference equation diagram (Direct Form I Realization):

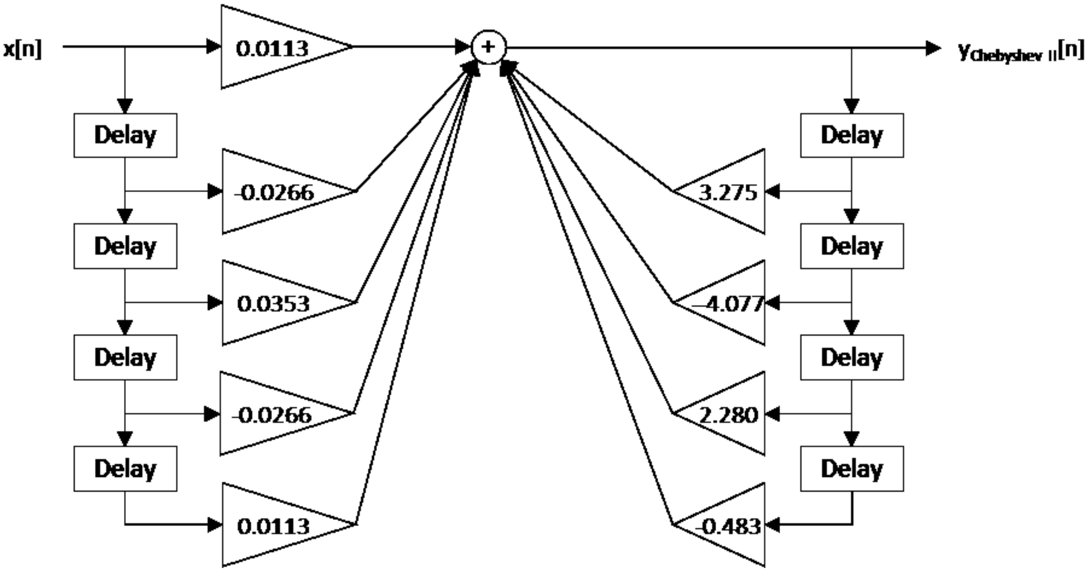

The filter for the tactor FSR was designed in the same way, only with slightly different specifications:

Pass band edge frequency, f_{p1}: 20 Hz
Stop band edge frequency, f_{s1}: 40 Hz

Appendix M. Matlab Code to Filter and Plot Data

The matlab code used to read in and filter the data (using the filters developed in previous appendices), is given below.

```
time = xlsread('Collecting raw data.xlsx','Tactor (tissue+liner)','A2:A3501');
rawV = xlsread('Collecting raw data.xlsx','Tactor (tissue+liner)','D2:D3501');

Length_array = length(rawV);
Length_FFT = 2^nextpow2(Length_array);
Frequency = fs/2*linspace(0,1,Length_FFT/2+1);

RawV_FFT = fft(rawV, Length_FFT)/Length_array;
RawV_phase = unwrap(angle(RawV_FFT))/Length_array;

Mov_avg_filterV = filter(Mov_avg,1,rawV);
Mov_avg_FilterV_FFT = fft(Mov_avg_filterV, Length_FFT)/Length_array;
Mov_avg_FilterV_phase = unwrap(angle(Mov_avg_FilterV_FFT))/Length_array;

Hann_filterV= filter(Hann,rawV);
Hann_FilterV_FFT = fft(Hann_filterV, Length_FFT)/Length_array;
Hann_FilterV_phase = unwrap(angle(Hann_FilterV_FFT))/Length_array;

Butter_filterV= filter(Butter,rawV);
Butter_FilterV_FFT = fft(Butter_filterV, Length_FFT)/Length_array;
Butter_FilterV_phase = unwrap(angle(Butter_FilterV_FFT))/Length_array;

Cheby_filterV= filter(Cheby,rawV);
Cheby_FilterV_FFT = fft(Cheby_filterV, Length_FFT)/Length_array;
Cheby_FilterV_phase = unwrap(angle(Cheby_FilterV_FFT))/Length_array;
```

The code to plot the raw and filtered data is shown below, in this case for the Hanning filter.

```
plot(time, rawV, time, Hann_filterV);
title('Time data from reference FSR'); xlabel('Time (s)'); ylabel('Voltage (V)');
legend('Raw FSR voltage','Hanning filter');

plot(Frequency,2*abs(RawV_FFT(1:Length_FFT/2+1)),Frequency,2*abs(Hann_FilterV_FFT(1:Length_F
FT/2+1)))
title('Amplitude of reference FSR')
xlabel('Frequency (Hz)')
ylabel('Voltage (V)')
legend('Raw FSR voltage','Hanning filter');
```

Note that many of the graphs were plotted in excel for ease of formatting.

Appendix N. Arduino Code for Open Loop Control

Sine Loading

```
// Arduino Tactor testing, setting displacement
//----------------------------------------------------------------------------------------------------------

// This script allows for a sine wave input to be sent to the servo motor to control its movement up
// and down. The period and maximum displacement can be set by manupulating parameters "period" and
// "MaxDisp" to achieve a desired load (measured with the load cell).

// Wiring: See wiring diagram in documentation

//----------------------------------------------------------------------------------------------------------

// Create servo object
#include <Servo.h>
Servo ch1_servo;       // Create servo object to control a servo

// Include timer
#include <Timer.h>

//-----------------------------------------------------------------------------------------------------------

// Initialize variables

// Force and displacement
int FSRpin = 0;              // Analog pin used to connect the FSR (A0)
int FSRread = 0;             // Read the value from the analog pin (FRSpin), between 0 and 1023

double Microsec = 2400;      // Angular position of servo in micro seconds

// Information for running through
int worn = 0;                // Variable to determine when to stop loading
double i = 0;                // Index to count cycles
int j = 0;                   // Index to count number of period changes
Timer t;                     // Initialize timer

double period = 2.0;         // Period of sine wave in seconds
double period2 = 1.0;
double period3 = 0.5;
int MaxDisp = 1400;          // Maximum displacement travelled (baseline = 2400)

int amp = (2400-MaxDisp)/2;  // Amplitude of sine wave
double freq = 3.1416*2/period;  // Frequency of sine wave

//-------------------------------------------------------------------------------------------------------------

void setup()
{
  // Servo set-up
  ch1_servo.attach(3);       // Attach servo on pin 3 to the servo object ch1_servo
  ch1_servo.write(2400);     // Set the servo position in microseconds

  t.every(10, changeLoad);   // Change load input every 0.01 s
  t.after(period*3000+1000, changePeriod); // Change period of input
  t.after(period*3000+period2*3000+2000, changePeriod); // Change period of input
}

//-------------------------------------------------------------------------------------------------------------
```

```
void loop()
{
    t.update();              // Update timer
}

//-----------------------------------------------------------------------------------------------
----------
// Set displacement of tactor head
void changeLoad()
{
  if (i <= 3*period)
  {
    Microsec = 2400+amp*(cos(freq*i)-1);
                                        // Determine new position in microseconds
    ch1_servo.write(Microsec);          // Set the servo position in microseconds
    FSRread = analogRead(FSRpin);       // Read the value of the FSR (value between 0 and 1023)
    i = i + 0.01;                       // Increment index
  }
}

//-----------------------------------------------------------------------------------------------
----------
// Change period of system
void changePeriod()
{
  if (j == 0)
  {
    period = period2;                   // Period changed to second
  }
  if (j == 1)
  {
    period = period3;                   // Period changed to third
  }

  amp = (2400-MaxDisp)/2;
  freq = 3.1416*2/period;
  j = j + 1;                          // Increment index
  i = 0;
}
```

Stepped Loading

```
// Arduino Tactor testing with logging capabilities
//-----------------------------------------------------------------------------------------------
-------

// This script has multiple functions:
// 1) Reads in FSR voltages and converts to force in N (from calibration curve)
// 2) Displays real-time graph of forces being read from the FSR
// 3) Allows real-time manipulation of PID tuning parameters in GUI
// 4) Displays output of PID controller to visualize how it is functioning
// 5) Displays angular position of the servo motor, which has set limits of extension
// 6) Tracks number of loops per 5 s cycle so that sampling frequency can be calculated
// 7) Code can be adjusted so the different digital low-pass filter cut-off is implemented

// Note: Low-pass filter values will need to be updated once final controller is implemented

// Wiring: See wiring diagram in documentation

// Note: A maximum of eight servo objects can be created
// Note: If you want to power more than 1 servo you need to attach a separate power supply that
can
//       handle more current.

//-----------------------------------------------------------------------------------------------
-------

// Create servo object
#include <Servo.h>
Servo ch1_servo;  // Create servo object to control a servo
```

```
// Include timer
#include <Timer.h>

//-----------------------------------------------------------------------------------------------
--------

// Initialize variables

// Force and displacement
int FSRpin = 0;        // Analog pin used to connect the FSR (A0)
int FSRread = 0;       // Read the value from the analog pin (FRSpin), between 0 and 1023
int FSRsmooth = 0;     // Hold smoothed FSR data
int FSRvolt = 0;       // Display FSR voltage in mV, between 0 and 5000 mV
int FSRforce = 0;      // Display FSR force in N^-1, between 0 and 100 N^-1
double Microsec = 2400;                  // Angular position of servo in micro seconds

Timer t;                                 // Initialize timer

int dir = 0;                             // Direction of travel
double minDisp = 1400;                      // Minimum displacement to travel to

double numSteps = 5;
double numSteps2 = 3;
double numSteps3 = 2;

double Step = (2400-minDisp)/(numSteps-1.0);      // Step size
double Step2 = (2400-minDisp)/(numSteps2-1.0);      // Step size
double Step3 = (2400-minDisp)/(numSteps3-1.0);      // Step size

double step_time = 2.0;                  // Time for each step in seconds

//-----------------------------------------------------------------------------------------------
----------

void setup()
{
  // Servo set-up
  ch1_servo.attach(3); // Attach servo on pin 3 to the servo object ch1_servo
  ch1_servo.write(2400); // Set the servo position in microseconds

  t.every(step_time*1000, changeMicrosec);
  t.after(step_time*(numSteps-1.0)*4*1000, changeStep2);
  t.after(step_time*(numSteps-1.0)*4*1000+step_time*(numSteps2-1.0)*4*1000, changeStep3);
  t.after(step_time*(numSteps-1.0)*4*1000+step_time*(numSteps2-1.0)*4*1000+step_time*(numSteps3-
1.0)*4*1000, complete);
}

//-----------------------------------------------------------------------------------------------
----------

void loop()
{
  ch1_servo.write(Microsec);        // Set the servo position in microseconds
  FSRread = analogRead(FSRpin);     // Read the value of the FSR (value between 0 and 1023)
  t.update();

}

//-----------------------------------------------------------------------------------------------
----------
// Set displacement
void changeMicrosec()
{
  if (dir == 0)
  {
    Microsec = Microsec - Step;
    if (Microsec <= minDisp)
    {
      Microsec = minDisp;
      dir = 1;
```

```
      return;
    }
  }
  if (dir == 1)
  {
    Microsec = Microsec + Step;
    if (Microsec >= 2400)
    {
      Microsec = 2400;
      dir = 0;
      return;
    }
  }
  if (dir == 2)
  {
    return;
  }
}
//-----------------------------------------------------------------------------------------------
----------
// Change step size
void changeStep2()
{
  Step = Step2;
}

//-----------------------------------------------------------------------------------------------
----------
// Change step size
void changeStep3()
{
  Step = Step3;
}

//-----------------------------------------------------------------------------------------------
----------
// End
void complete()
{
  dir = 2;
}
```

Appendix O. Arduino Code for Closed Loop Control

```
// Arduino Tactor testing with logging capabilities
//-----------------------------------------------------------------------------------------------
-------

// This script has multiple functions:
// 1) Reads in FSR voltages from reference and tactor
// 2) Filters voltages using a Chebyshev Type II low pass filter
// 3) Controls applied force of the tactor through a PID controller (parameters change based on
input)
// 4) Converts voltage from tactor FSR to force in N (from calibration curve)
// 5) Limits servo motor position to within its limits of extension
// 6) Logs time, reference FSR voltage, tactor FSR voltage, and angular position of the servo
motor
// 7) Can be set to read in force from reference FSR to control tactor, or set displacement

// Wiring: See wiring diagram in documentation

//-----------------------------------------------------------------------------------------------
-------

// Include PID
#include <PID_v1.h>

// Include timer
#include <Timer.h>

// Create servo object
#include <Servo.h>
Servo ch1_servo;  // Create servo object to control a servo

// Include SD logging
#include <SPI.h>
#include <SD.h>

//-----------------------------------------------------------------------------------------------
--------
// Initialize variables

// Forces from FSRs
int referenceFSRpin = 1;        // Analog pin used to connect the FSR (A1)
double referenceFSRraw = 0;        // Read the value from the analog pin (FRSpin), between 0 and
1023
double referenceFSRsmooth = 0;     // Hold smoothed FSR data
double referenceFSRforce = 0;         // Display FSR force in N

int tactorFSRpin = 0;           // Analog pin used to connect the FSR (A0)
double tactorFSRraw = 0;           // Read the value from the analog pin (FRSpin), between 0 and
1023
double tactorFSRsmooth = 0;        // Hold smoothed FSR data
double tactorFSRforce = 0;         // Display FSR force in N

// Chebyshev Type II filter coefficients
double referenceChebya[] = {-3.274875456, 4.077205777, -2.280262547, 0.482671488};
double referenceChebyb[] = {0.011300372, -0.026602723, 0.035343963, -0.026602723, 0.011300372};
double referenceInputs[] = {0.0, 0.0, 0.0, 0.0, 0.0};
double referenceOutputs[] = {0.0, 0.0, 0.0, 0.0};

double tactorChebya[] = {-2.73478376994962, 3.32413592591151, -2.12073179506603,
0.708514340005999, -0.0969045892706058};
double tactorChebyb[] = {0.0214542546435920, -0.00282706517445090, 0.0214878663464866,
0.0214878663464866, -0.00282706517445090, 0.0214542546435920};
double tactorInputs[] = {0.0, 0.0, 0.0, 0.0, 0.0, 0.0};
double tactorOutputs[] = {0.0, 0.0, 0.0, 0.0, 0.0};

// Servo displacement
double Microsec = 2400;           // Angular position of servo in micro seconds

// PID controller
```

```
double Setpoint = 0.0;            // Setpoint for PID controller
double Input, Output;             // Variables to connect to with PID controller
PID myPID(&Input, &Output, &Setpoint,0.23,0.00,0,DIRECT);    // Links and tuning parameters

// Aggressive and conservative tuning parameters
double Kp = 1.0;               // Position term of PID controller
double Ki = 0.05;              // Integral term of PID controller
double Kd = 0.05;              // Derivative term of PID controller

// Recording to microSD card
unsigned long time;              // Displays time in milliseconds since program started
int worn = 0;                    // Variable to determine if worn out
int IntMicro = 0;

// Timer used to control initiation of various events
Timer t;                        // Initialize timer
int count = 0;
double gap = 0;

//-----------------------------------------------------------------------------------------------
----------

void setup()
{
  // Servo set-up
  ch1_servo.attach(3);         // Attach servo on pin 3 to the servo object ch1_servo
  ch1_servo.write(2400);       // Set the servo position in microseconds

  // PID controller set-up
  myPID.SetMode(AUTOMATIC);                  // Turn the PID controller on
  myPID.SetOutputLimits(-100,100);           // Set output limits to include negative value
  myPID.SetTunings(Kp, Ki, Kd);              // Set PID tuning values

  // Start the SD card logging
  pinMode(10, OUTPUT);                       // Default chip select pin must be set to output to
function
  // On the Ethernet Shield, CS is pin 4. Note that even if it's not used as the CS pin, the
hardware
  // CS pin (10 must be left as an output or the SD library functions will not work).
  SD.begin(4);
  SPI.setClockDivider(SPI_CLOCK_DIV2);       // Make the SPI fastest possible to send information
faster

  // Output notes and headers to file
  File dataFile = SD.open("PID.txt", FILE_WRITE);

  dataFile.println("Time (ms), Reference voltage (*5/1023), Tactor voltage (*5/1023),
Displacement (microsec)");
                           // Create headers for columns
  dataFile.close();

  // Operate functions based on timer so that cycle time is repeatable
  t.every(1000, sendSD);         // Write data every 1 s
  t.every(4, referenceFSRread);  // Read in FSR voltage from input on prosthesis every 0.004 s
  t.every(4, tactorFSRread);     // Read in FSR voltage from tactor every 0.004 s
  t.every(4, PIDset);            // Set position based on PID controller every 0.004 s (so no
delay from sensors)
  //t.every(2000,changeLoad);
}

//-----------------------------------------------------------------------------------------------
----------

void loop()
{
  t.update();                    // Update the timer
}

//-----------------------------------------------------------------------------------------------
----------
// Read FSR value from sensor on prosthesis (reference) and filter with low-pass filter
```

```
void referenceFSRread()
{
  referenceFSRraw = analogRead(referenceFSRpin);   // Read the value of the FSR (value between 0 
and 1023)

  // Shift values in the inputs array to the left
  for(int i = 4; i > 0; i--)
  {
    referenceInputs[i] = referenceInputs[i-1];
  }
  referenceInputs[0] = referenceFSRraw;             // Add new input value

  // Shift values in the outputs array to the left
  for(int i = 3; i > 0; i--)
  {
    referenceOutputs[i] = referenceOutputs[i-1];
  }
  referenceOutputs[0] = referenceFSRsmooth;         // Add previous output value
  referenceFSRsmooth = 
referenceChebyb[0]*referenceInputs[0]+referenceChebyb[1]*referenceInputs[1]+referenceChebyb[2]*re
ferenceInputs[2]+referenceChebyb[3]*referenceInputs[3]+referenceChebyb[4]*referenceInputs[4]-
referenceChebya[0]*referenceOutputs[0]-referenceChebya[1]*referenceOutputs[1]-
referenceChebya[2]*referenceOutputs[2]-referenceChebya[3]*referenceOutputs[3];
  referenceFSRforce = 0.056069*exp(referenceFSRsmooth*0.006286)-0.056069;    // Calculate the 
value of the FSR in N^-1
}

//-----------------------------------------------------------------------------------------------
----------
// Read FSR value from sensor on tactor (response) and filter with low-pass filter

void tactorFSRread()
{
                       // Number of milliseconds since the program started

  tactorFSRraw = analogRead(tactorFSRpin);   // Read the value of the FSR (value between 0 and 
1023)

  // Shift values in the inputs array to the left
  for(int i = 5; i > 0; i--)
  {
    tactorInputs[i] = tactorInputs[i-1];
  }
  tactorInputs[0] = tactorFSRraw;             // Add new input value

  // Shift values in the outputs array to the left
  for(int i = 4; i > 0; i--)
  {
    tactorOutputs[i] = tactorOutputs[i-1];
  }
  tactorOutputs[0] = tactorFSRsmooth;         // Add previous output value
  tactorFSRsmooth = 
tactorChebyb[0]*tactorInputs[0]+tactorChebyb[1]*tactorInputs[1]+tactorChebyb[2]*tactorInputs[2]+t
actorChebyb[3]*tactorInputs[3]+tactorChebyb[4]*tactorInputs[4]+tactorChebyb[5]*tactorInputs[5]-
tactorChebya[0]*tactorOutputs[0]-tactorChebya[1]*tactorOutputs[1]-
tactorChebya[2]*tactorOutputs[2]-tactorChebya[3]*tactorOutputs[3]-
tactorChebya[4]*tactorOutputs[4];
  tactorFSRforce = 0.056069*exp(tactorFSRsmooth*0.006286)-0.056069;    // Calculate the value of 
the FSR in N^-1
}

//-----------------------------------------------------------------------------------------------
----------
// Determine position servo motor needs to move to

void PIDset()
{
  if(referenceFSRforce <= 0.01)         // Prevent servo from trying to set a force of 0; not 
possible with exponential fit
  {
```

```
    Microsec = 2400;
    myPID.SetMode(MANUAL);      // Turn PID off to prevent wind up
    Output = 0.0;               // Reduce output to 0 so no jump upon start-up
  }
  else if (referenceFSRforce >= 10.0)
  {
    Setpoint = 10.0;
  }
  else
  {
    Setpoint = referenceFSRforce; // Update setpoint to equal the input from the reference FSR
  }

  if(Setpoint > 0.01)          // Start controlling if desired force is greater than 0
  {
    //  PID control
    myPID.SetMode(AUTOMATIC);         // Turn PID on
    Input = tactorFSRforce;          // Link input of controller to force being read from FSR
    myPID.Compute();                  // Compute output of controller
    Microsec = Microsec - Output;     // Update position of servo (minus since higher force needs
lower angular position)

    // Check that angular position is within limits of servo motor, if not keep position within
limits
    if (Microsec > 2400)
    {
      Microsec = 2400;        // Set angular position to minimum
      myPID.SetMode(MANUAL);  // Turn PID off (prevents wind up)
      Output = 0.0;           // Reduce output to 0 so no jump upon start-up
    }
    if (Microsec < 600)
    {
      Microsec = 600;         // Set angular position to maximum
      myPID.SetMode(MANUAL);  // Turn PID off (prevents wind up)
      Output = 0.0;           // Reduce output to 0 so no jump upon start-up
      worn = 1;
      return;
    }
  }

  ch1_servo.write(Microsec);  // Set the servo position in microseconds
}

//-----------------------------------------------------------------------------------------------
----------
// Send SD data to SD port on ethernet shield
void sendSD()
{
  time = millis();                     // Number of milliseconds since the program started

  File dataFile = SD.open("PID.txt", FILE_WRITE);

  if (dataFile)                        // If the file is available, write to it:
  {
    dataFile.print(time);              // Print information to SD card
    dataFile.print(",");
    dataFile.print(",");
    dataFile.print(referenceFSRsmooth);
    dataFile.print(",");
    dataFile.print(tactorFSRsmooth);
    dataFile.print(",");
    IntMicro = int(Microsec);
    dataFile.println(IntMicro);

    dataFile.close();
  }
}

//-----------------------------------------------------------------------------------------------
----------
// Change load
```

```
void changeLoad()
{
  if (count == 0)
  {
    referenceFSRforce = 2.5;
  }
  if (count == 1)
  {
    referenceFSRforce = 0.1;
  }
  if (count == 2)
  {
    referenceFSRforce = 2.5;
  }
  if (count == 3)
  {
    referenceFSRforce = 0.1;
  }
  if (count == 4)
  {
    referenceFSRforce = 5.0;
  }
  if (count == 5)
  {
    referenceFSRforce = 0.1;
  }
  if (count == 6)
  {
    referenceFSRforce = 8.0;
  }
  if (count == 7)
  {
    referenceFSRforce = 5.0;
  }
  if (count == 8)
  {
    referenceFSRforce = 8.0;
  }
  if (count == 9)
  {
    referenceFSRforce = 2.5;
  }
  if (count == 10)
  {
    referenceFSRforce = 8.0;
  }
  if (count == 11)
  {
    referenceFSRforce = 0.1;
  }
  count = count+1;
}
```

Appendix O.5

Appendix P. PID Control using Load Cell in Simulink

A linear tactor was placed in-line with a load cell with the goal of developing a more accurate tactor (Figure P.1). While this would not be useful as a socket mounted tactor due to its bulk, it was designed to allow for other testing applications requiring more accurate force application.

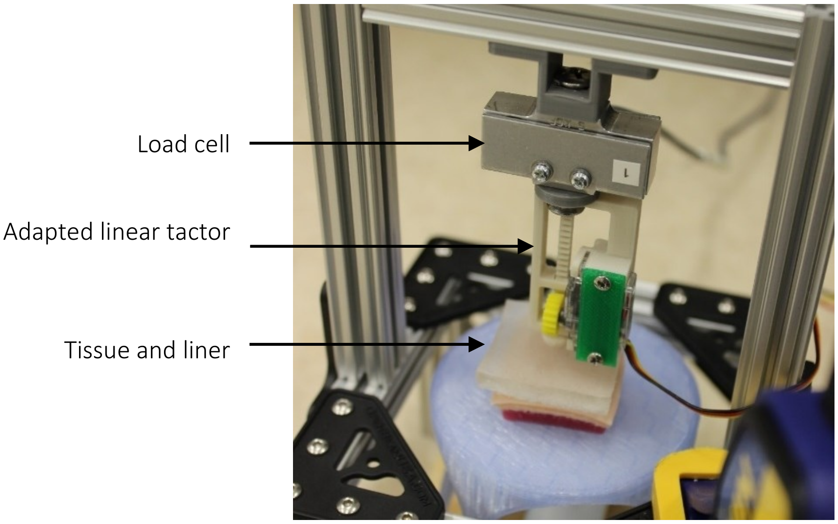

Figure P.1 Tactor with in-line load cell

A Simulink model was built to control the tactor (Figure P.2), where data is read in from the load cell and reference FSR, filtered, and input to the PID controller, and the output is converted to a PWM signal and sent to the servo motor. Data was logged to the computer to allow for post processing.

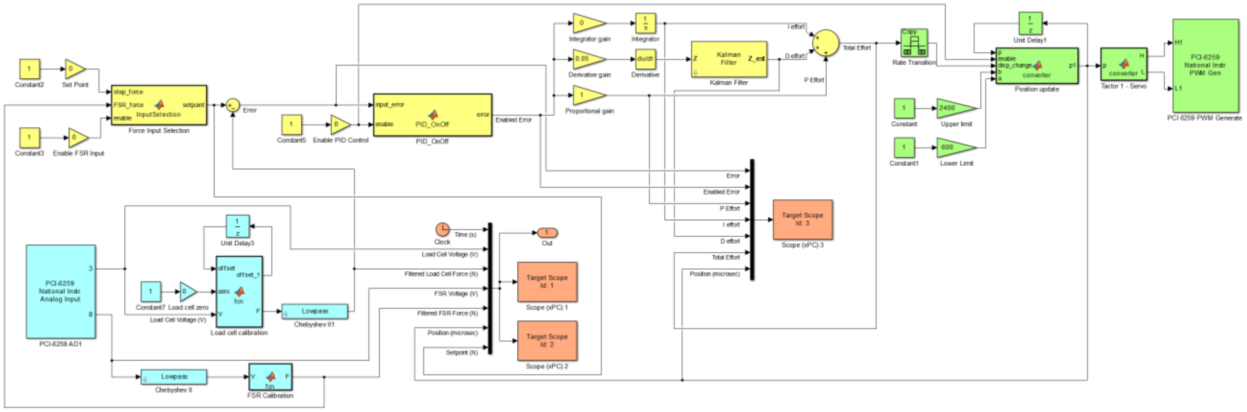

Figure P.2 Evaluation of closed-loop control on (a) tissue analog, and (b) covered with alpha liner

Initially, the same tuning parameters as those used in the FSR controller were applied (K_p = 1.0, K_i = 0.05, K_d = 0.05). While these parameters worked well for the case of loads applied by hand, they produced oscillations for the step inputs (Figure P.3). This is likely due to some play between the rack and pinion gears being measured by the load cell, so a better mesh between teeth would likely help mitigate this issue.

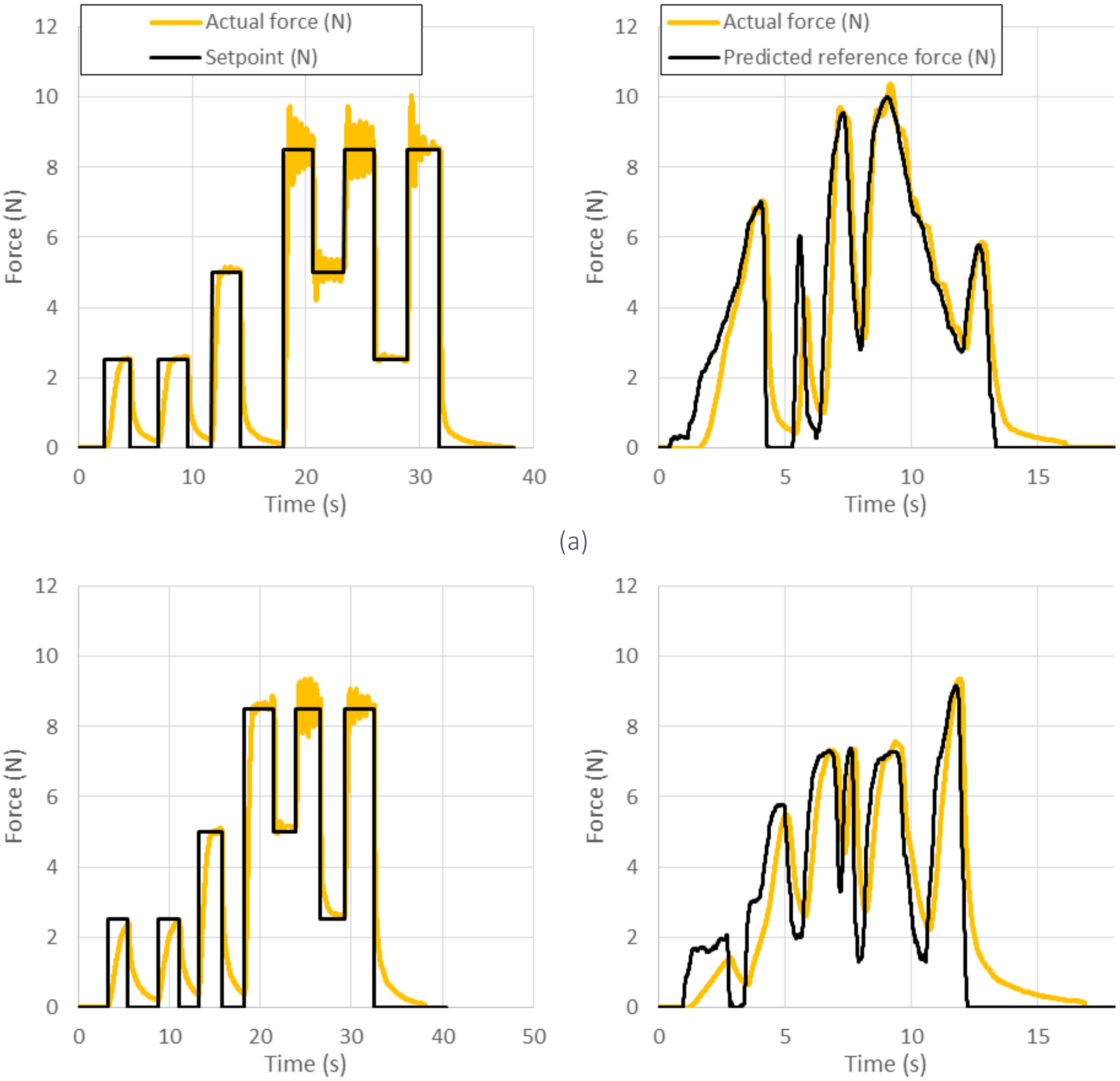

(a)

(b)

Figure P.3 Evaluation of closed-loop control on (a) tissue analog, and (b) covered with alpha liner

An alternative solution was to reduce the K_p term to 0.5 and remove the K_i term, however this increased the overall response time to a typical delay of 0.5 to 0.7 s (Figure E.1). Taken together, this suggests that more gradual loading with higher gains will be more accurate; if step loading is required, lower gains will be required, resulting in longer time delays.

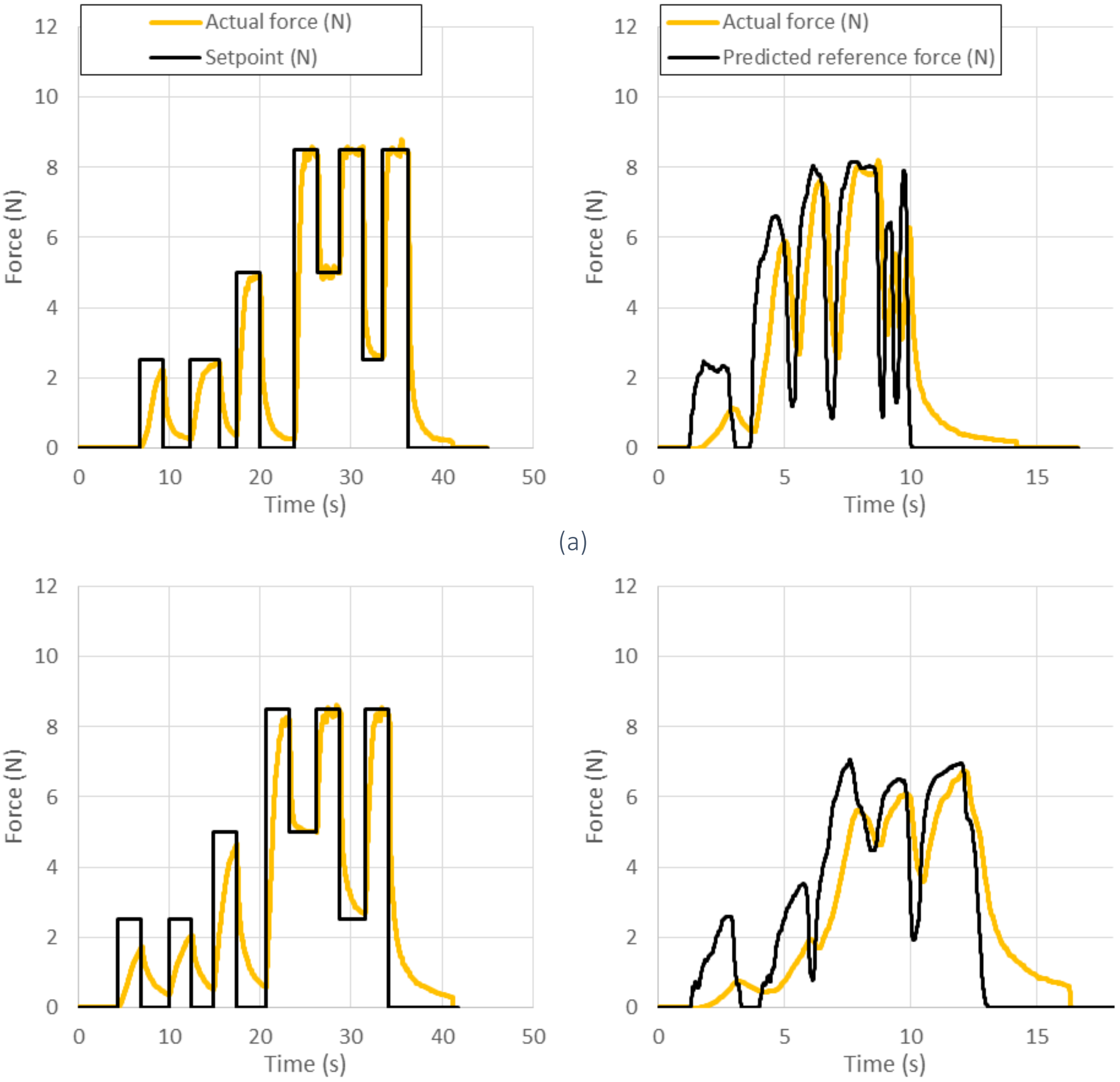

(a)

(b)

Figure P.4 Evaluation of closed-loop control on (a) tissue analog, and (b) covered with alpha liner, with reduced controller gains

Appendix Q. Interface Decision Matrix

Table Q.1 Decision matrix used to select interface sealing method

Item #	Component / system description	Design specification / requirement	Design authority	Weight [a]	Maximum	Absolute [b]			Normalized			Weighted			Notes
						C.1 [c]	C.2	C.3	C.1	C.2	C.3	C.1	C.2	C.3	
1.00	**Overall**														
1.20	**Total weight (max)**														
1.22	Tactor	< 50 g per tactor	BLINC	-2	5	1	5	2	2	10	4	-4	-20	-8	Enclosure requires significant bulk
1.30	**Total cost**														
	Tactor	< $200	BLINC	-2	1	1	1	1	10	10	10	-20	-20	-20	All methods should be inexpensive
1.40	**Manufacturability**														
1.41	Off-the-shelf components	Components should be purchased off-the-shelf where possible	BLINC	2	5	5	1	3	10	2	6	20	4	12	Interface and enclosure requires some manufacturing
1.42	In-house manufacturing	Components should be easily manufactured with available equipment	BLINC	3	5	5	5	5	10	10	10	30	30	30	All methods can be easily manufactured
1.50	**Timing**														
1.52	Device lifetime	Last up to 1 month of intermittent testing	BLINC	3	5	5	5	3	10	10	6	30	30	18	Repetitive loading may reduce lifetime of interface

Item #	Component / system description	Design specification / requirement	Design authority	Weight (a)	Maximum	Absolute (b)			Normalized			Weighted			Notes
1.60	**Materials allowed**	**Biocompatible with no cytotoxicity, irritation, and sensitization**	**ISO-22523**	**5**	5	**5**	**5**	**5**	10	10	10	50	50	50	**All materials must be biocompatible**
2.00	Mechanical Requirements														
2.40	**Skin interaction**														
2.41	Minimized risk to skin	Reduce unacceptable pressure on and stress levels to body tissue	ISO-22523	5	5	1	3	5	2	6	10	10	30	50	Compartment may cause localized pressure point, interface may help distribute force
2.42	Moving parts	Remove risk of trapping or damaging skin, hair, clothing, during normal usage	ISO-22523	5	3	1	3	3	3	10	10	17	50	50	Compartment may cause localized pressure point, interface will prevent pinching at skin interface, enclosure will reduce likelihood of catching
2.43	Skin fatigue	Prevent tissue breakdown from continuous skin fatigue	BLINC	5	5	1	3	5	2	6	10	10	30	50	Compartment may cause localized pressure point, interface may help distribute applied force and prevent abrasion
2.44	Skin abrasions	Prevent penetration of the skin	BLINC	5	5	3	3	5	6	6	10	30	30	50	Interface may distribute applied force

Item #	Component / system description	Design specification / requirement	Design authority	Weight [(a)]	Maximum	Absolute [(b)]			Normalized			Weighted			Notes
2.45	Maximum allowable force	7 N maximum	BLINC	4	5	5	5	1	10	10	2	40	40	8	Interface may interfere with maximum applied force
2.50	**Socket integration**														
2.51	Vacuum seal	Must be maintained	BLINC	5	5	5	5	5	10	10	10	50	50	50	All methods will maintain suction seal
2.52	Interference with tactor	Minimal interference with applied force of tactor	BLINC	3	5	5	5	1	10	10	2	30	30	6	Interface may interfere with applied force
2.53	Skin protrusion	Prevent skin from bulging out of socket	BLINC	3	5	1	2	5	2	4	10	6	12	30	Compartment may force more skin protrusion, interface may prevent protrusion
Total												299	346	**376**	

(a) Weight based on design importance specified

(b) All absolute values are relative

(c) C.1 refers to the compartmentalized arm concept, C.2 the tactor-skin interface seal, and C.3 the enclosed tactor

Based on this decision matrix, the optimal sealing method to move forward with development is the tactor-skin interface seal.

Appendix R. Silicone Shaping

An attempt was made to shape the silicone using a mould by clamping a silicone sheet within the mould for three days.

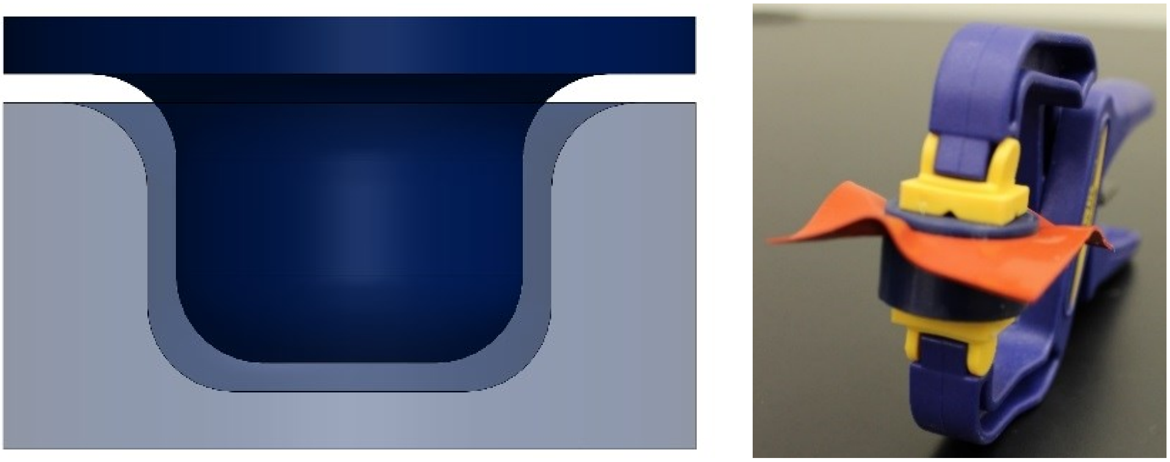

(a) (b)

Figure R.1 Silicone mould (a) designed, and (b) manufactured and clamped over silicone sheet

The shape of the silicone did not remain permanently deformed, and returned to near its original shape within 48 hours. It is possible that this shaping could be more permanent if set at higher temperatures, however the melting point of PLA (used for the mould construction) is between 110 and 170°C [128], which is only slightly higher than the approximate 100°C required to enhance the recovery of a rubber material [124]. So either a different moulding or forming process would be required.

(a) (b) (c)

Figure R.2 Silicone sheet (a) immediately, (b) 30 minutes, and (d) 48 hours after removal